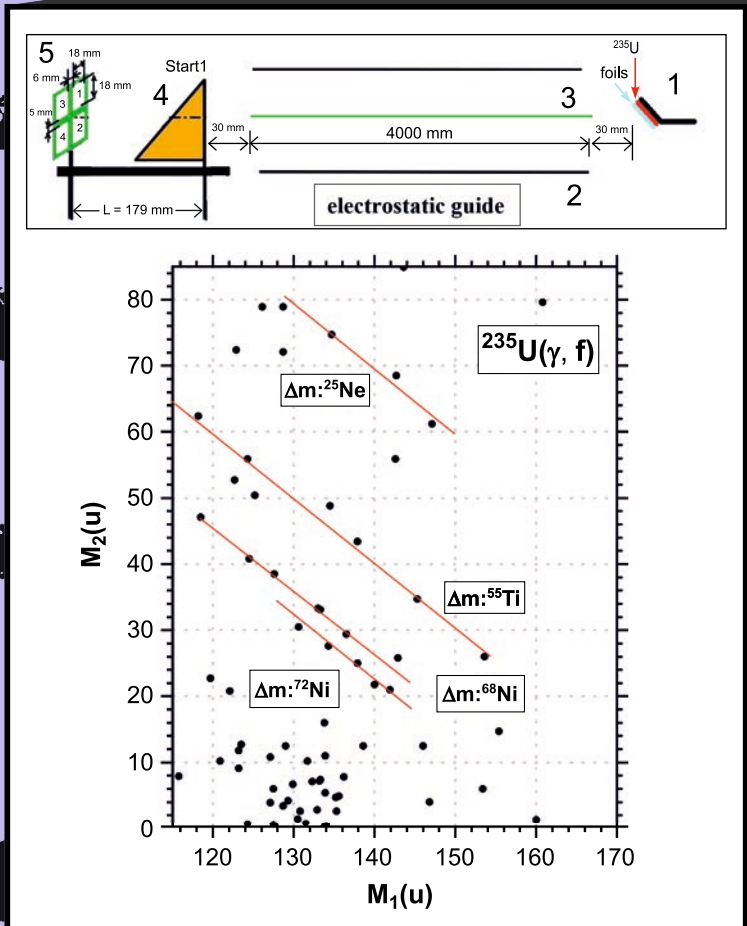


# ISINN-27

Neutron Spectroscopy,  
Nuclear Structure,  
Related Topics



Joint Institute for Nuclear Research

**FUNDAMENTAL  
INTERACTIONS & NEUTRONS,  
NUCLEAR STRUCTURE,  
ULTRACOLD NEUTRONS,  
RELATED TOPICS**

*XXVII International Seminar  
on Interaction of Neutrons with Nuclei*

Dubna, Russia, June 10–14, 2019

*Proceedings of the Seminar*

УДК 539.125.5(042)  
ББК 22.383.2я431+22.383.5я431+22.383.25я431  
F97

### *Organizing Committee*

V. N. Shvetsov (*co-chairman*), W. I. Furman (*co-chairman*),  
E. V. Lychagin (*scientific secretary*), Yu. N. Kopatch,  
P. V. Sedyshev, L. V. Mitsyna, M. V. Frontasyeva

Secretariat: T. S. Donskova (*seminar coordinator*),  
N. A. Malysheva, T. L. Pikelner, E. S. Kopatch

The contributions are reproduced directly from the originals presented  
by the Organizing Committee.

**Fundamental Interactions & Neutrons, Nuclear Structure, Ultracold Neutrons, Related**  
F97 Topics: Proceedings of the XXVII International Seminar on Interaction of Neutrons with  
Nuclei (Dubna, Russia, June 10–14, 2019). — Dubna: JINR, 2020. — 268 p.  
ISBN 978-5-9530-0533-3

This collection of papers reflects the present state of neutron-aided investigations of the properties of the nucleus, including fundamental symmetries, properties of the neutron itself, neutron-excited reactions, and the parameters of the nucleus that determine the reaction cross section, as well as the latest theoretical development of all these problems. The works on experimental investigations in the physics of fission by neutrons of various energies are presented in great detail. The present state of experiments on the physics of ultracold neutrons and facilities to obtain them is described at length. The status achieved by now of the latest (from the viewpoint of technique) experiments and environment studies is covered as well.

**Фундаментальные взаимодействия и нейтроны, структура ядра, ультрахолодные нейтроны, связанные темы:** Труды XXVII Международного семинара по взаимодействию нейтронов с ядрами (Дубна, Россия, 10–14 июня 2019 г.). — Дубна: ОИЯИ, 2020. — 268 с.  
ISBN 978-5-9530-0533-3

В сборнике представлено современное состояние исследований свойств ядра с помощью нейтронов: фундаментальных симметрий и свойств самого нейтрона, возбуждаемых им реакций и параметров ядра, определяющих их сечения, а также последние теоретические разработки всех этих вопросов. Очень детально представлены работы по всем аспектам, связанным с экспериментальными исследованиями физики деления ядра нейтронами различных энергий. Достаточно полно описано современное состояние экспериментов по физике ультрахолодных нейтронов и установок для их получения, а также достигнутый к настоящему времени статус методически новейших экспериментов и результаты экологических исследований.

УДК 539.125.5(042)  
ББК 22.383.2я431+22.383.5я431+22.383.25я431

ISBN 978-5-9530-0533-3

© Joint Institute for Nuclear  
Research, 2020

# CONTENTS

<b>Preface</b> .....	7
<b><u>Neutron Sources</u></b>	
<b>The Scheme of Antineutrino Source with Regulated Hard Spectrum on the Base of Nuclear Reactor and Possible Experiment for Search of Sterile Neutrinos</b> <i>Lyashuk V.I.</i> .....	11
<b>Formation and Measurement of the Thermal Neutron Beam at the Tandetron Accelerator</b> <i>Mitrofanov K.V., Egorov A.S., Gremyachkin D.E., Piksaikin V.M.</i> .....	23
<b><u>Nuclear Structure</u></b>	
<b>Creation of Transuraniums under Neutron Fluxes of Nuclear Explosions</b> <i>Lotostansky Yu.S., Lyashuk V.I.</i> .....	33
<b>Analysis of Nuclear Excitations in Different Elements</b> <i>Sukhoruchkin S.I., Soroko Z.N., Sukhoruchkin D.S.</i> .....	40
<b>Combined Analysis of Nuclear Data and Particle Masses. II</b> <i>Sukhoruchkin S.I., Sukhoruchkina M.S.</i> .....	54
<b>Problems and Possibilities of a Study of the Cascade Gamma-Decay of a Nucleus Excited below the Neutron Binding Energy</b> <i>Sukhovej A.M., Mitsyna L.V., Vu D.C., Jovančević N., Knežević D., Krmar M., Dragić A.</i> .....	70
<b>Experimental Study of the Gamma-Decay of Compound-States of <math>^{56}\text{Mn}</math> and <math>^{94}\text{Nb}</math> Nuclei in the <math>(n_{\text{th}}, 2\gamma)</math>-Reaction</b> <i>Sukhovej A.M., Mitsyna L.V., Jovančević N., Knežević D., Dragić A., Szentmiklósi L., Belgya T., Revay Z., Stieghorst Ch., Oberstedt S., Krmar M., Maletić D., Joković D.</i> .....	80
<b>Neutroneum — Applications of the Half-Phenomenological Approach</b> <i>Ratis Yu.L.</i> .....	88

## **Neutron Induced Reactions**

### **Statistical Model Analysis of (n,t) Cross Sections for 14–15 MeV Neutrons**

*Khuukhenkhuu G., Munkhsaikhan J., Odsuren M., Saikhanbayar Ch., Batchimeg B., Gledenov Yu.M., Sansarbayar E., Sedysheva M.V. ....*97

### **Fast Neutrons Processes on Molybdenum Isotopes**

*Oprea C., Oprea A.I. ....*103

### **Asymmetry and Spatial Symmetry Breaking Effects Modeling in (n,p) Reactions**

*Oprea C., Oprea A.I. ....*110

### **Angular Distribution of 1.368 MeV Gamma-Rays from Inelastic Scattering of 14.1 MeV Neutrons on <sup>24</sup>Mg**

*Ruskov I.N., Kopatch Yu.N., Bystritsky V.M., Grozdanov D.N., Fedorov N.A., Tretyakova T.Yu., Skoy V.R., Dabylova S., Aliyev F.A., Hramco C., Kumar A., Gandhi A., Wang D., Bogolyubov E.P., Barmakov Yu.N., and TANGRA Collaboration.....*117

## **Applied and Methodical Aspects of Neutron Physics, Calculations**

### **Comparison of Artificial Neural Network Architectures by the Separation Quality of Signals from a Digital Neutron Spectrometer**

*Bobrovsky T., Prusachenko P., Khryachkov V. ....*133

### **Some Improvements of the Data Processing Algorithms in the Time-of-Flight Mass-Spectrometry of Heavy Ions**

*Kamanin D.V., Pyatkov Yu.V., Goryainova Z.I., Zhuchko V.E., Alexandrov A.A., Alexandrova I.A., Naumov P.Yu., Korsten R., Malaza V., Kuznetsova E.A., Strekalovsky A.O., Strekalovsky O.V. ....*138

### **Monte Carlo Simulation of Ions in the Radiative Neutron Decay Experiment**

*Khafizov R.U., Kolesnikov I.A., Nikolenko M.V., Tarnovitsky S.A., Tolokonnikov S.V., Torokhov V.D., Trifonov G.M., Solovei V.A., Kolkhidashvili M.R., Konorov I.V.....*145

### **Programs for the R-Matrix Description of Neutron Cross-Section Structure**

*Popov A.B.....*158

**Investigation of the Systematic Time Mark Shift for the Signals from the Organic Scintillator Based Neutron Spectrometer**  
*Prusachenko P., Khryachkov V., Bobrovsky T., Ketterov V., Bondarenko I. ....*162

**TySSA — A Set of Means for Building of Distributed Software Systems for the Automation of Experiments by the User**  
*Shvetsov V.N., Salamatin K.M., Salamatin I.M., Tsulaia M.I. ....*170

### **Nuclear Analytical Methods in the Life Sciences**

**Using XRF Analysis to Determine the Elemental Composition of Pigments in the Painting of Medieval Oriental Faïences**  
*Koval V.Yu., Dmitriev A.Yu., Smirnova V.S., Lobachev V.V.....*179

**Investigation of the Element Composition of Barmas Medallion (the 12th – First Half of the 13th Centuries) by Method of Neutron Resonance Capture Analysis**  
*Simbirtseva N.V., Sedyshev P.V., Mazhen S.T., Mareev Yu.D., Shvetsov V.N., Yergashov A.M., Dmitriev A.Yu., Saprykina I.A., Khokhlov A.N., Kozlova O., Artemicheva T.....*187

**Trace Element Concentrations in the Prostatic Secretion of Patients with Chronic Prostatitis and Benign Prostatic Hyperplasia Investigated by X-Ray Fluorescence**  
*Zaichick V., Zaichick S. ....*192

**Neutron Activation Analysis of Br, Ca, Cl, K, Mg, Mn, Na, and Sr Concentrations in Human Saliva in Health and Parodontopathy**  
*Zaichick V., Zaichick S. ....*199

**Relationship between Ca, Cl, K, Mg, Mn, Na, P, and Sr Contents in the Intact Crowns of Female Teeth Investigated by Neutron Activation Analysis**  
*Zaichick V., Zaichick S. ....*203

### **Fission**

**Acceleration Induced Neutron Emission in Heavy Nuclei**  
*Carjan N., Rizea M.....*211

<b>Measuring Method of the Delayed Neutron Time Parameters for U-236 Fission by Neutrons with Energies from 14 to 18 MeV</b> <i>Gremyachkin D.E., Piksaikin V.M., Egorov A.S., Mitrofanov V.F., Mitrofanov K.V. ....</i>	221
<b>Dependence of the ROT Effect on the Energy of Light Charged Particles and on the Incident Neutron Energy</b> <i>Guseva I., Gagarski A., Gönnewein F., Gusev Yu. ....</i>	227
<b>Measurement of Gamma and Neutron ROT-Effects in 0.3 eV Resonance of <math>^{235}\text{U}</math> at a Hot Source of Polarized Neutrons</b> <i>Kopatch Yu.N., Novitsky V.V., Ahmadov G.S., Gagarsky A.M., Berikov D.B., Zhumadilov K.Sh., Danilyan G.V., Hutanu V., Klenke J., Masalovich S. ....</i>	235
<b>The ROT-Effect in the Angular Distribution of Prompt <math>\gamma</math>-Rays in Binary Fission Induced by Polarized Neutrons with the Energy of 60 meV</b> <i>Kopatch Yu.N., Berikov D.B., Ahmadov G.S., Gagarsky A.M., Novitsky V.V., Danilyan G.V., Hutanu V., Masalovich S., Klenke J., Deng H. ....</i>	242
<b>New Side of the Collinear Cluster Tri-Partition Scenario</b> <i>Pyatkov Yu.V., Kamanin D.V., Alexandrov A.A., Alexandrova I.A., Goryainova Z.I., Malaza V., Mishinsky G.V., Kuznetsova E.A., Solodov A.N., Strekalovsky A.O., Strekalovsky O.V., Zhuchko V.E. ....</i>	249
<b>Fission Fragments Binary Brake-Up at Crossing of the Solid-State Foils</b> <i>Strekalovsky A.O., Kamanin D.V., Pyatkov Yu.V., Goryainova Z.I., Zhuchko V.E., Alexandrov A.A., Alexandrova I.A., Korsten R., Malaza V., Kuznetsova E.A., Strekalovsky O.V. ....</i>	253
<b>Measurements and Analysis of Angular Distributions and Anisotropy of Fission Fragments from Neutron-Induced Fission of <math>^{232}\text{Th}</math>, <math>^{233}\text{U}</math>, <math>^{235}\text{U}</math>, <math>^{238}\text{U}</math>, <math>^{239}\text{Pu}</math>, <math>^{237}\text{Np}</math>, <math>^{\text{nat}}\text{Pb}</math>, and <math>^{209}\text{Bi}</math> in Intermediate Energy Range 1–200 MeV</b> <i>Vorobyev A.S., Gagarski A.M., Shcherbakov O.A., Vaishnena L.A., Barabanov A.L. ....</i>	259



## ISINN-27 Preface

On 10–14 June 2019, Dubna hosted the annual International Seminar on Interaction of Neutrons with Nuclei ISINN-27 which returned to its “homeland” after last year’s “visit” to Xi’an, the ancient capital of China, where ISINN-26 was organized by the Frank Laboratory of Neutron Physics of JINR together with the colleagues from Chinese institutes and universities. The scientific program of the Seminar traditionally covered a wide range of topics in neutron physics varying from the fundamental properties of the neutron and fundamental interactions in reactions with neutrons, nuclear fission, ultracold neutrons (UCN) to analytical methods in materials science and life sciences. The Seminar brought together over 100 participants from the physics research centers of Azerbaijan, Bulgaria, China, the Czech Republic, Egypt, France, Germany, Moldova, Romania, Serbia, South Africa, and Vietnam, as well as from the Institute of Physics and Power Engineering (IPPE) and the Medical Radiological Research Center (MRRC) (Obninsk), the National Research Center “Kurchatov Institute” (NRC KI) and the Institute of Theoretical and Experimental Physics (ITEP) of NRC KI (Moscow), Petersburg Nuclear Physics Institute (PNPI) of NRC KI (Gatchina), Institute for Nuclear Research of RAS (Troitsk), L. D. Landau Institute for Theoretical Physics of RAS (Chernogolovka), SINP MSU (Moscow), VNIIA (Moscow). The staff members of JINR FLNP and FLNR also attended the Seminar. A total of 49 oral and 41 poster reports were presented (for more details see the Seminar website <http://isinn.jinr.ru/past-isinns/isinn-27/program.html>). Note that the significant share of review reports of the Seminar program was not included in the present Proceedings (in particular, presentations by our Chinese colleagues) and is available only on the ISINN-27 website.

Among all these presentations it is necessary to highlight two very important ones of Prof. Tang from the Institute of High Energy Physics, CAS (Beijing) that provided an overview of the program and first results of experimental studies at the newly commissioned Chinese Spallation Neutron Source (CSNS) and CSNS Back-n White Neutron facility. This facility makes it possible to obtain the world’s most intense resonance neutron fluxes, and in the next three years it is planned to increase its beam power from present 100 kW by a factor of five. Prof. Tang emphasized the interest of his Institute in maximally expanding the international cooperation in the use of this unique neutron source and invited colleagues from JINR and the JINR Member States to take an active part in the development of new experimental instruments on CSNS beamlines.

And it should be mentioned another significant presentation devoted to the plans to construct a new neutron source at JINR, which should replace the IBR-2 reactor after its service life expires. The parameters of this source should be higher than those of the European Spallation Source (ESS) in Sweden, since it is expected to start operating after 2030.

Very useful results were presented by K. Mitrofanov on the formation of a thermal neutron beam at the Tandetron proton accelerator in IPPE which is necessary for metrological measurements. V. Lyashuk (INR RAS) reported on the scheme and possible parameters of an intense antineutrino source on the basis of a nuclear reactor designed to detect sterile neutrinos.

New results obtained in the study of the ( $n_{th}$ ,  $2\gamma$ )-reaction on  $^{56}\text{Mn}$  and  $^{94}\text{Nb}$  nuclei were reported by A. Sukhovej (FLNP JINR). First and very promising applications of tagged neutrons for online analysis of the composition of apatite ores were reviewed in the report delivered by Yu. Rogov (Diamant LLC, Dubna). The paper by I. Ruskov, D. Grozdanov, and N. Fedorov (FLNP JINR) gives an overview of the methodological improvements of the TANGRA setup that employs 14-MeV tagged neutrons to study the inelastic neutron scattering in combination with the angular distribution of  $\gamma$  rays, as well as covers the results of recent measurements. N. Simbirtseva (FLNP JINR) presented the investigation of the

elemental composition of the Old Russian medallion (12th–13th centuries) using neutron resonance capture analysis at the IREN facility.

The methodological aspects of using neutron-induced reactions were considered by N. Jovančević (IPN, Orsay) who reported on the construction of a new unique  $\nu$ -ball hybrid spectrometer comprising 34 HP germanium and 20 LaBr<sub>3</sub> detectors, as well as on the results of the first experiments. Z. Goryainova (FLNR JINR) described a new method for analyzing time-of-flight mass spectrometry of heavy ions, which had been developed to study collinear cluster decay of heavy nuclei.

The research field “Nuclear Analytical Methods in the Life Sciences and Materials Science”, popular among the JINR Member States, was presented by the review report of O. Duliu (FLNP JINR), in which the final results of years-long studies of sediments in the western part of the Black Sea were discussed. V. Zaichick (MRRC, Obninsk) provided very important results about a new method for the early diagnosis of human prostate diseases, which inspired an active discussion.

The poster session featured studies of young scientists from Azerbaijan, Bulgaria, Vietnam, Egypt, China, JINR, and Russia on the biomonitoring of territories with a strong anthropogenic load, methods of experiments with neutrons, as well as on the fundamental problems in nuclear physics.

The last day of the Seminar was entirely devoted to the discussion of a wide range of problems in the physics of nuclear fission. I. Guseva (NRC KI PNPI, Gatchina) explained the measured energy dependence of the ROT effect in the <sup>235</sup>U ternary fission induced by thermal polarized neutrons on the basis of quasi-classical trajectory calculations. D. Berikov (FLNP JINR) reported on the measurement of the ROT effect in the <sup>235</sup>U( $n, f$ ) binary fission induced by polarized neutrons with a nonthermal energy (60 meV). For the first time, a strong dependence of the effect on the neutron energy was demonstrated, which suggests the interference nature of the observed phenomenon. A. Vorobyev (NRC KI PNPI, Gatchina) presented the results of the study of the angular anisotropy of fission fragments for a wide variety of heavy nuclei from Pb to <sup>237</sup>Np in the neutron energy range of 1–200 MeV. The theoretical analysis of these results was carried out in the report of A. Barabanov (NRC KI, Moscow) performed on the basis of the Hauser-Feshbach approach modernized by the author. The importance of the correct account of the role of the quantum number  $K$  – projection of the total spin of the system on the fission-fragment separation axis was demonstrated. N. Carjan (IFIN-HH, Bucharest) presented new approach on the multiplicity of neutrons released at scission based on the dynamical scission model developed by him recently.

The final session of the Seminar was focused on the discussion of the so-called collinear cluster tri-partition discovered at FLNR JINR. As D. Kamanin (FLNR JINR) noted in his report, this phenomenon has been discussed at the ISINN conferences for more than 10 years, and each time it sparked a lively discussion. Yu. Pyatkov (MEPhI and FLNR JINR) reported on the first observation of heavy fission fragments that were transported through a special channel over a distance of 4 m. They live more than 400 ns and split after that hitting the foil for two secondary fission products. This is really new phenomenon in study of nuclear fission!

The success of ISINN-27 has confirmed the usefulness and attractiveness of the format of annual meetings on a wide range of issues in neutron physics that had been chosen for this conference a little more than a quarter of a century ago. The feasibility and effectiveness of neutron methods for solving fundamental and applied problems of science have been proved as well. The growing number of young participants attending the Seminar shows that it has a future.

V. N. Shvetsov, the Chairman of ISINN-27

# **Neutron Sources**

# THE SCHEME OF ANTINEUTRINO SOURCE WITH REGULATED HARD SPECTRUM ON THE BASE OF NUCLEAR REACTOR AND POSSIBLE EXPERIMENT FOR SEARCH OF STERILE NEUTRINOS

V. I. Lyashuk<sup>1,2,§</sup>

<sup>1</sup> *Institute for Nuclear Research of the Russian Academy of Sciences, Moscow, Russia*

<sup>2</sup> *National Research Center "Kurchatov Institute", Moscow, Russia*

**Abstract:** The new principle of  $\bar{\nu}_e$ -source for future short-baseline experiments is considered. The scheme is based on  ${}^7\text{Li}(n,\gamma){}^8\text{Li}$  activation near the reactor active zone (AZ) and transport of the fast  $\beta^-$ -decaying  ${}^8\text{Li}$  ( $T_{1/2}({}^8\text{Li}) = 0.84$  s) toward a remote neutrino detector and back in the closed loop to AZ for the next  $(n,\gamma)$ -activation of lithium in the continuous cycle. The scheme with closed loop ensures well defined total spectrum (in the position of the neutrino detector) that will allow to decrease the count errors below  $\lesssim 1\%$ . Owing to  $\sigma \sim E_\nu^2$  dependence of neutrino cross section the count rate will be more than  $\sim 10^3$  per day for the compact detector with volume about  $\text{m}^3$ . The proposed experiment allows to detect  $(\bar{\nu}_e, p)$ -interaction with high precision and directed to search of sterile neutrinos with  $\Delta m^2 \sim 1$   $\text{eV}^2$ . Basing on the proposed algorithm it were indicated the space regions for search of  $\bar{\nu}_e$ -disappearance for (3+1) and (3+2) neutrino models in the discussed experiment with new hard spectrum intensive  $\bar{\nu}_e$ -source.

## 1. INTRODUCTION. NUCLEAR REACTOR AS ANTINEUTRINO SOURCE: THE ADVANTAGES FOR THE EXPERIMENT AND PROBLEMS OF ITS SPECTRUM

The undoubted advance in solution of the discussed problem (search of sterile neutrinos) is creation of the intensive antineutrino source with well-known hard spectrum. The most intensive artificial antineutrino sources used for neutrino experiments are the nuclear reactors. The resulting reactor antineutrino flux is the complicated additive function of fluxes: from fission fragments; from beta decay of heavy (transuranium) nuclei (produced in  $(n,\gamma)$ - and  $(n,2n)$ -reactions); and  $\beta$ -decay of  $(n,\gamma)$ -activated elements of the constructions and water. In spite of the doubtless superiority in flux value the antineutrino reactor spectra (formed by main fuel isotopes –  ${}^{235}\text{U}$ ,  ${}^{238}\text{U}$ ,  ${}^{239}\text{Pu}$ ,  ${}^{241}\text{Pu}$ ) are characterized by large uncertainties in the total  $\bar{\nu}_e$ -spectrum that lead to very serious problems in interpretation of neutrino oscillation results. The reactor spectrum is known with  $\sim (4-6)\%$  -precision at energy up to  $\sim 6$  MeV and these errors dramatically rise up to tens percent at more higher energies (see spectrum errors in Fig. 1) [1–4].

An equilibrium  $\bar{\nu}_e$ -spectrum of nucleus-fission products from nuclear fuel composition varies in time in operation period and in case of reactor stops: the isotope  ${}^{235}\text{U}$  burns away (it's part in number of fissions decrease in operation period from  $\sim 73\%$  down to  $45\%$ ), but the contributions of  ${}^{238}\text{U}$ ,  ${}^{239}\text{Pu}$  and  ${}^{241}\text{Pu}$  rise (so, for  ${}^{239}\text{Pu}$  the yield to fissions increases from  $18\%$  up to  $37\%$  for the same time). The large changing in composition leads to variation in  $\bar{\nu}_e$ -fluxes which are recalculated by means of correction factors for four main fuel isotopes.

---

§ lyashuk@itep.ru

The all spectra drop rapidly as energy increases (that is especially negatively for registration of threshold  $\bar{\nu}_e$ -reactions): at increase  $E_{\bar{\nu}}$  from 2 MeV to 4, 6 and 8 MeV the neutrino spectrum of  $^{235}\text{U}$  drops in 5, 35 and 956 times, correspondingly (example in Fig. 1 for spectrum from  $^{235}\text{U}$ ).

An additional unaccounted error for  $\bar{\nu}_e$ -flux evaluation appears during reactor stops due to permanent presence of cooling pond for spent fuel. These errors can rise up to 1%. The summary neutrino flux depends on number of fissions in the active zone as:  $n_f(t) = W(t)/E_f(t)$ , where  $W(t)$  is a full reactor heat power for the current time and  $E_f$  is the mean energy released per one fission. But the  $E_f$  value is also changing during the reactor life time: it increasing on 1.5% [3].

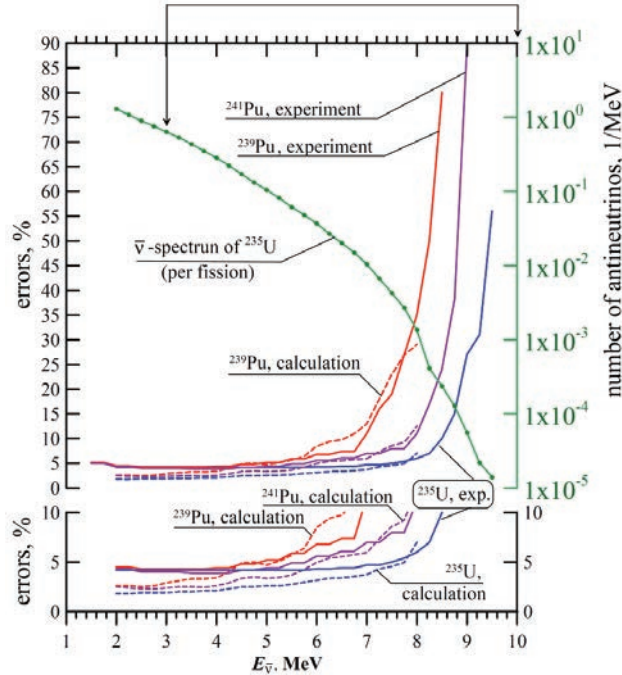


Fig.1. Dependence of antineutrino spectrum errors from energy for  $\bar{\nu}_e$ -spectrum of fission products of  $^{235}\text{U}$ ,  $^{239}\text{Pu}$  and  $^{241}\text{Pu}$  (see left vertical axes); the results presented in two scales of errors for experimental data (solid lines [1]) and calculations (dotted lines [2]). Antineutrino spectrum of  $^{235}\text{U}$  is shown by solid line with point (see right vertical axis [2]) on the top part.

In the recent measurements of  $\bar{\nu}_e$ -spectrum in Daya Bay, Reno and Double Chooz experiments it was detected significant excess of antineutrinos in the interval  $\sim (5-7)$  MeV of the spectrum [5-7]. This excess in experimental spectrum (called as bump) was unexpected and significantly activated efforts in order to clarify the matter. Here we want to emphasize that the requirement of well definite antineutrino spectrum of the source is exclusively important for excluding of the possible errors in the proposed experiment (see below) for search of sterile neutrinos.

## 2. PROPOSED HIGH FLUX $\bar{\nu}_e$ -SOURCE OF HARD REGULATED SPECTRUM

In spite of the apparent superiority on neutrino flux the nuclear reactors has a

disadvantage: too-small hardness of  $\bar{\nu}_e$ -spectrum. This character is extremely negative as the probability of registration strongly depends on neutrino energy. For the considered here reactor antineutrino energy the neutrino cross section is proportional to its energy squared ( $\sigma_{\nu} \sim E_{\nu}^2$ ). In case of hard  ${}^8\text{Li}$  spectrum the square-law dependence results in strong rise of neutrino cross section. The disadvantage of rapidly dropping reactor spectrum can be filled having realized the idea [8] to use a high-purified isotope  ${}^7\text{Li}$  for construction of lithium blanket (or converter) around the active zone (AZ) of a reactor. A short-lived isotope  ${}^8\text{Li}$  ( $T_{1/2} = 0.84$  s) is created under AZ neutrons flux in reaction  ${}^7\text{Li}(n,\gamma){}^8\text{Li}$  and at  $\beta^-$ -decay it emits hard antineutrinos of a well determined spectrum with the maximal energy  $E_{\bar{\nu}}^{\max} \approx 13.0$  MeV and mean one  $\bar{E}_{\bar{\nu}} \approx 6.5$  MeV.

The scheme of  $\beta^-$ -decay of  ${}^8\text{Li}$  (with  $\sim 100\%$  branching) to broad 3.03 MeV level of  ${}^8\text{Be}^*$  (first-excited state of  ${}^8\text{Be}$ ;  $\Gamma \approx 1.513$  MeV) and then to two alpha-particles is presented in Fig.2 [9]. The  $\beta^-$ -decay of  ${}^8\text{Li}$  is a pure Gamov-Teller ( $\Delta T = 1$ ) transition.

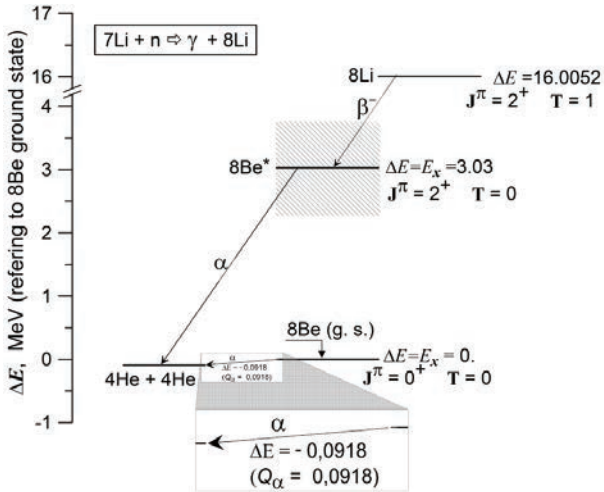


Fig. 2. The scheme of  $\beta^-$ -decay for  ${}^8\text{Li}$  with delayed  $\alpha$ -decay. The indicated energies  $\Delta E$  (shown right to the levels) are given refer to the ground state (g.s.) level of  ${}^8\text{Be}$  ( $J^\pi = 0^+$ ,  $T = 0$ ). The broad 3.03 MeV level of  ${}^8\text{Be}^*$  is shown by shading ( $\Gamma \approx 1.513$  MeV).  $J$  – the angular momentum;  $\pi$  – parity; and  $T$  – isobaric spin;  $E_x$  – excited level of  ${}^8\text{Be}$ ;  $Q_\alpha$  – energy of  $\alpha$ -decay. The  $\alpha$ -decay of  ${}^8\text{Be(g.s.)} \rightarrow {}^4\text{He} + {}^4\text{He}$  is shown by means the magnification software.

The resulting antineutrino flux from such a source (AZ plus  ${}^7\text{Li}$  blanket-converter) will be total one (produced by  $\beta^-$ -decay of  ${}^8\text{Li}$  and from AZ). The problem of creation of intensive antineutrino source with well definite hard spectrum can be solved by the scheme of (n, $\gamma$ )-activated  ${}^7\text{Li}$  isotope (irradiated by reactor neutrons close the AZ as lithium blanket) and continuous circulation of lithium isotope (or liquid lithium substance) in the close loop from AZ to remote neutrino detector [10–16]. The most perspective lithium substance can be

heavy water solution of lithium hydroxides  ${}^7\text{LiOD}$  or  ${}^7\text{LiOD-D}_2\text{O}$  [16, 19]. With purpose to increase the hard lithium antineutrino part (in the total antineutrino spectrum) we propose to construct the volumable pumped reservoir close to the antineutrino detector.

The scheme for this type of the dynamical (with pumped lithium)  $\bar{\nu}_e$ -source is presented in Fig.3 [15, 16]. Namely this scheme (with specified dimensions) was used in the discussed below simulation for search of sterile neutrinos.

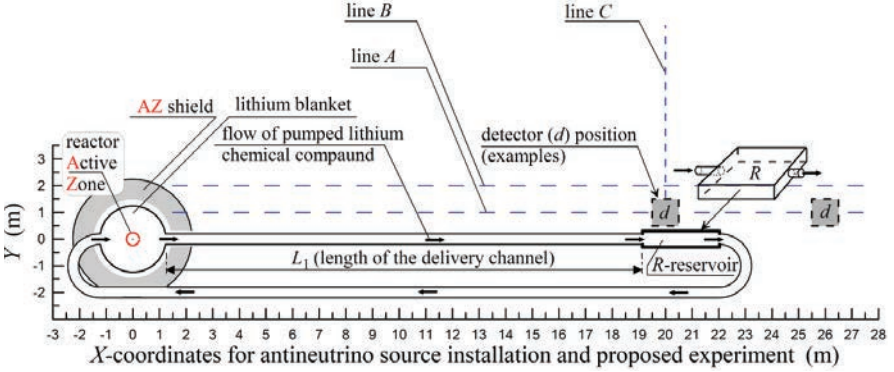


Fig. 3. The conceptual scheme of  $\bar{\nu}_e$ -source (with circulation of  ${}^8\text{Li}$  or lithium chemical substance in the closed loop) with variable (regulated and controlled) spectrum for short base line experiment. The distribution of the total antineutrino spectrum is regulated by the rate of lithium pumping (which can be smoothly varied by means the pump in the installation). The all dimensions in the scheme fully correspond to sizes used in the simulation of the experiment. Lithium substance in the blanket (activated by AZ-neutrons) is pumped continuously through the delivery channel to the remote reservoir (volume which is set close to the  $\bar{\nu}_e$ -detector) and further back to the blanket. The examples of detector positions are labelled as "d". The 3-dimensional view of the reservoir (labeled by "R") is given separately. At simulation of the antineutrino disappearance (see below) we used the coordinates of points along lines: A ( $y = 1$ ), B ( $y = 2$ ) and C ( $x = 20$ ).

For our purpose (creation of the neutrino source of significantly larger hardness than possible to obtain by above mentioned simple scheme of lithium blanket around the AZ) we introduce the definition of the generalized hardness for total neutrino spectrum [15, 16]. Let  $F_{\text{Li}}(\vec{r})$  and  $F_{\text{AZ}}(\vec{r})$  – densities of lithium  $\bar{\nu}_e$ -fluxes from the blanket and from AZ,  $\bar{n}_\nu \approx 6.14$  is number of reactor antineutrinos emitted per one fission in the AZ. We admit that the hardness of the summary  $\bar{\nu}_e$ - spectrum at the point  $\vec{r}$  equals one unit of hardness if the ratio of densities  $F_{\text{Li}}(\vec{r})/F_{\text{AZ}}(\vec{r})$  equals to  $1/\bar{n}_\nu$ . Let us define the total spectrum generalized hardness as:

$$H(\vec{r}) = \bar{n}_\nu \frac{F_{\text{Li}}(\vec{r})}{F_{\text{AZ}}(\vec{r})}. \quad (1)$$

In the simulation we specified the next parameters of the source and regime of the operation. Volume of the compact spherical AZ corresponds to 51 liters volume of the high flux research reactor PIK near the Saint-Petersburg in Russia [20, 21]. Thickness of the spherical lithium blanket is 1 m. Volume of the reservoir (rectangular parallelepiped of 0.5 m thickness) was set equal to blanket one.  $L_1$  is a distance between lithium blanket and pumped reservoir. In the simulation the volume rate of pumping was  $w = 2.25 \text{ m}^3/\text{s}$ . The distance  $L_1$  corresponds to the time 1 s of lithium delivery from the blanket to reservoir for appointed  $w$  rate.

### 3. POSSIBLE EXPERIMENT FOR SEARCH OF STERILE NEUTRINOS

In some realized oscillation experiments (LSND [22], SAGE [23], MiniBooNe [24, 25], GALLEX [26], reactor experiments [27]) it were revealed anomalous  $\bar{\nu}_e$ -fluxes and strongly stimulated the discussion on existence of sterile neutrinos and extension of the Standard Model. The discussed variants include models with one, two and three type of sterile neutrinos [28–32]. Some results indicate on the squared-mass difference between sterile and active neutrinos ( $\Delta m^2 \sim 1 \text{ eV}^2$ ).

The discussed here short base line experiment on sterile neutrino search (in the geometry of Fig. 3) has advantages namely at short distances where the large hardness is ensured. For short base line geometry in case of (3+1)-model (i.e., three active neutrinos plus one sterile) the probability of existence at distance  $L$  is given by means two-flavor model:

$$P = 1 - \sin^2(2\theta)\sin^2[1.27\Delta m_{41}^2(L(\text{m})/E(\text{MeV}))], \quad (2)$$

$$\sin^2(2\theta) = 4|U_{i4}|^2(1 - |U_{i4}|^2), \quad (3)$$

where  $\theta$  – angle of mixing,  $\Delta m_{41}^2$  ( $\text{eV}^2$ ) – maximum squared-mass difference between sterile and active neutrinos (i.e.,  $|\Delta m_{41}^2| \gg |\Delta m_{31}^2| \gg |\Delta m_{21}^2|$ ),  $U_{i4}$  – element of mixing matrix for active neutrino flavor  $i = e, \mu, \tau$ .

Probability for (3+2)-model (i.e., three active neutrinos plus two sterile neutrinos) for short base geometry will be:

$$P_e = 1 - 4(1 - |U_{e4}|^2 - |U_{e5}|^2) \times \{|U_{e4}|^2 \sin^2[1.27\Delta m_{41}^2(L/E)] + |U_{e5}|^2 \sin^2[1.27\Delta m_{51}^2(L/E)]\} - 4|U_{e4}|^2|U_{e5}|^2 \sin^2[1.27\Delta m_{54}^2(L/E)]. \quad (4)$$

For simulation of the probability of  $\bar{\nu}_e$ -existence, fluxes and expected ( $\bar{\nu}_e, p$ )-events in the detector the full volume of the source (i.e., AZ, lithium blanket, channels and reservoir in the Fig. 3) was divided on small cell. The obtained equations of  ${}^8\text{Li}$  production depending on the parameters of the source scheme (the geometry, yield of  ${}^8\text{Li}$ , the pumping regime (see details of calculations in [15–16]) allows to calculate the number of  ${}^8\text{Li}$  nuclei in any cells for the given geometry and pumping regime. It allows to calculate the flux, spectrum, hardness at the detector positions (for the specified AZ power). The highest level of hardness (that is important for high rate of counts and low errors) is supported in the closed space around the voluminous reservoir. For analysis of oscillation we considered the next simple realistic geometry: the detector (or detectors) can be set and shifted along the line  $A, B$  or  $C$  (Fig. 3). This detector geometry is realistic owing to high count rate in the hard spectrum and possibility to reduce the sensitive volume up to  $\sim \text{m}^3$  (see below). For AZ spectrum it was taken that the single fuel element is  ${}^{235}\text{U}$  similar to reactor PIK [20, 21]. The density of  $\bar{\nu}_e$ -flux from AZ is determined by its power  $P$  and for distance  $R$  is:

$$F (\text{cm}^{-2} \cdot \text{s}^{-1}) = \bar{n}_\nu P / 4\pi R^2 \bar{E} \approx 1.5 \times 10^{12} P (\text{MW}) / R^2 (\text{m}), \quad (5)$$

where  $\bar{E} \approx 200 \text{ MeV}$  - mean energy released at  $^{235}\text{U}$ -fission.

In the calculation the applied proton concentration in the detector is typical – about  $6.6 \times 10^{22} \text{ cm}^{-3}$  (KamLAND liquid scintillator [33]). The matrix elements for (3+1) and (3+2)-models correspond to best fits of the work [28]: for (3+1) model –  $\Delta m_{41}^2 = 1.78 \text{ eV}^2$ ,  $U_{e4} = 0.151$ ; for (3+2)a-model –  $\Delta m_{41}^2 = 0.46 \text{ eV}^2$ ,  $U_{e4} = 0.108$ ,  $\Delta m_{51}^2 = 0.89 \text{ eV}^2$ ,  $U_{e5} = 0.124$ ; for (3+2)b-model –  $\Delta m_{41}^2 = 0.47 \text{ eV}^2$ ,  $U_{e4} = 0.128$ ,  $\Delta m_{51}^2 = 0.87 \text{ eV}^2$ ,  $U_{e5} = 0.138$ . The update analysis of last neutrino experiments gives (some differing global-fit-parameters for sterile neutrinos with  $\Delta m^2 \sim 1 \text{ eV}^2$  was obtained in the [34]).

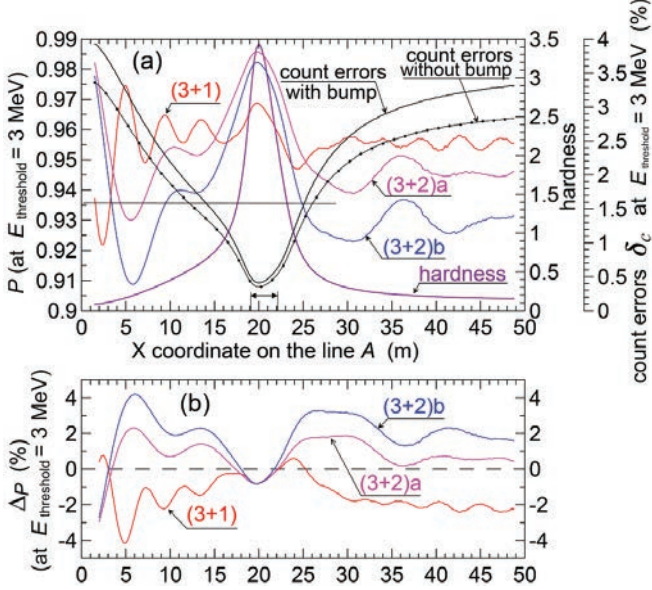


Fig.4. Probability  $P$  of  $\bar{\nu}_e$ -existence for three models [(3+1), (3+2)a and (3+2)b on the part (a)], hardness  $H$  of the total  $\bar{\nu}_e$ -spectrum [part (a)], count errors  $\delta_c$  (caused by uncertainties of AZ spectrum) [part (a)] and functional  $\Delta P(x)$  for opportunity of  $\bar{\nu}_e$ -detecting [part (b)] for models: (3+1), (3+2)a and (3+2)b depending on the  $X$  coordinate **along the line A** (for the detector geometry of Fig. 3). Probability  $P$ , count errors  $\delta_c$  and functional  $\Delta P$  are presented for the threshold of registration  $E = 3 \text{ MeV}$ . The all solid lines correspond the values obtained for  $\bar{\nu}_e$ -spectrum with reactor bump taken into account. The curves with points [count errors  $\delta_c$  in the parts (a)] – the errors of  $\bar{\nu}_e$ -counts for reactor spectrum without bump. Position of the reservoir is shown by the two-sided arrow on the part (a).  $X$  coordinates of the positive  $\Delta P$  values are the regions where probability of  $\bar{\nu}_e$ -detecting is higher to level of total spectrum errors (see part (b)).

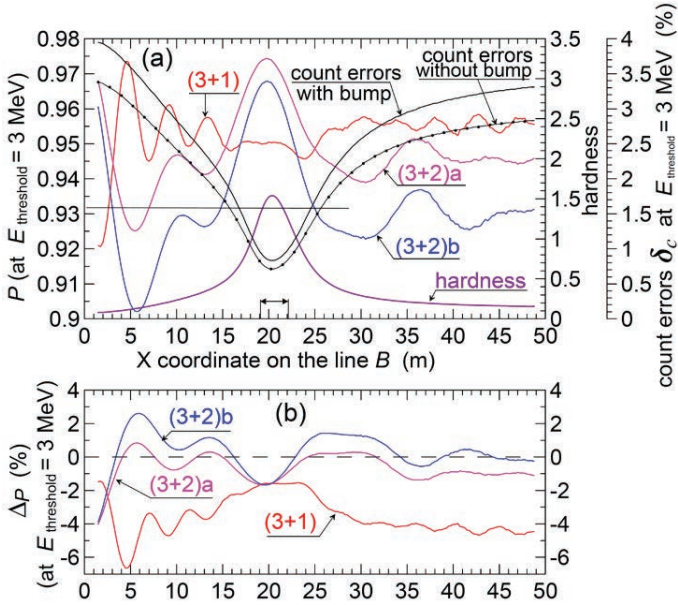


Fig.5. Probability  $P$  of  $\bar{\nu}_e$ -existence for three models [(3+1), (3+2)a and (3+2)b on the part (a)], hardness  $H$  of the total  $\bar{\nu}_e$ -spectrum [part (a)], count errors  $\delta_C$  (caused by uncertainties of AZ spectrum) [part (a)] and functional  $\Delta P(x)$  for opportunity of  $\bar{\nu}_e$ -detecting [part (b) for models: (3+1), (3+2)a and (3+2)b] depending on the  $X$  coordinate **along the line B** (for the detector geometry of Fig. 3). Probability  $P$ , count errors  $\delta_C$  and functional  $\Delta P$  are presented for the threshold of registration  $E = 3 \text{ MeV}$ . The all solid lines correspond the values obtained for  $\bar{\nu}_e$ -spectrum with reactor bump taken into account. The curves with points [count errors  $\delta_C$  in the parts (a)] – the errors of  $\bar{\nu}_e$ -counts for reactor spectrum without bump. Position of the reservoir is shown by the two-sided arrow on the part (a).  $X$  coordinates of the positive  $\Delta P$  values are the regions where probability of  $\bar{\nu}_e$ -detecting is higher to level of total spectrum errors (see part (b)).

The calculated errors for count events are given here at 100% efficiency of registration. Fig. 4(a) shows the probability  $P$  of existence, hardness and count errors for models (3+1), (3+2)a and (3+2)b at the antineutrino registration threshold  $E_{\text{threshold}} = 3 \text{ MeV}$  for detector positions along lines A (see Fig. 3). Note that hardness  $H$  does not depend on the threshold on registration [according to definition (1)]. Fig. 5(a) presents the same values for detector positions along line B (see Fig. 3). Fig. 6(a) shows the above mentioned values for orthogonal line C (see Fig. 3). At coordinates of the reservoir the hardness reaches the maximum with small shift to AZ-position due to decrease of  ${}^8\text{Li}$  concentration along the flow (see Fig. 4(a) and 5(a)). Owing to large lithium mass in the reservoir the maximum of probability  $P$  is detected close to its position (marked by double arrow) in Figs. 4(a) and 5(a). Large hardness

around the reservoir ensure smallest count errors (below 0.5–1.0%) in the nearby space; shift from line *A* to line *B* leads to fall of hardness and increase of errors (compare the Fig. 4(a) and 5(a)). The most rapid decrease of hardness and rise of errors take place for line *C* - at the remote from lithium mass (see Fig. 6(a)).

In the next step we introduce the functional for possibility (or opportunity) to detect the oscillation of active to sterile neutrinos. The functional based on comparison of the maximal probability  $P$  (at the  $x_{\text{fix}}$ ) with the current  $P(x)$  **along A-line** ( $y=1$  m, according to the geometry in Fig. 3):

$$\Delta_P(x) = [1 - \delta_C(x_{\text{fix}}, y=1 \text{ m})] \times P(x_{\text{fix}}, y=1 \text{ m}) - [1 + \delta_C(x, y=1 \text{ m})] \times P(x, y=1 \text{ m}), \quad (6)$$

where  $\delta_C$  – count errors; coordinate  $x_{\text{fix}}$  corresponds to maximal  $P$  value close to reservoir:  $x_{\text{fix}} \approx 20$  m. The functional helps to search change in probability  $P$  avoiding the errors caused by reactor  $\bar{\nu}_e$ -spectrum. The positive  $\Delta_P$  values determine the  $X$  coordinate regions (along *A*-line) where probability of  $\bar{\nu}_e$ -detecting is higher to level of total spectrum errors.

The  $\Delta_P(x)$  results are labelled as (b) and presented in the bottom parts of all Figs. 4–6 for threshold of  $\bar{\nu}_e$ -registration  $E_{\text{threshold}} = 3$  MeV. The analysis for detector position along the line *A* (Fig. 4) revealed that the probability to detect oscillation in case of (3+1)-model is close to zero: the  $\Delta_P(x)$  curves lay below zero or nearby to it. The model (3+2)a allows to reach the probability up to  $\approx 2\%$ , but effects for the model (3+2)b can exceed zero level by 4% (at  $x \approx 6$  m, Fig. 4(b)).

The functional for possibility (to detect an oscillation to sterile neutrinos) **along B-line** ( $y=2$  m, see Fig. 3) is the similar to (6):

$$\Delta_P(x) = [1 - \delta_C(x_{\text{fix}}, y=2 \text{ m})] \times P(x_{\text{fix}}, y=2 \text{ m}) - [1 + \delta_C(x, y=2 \text{ m})] \times P(x, y=2 \text{ m}). \quad (7)$$

In case of the **C-line** we compare the current probability **along the C-line** ( $x = x_{\text{fix}}$ ) with maximal  $P$  value close to reservoir (at the coordinates:  $x_{\text{fix}} \approx 20$  m,  $y=1$  m):

$$\Delta_P(y) = [1 - \delta_C(x_{\text{fix}}, y=1 \text{ m})] \times P(x_{\text{fix}}, y=1 \text{ m}) - [1 + \delta_C(x_{\text{fix}}, y)] \times P(x_{\text{fix}}, y). \quad (8)$$

The opportunities to reveal the oscillation in the geometries along line *B* and *C* are lower (see Fig. 5(b) and 6(b)) that are explained by increased errors for lower hardness in the total spectrum.

For the discussed source the nuclear reactor acts as intensive (n, $\gamma$ )-activator. The remote volumable reservoir acts as geometry factor for creation of the hard  $\bar{\nu}_e$ -spectrum. As a result the proposed source ensures high neutrino flux with hard spectrum in the space close to the reservoir. Here the  $^8\text{Li}$  isotope acts as **effective shifter** in forming of the hard spectrum. The quadratic dependence of cross section as  $\sigma_{\nu} \sim E_{\nu}^2$  strongly amplifies the effect: the number of ( $\bar{\nu}_e, p$ )-events strongly increasing in the detector. The results of calculated counts for points on the line *A* (see detector geometry in Fig. 3) is given in the Fig. 7. Thanks to the reservoir the total flux and number of events has "lithium bump" close to the reservoir position. The number of events from  $^8\text{Li}$  strongly dominates over the number of events from reactor antineutrinos (Fig. 7).

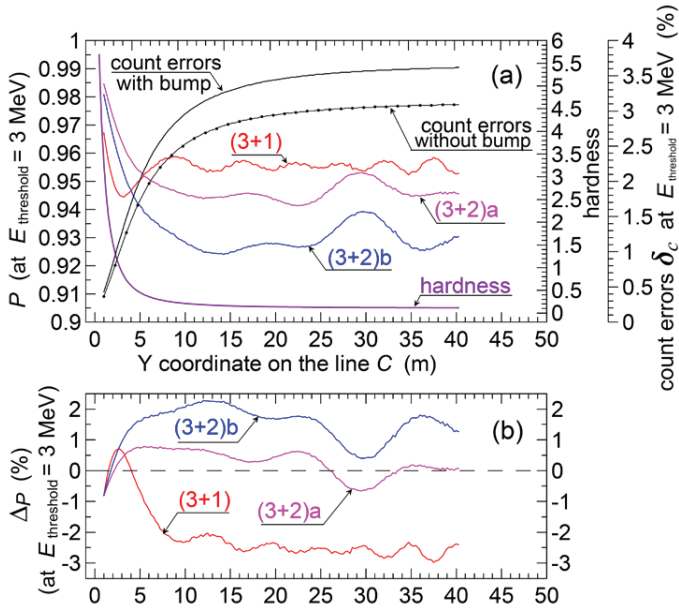


Fig.6. Probability  $P$  of  $\bar{\nu}_e$ -existence for three models [(3+1), (3+2)a and (3+2)b] on the part (a), hardness  $H$  of the total  $\bar{\nu}_e$ -spectrum [part (a)], count errors  $\delta_C$  (caused by uncertainties of AZ spectrum) [part (a)] and functional  $\Delta P(x)$  for opportunity of  $\bar{\nu}_e$ -detecting [part (b)] for models: (3+1), (3+2)a and (3+2)b] depending on the  $X$  coordinate along the line C (for the detector geometry of Fig. 3). Probability  $P$ , count errors  $\delta_C$  and functional  $\Delta P$  are presented for the threshold of registration  $E = 3 \text{ MeV}$ . The all solid lines correspond the values obtained for  $\bar{\nu}_e$ -spectrum with reactor bump taken into account. The curves with points [count errors  $\delta_C$  in the parts (a)] - the errors of  $\bar{\nu}_e$ -counts for reactor spectrum without bump. Position of the reservoir is shown by the two-sided arrow on the part (a).  $X$  coordinates of the positive  $\Delta P$  values are the regions where probability of  $\bar{\nu}_e$ -detecting is higher to level of total spectrum errors (see part (b)).

The results in Fig. 7 are normalized per cubic meter, day and gigawatt of the reactor power. We note that really the power of the investigating reactors is lower; the exclusively interesting variant (for the discussed  $\bar{\nu}_e$ -source) of such reactor is new reactor PIK with the thermal power 100 MW [20–21]. The events ensured by the  ${}^8\text{Li}$  antineutrinos are strongly dominates (compare to yield from AZ neutrinos) owing to the hardness of  $\bar{\nu}_e$ -spectrum of  ${}^8\text{Li}$ .

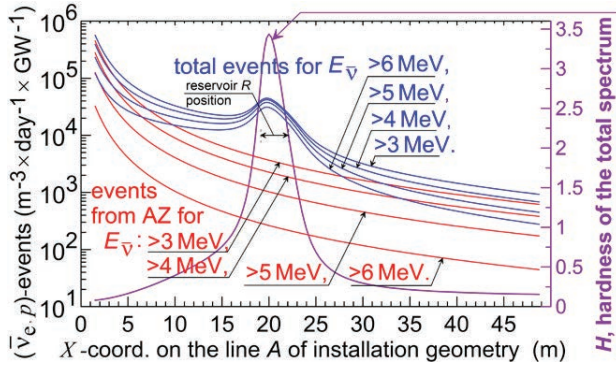


Fig. 7. The expected normalized number of  $(\bar{\nu}_e, p)$ -events in the detector depending on the  $X$  coordinates along the line  $A$  (geometry of the Fig. 3). The results are given for thresholds of antineutrino registration  $E_{\text{threshold}} = 3, 4, 5,$  and  $6$  MeV. The total number of events is ensured by  $\bar{\nu}_e$  from  ${}^8\text{Li}$  and AZ. Position of the reservoir is shown by the two-sided arrow.

The presented dependencies (Fig. 7) are calculated for thresholds of registration with increasing values from 3 to 6 MeV. Here it is very important to emphasize that registration with increasing threshold allows to decrease the count errors in order of values (in case of threshold rising from 3 to 6 MeV). This important result is explained by greater yield of  ${}^8\text{Li}$  flux in the total  $\bar{\nu}_e$ -flux (remembering that: the reactor spectrum is known with significant errors; the reactor spectrum drop rapidly as energy increases compare to well-known hard  $\bar{\nu}_e$ -spectrum with mean energy  $\sim 6.5$  MeV). The problems of errors lowering for  $\bar{\nu}_e$ -spectrum and proposal to increase the threshold of  $\bar{\nu}_e$ -registration are considered in details in [14–16]. The function of errors from the hardness  $H$  of the total spectrum was obtained (see in [14–16]).

#### 4. CONCLUSION

The principle of the source operation is  $(n, \gamma)$ -activation of pure  ${}^7\text{Li}$  near the reactor active zone and transfer of the activated lithium to remote detector by the loop scheme. The more perspective way of the source realization is to use the heavy water solution of  ${}^7\text{Li}$  instead of metallic lithium [16–18] (taking in mind the requestion of  ${}^7\text{Li}$  purification and price of very pure  ${}^7\text{Li}$  (with grade of purification  $\sim 99.99\%$  and higher) [16, 19]).

Namely owing to cross section dependence  $\sigma_{\nu} \sim E_{\nu}^2$  the number of neutrino interaction strongly increases at rise of the hardness (thanks to  ${}^8\text{Li}$  neutrinos) of the total spectrum. High rate of the detector counts allows to use compact neutrino detector ( $\sim \text{m}^3$ ).

Here it was considered the variant of the  $\bar{\nu}_e$  source with realistic dimension and regime of operation. The possible scheme of the experiment for search of sterile neutrinos with  $\Delta m^2 \sim 1 \text{ eV}^2$  is discussed for neutrino models (3+1) and (3+2). For this cases the total antineutrino fluxes were calculated taking into account both lithium and reactor spectra and corresponding errors, the dynamics of lithium transfer and dimensions of all parts of the installation. The oscillation probabilities for (3+1)-model and two variants of (3+2)-models

were simulated for different geometries of detector positions that allowed to indicate the space coordinates for search  $\bar{\nu}_e$ -disappearance outside the spectrum errors.

## Acknowledgements

We are grateful to L.B. Bezrukov, B.K. Lubsandorzhev, Yu.S. Lutostansky and I.I. Tkachev for stimulating discussions and support of the work.

The work is supported by the Russian Foundation for Basic Research Grants no.18-02-00670\_a.

## References

1. Schreckenbach K., Colvin G., Gelletly W. and von Feilitzsch F., *Determination of the anti-neutrino spectrum from  $^{235}\text{U}$  thermal neutron fission products up to 9.5 MeV*, Phys. Lett. B., **160** (1985) 325.
2. Huber Patrick, *Determination of antineutrino spectra from nuclear reactors*, Phys. Rev. C., **84** (2011) 024617.
3. Kopeikin V.I., *Flux and spectrum of reactor antineutrinos*, Phys. At. Nucl., **75** (2012) 143–152.
4. Lyashuk V.I. and Lutostansky Yu.S., *Intensive neutrino source on the base of lithium converter*, (2015). arXiv:1503.01280v2.
5. An F.P. et al., (Daya Bay Collaboration), *Phys. Rev. Lett.* **116**. (2016) 061801.
6. Hayes A.C., Friar J.L., Garvey G.T., Ibeling Duligur, Jungman Gerard, Kawano T., Mills Robert W., *Possible Origins and Implications of the Shoulder in Reactor Neutrino Spectra*. (2015). arXiv:1506.00583v2 [nucl-th].
7. Huber Patrick, *Reactor antineutrino fluxes – status and challenges*.(2016). arXiv:1602.01499v1 [hep-ph].
8. Mikaelian L.A., Spivak P. E. and Tsinoev V.G., *A proposal for experiments in low-energy antineutrino physics*, Nucl. Phys. **70** (1965) 574–576.
9. Energy Levels of Light Nuclei  $A = 8$ , Nucl. Phys. **A745** (2004) 155.
10. Lyashuk V.I. and Lyutostansky Yu.S. *The conception of the powerful dynamic neutrino source with modifiable hard spectrum*. Preprint ITEP-38-97, Moscow: ITEP (1997); <https://iss.fnal.gov/archive/other/itep-38-97.pdf>
11. Lutostansky Yu.S. and Lyashuk V.I., *Powerful dynamical neutrino source with a hard spectrum*,/ Phys. Atom. Nucl. **63** (2000) 1288.
12. Lutostansky Yu.S. and Lyashuk V.I., *The concept of a powerful antineutrino source*,/ Bull. Russ. Acad. Sci. Phys. **75** (2011) 468.
13. Lyashuk V.I., *High ux lithium antineutrino source with variable hard spectrum*.(2017). arXiv:1609.02934.
14. Lyashuk V.I., *Problem of reactor antineutrino spectrum errors and it's alternative solution in the regulated spectrum scheme*. Results Phys. **7** (2017) 1212.
15. Lyashuk V.I. (2018). arXiv:1809.05949.
16. Lyashuk V.I., *Intensive electron antineutrino source with well defined hard spectrum on the base of nuclear reactor and 8-lithium transfer. The promising experiment for sterile neutrinos search*, JHEP 06 (2019)135.
17. Lyutostansky Yu.S. and Lyashuk V.I., *Reactor neutrino-antineutrino converter on the basis of lithium compounds and their solutions*, Sov. J. At. Energ. **69** (1990) 696–699.
18. Lyashuk V.I., Lutostansky Yu.S. *Neutron sources for neutrino factory on the base of*

- lithium converter*, Proc. XXI Int. Seminar of Interaction of Neutrons with Nuclei. Alushta, May 20–25, 2013. Dubna, JINR, 2014, P. 156–164.
19. Lyashuk V.I., *Hard Antineutrino Source Based on a Lithium Blanket: A Version for the Accelerator Target*, Phys. Part. Nucl. Lett., **14** (2017) 465.
  20. <http://www.pnpi.spb.ru/en/facilities/reactor-pik>.
  21. Aksenov V.L., *Reactor PIK. Present status and trends*. Proceedings of Collaboration and Perspectives of Russian and Chinese Mega Projects, Dubna, Russia, December 3–4, 2014.
  22. LSND collaboration. *Evidence for neutrino oscillations from the observation of anti-neutrino(electron) appearance in a anti-neutrino(muon) beam*, Phys. Rev. D **64** (2001) 112007 [hep-ex/0104049].
  23. SAGE collaboration. *Measurement of the solar neutrino capture rate with gallium metal. III: Results for the 2002-2007 data-taking period,* Phys. Rev. C **80** (2009) 015807. [arXiv:0901.2200].
  24. MiniBooNE collaboration. *Event Excess in the MiniBooNE Search for  $\bar{\nu}_\mu \rightarrow \bar{\nu}_e$  Oscillations*, Phys. Rev. Lett. **105** (2010) 181801 [arXiv:1007.1150].
  25. MiniBooNE collaboration. *Significant Excess of ElectronLike Events in the MiniBooNE Short-Baseline Neutrino Experiment*, Phys. Rev. Lett. **121** (2018) 221801. [arXiv:1805.12028].
  26. Giunti C. and Laveder M., *Statistical Significance of the Gallium Anomaly*, Phys. Rev. C **83** (2011) 065504 [arXiv:1006.3244].
  27. Mention G. et al., *The Reactor Antineutrino Anomaly*, Phys. Rev. D **83** (2011) 073006. [arXiv:1101.2755].
  28. Kopp J., Maltoni M. and Schwetz T. *Are there sterile neutrinos at the eV scale ?* Phys. Rev. Lett. **107** (2011) 091801 [arXiv:1103.4570].
  29. Maltoni M. and Schwetz T., *Sterile neutrino oscillations after first MiniBooNE results*, Phys. Rev. D **76** (2007) 093005 [arXiv:0705.0107].
  30. Conrad J.M., Ignarra C.M., Karagiorgi G., Shaevitz M.H. and Spitz J., *Sterile Neutrino Fits to Short Baseline Neutrino Oscillation Measurements*, Adv. High Energy Phys. **2013** (2013) 163897; [arXiv:1207.4765].
  31. Zysina N. Yu., Fomichev S.V. and Khrushov V.V., *Mass properties of active and sterile neutrinos in a phenomenological (3+1+2) model*, Phys. Atom. Nucl. **77** (2014) 890; [arXiv:1401.6306].
  32. Khrushov V.V., Fomichev, *Sterile neutrinos in uence on oscillation characteristics of active neutrinos at short distances in the generalized model of neutrino mixing,* Int. J. of Modern Physics A, **34**, No. 29 (2019) 1950175.
  33. KamLAND RCNS Group collaboration. *An overview of the KamLAND 1-kiloton liquid scintillator*. physics/0404071.
  34. Kopp J., Machado P.A.N., Maltoni M. and Schwetz T., *Sterile Neutrino Oscillations: The Global Picture*, JHEP 05 (2013) 050 [arXiv:1303.3011].

# Formation and Measurement of the Thermal Neutron Beam at the Tandetron Accelerator

Mitrofanov K.V., Egorov A.S., Gremyachkin D.E., Piksaikin V.M.

*JSC "SSC RF – IPPE", Obninsk, Russia*

## Abstract

The neutron beams generated at accelerators using nuclear reactions with well-known parameters are widely used in neutron physics and in many practical applications. This paper is devoted to the formation of a thermal neutron beam and the measurement of its intensity and spatial distribution at an angle of  $0^\circ$  to the beam axis using an activation method and an ionization chamber with a solid boron radiator KNT-10 that is not sensitive to  $\gamma$ -radiation. The nuclear reaction of  ${}^7\text{Li}(p,n)$  on metallic lithium installed in a cooled target device of the Tandetron accelerator was used as a neutron source.

**Description of the experiment.** The configuration of the Tandetron accelerator target device and the polyethylene block for slowing down the neutrons generated in the  ${}^7\text{Li}(p,n)$  reaction is shown in Fig. 1.

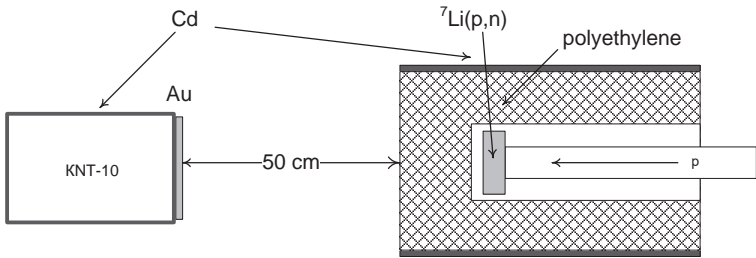


*Fig. 1. Block diagram of measurement for determining the thermal neutron flux by the gold foil activation method and for determining the cadmium ratio using the camera KNT-10.*

First, the gold foil was irradiated separately to determine the absolute neutron flux density, and then the number of pulses from the KNT-10 chamber installed at the same point as the gold foil was measured in a cadmium case and without a cadmium cover for determination of the cadmium ratio with the same accelerator and proton beam parameters.

The cadmium sheets 0.5 mm thick were used to reduce neutron leakage through the side surface of the cylinder. The distance from the lithium target to the end surface of the cylinder was 10 cm. The distance from the end surface of the cylinder moderator to the gold sample and to the KNT-10 chamber was 50 cm.

**Measurement of cadmium ratio of the thermal beam.** The absolute value of the thermal neutron flux was determined using activation analysis with thin gold foil as an indicator. The presence of resonant neutrons makes it difficult to interpret the activity induced in the gold foil.

The cadmium filters, which intensively absorb thermal neutrons, are used to separate the effects of activation from thermal and resonant neutrons. The cadmium neutron absorption

cross section is 2450 barn in the thermal region and decreases rapidly with increasing of the neutron energy. It decreases to 1 barn near the boundary of the thermal and resonant regions of the neutron energy. As a result, a 0.5 mm thick cadmium plate absorbs almost all thermal neutrons falling on it with an energy  $E < 0.4$  eV and passes resonant neutrons..

To determine the intensity ratio of thermal and resonant neutrons, we used the method of measuring the cadmium ratio

$$R_c = \frac{C_1 \varphi_{th} + C_2 \varphi_r}{C_2 \varphi_r},$$

where  $C_1$  and  $C_2$  are the sensitivity of the detector, respectively, to thermal and resonant neutrons,  $\varphi_{th}$  is the thermal neutron flux,  $\varphi_r$  is the resonant neutron flux [1].

The following expression can be written for the cadmium ratio measurement in the case of a neutron detector with sensitivity proportional to  $1/v$

$$R_c - 1 = \frac{\varphi_{th} \sigma_{acth}}{\varphi_r \int_{0.4}^{\infty} \sigma_r \frac{dE}{E}},$$

which takes into account the energy distribution of resonant neutrons  $dE/E$ .

Introducing the dependence of the cross section on the neutron energy, we obtain

$$R_c - 1 = \frac{\varphi_{th} \frac{1}{\sqrt{0.025}}}{\varphi_r \int_{0.4}^{\infty} \frac{dE}{E^{3/2}}} = 2 \frac{\varphi_{th}}{\varphi_r}.$$

Thus, the cadmium ratio provides the information on the fluxes of thermal and resonant neutrons at the point at which measurements are being made. The cadmium covers are used not only in the activation method. Any small neutron detector not sensitive to  $\gamma$ -radiation can be placed in a cadmium cover. When the thermal neutrons are absorbed in cadmium, a capture  $\gamma$ -radiation arises, the registration of which distorts the cadmium ratio.

In this experiment, an ionization chamber with a solid boron radiator KNT-10, which is not sensitive to  $\gamma$ -radiation, was used to measure the cadmium ratio. KNT-10 is an ionization two-electrode chamber with a solid boron ( $^{10}\text{B}$ ) coating [2]. It is known that the reaction cross section  $^{10}\text{B}(n,\alpha)$  obeys the  $1/v$  law. Therefore, the above expression for estimating the intensity of thermal and resonant neutrons based on measurements of the cadmium ratio is quite correct for analyzing the results for both the KNT-10 ionization chamber and the activation of the gold indicator.

For the experimental determination of the cadmium ratio, the neutron flux was measured using a KNT-10 ionization chamber, which is not sensitive to gamma radiation, in and without the cadmium cover under the same experimental conditions indicated above in Figure 1. Figure 2 shows the neutron spectra measured during irradiation of a KNT-10 camera in and without a cadmium cover at a distance of 50 cm from the end of the moderator.

Integrating these spectra and dividing the obtained values one by one, we obtain the average flux ratio 29.9898, from which we determine the cadmium ratio:  $R_{Cd} = 58.9796$ . The obtained sufficiently high value of the cadmium ratio allows us to further neglect the effects of resonant neutrons.

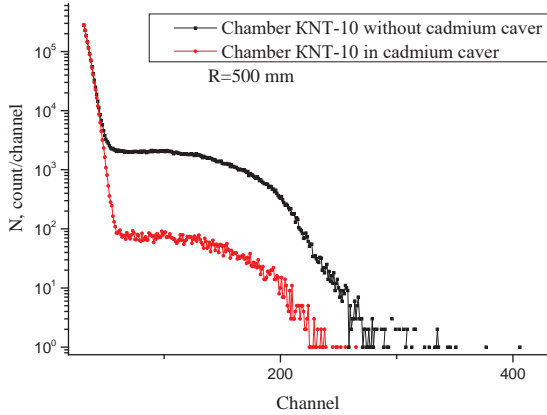


Fig. 2. The neutron spectra measured by a KNT-10 ionization chamber at a distance of 50 cm from the moderator with cadmium cover and without it.

**The measurement of the spatial distribution of the thermal neutron flux.** The KNT-10 ionization chamber was used to measure the spatial distribution of the thermal neutrons generated in the Tandetron target using the  ${}^7\text{Li}(p,n)$  nuclear reaction. The range of distances from the target was varied from 10 cm to 250 cm. The experiment procedure consisted in measuring the amplitude distribution of the ionization chamber KNT-10 and the number of counts of the proton current integrator of the target. At each point 5 measurements were taken. Then, when the ion current was turned off, the neutron background was measured. Fig. 3 shows the results of measuring the amplitude distribution of neutrons with the current on the accelerator target and the background of neutrons corresponding to this point measured with the accelerator current turned off.

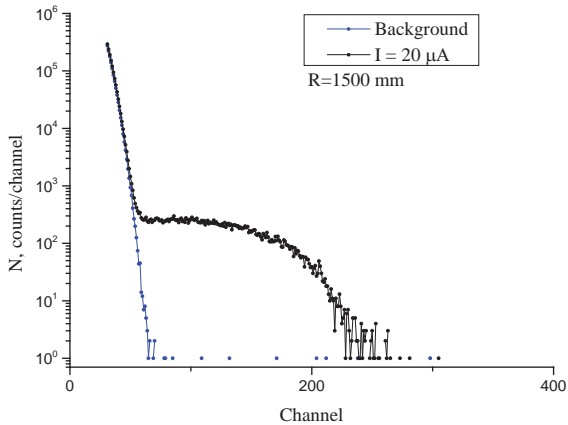


Fig. 3. The amplitude distribution of the ionization chamber KNT-10 with the accelerator current turned on and off. The current on the accelerator target was 20  $\mu\text{A}$ .

This procedure was performed at each point of the investigated range of distances. The dependence of the number of the camera counts on the distance to the moderator was obtained after subtracting the neutron background, integrating the amplitude spectrum of the KNT-10 ionization chamber and normalizing it to the value of the current integrator. The results are presented in Fig. 4.

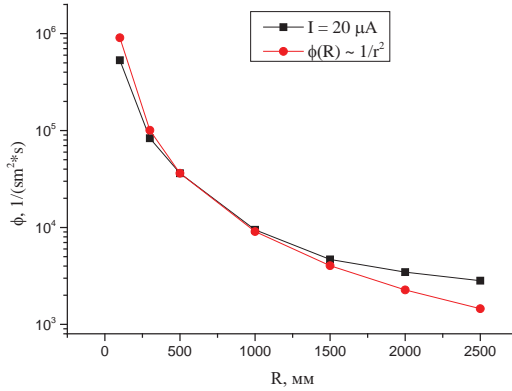


Fig.4. The spatial distribution of thermal neutron flux at the Tandetron accelerator.

Fig. 4 shows that in the range of 0.5 to 1.5 m the dependency of the neutron flux obeys the  $1/R^2$ , which is valid for a point source. At the distances less than 0.5 m, the discrepancy of the observed dependence on the law  $1/R^2$  is due to the fact that the source is different from the point source. At the distances of more than 1.5 m, the distorting factor is the neutrons reflected from the walls of the experimental hall of the Tandetron accelerator.

**Absolute neutron flux.** The absolutization of the neutron flux was carried out using an activation method for measuring the neutron spectra, which uses a link between the induced activity of detector-monitors and the neutron flux density [3]. This link is expressed by the following equation:

$$S_{peak} = \frac{m}{\lambda \cdot A} \cdot \varepsilon_{\gamma} \cdot f \cdot g \cdot N_a \cdot (1 - e^{-\lambda t_{irr}}) \cdot e^{-\lambda t_d} \cdot (1 - e^{-\lambda t_m}) \cdot \Phi \cdot \sigma, \quad (1)$$

- $S_{peak}$  – the peak area of specific gamma-line
- $m$  – mass of the activation of the monitor in grams,
- $\lambda$  – decay constant,
- $A$  – atomic weight of the monitor,
- $\varepsilon_{\gamma}$  – Ge detector efficiency for a particular gamma-line,
- $f$  – isotopic purity of the monitor,
- $g$  – the intensity of the particular gamma-line,
- $N_a$  – Avogadro constant,
- $t_{irr}$  – irradiation time of the monitor,
- $t_d$  – delay time of the monitor,
- $t_m$  – measurement time of the monitor,
- $\Phi$  – the energy spectrum of neutrons (neutron/cm<sup>2</sup>·s),
- $\sigma$  – cross section of reaction (barn).

As was already shown above, there is a negligible number of neutrons with energies above 0.025 eV, that is, the epithermal neutrons, because the cadmium ratio was 58.9796.

Figure 5 shows a comparison of two exactly identical activation samples (weight, size, thickness, chemical purity of gold) irradiated with the same parameters, only one was in a cadmium case, and the second without a cadmium case.

It is clearly seen from the figure that epithermal and resonant neutrons were not registered in the activation sample, which was irradiated in a cadmium case.

On this basis, the  $^{197}\text{Au}(n,\gamma)^{198}\text{Au}$  reaction cross section was taken equal to 98.8 barn with a neutron energy of 0.025 eV to determine the neutron flux.

The energy dependence of the efficiency  $\varepsilon(E_\gamma)$  of a Ge(Li)-gamma spectrometer was determined on the basis of experimental data for discrete values of the energies of gamma ray. The spectrometer was calibrated according to the efficiency of the total absorption of gamma ray using the reference gamma ray sources (OSGI). The distance between the reference source and the Ge(Li) detector, the diameter of the reference source when calibrating the spectrometer and measuring the activity of monitors were the same.

The absorption efficiency of gamma ray with the energy of 411.8 keV was 0.07016 for a Ge (Li) gamma spectrometer.

The activation sample was irradiated at the IPPE Tandetron accelerator. The monitor was irradiated continuously for 1 hour at a proton energy of  $E_p = 2.3$  MeV and a current of 20.6  $\mu\text{A}$ . The reaction  $^7\text{Li}(p,n)$  was used to generate the neutron flux. The activation sample was made of chemically pure gold weighing 1.0415 g.

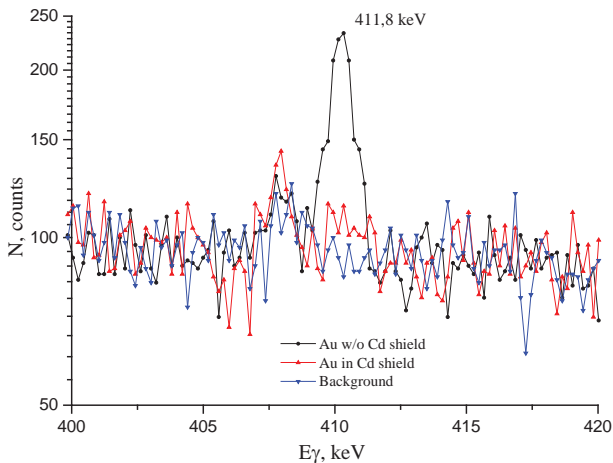


*Fig. 5. Two Au samples irradiated in the Cd cover and without the Cd cover in comparison with background measurement.*

The Canberra GX5019 HPGc detector was used as the spectrometer for measuring the induced gamma activity [4]. Figure 6 shows the apparatus spectrum of gamma rays of the  $^{197}\text{Au}(n,\gamma)^{198}\text{Au}$  reaction products in a gold sample after its irradiation in the neutron flux.

A number of counts at the peak of the gamma ray total absorption for the 411.8 keV gamma rays energy were obtained as a result of the Au monitor measurements and the subsequent processing of the gamma ray spectra. The 5 irradiations were carried out under the same conditions of the 5 activation monitors to increase the statistical accuracy of the determination of the induced activity.

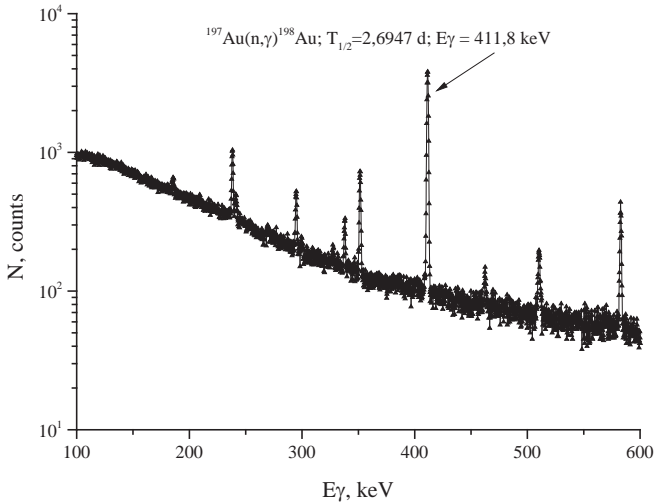


Fig. 6. The apparatus spectrum of gamma rays of the  $^{197}\text{Au}(n,\gamma)^{198}\text{Au}$  reaction products in the gold sample after its irradiation in the neutron flux.

Thus, all the parameters of equation (1) are defined, namely, the characteristics of the monitor, the characteristics of the gamma ray spectrometer, the times of irradiation, exposures and measurements, as well as the cross section of the  $^{197}\text{Au}(n,\gamma)^{198}\text{Au}$  reaction.

Then the neutron flux density  $\Phi$  can be determined using the expression

$$\Phi = \frac{S_{peak}}{\frac{m}{\lambda \cdot A} \cdot \varepsilon_{\gamma} \cdot f \cdot g \cdot N_a \cdot (1 - e^{-\lambda \cdot t_{ir}}) \cdot e^{-\lambda \cdot t_d} \cdot (1 - e^{-\lambda \cdot t_m}) \cdot \sigma} \quad (2)$$

The thermal neutron flux density is determined by the following formula

$$\Phi_{th} = \Phi \cdot \frac{(R_{cd} - I)}{R_{cd}} \quad (3)$$

The average thermal neutron flux  $\Phi_{th}$  was obtained as a result of analyzing the activation gamma spectra of the irradiated Au monitor by the neutron flux from the  $^7\text{Li}(p,n)$  reaction on a thick target bombarded by protons with an energy  $E_p = 2.3$  MeV and at a current of  $20.6 \mu\text{A}$ . The average thermal neutron flux  $\Phi_{th}$  is equal  $3.63 \cdot 10^4$  neutrons/( $\text{cm}^2 \cdot \text{s}$ ) at the distance of 50 cm from the moderator.

Based on the obtained absolute value of the thermal neutron flux and the measured spatial distribution of the thermal neutron flux, it can be concluded that the scale of the

change of the absolute value of the thermal neutron flux at the Tandetron accelerator using this neutron moderator design and the  ${}^7\text{Li}(p,n)$  reaction varies from the maximum value of  $5.31 \cdot 10^5 \text{ n}/(\text{cm}^2 \cdot \text{s})$  at the proton current of  $20 \mu\text{A}$  at the distance of 100 mm from the target to the minimum value of  $14.12 \text{ n}/(\text{cm}^2 \cdot \text{s})$  at the proton current of  $0.1 \mu\text{A}$  at the distance of 2500 mm from the target.

### References

1. L. Curtis, Introduction to neutron physics, Atomizdat, Moscow, 1965.
2. M.L. Baranochnikov, Receivers and detectors of radiation, DMK Press, Moscow, 2012.
3. Mitrofanov K.V., Egorov A.S., Piksaikin V.M., Goverdovskii A.A., Zolotarev K.I., Samylin B.F., Gremyachkin D.E., Sedyshev P.V., Zontikov A.O., Zeynalov S.S., Shvetsov V.N., Neutron-physical characteristics of the neutron source for the production of radioactive isotopes on the basis of the interaction of electrons with liquid gallium, Atomic Energy. - 2014 - Volume 116 - Issue. 4. - pp. 204-209. - ISSN 0004-7163.
4. Canberra SEGe detectors. <http://www.canberra.com/products/detectors/pdf/XtRa-detectors-C40024.pdf>

# **Nuclear Structure**

# CREATION OF TRANSURANIUMS UNDER NEUTRON FLUXES OF NUCLEAR EXPLOSIONS

Yu. S. Lutostansky<sup>1</sup>, V. I. Lyashuk<sup>1, 2, §</sup>

<sup>1</sup>*National Research Center "Kurchatov Institute", Moscow, Russia*

<sup>2</sup>*Institute for Nuclear Research of the Russian Academy of Sciences, Moscow, Russia*

**Abstract:** The artificial  $r$ (rapid)-process of nucleosynthesis goes under high neutron flux densities: the obtained neutron fluences in the irradiated volume of thermonuclear devices reach  $\sim 10^{25}$  neutrons/cm<sup>2</sup> during the time interval  $\sim 10^{-6}$  s. The extreme condition (in neutron flux and temperature ( $\sim 10^8$  °K)) can be reached under conditions of (thermo)nuclear explosions. The creation of transuranium nuclides under pulsed neutron fluxes of thermonuclear explosions is investigated by means of dynamical model (as in the kinetic model of the astrophysical  $r$ -process) taking into account the time dependence of the external parameters and the processes accompanying the beta decays of neutron-rich nuclei. Time-dependent neutron fluxes in the interval  $\sim 10^{-6}$  s were simulated within the framework of the developed adiabatic binary model (ABM). The beta-delayed processes are taken into account for isotope yields correction after the pulse neutron wave. Calculations of transuranium nuclides yields  $Y(A)$  are made for five large scale explosion USA experiments ("Mike", "Anacostia", "Par", "Barbel" and "Vulcan") and it were obtained good or satisfied agreement. The corresponding root-mean-square deviations of the model yields compare to the experimental data (r.m.s.) are: 91% (for "Mike"); 70% ("Anacostia"); 33% ("Par"); 29% ("Barbel"); and 45% ("Vulcan"). An even-odd anomaly in the observed yields of transuraniums is explained by the predominant processes of decays after creation of neutron rich isotopes.

## 1. INTRODUCTION. MODEL OF ARTIFICIAL RAPID NUCLEOSYNTHESIS

In nature the creation of nuclides with mass  $A \approx 65-70$  occurs in  $r$  (rapid) and  $s$  (slow) processes of  $(n, \gamma)$ -captures. The cosmological  $r$ -process taking place in supernova explosions [1] is really fast one compare to  $s$ -process (as at the helium and carbon burning in red giants): so, the corresponding  $r$ -duration is up to  $\sim 10^2$  s when the slow process – up to thousands of years. Duration of the artificial  $r$ -process considered in this article is determined by the very small mass of the explosives (compare to stars) and as a result is strongly shorter (than cosmological one) with the time length  $\sim 10^{-6}$ s. An artificial  $r$ -process under the explosions of (thermo)nuclear devices goes intensively in the specially constructed target installed within the volume of the exploding experimental installation. For successful results (i.e., creation of the most heaviest elements by  $(n, \gamma)$ -captures) the target is manufactured from uranium or transuranium isotopes. The most full and significant results were obtained with <sup>238</sup>U-target.

Studies of the transuranium nuclei formation under thermonuclear tests were widely carried out in the USA (starting from 1952 year when it was realized the thermonuclear test "Mike") in (thermo)nuclear explosions. Namely in air debris of "Mike" it were first detected the transuranium isotopes (up to <sup>255</sup>Fm) [2, 3]. Later for peaceful use of nuclear explosions and scientific purposes it were proposed the USA program "Plowshare" [4] which were

---

§ lyashuk@itep.ru

continued from 1958 to 1975 years. In the frame of the Plowshare program it were conducted 27 (thermo)nuclear experiments. Specifications of some experiments (in which the transuranium isotopes were detected) are indicated in the table 1.

**Table 1.** Experiments on production of transuranium isotopes.

Test (experiment)	Date	released energy, kt	Obtained neutron fluence, neutron/cm <sup>2</sup>	irradiated target	detected isotopes up to A-mass (and not detected A-mass)
“Mike” [2,3]	October 31, 1952	10400	(1.2–1.8) · 10 <sup>24</sup>	<sup>238</sup> U	255 (250, 251)
“Anacostia” [5]	November 27, 1962	5.2	1.8 · 10 <sup>24</sup>	<sup>238</sup> U	254 (241, 247–251, 253)
“Kennebec” [6]	June 25, 1963	< 20	(2.7–3.6) · 10 <sup>24</sup>	<sup>238</sup> U	–
“Par” [7]	October 9, 1964	30 [7], 38 [6]	(4.2–4.8) · 10 <sup>24</sup> [7] 6.6 · 10 <sup>24</sup> [6,8]	<sup>238</sup> U	257
“Barbel” [9]	October 16, 1964	20 [9], <20 [6]	6.6 · 10 <sup>24</sup> [6,8]	<sup>238</sup> U	257 (not measured: 251 and 256) [9]
“Tweed” [6,8]	May 21, 1965	< 20 [6]	7.2 · 10 <sup>24</sup> [6,8]	<sup>242</sup> Pu and small part of <sup>237</sup> Np	255
“Cyclamen” [6,8]	May 5, 1966	12	1.1 · 10 <sup>25</sup>	<sup>238</sup> U and small part of <sup>243</sup> Am	257 (249, 256)
“Kankakee” [6,8,10]	May 15, 1966	(20-200)	7.2 · 10 <sup>24</sup>	<sup>238</sup> U	255 (249, 251)
“Vulcan” [6,8,10]	June 25, 1966	25	7.2 · 10 <sup>24</sup>	<sup>238</sup> U	257 (256)
“Hutch” [6,8,10,11]	July 16, 1969	(20-200)	(2.1–2.4) · 10 <sup>25</sup>	<sup>238</sup> U and <sup>232</sup> Th	257 (249, 256)

The short duration of explosive nuclear process ( $t < 10^{-6}$  s) allows to split it into two phases: neutron capturing process and the following decays of neutron-rich nuclei [12, 13]. Such a process can be called as “prompt rapid” or *pr*-process and solution of equations for the concentration  $N_{A,Z}(t)$  of formed nuclei can be greatly simplified.

The significant part of Plowshare program was devoted to nucleosynthesis of transuranium isotopes under neutron pulse of exploding devices. The complete analysis on identification of isotopes produced in underground tests is possible only after drilling from the surface to the zone of explosion to the produced cavity volume. In order to imagine the scale of drilling it is need to note that depth of drilling can be several hundred meters (up to about kilometer). So the “Hutch” device was exploded at the depth 600 m [8]. The process of debris recovery by drilling can take days: the first debris from “Hutch” was delivered to the laboratory after 7 days since the explosion. But an exceptions are possible as in case of “Cyclamen” test (when the debris were obtained within 24 hours) [8]. As a result the short lived isotopes decay before isotope analysis in the laboratory.

In Plowshare program the first experiment for transuraniums production was “Anacostia” [5] with strongly lower released energy yield (compare to “Mike”) and significantly more

poor list of created isotopes. The most complete data of transuraniums yields up to  $A = 257$  were obtained in the "Par" experiment [7]. In the similar test "Barbel" test [9] a close fluence was achieved as in "Par", but yield of  $^{257}\text{Fm}$  was lower. In "Cyclamen" test it was obtained more high fluence ( $\sim 1.1 \cdot 10^{24}$  neutron/cm $^2$ ) but without new isotopes creation. The more heavy shot "Vulcan" (compare to "Cyclamen") was constructed as device-development experiment. But production of isotopes with  $A > 257$  were not detected too (see table 1). In the test "Hutch" it was ensured the record fluence  $(2.1-2.4) \cdot 10^{25}$  neutron/cm $^2$  but also without creation of isotopes with  $A > 257$ .

The figure 1 shows the experimental data normalized on  $Y(A_i)$  yields for five explosions "Mike" [2, 3], "Par" [7], Barbel" [9], "Anacostia" [5] and "Vulcan" [10]. The decreasing dependence of  $Y(A)$  is fitted as follows:

$$Y(A)/Y(A_i) = \exp\{-b_i A + c_i\} \quad (1)$$

$$i = 1 \text{ ("Mike")} \quad A_1 = 239, b_1 = 1.570, c_1 = 375.491 \quad (1a)$$

$$i = 2 \text{ ("Barbel")} \quad A_2 = 244, b_2 = 1.395, c_2 = 340.584 \quad (1b)$$

$$i = 3 \text{ ("Par")} \quad A_3 = 245, b_3 = 1.388, c_3 = 341.015 \quad (1c)$$

$$i = 4 \text{ ("Anacostia")} \quad A_4 = 239, b_4 = 1.739, c_4 = 417.941 \quad (1d)$$

$$i = 5 \text{ ("Vulcan")} \quad A_5 = 244, b_5 = 1.325, c_5 = 370.441 \quad (1e)$$

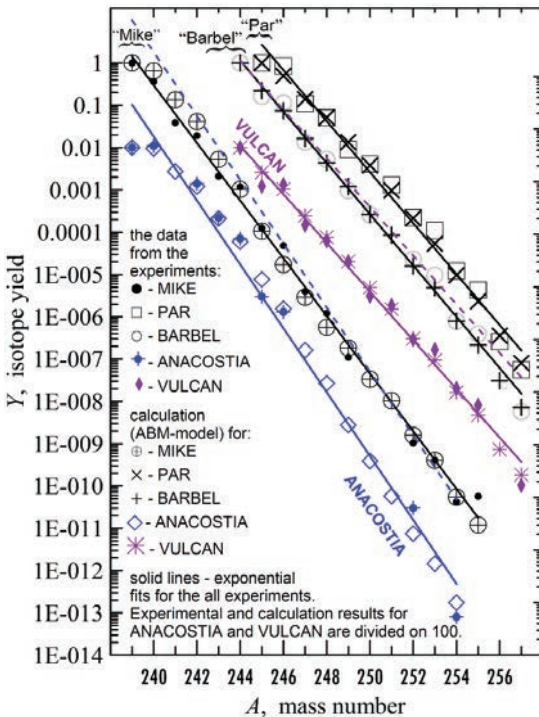


**Figure 1.** Results of isotope yield calculations in ABM-model compare to the experimental yields in tests "Mike", "Par", "Barbel", "Anacostia" and "Vulcan". An exponential fitting of the experimental data are shown by the solid lines. The experimental data and calculation results for "Anacostia" and "Vulcan" are divided on 100. The dashed lines are exponential fitting for "Anacostia" and "Vulcan" without dividing on 100.

The standard deviations of this approximation are:  $\delta_1 = 56\%$  ("Mike"),  $\delta_2 = 60.2\%$  ("Barbel"),  $\delta_3 = 86.8\%$  ("Par"),  $\delta_4 = 357\%$  ("Anacostia"),  $\delta_5 = 86.4\%$  ("Vulcan"), which are comparable to the accuracy of the known calculations. The results of isotope yield calculations on the base ABM model (Adiabatic Binary Model [13, 12]) are presented in the figure 1 to compare to the experimental data and its exponential fitting (1, 1a-1e). The details of calculation for "Mike", "Barbel" and "Par" are discussed in [14, 15].

For the *pr*-process modeling of (thermo)nuclear explosions the serious simplification were made owing to the fact that neutron captures and decays of the nuclides are separated in time. So the system of equations for the time dependence of concentrations  $N(A; Z; t)$  of nuclei with the mass number  $A$  and the charge  $Z$  have the form:

$$\begin{aligned} dN(A, Z, t)/dt = & -\lambda_{n\gamma}(A, Z, t)N(A, Z, t) + \lambda_{n\gamma}(A-1, Z, t)N(A-1, Z, t) + \\ & \lambda_{n,2n}(A+1, Z, t) \cdot N(A+1, Z, t) - \lambda_{n,2n}(A, Z, t) \cdot N(A, Z, t) - \lambda_{n,f}(A, Z, t)N(A, Z, t) - \\ & \Phi[\lambda_{\beta}, \lambda_{\beta n}, \lambda_{\beta f}, \lambda_{\alpha}, \lambda_{sf}], \end{aligned} \quad (2)$$

where  $\lambda_{n\gamma}$  – is the capture rate of neutrons in the  $(n, \gamma)$ -reaction,  $\lambda_{n,2n}$  is the same for  $(n, 2n)$  reaction, and  $\lambda_{n,f}$  is the neutron fission rate. The reactions with  $\gamma$ -quantum were not taken into account because of lower temperatures in comparison with astrophysical processes. The term  $\Phi[\lambda_{\beta}, \lambda_{\beta n}, \lambda_{\beta f}, \lambda_{\alpha}, \lambda_{sf}]$  in the system of equations (2) does not depend on time since it includes the processes occurring after the active phase of the explosion:  $\beta$ -decay processes,  $(\beta, n)$ -emission of delayed neutrons (DN),  $\alpha$ -decay,  $(\beta, f)$ -delayed (DF) and  $(s, f)$ -spontaneous fission. The DF and DN probabilities were calculated basing on the microscopic theory of finite Fermi systems [16]. The effect of the resonant structure of the  $\beta$ -decay strength function, including the pigmy resonances, was taken into account [17].

The time-dependent part of the system of equations (2) was solved using the adiabatic binary model (ABM) [18] where numerical simulation is performed by dividing duration of *pr*-process on small nanosecond time steps with calculations of isotope yields in succession for each step. The step initial conditions are also determined by the isotope composition of the target and yields of the preceding isotopes in the previous time step. In view of the binary, two-stage character of the thermonuclear explosion: the nuclear explosion (the first stage with the fission reaction) and the second stage associated with the thermonuclear reaction, two neutron fluxes and two sets of initial concentrations were used in the calculations.

## 2. RESULTS OF ISOTOPE YIELDS CALCULATIONS

For model calculations a unified approach was adopt within the framework of the adiabatic binary model (ABM) – it was assumed that there was an admixture of  $^{239}\text{Pu}$  in the primary  $^{238}\text{U}$  target. The specificity of the binary, two-stage explosion process also allowed to the irradiation of the uranium-plutonium target by two different fluxes. In accordance with the experimental data the all model yields of the isotopes  $Y(A)_{\text{calc}}$  are normalized (see (1)): note that for “Anacostia” the yields are normalized on  $Y(A=239)$  which in [5] is considered as unit; for “Vulcan” the experimental yields for every  $A$ -value are absolute numbers of nuclei which produced from starting  $3.4 \cdot 10^{22}$  nuclei of  $^{238}\text{U}$ -target. The calculated yields and experimental data for “Anacostia” and “Vulcan” tests are presented in the table 2, where the standard (r.m.s.) deviations  $\delta$  are also given for ABM calculations and for approximation (1).

Results for "Anacostia" are obtained at the conditions:  $^{238}\text{U}$  (99.994% in the target) was irradiated with neutron fluence  $1.3 \cdot 10^{24}$  neutron/cm<sup>2</sup>;  $^{239}\text{Pu}$  (0.006% in the target) was irradiated with fluence  $2.7 \cdot 10^{24}$  neutron/cm<sup>2</sup>.

Results for "Vulcan" are obtained at the conditions:  $^{238}\text{U}$  (99.3% in the target) was irradiated with neutron fluence  $4.21 \cdot 10^{24}$  neutron/cm<sup>2</sup>;  $^{239}\text{Pu}$  (0.7% in the target) was irradiated with fluence  $7.55 \cdot 10^{24}$  neutron/cm<sup>2</sup>.

**Table 2.** Experimental and calculated yields of isotopes in "Anacostia" and "Vulcan" tests.

"Anacostia"			"Vulcan"		
A	$Y(A)_{\text{exper}}$ [5]	$Y(A)_{\text{calc}}$	A	$Y(A)_{\text{exper}}$ [10]	$Y(A)_{\text{calc}}$
239	1±0,3	1.00	244	2.7E+20	2.56E+20
240	1,09±0,22	9.51E-1	245	3.3E+19	6.60E+19
241		2.71E-1	246	3.6E+19	2.64E+19
242	(1,4±0,2)E-1	1.20E-1	247	4.0E+18	6.30E+18
243	(2,2±0,1)E-2	2.12E-2	248	1.7E+18	1.95E+18
244	(7,0±0,4)E-3	5.95E-3	249	5.4E+17	5.16E+17
245	(3,0±0,4)E-4	7.64E-4	250	8.4E+16	1.26E+17
246	(1,3±0,2)E-4	1.56E-4	251	≤5E+16	3.88E+16
247	–	1.62E-5	252	7.9E+15	7.77E+15
248	–	2.65E-6	253	4.5E+15	2.39E+15
249	–	2.76E-7	254	5.4E+14	4.20E+14
250	–	3.87E-8	255	2.2E+14	1.20E+14
251	–	5.73E-3	256	–	1.86E+13
252	<3.E-9	7.45E-10	257	2.8E+12	4.69E+12
253	–	1.45E-10			
254	<8.E-12	1.75E-11			
δ %	357 (1d)	70		86 (1e)	45

To illustrate the degree of agreement between calculations and experiments "Anacostia" and "Vulcan" the calculated yields are normalized on experimental data (figures 2 and 3).

The table with experimental and calculated yields for "Mike", "Par" and "Barbel", the relations of normalized data ( $Y_{\text{calculation}} / Y_{\text{experimental}}$ ) and comparison with known simulation results are given in [14,15].

The most successful setup of nucleosynthesis experiment for production of transuraniums was the "Par" [7], where all nuclides with mass numbers up to  $A = 257$  were detected. In the very similar test "Barbel" [9] the yields had considerable differences compare to "Par". The most high yields were obtained in the "Hutch" test where it was reached the record fluence  $(2.1-2.4) \cdot 10^{25}$  neutron/cm<sup>2</sup>. It is need to underline that the values of obtained fluences are strongly device-dependent ones.

The ABM model applied to yields simulation in several explosive experiments have demonstrated the adequate algorithm for describing of *pr*-process with good or (at least) satisfactory agreement.

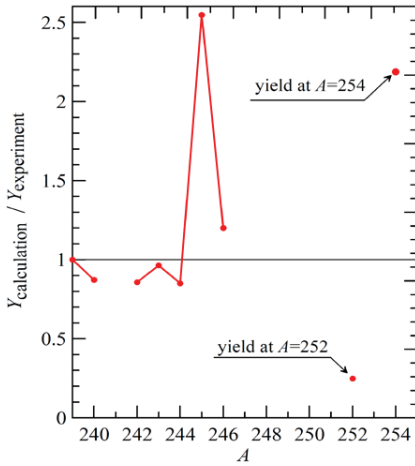


**Figure 2.** Relation of normalized (on  $Y(A=243)_{\text{calc}}$ ) calculated yields to normalized (on  $Y(A=243)_{\text{exp}}$ ) experimental yield of "Anacostia".

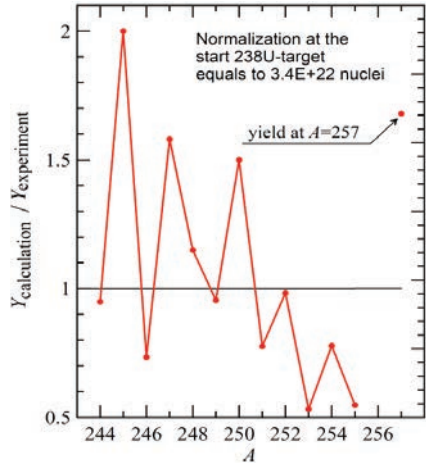


**Figure 3.** Relation of calculated yields to the experimental yield  $Y(A=244)_{\text{exp}}$  (in number of nuclei) of "Vulcan" for  $^{238}\text{U}$ -target (with number of nuclei  $3.4\text{E}+22$ ).

### 3. CONCLUSION

The article devoted to simulation of artificial *pr*-process of nucleosynthesis in which the neutron fluences reach the values up to  $\sim 10^{25}$  neutrons/cm<sup>2</sup> during the short exposition – about  $10^{-6}$ s. The results of calculation on the base of the developed ABM model are compared with the experimental date for all mass numbers in the region  $A = 239 - 257$ . The Adiabatic Binary Model has confirmed the adequacy of used algorithm. The model is confirmed as in previous our calculations (the  $\delta$  -values of standard r.m.s. [root mean square] deviation for "Mike", "Par" and "Barbel" experiment are: 91%, 33% and 29% [14, 15]) as in the current results:  $\delta$  -values for "Anacostia" and "Vulcan" – 70% and 45% correspondingly.

The calculations include the processes of delayed fission (DF) and the emission of delayed neutrons (DN), which determine the "losing factor" – the total loss of isotope concentration in the isobaric chains. The DF and DN probabilities were calculated in the microscopic theory of finite Fermi systems [8]. Thus, it was possible to describe the even-odd anomaly in the distribution of concentrations  $N(A)$  in the mass number region  $A = 251 - 257$ . It is shown qualitatively also that the odd-even anomaly may be explained mainly by DF and DN processes in very neutron-rich uranium isotopes.

The results confirms that the assumptions [14, 15] (1. emission of other isotopes [ $^{239}\text{Pu}$  in our calculations] into the target volume at stage of plasma ball and 2. irradiation of admixture [ $^{239}\text{Pu}$  in this case] and the main target under different fluences at the stage of plasma ball) are reasonable.

## Acknowledgements

We are grateful to L.B. Bezrukov, B.K. Lubsandorzhev, I.V. Panov, E.E., V.N. Tikhonov, I.I. Tkachev and S.V. Tolokonnikov for stimulating discussions and assistance in the work. The work is supported by the Russian Foundation for Basic Research Grants no.18-02-00670\_a.

## References

1. Burbridge B. M., Burbridge G., Fowler W., Hoyle P., *Rev. Mod. Phys.* **29** (1957) 547.
2. Ghiorso A., Thompson S. G., Higgins G. H. *et al.*, *Phys. Rev.* **99** (1955) 1048.
3. Diamond H., Fields P. R., Stevens C. S. *et al.*, *Phys. Rev.* **119** (1960) 2000.
4. United States Nuclear Tests. July 1945 through September 1992. DOE/NV-209-REV 16 September 2015.
5. Hoff R.W., Dorn D.W., *Production of Transuranium Elements in a Thermonuclear Explosion – Anacostia. Nuclear Science and Engineering*, **18**, (1964) 110–112.
6. Becker, Stephen A., *Approximating the r-Process on Earth with Thermonuclear Explosions. Lessons Learned and Unanswered Questions* (2012). LA-UR-12-25146
7. Dorn D.W., Hoff R.W., *Spontaneous fission in very neutron-rich isotopes*, *Phys. Rev. Lett.* **14** (1965) 440.
8. Hoff. R.W., *Production einsteinium and fermium in nuclear explosions*. Lawrence Livermore Laboratory. UCRL-81566. August 21, 1978.
9. Los Alamos Radiochemistry Group. *Production of very heavy elements in thermonuclear explosion - test Barbel*. *Phys. Rev. Lett.* **14** (1965) 962–964.
10. John S. Ingley, *Nucl. Phys. A* **124** (1969) 130–144.
11. Hoff. Richard W., *Beta decay of neutron-rich transuranic nuclei*. UCRL-94252. June 6, 1986.
12. Lutostansky Yu.S., Lyashuk V.I., Panov I.V., *Calculation of Transuranium Element Synthesis in Intensive Neutron Fluxes under Adiabatic Conditions*. *Bull. Russ. Acad. Sci. Phys.* **74** (2010) 504.
13. Lyashuk V.I., *Taking into consideration the dynamics at creation of transuranium isotopes*. Preprint of of Alikhanov Institute for Theoretical and Experimental Physics, Moscow: ITEP, 1997, no.7; <http://lss.fnal.gov/archive/other/itep-7-97.pdf>
14. Lutostansky Yu.S., Lyashuk V.I., *Production of Transuranium Nuclides in Pulsed Neutron Fluxes from Thermonuclear Explosions*. *JETP Letters*, **107**, No.2 (2018) 79–85.
15. Lutostansky Yu.S., Lyashuk V.I., *Nucleosynthesis of Heavy Elements in Thermonuclear Explosions "Mike", "Par" and "Barbell", in the 3rd International Conference on Particle Physics and Astrophysics*, KnE Energy & Physics, pages 57–64, DOI 10.18502/ken.v3i1.1723.
16. Migdal A.B., *Theory of Finite Fermi Systems and Applications to Atomic Nuclei* (1983) Nauka Moscow; 1967 Inter-Sci. New York.
17. Lutostansky Yu.S., *JETP Lett.* **106** (2017) 7.
18. Lyashuk V.I., *Simulating Transuranium Isotope Yields upon Explosive Nucleosynthesis with Allowance for Elements of Process Dynamics*, *Bull. Russ. Acad. Sci. Phys.* **76** (2012) 1182.

# ANALYSIS OF NUCLEAR EXCITATIONS IN DIFFERENT ELEMENTS

S.I. Sukhoruchkin, Z.N. Soroko, D.S. Sukhoruchkin

*Petersburg Nuclear Physics Institute NRC "Kurchatov Institute" 188300 Gatchina*

## 1. Introduction

Nuclear Physics deals with nucleons and their interactions. The nucleon masses ( $m_n$ ,  $m_p$  and the nucleon mass difference  $\delta m_N$ ) are well known [1]. Their numerical relation to the mass of the electron ( $m_e$ ) makes it possible to obtain a very simple representation, called the "CODATA relations" with a period  $\delta = 16m_e = 8176.0$  keV:

$$m_n = 115 \cdot 16m_e - m_e - \delta m_N/8, \quad m_p = 115 \cdot 16m_e - m_e - 9(\delta m_N/8). \quad (1)$$

The difference of 8.67 keV between the two CODATA parameters  $m_e/3 = 170.33$  keV and  $\delta m_N/8 = 161.66$  keV is close to the empirically determined period of the fine structure  $\delta' = 9.5$  keV in the neutron resonance data [2] and the value  $m_e/(18 \times 3) = 9.46$  keV, corresponding to the proposed ratio 18:17 in the CODATA parameters:

$$\delta' = 9.5 \text{ keV}, \quad \delta' = m_e/(18 \times 3) = 9.46 \text{ keV}, \quad \delta' = (\alpha/2\pi) \cdot (\delta = 16m_e) = 9.48 \text{ keV}. \quad (2)$$

The fine structure effects in the distribution of positions and spacings of neutron resonances were connected [2-5] with the empirical observation that the fine structure parameter  $9.5 \text{ keV} = \delta'$  in the resonance positions is close to the difference between the CODATA parameters 161 keV and 170 keV. This may be due to QED correction  $\alpha/2\pi$  to the pion mass and nucleon  $\Delta$ -excitation, the effect of the influence of physical condensate [6]:

$$\delta m_n = 161 \text{ keV} = \delta m_N/8 = (\alpha/2\pi)m_\pi, \quad m_e/3 = 170 \text{ keV} = (\alpha/2\pi)\Delta M_\Delta. \quad (3)$$

The parameter  $\delta' = 8\varepsilon'$  was introduced [7-9] from the empirically found proximity of the ratios between the stable mass/energy intervals in neutron data ( $\varepsilon'' = 1.35$  eV and  $\varepsilon' = 1.2$  keV), nuclear spectroscopic data ( $\varepsilon' = 1.2$  keV and  $\varepsilon_o = 1.02$  MeV) and intervals in particle mass values ( $M_q = 441$  MeV) noticed by R. Sternheimer and P. Kropotkin [10,11]:

$$(\varepsilon'' = \delta''/8) : (\varepsilon' = \delta'/8) : (\varepsilon_o = 2m_e) : 2M_q = \alpha/2\pi = 115.9 \cdot 10^{-5}. \quad (4)$$

The values  $16\varepsilon' = 2\delta' = 19$  keV and  $4\varepsilon' = 4.7$  keV were observed independently in the neutron resonance positions and other nuclear spectroscopic data [1,2,12]. The parameters  $\delta' = 9.5$  keV and  $\varepsilon' = \delta'/8 = 1.2$  keV were introduced by M. Ohkubo and others from the proximity in the positions of strong resonance in the  $N=82$  near-magic  $^{141}\text{Ce}$ ,  $^{142}\text{Pr}$ ,  $^{140}\text{La}$  etc. In Fig. 1, the observed nonstatistical character of the sum of the positions of neutron resonances of different nuclei is shown (maxima at  $4\delta'' = 44$  eV and at  $572 \text{ eV} = 13 \times \delta''$ ) [2].

## 2. Analysis of data on excitations in light nuclei

The position of the neutron resonance corresponds to the difference between the energy of the excited compound nuclear state  $E^*$  and the binding energy of the neutron  $S_n$  in this compound nucleus. The effect of systematic grouping of resonance positions means

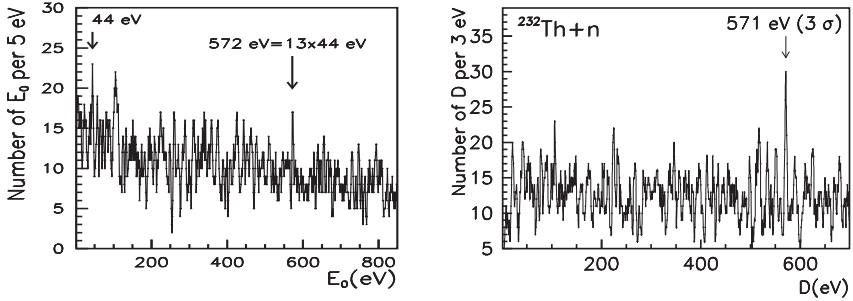


Fig. 1. Distributions of resonance positions in nuclei  $Z=33-56$  [13] and spacings ( $\Gamma_n^\circ$ ) in  $^{233}\text{Th}$ .

that  $E^*$  and  $S_n$  are not independent. The observed width of the maxima in the grouping effects shown in Fig. 1, is several eV. Similar structure in  $D$ -distributions between neutron resonances were noticed by many authors (W. Havens, M. Ohkubo, K. Ideno, C. Coceva and others). The maxima appear with the averaging interval of ideohistograms of 3-5 eV in heavy nuclei and 3-5 keV in light nuclei. This new approach to the development of nuclear physics is based on the confirmation of CODATA relations with an exact mass presentation with the period  $\delta=16m_e$ . In Figs. 2a, 2b spacing distributions in three near-magic light nuclei  $^{42}\text{Ca}$ ,  $^{58}\text{Ni}$  (two valence neutrons) and  $^{55}\text{Co}$  (one proton hole) are presented together with the spacing distributions  $D^{AID}$  adjusted to stable intervals  $D_{ij}=2 \times 511 \text{ keV} = 2m_e = \varepsilon_0$  (see relation (3) above). The strong maxima observed with the averaging interval of the ideohistogram 3 keV, and rational relations between their values correspond to exact integer relations with the value  $m_w$  in CODATA relations (1).

We describe here a global analysis of nuclear data collected at PNPI [14] and published in the Springer Landolt-Boernstein Library New Series, in accordance with a comment of the editor-in-chief of the LBL W. Martienssen [15] that data compilations could serve as bridges between different branches of science. These nuclear files were used to check the observed relations in the particle masses due to the well-known fact that the QCD-based theoretical models provide the description of the origin of the nucleon masses, and QCD is a general theory of nuclear excitations and nuclear binding energies.

We use two new methods of data analysis based on the selection of data for all isotopes of each element and the location of the grouping effect in the excitation energies.

The first method of data analysis consists in a production and the analysis of the combined data for isotopes of the neighboring near-magic elements (nuclei with  $Z=8, 9, 10, Z=20, 22$  etc.). The first step was the grouping effect in the values of the excitation energies of different isotopes of a certain element, which was considered in the previous subsection. The second step is based on the observation of similarities in excitations of several near-magic nuclei. For example, it was noticed long ago that the first excitations of  $^{18}\text{O}$  and  $^{24}\text{Ne}$   $E_1^*(2^+)=1982.1(1) \text{ keV}$  and  $E_1^*(2)=1981.6(4) \text{ keV}$  are unexpectedly close to each other. Now we find that the grouping effect in the sum of the usual  $D$ -distributions in neighbor elements  $Z=8, 9, 10$  at the first excitations of  $^{18}\text{O}$  and  $^{24}\text{Ne}$  at  $D=1982 \text{ keV}$  (161 intervals with a deviation of  $2.4\sigma$  over the mean value) can be compared with the

maximum at a same value (Fig. 3, deviation of  $3.0\sigma$ ) in a similar analysis of the combined spectrum of the same three elements ( $n=546+804+701=2051$ , for  $Z=8, 9, 10$ ). The mean value  $n\approx 1200$  in the combined spectrum of all 55 isotopes of these three elements is much larger than the mean value  $n=126$  (the sum of results of the separate analyses), and the effect of about 160 values (over the mean level, in the combined analysis) is much larger than the effect of 35 values obtained during the usual analysis of separate data.

To study this effect, we use the AIM-method of data analysis [3-5,13]. Fixing the intervals  $x=1982$  keV in the combined spectrum (Fig. 3 center), we observe the strongest maximum at exactly twice the value of 3963 keV (marked by an arrow), which is absent in the sum  $D^{AIM}$ -distribution for separately analyzed spectra of the same isotopes.

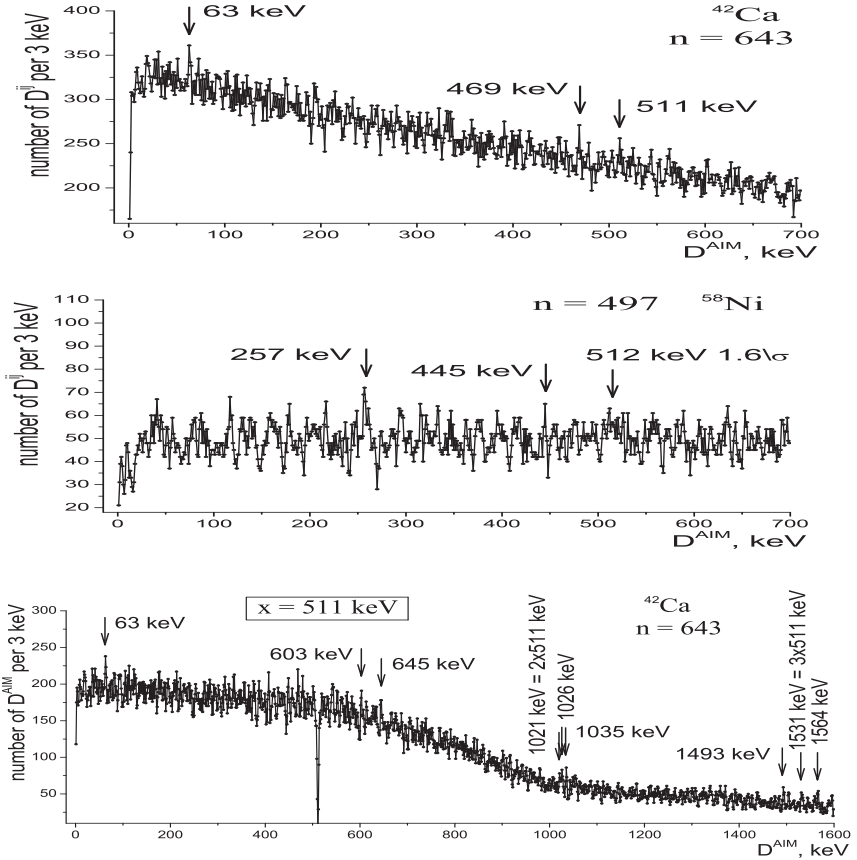


**Fig. 2a.** Top:  $D$ -distributions of levels in  $^{42}\text{Ca}$  with maxima at 511 keV.

Center: The same for  $^{59}\text{Ni}$ .

Bottom:  $D^{AIM}$ -distribution in  $^{42}\text{Ca}$  for  $x=511$  keV= $m_e$  with maxima at  $2m_e$  and  $3m_e$ .

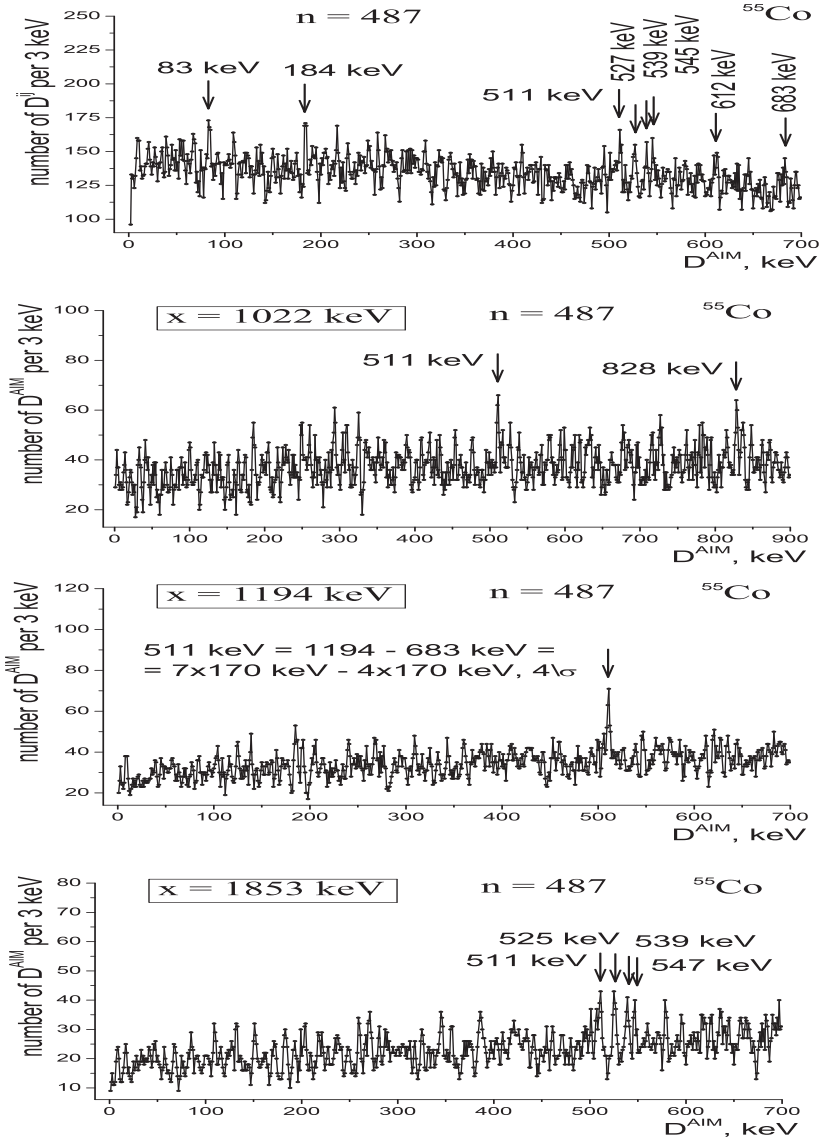
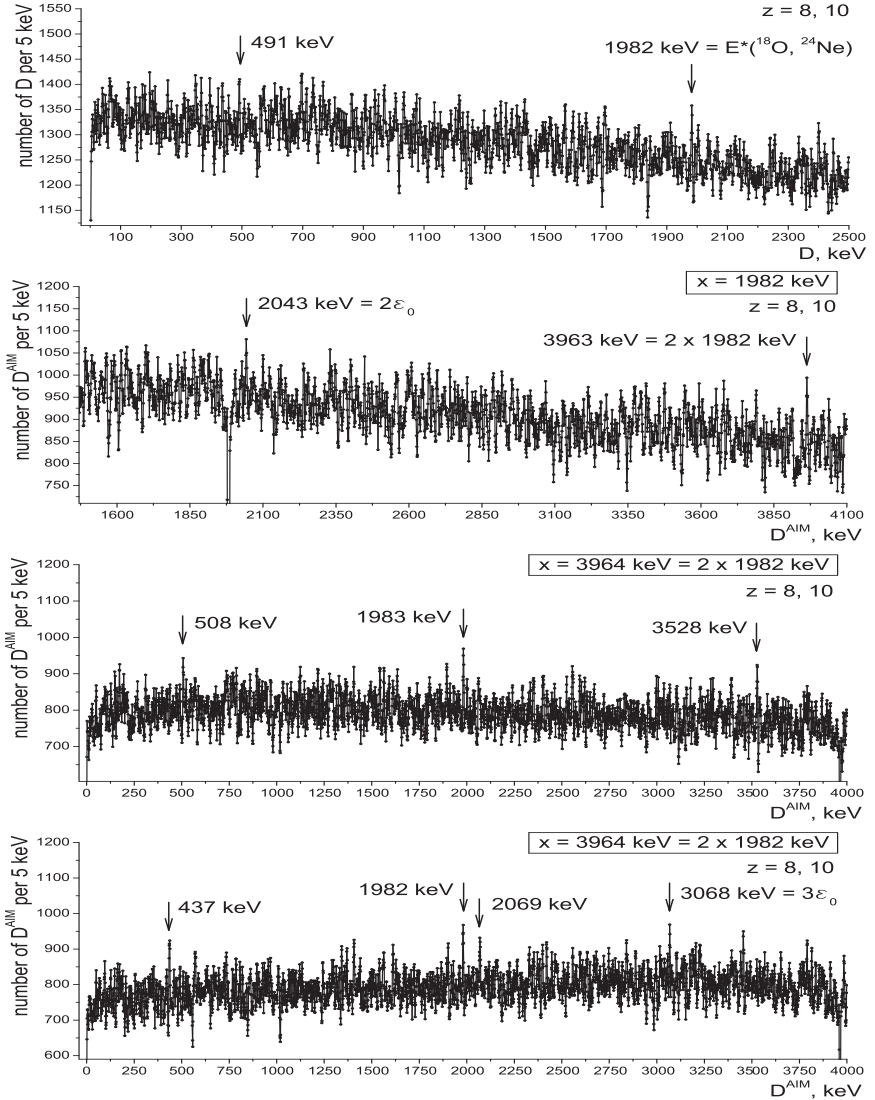


Fig. 2b. Top:  $D$ -distribution in  $^{55}\text{Co}$ .

2nd line:  $D^{AIM}$ -distribution in  $^{55}\text{Co}$  for  $x=1022$  keV with maxima at 511 keV and 828 keV.

Center:  $D^{AIM}$ -distributions in  $^{55}\text{Co}$  for  $x=1194$  keV.

Bottom:  $D^{AIM}$ -distributions in  $^{55}\text{Co}$  for  $x=1853$  keV with four closely spaced maxima started with 511 keV, also observed in  $D$ -distribution in  $^{55}\text{Co}$  (right part of the top figure).



**Fig. 3.** *Top:*  $D^{AIM}$ -distributions for  $x=1982$  keV in the combined spectrum of isotopes with  $Z=8, 9, 10$  (number of levels  $n=546+804+701$ ). *2nd line:* The same for  $x=2043$  keV. The interval  $D^{AIM}=347$  MeV is close to  $2043$  keV/6=341 keV. *Center:* The same for  $x=2 \times 1982$  keV (upward AIM direction). *Bottom:* The same for  $x=2 \times 1982$  keV (downward AIM direction). Maximum at 1982 keV in all distributions is marked by an arrow.

The obtained result means that the excitations in individual nuclei with different nucleon configurations in the case of near-magic nuclei are not independent. This is a manifestation of traces of the common general quantitative effect of the quark structure in the case of a nucleon in a few-particle configuration. To study these unexpected effects, we use the presence in Fig. 3 (top) of the second strong maximum at  $D=2043$  keV, which coincides with  $2\varepsilon_o = 4m_e=2044$  keV (the main CODATA parameter). The strongest maximum at 1982 MeV in the  $D^{AIM}$  distribution for  $x=2043$  keV (Fig. 3, 2nd line) and the same maxima (in Fig. 3, center and bottom), corresponding to the upward and downward directions in the AIM-analysis with  $x=2\times 1982$  keV. This allows us to conclude that the position of the strongest maximum in the  $D^{AIM}$ -distribution in the combined spectrum (at  $2x=3963$  keV) reflects the very general and systematic character of the intervals, considered earlier as examples of the distinguished character of the parameters involved in the CODATA relations. The appearance of maxima at  $D = 3\varepsilon_o=3068$  keV and at  $D=508$  keV= $\varepsilon_o/2$  in the  $D^{AIM}$ -distribution for  $x=2\times 1982$  keV (Fig. 3, center and bottom) and maxima at  $2\varepsilon_o=2043$  keV and  $4096$  keV $\approx 4\varepsilon_o$  in  $D^{AIM}$ -distribution for  $x=347$  keV (close to  $(2/3)\varepsilon_o=341$  keV), confirms the role of the main CODATA fine structure parameter directly connected with  $m_e$ . This new method of the indirect confirmation of CODATA fine structure parameters was applied to the data for nuclei situated at all other closed nucleon shells ( $Z=20, 28, 40, 50$  and  $82$ ).

We conclude that the analysis of nuclear data is a part of an empirical approach to the further SM development and consequent production of the nuclear microscopic models based on the fundamental aspects of nucleon quark structure [16]. This new nuclear spectroscopy will possess, according to F. Wilczek [17], a very unexpected high accuracy.

The presence of strong maxima at doubled values of the initial intervals  $x$  in the combined spectra of the light near-magic nuclei, namely,  $^{18}\text{O}$ ,  $^{24}\text{Ne}$ ,  $D^{AIM}=3963$  keV for  $x=1982$  keV= $E^*$  means that there exists a number of fixed mass/energy intervals ("expanded intervals") in the total combined spectrum, which are not observed in excitations of the individual nuclei. The AIM-method allows one to observe their interconnection with the fine structure parameters associated with the quark structure of nucleons.

**Table 1.** Stable spacing in the combined spectra of light near-magic nuclei with  $Z=8-10$ . The relations between the observed maxima in the distributions of spacing  $D$  and  $D^{AIM}$  and other nuclear parameters are commented on the right and are discussed in the text.

No	Z	D, x	$D^{AIM}$	$D^{AIM}$	$D^{AIM}$	$D^{AIM}$	Comments	Parameters
1	8,9,10	1982	2043			3963	Fig.3	top $2\varepsilon_o$
		Signif.	$5.5\sigma$					
		3964	1982	3068		508	Fig.3	$3\varepsilon_o$ $\varepsilon_o$
		Signif.	$5.5\sigma$	$5.5\sigma$				
		2043	1982			347	Fig.3	2-nd line
		Signif.				$5.5\sigma$	$\Delta$	=5 keV

### 3. Analysis of nuclear excitations in different elements

To find out a presence of stable nuclear excitations similar to fine structure intervals observed in CODATA relations (periods  $16m_e/3=\delta$ ,  $m_e/3=170$  keV and  $\delta m_N/8=161$  keV), a global analysis of excitations  $E^*$  in all nuclei was performed. About 100 independent sum  $E^*$ -distributions for all isotopes for each of known element were obtained. This second new method of nuclear data analysis is to search for areas of the nuclear chart where groupings of nuclear excitations can be found.

The grouping of  $E^*$  at integer values of  $m_e$  is presented in Table 2. The value  $m_e$  is known from CODATA relations as the parameter connected with the nucleon quark structure. It has been suggested that the up-quark mass  $m_u$  is close to half of the groupings of  $E^*$  at  $9 \times (m_e/3)=3m_e$ , namely at  $E^*=6m_e=3.07$  MeV (14 boxed values in Table 2, observed in the region  $E^*=3057-3075$  keV, can be compared with the expected number  $n \leq 3$  for a random distribution, the small probability of occasional grouping is about  $10^{-5}$ ).

Here we consider groupings at  $m_e$  ( $3m_e/3$ , the first fine structure period) together with groupings at integer values of the second CODATA parameter, period  $161$  keV  $=\delta m_N/8$ . In Fig. 4, the first maximum at  $1454$  keV  $=9\Delta^{TF}$  corresponds to the discreteness in  $E^*$  nuclei around  $Z=20-28$  with parameter  $161$  keV (Table 3).

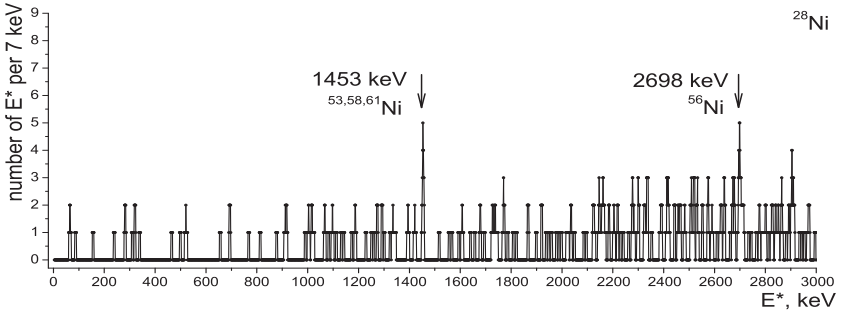


Fig. 4. Sum  $E^*$ -distribution for isotopes with  $Z=28$ .

Values close to  $1454$  keV  $=9\Delta^{TF}$  are double-boxed in Table 5, where other values of the sequence  $E^*=k \times \Delta^{TF}$  in near-magic nuclei are boxed and compared (in the bottom lines of each section) with integers  $k$  of parameter  $161$  keV  $=17\delta=\Delta^{TF}$ .

The values of  $1942$  keV: $1454$  keV: $1292$  keV: $646$  keV: $322$  keV  $=12:9:8:4:2$  can be represented as rational to the value  $E^*=321$  keV, which is the effect of the residual interaction of a neutron hole in the subshell  $1f_{7/2}$  ( $\Delta N=7$ ) and a pair of protons in  $1d_{3/2}$  subshell in the nucleus  $^{43}\text{S}$ . The corresponding  $E^*$  is double-boxed in the fourth section, where the linear trend in the excitation energies (in keV) in nuclei with  $N=21, 22$  ( $\Delta N=1, 2$  over  $N=20$ , boxed) is compared with the number of valence proton pairs  $(Z-14)/2$  (also boxed). The interval from the residual interaction of three valence neutrons in  $^{61}\text{Ni}$  ( $339$  keV) and the similar interval from the interaction of three neutron holes in  $^{53}\text{Ni}$  ( $320$  keV, which coincides with  $E^*$  in  $^{43}\text{S}$ ) – this is twice the CODATA fine structure parameters ( $340$  keV and  $322$  keV).

**Table 2.** Stable excitations  $E^*$  (keV) in all isotopes of different elements (Z, El.  $N^m$ ), observed as maxima in  $E^*$ -distributions with the averaging parameter of the ideohistogram  $\Delta=7$  keV.  $N^m-N^{minimal}$  corresponds to the minimal number of neutron in the sequence of isotopes under the study. Boxed are values close to the integers of the parameter  $\varepsilon_o/2$ . One asterisk marks  $E^*$  close to  $1454$  keV= $9 \times \Delta^{TF}$ , two asterisks – close to the first  $E^*$  of double-magic nuclei.

Z El.	$N^m$	$E^*$	$E^*$	$E^*$	$E^*$	$E^*$	$E^*$	$E^*$	$E^*$	$E^*$	$E^*$
<b>20</b> Ca	16	3027	3335	4993	6159						
24 Cr	21	3163	3897	5859	<b>6135</b>	6257	6329	6377	7117		
26 Fe	22	<b>367</b>	2115	2756	<b>3073</b>	3309	4275	6669			
27 Co	25	<b>508</b>	1271	2105	2733	2910	2979	3869			
<b>28</b> Ni	24	1453*	2698**	3010							
29 Cu	27	63	1430	<b>3577</b>							
31 Ga	30	65	<b>513</b>	711	1233	1619	1975	2600	2655		
32 Ge	29	1189	1409	1430	2140	2572	2694	3035	3680	<b>4083</b>	
33 As	32	310	<b>507</b>	517	1872	1902	3260				
35 Br	35	205	242	273	331	472	<b>1023</b>	1486	1515	2800	
36 Kr	34	147	485	674	985	1015	<b>1027</b>	1100	2106	2147	3286
37 Rb	37	190	617	1036	1352	1951	2093	2599	<b>3057</b>	3242	3409
39 Y	39	567	597	666	806	1214	2209	2242	2258	2277	
<b>40</b> Zr	40	1063	2927	3018	3032	3213	3555	<b>3577</b>			
42 Mo	42	2221	2610	2962	3009	<b>3066</b>	3367				
43 Tc	43	141	267	684	689	709	885	1580	<b>2555</b>	3216	3886
44 Ru	44	616	1182	1844	2150	2523	2997	3017	<b>3062</b>	3074	3289
46 Pd	46	812	<b>1537</b>	2138	2281	2620	<b>3068</b>	3116	3625	3737	4638
48 Cd	50	<b>508</b>	1052	1325	1923	2166	2198	2759	2820	2976	<b>3059</b>
49 In	52	158	309	794	<b>1025</b>	2108	2372	<b>3068</b>	3190	3858	3970
<b>50</b> Sn	51	31	924	1067	1909	1941	<b>2053**</b>	2161	2194	2258	3230
51 Sb	54	85	166	644	<b>1020</b>	1032	1045	1162	1328	1384	<b>2038</b>
52 Te	53	536	1484	1656	2518	2934	2965	2999	<b>3072</b>	3997	4174
54 Xe	56	243	527	1399	1582	2305	2969	<b>3073</b>	<b>3213</b>	3589	3959
58 Ce	64	133	255	1157	1810	2030	2153	2540	<b>3070</b>	<b>3317</b>	3533
59 Pr	66	60	289	382	680	977	1158	1173	1186	<b>2048</b>	2104
<b>64</b> Gd	74	426	<b>512</b>	752	1013	1051	1059	2137	2302	2445	3010
<b>70</b> Yb	81	485	1435	1533**	1674	<b>2047</b>	2138	2426	2481	2526	<b>3074</b>
71 Lu	79	434	594	960	1244	1337	1331	2086	2893	<b>3068</b>	3417
74 W	83	1440	<b>1536</b>	1711	1745	2060	2433	<b>2555</b>	2653	2720	3341
76 Os	86	437	791	889	1517	1878	1989	2017	2222	2818	<b>3075</b>
78 Pt	90	423	532	918	968	1442	2161	2437	2606	2629	<b>3068</b>
80 Hg	92	376	413	550	<b>1027</b>	1848	1974	2059	2427	2465	2199
81 Tl	96	255	999	1408	1552	1619	1713	2216	2643		
<b>82</b> Pb	98	<b>1019</b>	1680	2624**	2702	3696	4001	4697	5286		
84 Po	105	685	1545	1583	2108	2295	2863	2978	3871		

**Table 3.** Excitations (in keV)  $^{53}\text{Ni}$ ,  $^{53}\text{Mn}$  and  $^{53}\text{Co}$  with the nucleon configuration of three holes in the magic  $^{56}\text{Ni}$  are compared with the integer values of the tensor force parameter  $161 \text{ keV} = \Delta^{TF} = \delta m_N / 8$  determined in the data for nuclei with  $Z=50, 51$ . Excitations close to the integers  $161 \text{ keV} = \delta m_N / 8$  are boxed, and close to  $9\Delta^{TF}$  – double-boxed.

$AZ$	$^{53}\text{Ni } 2J_o=7^-$	$^{58}\text{Ni}$	$^{59}\text{Ni}$	$^{61}\text{Ni}$	$^{63}\text{Ni}$	$1^-5^-$	$^{69}\text{Ni}$		
$E^*$	<span style="border: 1px solid black;">320(3)</span>	<span style="border: 1px solid black;">1292</span>	<span style="border: 1px solid black;">1456</span>	<span style="border: 1px solid black;">1454.2</span>	339.4	<span style="border: 1px solid black;">1454.8</span>	<span style="border: 1px solid black;">1289.1</span>	<span style="border: 1px solid black;">1451</span>	<span style="border: 1px solid black;">1450(3)</span>
$2J^\pi$	(5 <sup>-</sup> )	(3 <sup>-</sup> )	(11 <sup>-</sup> )	2 <sup>+</sup>	3 <sup>-</sup> 5 <sup>-</sup>	7 <sup>-</sup>	9 <sup>+</sup>	(5,7,9)	(1 <sup>-</sup> ,3 <sup>-</sup> )
$k \frac{\delta m_N}{8}$	322	1293	1454	1454	322	1454	1293	1454	1454
$k$	2	8	9	9	2	9	8	9	9

$AZ$	$^{53}\text{Mn}$	$^{55}\text{Mn}$							
$E^*$	378	<span style="border: 1px solid black;">1289.9</span>	<span style="border: 1px solid black;">1441.3</span>	2563.1	2573.1	<span style="border: 1px solid black;">1289.1</span>	<span style="border: 1px solid black;">1292.1</span>	<span style="border: 1px solid black;">1293.0</span>	2582
$2J^\pi$	5 <sup>-</sup>	3 <sup>-</sup>	(11 <sup>-</sup> )	13 <sup>-</sup>	7 <sup>-</sup>	5 <sup>-</sup> 11 <sup>+</sup>	11 <sup>-</sup>	(1 <sup>-</sup> )	
$k \frac{\delta m_N}{8}$	322	1293	1454	2586	2586	1293	1283	1293	2586
$k$	2	8	9	16	16	8	8	8	16

$AZ$	$^{53}\text{Co}$	$^{59}\text{Co}$	$^{69}\text{Cu}$	$^{71}\text{Cu}$	$^{73}\text{Cu}$				
$E^*$	<span style="border: 1px solid black;">646.2</span>	<span style="border: 1px solid black;">1291.6</span>	<span style="border: 1px solid black;">1459</span>	<span style="border: 1px solid black;">2581.7</span>	2585.8	<span style="border: 1px solid black;">1297.9</span>	<span style="border: 1px solid black;">1453.3</span>	2576(3)	<span style="border: 1px solid black;">1298.0</span>
$2J^\pi$	7 <sup>-</sup>	3 <sup>-</sup>	11 <sup>-</sup>	3 <sup>-</sup> 7 <sup>-</sup>	7 <sup>-</sup>	3 <sup>-</sup> 1,3 <sup>-</sup>	3 <sup>-</sup> 9 <sup>-</sup>	(13 <sup>-</sup> )	(3 <sup>-</sup> ,7 <sup>-</sup> )
$k \frac{\delta m_N}{8}$	647	1293	1454	2586	2586	1293	1454	2586	1293
$k$	4	8	9	16	16	8	9	16	8

$(Z-14)/2$	$N$	$AZ$	$^{41}\text{Ca}$	$^{39}\text{Ar}$	$^{37}\text{S}$	$^{38}\text{S}$	$^{33}\text{S}$	$^{43}\text{S}$	$^{32}\text{Si}$	$^{35}\text{Si}$	
			<span style="border: 1px solid black;">3</span>	2	<span style="border: 1px solid black;">1</span>	<span style="border: 1px solid black;">1</span>	1	1	0	0	
					$\Delta N=1$	$\Delta N=2$		$\Delta N=7$			
$E^*$			0.0	<span style="border: 1px solid black;">1943</span>	1267	<span style="border: 1px solid black;">646.2</span>	<span style="border: 1px solid black;">1292</span>	322	<span style="border: 1px solid black;">320.7</span>	1942	973.9
$2J^\pi$			7 <sup>-</sup>	3 <sup>-</sup>	3 <sup>-</sup>	3 <sup>-</sup>	2 <sup>+</sup>	$D$	7 <sup>-</sup>	2 <sup>+</sup>	(3 <sup>+</sup> )
$k \frac{\delta m_N}{8}$			0.0	1941	1293	646	1293	322	322	1941	971
$k$				12		4	8	2	2	8	6

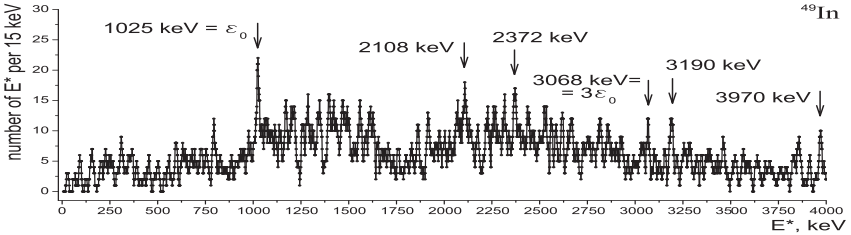
  

$AZ$	$^{33}\text{Mg}$	$^{41}\text{K}$	$^{47}\text{Sc}$	$^{47}\text{V}$	$^{50}\text{V}$	$^{51}\text{V}$	$^{55}\text{V}$		
$E^*$	159	484	980.4	<span style="border: 1px solid black;">1293.6</span>	807.9	<span style="border: 1px solid black;">1294.9</span>	<span style="border: 1px solid black;">320.2</span>	<span style="border: 1px solid black;">320.1</span>	<span style="border: 1px solid black;">323.3</span>
$2J_o^\pi$	3 <sup>-</sup>		3 <sup>+</sup>		2 <sup>+</sup>	3 <sup>-</sup>	6 <sup>+</sup>	7 <sup>-</sup>	(7 <sup>-</sup> )
$2J^\pi$	(7 <sup>-</sup> )	(3 <sup>-</sup> )	4 <sup>+</sup>	7 <sup>-</sup>	3 <sup>-</sup>	11 <sup>-</sup>	4 <sup>+</sup>	5 <sup>-</sup>	(5 <sup>-</sup> )
$k \frac{\delta m_N}{8}$	161	483	971	1293	808	1293	322	322	322
$k$	1	3	6	8	5	8	2	2	2

The maximum in the  $E^*$ -distribution for indium isotopes (Fig. 5) at  $E^*=1025 \text{ keV} \approx \varepsilon_o$  (deviation of about  $2.8\sigma$ ) corresponds to the phonon observed as two-phonon excitations  $E^*(0^+, 2^+)=2027, 2043$  and  $2057 \text{ keV}$  of the core-nuclei  $^{116,118}\text{Sn}$ . Similar phonon-like ( $\Delta J=2$  and 1) excitation in  $^{117}\text{Sn}$  at  $E^*=1020.0 \text{ keV}=\varepsilon_o$  and  $E^*=1004.5 \text{ keV}$ ,  $\Delta J=1$ ) and the same discreteness in many levels of  $^{113}\text{In}$  and  $^{116}\text{Te}$  was found in [1-2]. In Table 5, the excitations with  $\Delta J=1, 2$  in  $^{113}\text{In}$  are boxed.

**Table 4.** Stable excitations (keV) in all isotopes of different elements (Z) observed as maxima in  $E^*$ -distributions with averaging interval  $\Delta=7$  keV ((n)-number of  $E^*$ , Z=8-10, 8-14. 15-18 are marked by \*). Groupings of  $E^*$  values close to  $6m_e=3066$  keV and  $9m_e=4599$  keV are boxed.

Z	$E^*$	$E^*$	$E^*$	$E^*$	$E^*$	$E^*$	$E^*$	$E^*$	$E^*$
7	3129(3)	11939(3)							
8*	3063(3)	3840(4)	4588(4)	6283(7)	6855(0)				
8*	52(4)	94(4)	654(6)	1615(7)	2791(6)	3065(6)	4582(9)	4719(8)	5454(10)
15	86(7)	7923(6)							
15*	87(8)	105(7)	904(6)	1989(6)	2231(7)	3288(9)	5009(12)	6357(17)	9157(20)
17	107(6)	4351(6)							
19	2787(5)	4663(5)	4735(5)	4747(6)	7833(11)				
20	3027(4)	3335(5)	4883(6)	4993(?)	6158(7)	8367(8)	8449(0)	8520(8)	
21	1326	1797(5)	1934(5)	2107(6)	2224(6)	2986(8)			
22	4793(7)	6042(7)	6458(6)	6709(7)	6977(6)	8181(8)			
23	1664(4)	1727(4)	1750(4)	2763(4)	3520(6)	3876(6)	4395(6)	6602(6)	6977(6)
24	3163(5)	3897(6)	5859(9)	6135(6)	6257(6)	6329(6)	6377(7)	7117(9)	8121(7)
25	112(3)	839(4)	885(5)	1140(5)	2560(6)	4001(7)			
26	367(4)	2115(4)	2756(4)	3073(5)	3309(8)	4295(6)	6669(10)	8418(11)	9557(13)
27	508(4)	1271(5)	1677(5)	2105(6)	2733(7)	2910(7)	2979(7)	3869(7)	8419(12)
28	1453(5)	2698(5)	3010(6)	3276(6)	3379(6)	3525(7)	4022(7)	4712(8)	5903(8)
29	63(5)	1430(6)	3577(8)						



**Fig. 5.** Sum  $E^*$ -distribution for isotopes with Z=49 and maxima at 1026 keV  $\approx$  1022 keV =  $2m_e$  and 3068 keV  $\approx$  3066 keV =  $6m_e$ .

**Table 5.**  $E^*$  (keV) in In isotopes corresponding to a maximum at  $1026 \pm 7$  keV in Fig. 5.

$AZ$	$^{106}\text{In}$	$^{106}\text{In}$	$^{108}\text{In}$	$^{109}\text{In}$	$^{110}\text{In}$	$^{110}\text{In}$	$^{110}\text{In}$	$^{113}\text{In}$	$^{113}\text{In}$	$^{114}\text{In}$	$^{114}\text{In}$
$J^\pi$	$7^+$	$7^+$	$7^+$	$9/2^+$	$7^+$	$7^+$	$7^+$	$9/2^+$	$9/2^+$	$1^+$	$1^+$
$E^*$	1022.8	1027.1	1028.3	1026.4	1017.9	1020.8	1023.4	1024.3	1029.6	1018.7	1019.8
$J^*$	(4,5)	(4)	(4,3)	11/2 <sup>+</sup>	9* -	5 <sup>+</sup> , 6 <sup>+</sup>	3 <sup>-</sup>	5 <sup>+</sup>	1 <sup>+</sup> , 3 <sup>+</sup>	4 <sup>-</sup> , 5 <sup>-</sup>	7 <sup>+</sup>
$AZ$	$^{114}\text{In}$	$^{116}\text{In}$	$^{116}\text{In}$	$^{117}\text{In}$	$^{117}\text{In}$	$^{118}\text{In}$	$^{119}\text{In}$	$^{121}\text{In}$	$^{123}\text{In}$	$^{125}\text{In}$	$^{129}\text{In}$
$J^\pi$	$7^+$	$7^+$	$7^+$	$9/2^+$	$9/2^+$	$1^+$	$9/2^+$	$9/2^+$	$(9/2)^+$	$9/2^+$	$9/2^+$
$E^*$	1032.1	1019.0	1031.2	1028.4	1030.0	1028	1025.0	1020.8	1027.4	1027.4	1020.5
$J^*$	3 <sup>-</sup>	3 <sup>-</sup> , 4 <sup>-</sup> , 5 <sup>-</sup>	4 <sup>+</sup>	(5/2 <sup>-</sup> )	3/2 <sup>+</sup> , 5/2 <sup>+</sup>		7/2-11/2	9/2 <sup>+</sup> -11/2 <sup>+</sup>	11/2 <sup>+</sup>	11/2 <sup>+</sup>	(5)

In addition to the maximum in Fig. 5 at a triple value of  $3.07\text{ MeV}=3\varepsilon_o$  and the above maxima at  $3\varepsilon_o$  in many heavy elements (Figs. 6-8), one can notice the appearance of stable intervals close to  $3\varepsilon_o=3066\text{ keV}=6m_e$  and  $9m_e=4599\text{ keV}$  in light nuclei around  $Z=8$  (Table 4, boxed values).

**Table 6.** Stable excitations in light nuclei ( $Z=8-14$ ), corresponding to maxima at  $E^*=3959-3063\pm 4\text{ keV}$  (close to  $6m_e$ ) and  $E^*=4582-4588\pm 4\text{ keV}$  (close to  $9m_e$ ) in  $E^*$ -distribution (Table 3, top). For comparison, the values  $E^* = 12m_e$  and  $9m_e$  in  $^{16}\text{O}$ ,  $^{18}\text{Ne}$  are given.

$^AZ$	$^{19}\text{O}$	$^{19}\text{O}$	$^{18}\text{F}$	$^{20}\text{Na}$	$^{22}\text{Na}$	$^{29}\text{Na}$	$^{25}\text{Al}$	$^{29}\text{Al}$	$^{29}\text{Si}$	$^{16}\text{O}$
$J^\pi 5/2^+$	$5/2^+$	$1^+$	$2^+$	$3^+$	$3/2^+$	$5/2^+$	$(5/2^+)$	$1/2^+$	$0^+$	
$E^*, \text{keV}$	3064(3)	3067.4	3061.8	3057(3)	3060.4	3059	3062.0	3061.8	3067.1	6129.80(4)
$J^*$	$(5/2^-)$	$(3/2^+)$	$2^+$	$(4^-)$	$2^+$			$5/2^+$	$5/2^+$	$3^-$
$^AZ$	$^{19}\text{O}$	$^{22}\text{O}$	$^{20}\text{F}$	$^{20}\text{F}$	$^{21}\text{F}$	$^{22}\text{Na}$	$^{25}\text{Al}$	$^{27}\text{Al}$	$^{28}\text{Al}$	$^{18}\text{Ne}$
$J^\pi 5/2^+$	$0^+$	$2^+$	$2^+$	$5/2^+$	$3^+$	$5^+$	$5/2^+$	$3^+$	$0^+$	
$E^*, \text{keV}$	4582	4584(9)	4584.6	4591.7	4584.0	4582.8	4582(2)	4580.0	4578.6	4590(8)
$J^*$	$3/2^-$	$(3)^+$			$3/2^+, 5/2^+$	$2^-$	$5^+, 2$	$7/2^+$		$0^+$

It can be seen from Table 6 that the spins of many excited states have not yet been determined, and an additional analysis of the excitations and binding energies of light nuclei is needed. The independent appearing of equal stable mass/energy intervals in the spectra of light and heavy nuclei confirms the CODATA relations and manifests on the fundamental properties of the nucleon structure, observed as a fine structure.

#### 4. General remarks and conclusions

In Table 7 the components of the maximum in the  $E^*$ -distribution for the  $Z=70$  isotopes at  $E^*=1533\text{ keV}=3m_e$  (Fig. 6) are presented. The first excitations  $E^*$  of near-magic nuclei with  $N=82$  and  $82-1$  (of elements with  $Z=66, 68$  and  $70$ ) are given with differences between  $E^*$  of  $Z=82$  and  $Z=81$  isotopes of these elements. The coincidence of the first  $E^*$   $^{152}\text{Yb}$  and  $^{151}\text{Yb}$  with  $3m_e$  demonstrates that the tuning effect takes place only at  $Z=70$ , where all proton subshells (except the last,  $1\pi i_{11/2}$ ) are filled.

At the top of Table 8, the values  $E^*$  (keV) of light A-odd lead isotopes, rational or equal to the  $\varepsilon_o = 2m_e$ , are boxed. The proximity of values within 1 keV is observed. At the bottom of Table 8, the confirmation of the grouping  $E^*$  observed in other near-magic nuclei at the energy of the first excitation is shown (marked \*\* in Table 2).

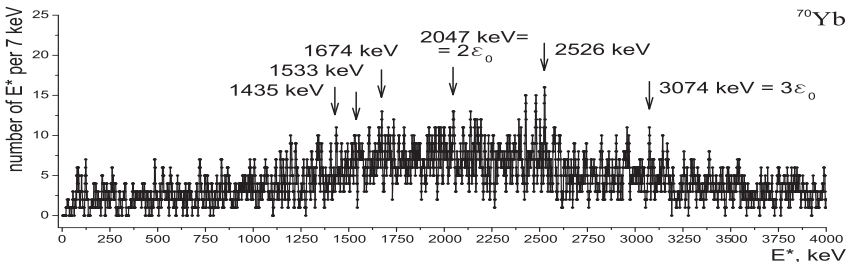


**Fig. 6.** The sum  $E^*$ -distributions for isotopes with  $Z=70$ . The positions of the maxima at  $k \times m_e$ ,  $k = 3, 4, 6$  (for  $1533\text{ keV}$ ,  $2047\text{ keV}$  and  $3074\text{ keV}$ ) are marked with arrows.

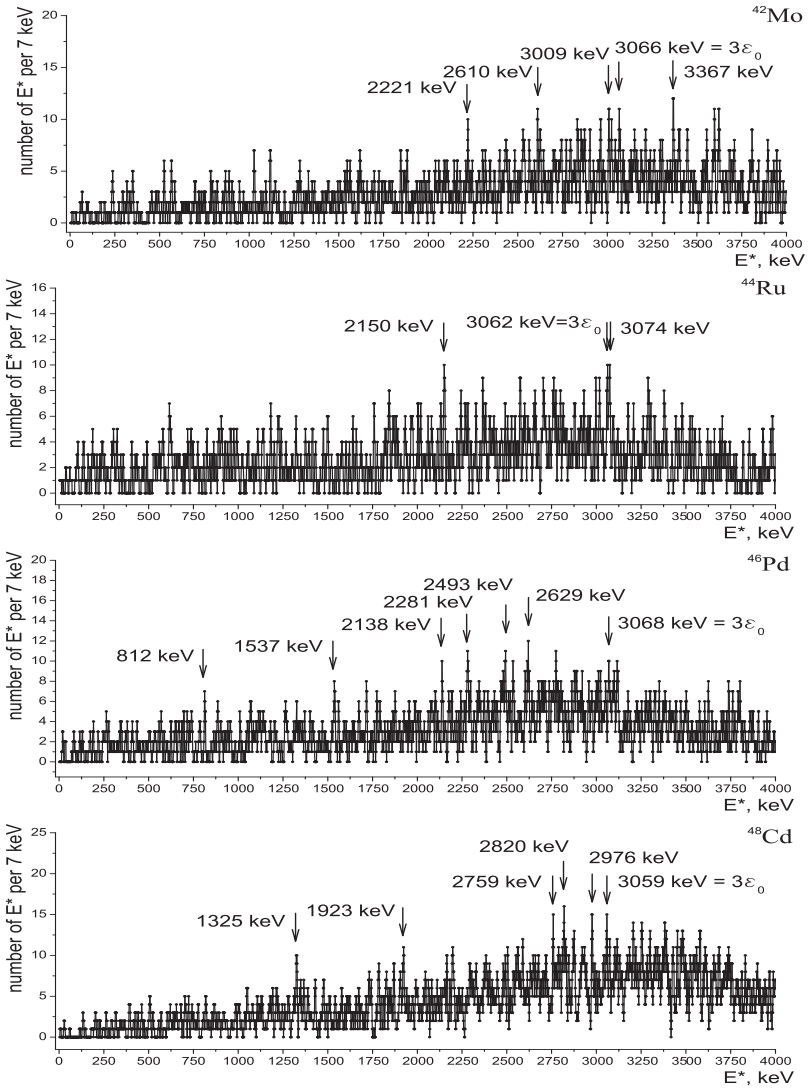


**Fig. 7.** Sum  $E^*$ -distributions for isotopes with  $Z=42$  (top),  $Z=44$  (2nd line),  $Z=46$  (center) and  $Z=48$  (bottom). In all four neighboring elements (even  $Z=42-48$ ), the grouping effect observed in the values of  $E^*$  in different isotopes takes place at nearly the same energy: 3068 keV, 3062-3073 keV, 3068 keV and 3059 keV (close to  $6m_e=3066$  keV).

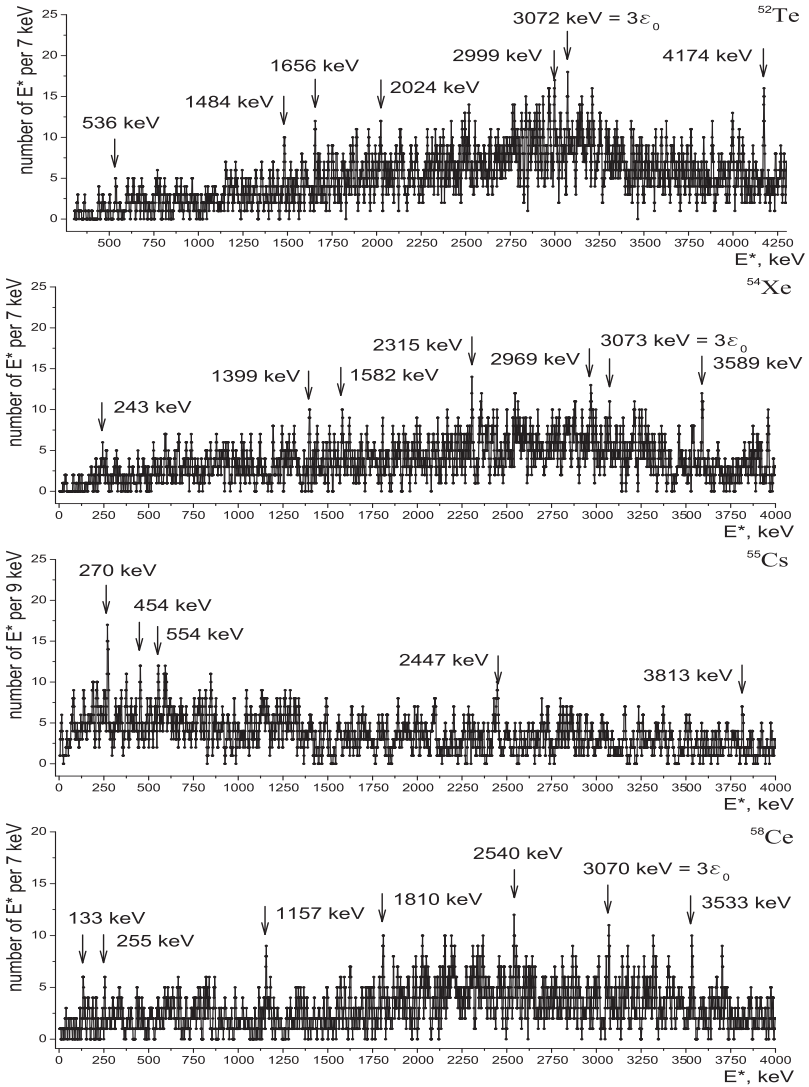


**Fig. 8.** Sum  $E^*$ -distributions for isotopes with  $Z=52$  (top),  $Z=54$  (2nd line),  $Z=56$  (center) and  $Z=58$  (bottom). In all four neighboring elements (even  $Z=52-58$ ), the grouping effect observed in the values of  $E^*$  in different isotopes takes place at nearly the same energy: 3072 keV, 3073 keV, 3072 keV (Table 4 for  $Z=56$ ) and 3070 keV. The maximum in Cs ( $Z=55$ ) corresponds to  $\delta m_N - \varepsilon_o = 271$  keV.

**Table 7.** Stable excitations  $E^*$  (keV) in neighboring near-magic Dy, Er, Yb, and the difference between isotopes with  $N=82$  and  $81=82-1$ .

Z	Elem.	$E^*(2^+)$	$E^*(15/2^-) - E^*(11/2^-)$	diff. $2^+, 15/2^-$	$E^*(15/2^-)$	$E^*(11/2^-)$
66	Dy	1677.3	1653.5	23.8	2404.0	750.5
68	Er	1578.3	1569.8	7.5	2311.6	741.8
70	Yb	<span style="border: 1px solid black;">1531.4</span>	<span style="border: 1px solid black;">1531.3</span>	<span style="border: 1px solid black;">0.1</span>	1531.3	0.0

**Table 8.**  $E^*$  (keV) in light A-odd lead isotopes rational or equal to  $\varepsilon_o = 2m_e$ .

Nucleous	$2J^\pi$	$E_1^*$	$2J^\pi$	$E_2^*$	$E_{3,4}^*$	$2J^\pi$
$^{193}\text{Pb}$	$13^+$	757(1)	( $17^+$ )	881.7	( $17^+$ )	<span style="border: 1px solid black;">1022.1(3)=<math>\varepsilon_o</math></span> ( $15^+$ )
$^{197}\text{Pb}$	$3^-$	<span style="border: 1px solid black;">84.88(7)=<math>\varepsilon_o/12</math></span>	$5^-$	952.0	$7^-$	988.5 $3^-, 5^-$
$^{199}\text{Pb}$	( $5^-$ )	19.1	( $X^-$ )	945.9	( $7^-, 9^-$ )	<span style="border: 1px solid black;">1022.7(4)=<math>\varepsilon_o</math></span>
$^{201}\text{Pb}$	$5^-$	88.5	( $3^-$ )	<span style="border: 1px solid black;">169.9(8)=<math>\varepsilon_o/6</math></span>		
$^{208}\text{Pb}$	$0^+$	2614.5	( $3^-$ )	3197.7	$5^-$	
$\Sigma E^*$		2620	n=13	3196	n=13	4697 n=16

We conclude that the analysis of the  $E^*$  values of all known nuclear excitations confirmed the distinguished character of the parameters derived from the correlations between the nucleon and lepton masses (CODATA relations and QED parameter  $\alpha/2\pi$ ) [1,8]. A standard analysis of the up-quark mass  $m_u$  can provide a comparison with the value found here  $E^* = 3m_e$ . Observation of superfine and fine structures in positions and spacings of neutron resonances, together with the proximity of some low-lying excitations in near-magic nuclei to integers of the electron mass, was the starting point for particle mass analysis [3-5]. Two new methods of nuclear data analysis provide additional indirect check of CODATA relations – an important property of nucleon masses.

## References

1. S.I. Sukhoruchkin, Nucl. Part. Phys. Proc. **294-296** (2018) 129.
2. S.I. Sukhoruchkin, M.S. Sukhoruchkina, these proceedings.
3. S. Sukhoruchkin, *Discreteness in particle masses*. Lambert Ac. Publ. 2017.
4. S.I. Sukhoruchkin, *Proc. L Winter School of PNPI*, pp. 45–119. S.-Petersburg, 2017.
5. S.I. Sukhoruchkin, *Proc. LI Winter School of PNPI*, pp. 43–139. S.-Petersburg, 2018.
6. V.V. Belokurov, D.V. Shirkov, *Theory Part. Inter..* AIP, 1991.
7. S.I. Sukhoruchkin, *Stat. Prop. Nuclei*, ed. G.Garg. Pl. Press, 1972, p. 215.
8. S.I. Sukhoruchkin, Sov. J. Nucl. Phys. **10** (1969) 261, 496.
9. S.I. Sukhoruchkin, Izv. Akad. Nauk SSSR Ser. Fiz. **36** (1972) 885.
10. R. Sternheimer, Phys. Rev. **136** (1964) 1364; **170** (1968) 1267.
11. P. Kropotkin, *Field and Matter* (in Russian), Moscow Univ., 1971, p. 106.
12. S.I. Sukhoruchkin *et al.* *Proc. ISINN-25*, 2017. JINR E3-2018-12, pp. 150, 163.
13. S.I. Sukhoruchkin *et al.* *Proc. ISINN-10*, 2003. JINR E3-2003-10, p. 308.
14. H. Schopper (Ed.), Landolt-Börnstein New Series, Springer. Vols. **I/22A,B**, 2009; **I/16B**, **1/16C**, **1/24**, **1/26A**, 1998-2015; **I/25A-H**, 2012-2016.
15. W. Martienssen, Landolt-Börnstein Completed Catalog, p. 3. Springer, 2000.
16. S.I. Sukhoruchkin, PoS(EPS-HEP2017)746, Venice, 2017.
17. F. Wilczek, Nature **520** (2015) 303.

## 1. Introduction

Neutron resonance spectroscopy is part of Nuclear Physics, and they both play an important role in the development of the Standard Model (SM) - a theory of all interactions except gravitation, with a representation of its components [1,2]:

$$SU(3)_{col} \otimes SU(2)_L \otimes U(1)_Y. \quad (1)$$

A recent analysis of particle masses [3-5] confirmed the existence of the period  $\delta = 16m_e$  introduced in [6], as well as unexpectedly accurate empirical relations between the nucleon masses and the electron mass. It was based on the exactly known ratio  $m_n/m_e=1838.6836605(11)$  of the neutron mass to the electron mass and the nucleon mass splitting  $\delta m_N=1293.3322(4)$  keV. The neutron mass shift from  $115 \cdot 16m_e - m_e$  is  $\delta m_n = 161.6491(6)$  keV, exactly  $1/8$  of  $\delta m_N$ . The ratio  $\delta m_N : \delta m_n = 8.00086(3) \approx 8 \times 1.0001(1)$  allows us to represent the nucleon mass ("CODATA relations"):

$$m_n = 115 \cdot 16m_e - m_e - \delta m_N/8 \quad m_p = 115 \cdot 16m_e - m_e - 9(\delta m_N/8). \quad (2)$$

The shift  $\delta m_n$  coincides with the parameter of tensor forces  $\Delta^{TF}=161$  keV, found in the excitations of nuclei where the one-pion exchange dynamics dominates [7,8]. The ratio of the  $\delta m_n=\Delta^{TF}$  to pion mass  $\delta m_n/m_\pi = 115.86 \cdot 10^{-5}$  is very close to QED radiative correction  $\alpha/2\pi = 115.96 \cdot 10^{-5}$  (see 2nd line in Table 1). R. Feynman [9], V. Belokurov and D. Shirkov [10] considered the appearance of the radiative correction as an indication on the important role of the influence of physical condensate on the particle mass.

The CODATA relations (2) mean the presence of two fine structures in the nucleon mass representation: the first, connected with the electron mass  $m_e$  (shift is  $-m_e/3=170$  keV in addition to the period  $16m_e = \delta$ ), and the second, with parameter  $161$  keV= $\Delta^{TF}=\delta m_N/8$ . Both parameters are connected by the factor  $\alpha/2\pi$  with the value of the nucleon  $\Delta$ -excitation  $\Delta M_\Delta=147$  MeV= $(m_\Delta-m_N)/2$  (the parameter of the Nonrelativistic Constituent Quark Model NRCQM, based on pion-like interaction) [11-13] and with the pion mass  $140$  MeV= $m_{\pi^\pm}$  itself (Table 1). The initial mass of the baryon constituent quark in NRCQM is three times  $\Delta M_\Delta$ , namely,  $M_q=441$  MeV= $m_\Xi/3$ . The mass of the meson constituent quark  $M_q''$  in NRCQM is derived as a half the masses of  $\omega$  and  $K^*$  mesons close to  $780$  MeV= $6f_\pi$  where  $f_\pi=130.7$  MeV= $16\delta$  is the pion  $\beta$ -decay parameter. The period  $f_\pi=16\delta=M_q''/6$  was used in the two-dimensional representation of particle masses (in Fig. 1), where the integers of the other NRCQM parameters  $m_\pi = (16 + 1)\delta$  and  $\Delta M_\Delta = M_q/3 = (16 + 2)\delta$  are represented as straight lines.

The important role of both NRCQM parameters  $M_q = 3 \times 18\delta$  and  $M_q'' = 3 \times 16\delta$  (presented in Table 2 under the corresponding numbers 16-16 and 16-18) is seen from empirical relations, starting with the proximity to  $\alpha/2\pi$  of the ratio of the NRCQM parameter  $\Delta M_\Delta=147$  MeV to the mass of the scalar field  $M_{H^0}=125$  GeV (last column in Table 2, line 11 in Table 1). NRCQM provides very accurate (within about 8 MeV) calculations of baryon masses. In combination with CODATA relations and QED radiative

correction, confirmed by neutron resonance data (Table 1 bottom), this provide the basis for the SM development.

**Table 1.** Comparison of the parameter  $\alpha/2\pi=115.96\cdot 10^{-5}$  with the anomalous magnetic moment of the electron  $\Delta\mu_e/\mu_e$  (top line), the ratio  $1/(32\times 25)=115.74\cdot 10^{-5}$  and ratios between the mass/energy values considered in the text (four important relations are boxed) [3-5,14-16].

No.	Parameter	Components of the ratio	Value $\times 10^5$
1	$\Delta\mu_e/\mu_e$	$=\alpha/2\pi\cdot 0.328 \alpha^2/\pi^2$	<span style="border: 1px solid black;">115.965</span>
2	$\delta m_n/m_\pi$	<span style="border: 1px solid black;"><math>(k\times m_e - m_n)/m_\pi = 161.649 \text{ keV}/m_\pi</math></span>	<span style="border: 1px solid black;">115.86</span>
3	$\delta m_\mu/m_\mu$	$(23\times 9m_e - m_\mu)/m_\mu$	112.1
4	$m_\mu/M_Z$	<span style="border: 1px solid black;"><math>m_\mu/M_Z = 91182(2) \text{ MeV}</math></span>	<span style="border: 1px solid black;">115.87(1)</span>
5	$\delta(\delta m_\pi)/9m_e$	<span style="border: 1px solid black;"><math>(\Delta - 4593,66(48) \text{ keV})/(9m_e = \Delta)</math></span>	116(10)
6	$m_d/m_b$	$m_d = 4.78(9) \text{ MeV} / m_b = 4.18(3) \text{ GeV}$	114
7	$m_u/m_c$	$m_u = 2.2(5) \text{ MeV} / m_c = 1275(25) \text{ MeV}$	173(40)
8	$\varepsilon''/\varepsilon'$	$1.35(2) \text{ eV} / 1.16(1) \text{ keV}$	116(3)
9	$\varepsilon'/\varepsilon_o$	$1.16(1) \text{ keV} / \varepsilon_o = 1022 \text{ keV}$	114(1)
10	$\varepsilon_o/2M_q \approx 1/(32 \times 27)$	$10 \varepsilon_o/3(m_\Delta - m_N) = (\varepsilon_o/6)/\Delta M_\Delta$	116.02
11	$(\Delta M_\Delta = M_q/3)/M_{H^o}$	$147 \text{ MeV} / 125 \text{ GeV}$	118
12	Sb, $D(187 \text{ eV})/161 \text{ keV}$	$(373 \text{ eV}/2 = 187 \text{ eV})/160 \text{ keV}$ , Table 3	114
13	Pd, $D(1497 \text{ eV})/1293 \text{ keV}$	Fig. 3, Fig. 4 bottom	115.7
14	Hf, $D(1501 \text{ eV})/\delta m_N$	${}^{172,176}\text{Hf } E^*(0^+) = 1293 \text{ keV} = \delta m_N$	116.1
15	Os, $D(1198 \text{ eV})/2m_e$	${}^{178,180}\text{Os } E^*(0^+) = 1023 \text{ keV} = 2m_e$	117

Evolution of the nucleon mass from the initial value of  $3M_q = m_\Xi$  ( $N=9 \times 18\delta = 162\delta$ , Fig. 1, top) to the deuteron mass  $\Delta$ , corresponding to  $N=151-150$  in units of  $\delta = 16m_e$  and the constituent quark  $M'_q = 50\delta$ , directly seen as the equidistance in masses of pseudoscalar mesons (shown in Fig. 1, bottom), means the transition of  $\Delta M_\Delta (N=18)$  in  $m_\pi$  or  $f_\pi$  ( $N=17,16$ ). The final stage of nucleon mass evolution (the mass of about 940 MeV-8 MeV-932 MeV) is situated close to  $6f_\pi + \Delta M_\Delta$  (circled point in Fig. 1). It corresponds to the important role of parameters  $f_\pi$  and  $3f_\pi \approx M'_q$  in the particle mass spectrum ( $N=16-16$ , in the central column of Table 2).

The two lightest particles, the electron and the muon, correspond to the last SM component (1). Their masses are in a ratio of  $m_\mu/m_e = 105.65937 \text{ MeV} / 510.9983 \text{ keV} = 206.77$  which slightly deviates (difference=0.232) from the integer value  $L=207=13 \times 16-1$  (lepton ratio) by a small factor of  $112.08 \cdot 10^{-5}$  (the ratio of the difference to L), close to QED radiative correction  $\alpha/2\pi = 115.96 \cdot 10^{-5}$  (lines 1 and 3 of Table 1). The ratio of the muon mass to the important SM parameter - the vector boson mass  $m_\mu/(M_Z=91.1816(21) \text{ GeV}) = 115.87 \cdot 10^{-5}$  is very close to  $\alpha/2\pi$  (4th line of Table 1). The difference 1566.70 MeV between the mass of heavy lepton  $m_\tau = 1776.82 \text{ MeV}$  and two muon masses 210.12 MeV is close to  $1569.79 = 4 \times 48\delta = 4 \times 392.45 \text{ MeV}$  (or to four constituent quarks  $M''_q = m_\rho/2 = 388 \text{ MeV}$  and the value of 1565.30 - the doubled value of  $m_\omega/2 = 782.65 \text{ MeV} = 2 \times 391.3 \text{ MeV}$ ).

The relations between the existing estimates of the quark masses ( $m_u, m_d, m_c, m_b$ ) and the proximity of the splitting of the pion mass to  $9m_e$  are presented in lines 5, 6 and 7. In the central part of Table 1 (lines 8-11), the ratios obtained previously [6] between different structures in nuclear excitations and in the particle mass spectrum (superfine period  $\varepsilon'' = 1.35 \text{ eV} = 5.5 \text{ eV} / 4 = \delta' / 8 = 11 \text{ eV} / 8$ , fine structure period  $\varepsilon' = 1.16 \text{ keV} = \delta' / 8 = 9.5 \text{ keV} / 8$ ,  $\varepsilon_o = 2m_e = 1.022 \text{ MeV}$  and  $M_q = 441 \text{ MeV} = 3\Delta M_\Delta$ ) are given [3-5,14-16] together with the

important parameter SM  $M_{H^0}$  (mass of the scalar field) and the ratios between the nuclear intervals considered in this work (Table 1, lines 13-16, and Table 2).

The empirical correlations in particle masses discussed here relate to the role of lepton masses ( $m_e, m_\mu, m_\tau$ ) together with the NRCQM parameters and the presence of integer relations  $1:13:16:17:18:48:54=\delta:m_\mu:f_\pi:m_\pi:\Delta M_\Delta:M_q'':M_q$  with the period of  $16m_e = \delta=8.176\text{ MeV}$  close to the doubled value of the pion  $\beta$ -decay energy [6]. The value  $M_q = m_\Xi/3$  (baryon constituent quark mass), as well as  $M_q''$  are interconnected with masses of quarks and fundamental fields. In Table 2 they are compared with the numbers of fermions in the central field. Additionally, ratios between them and both vector boson masses, namely,  $M_Z/M_q=206.8$  and  $M_W/M_q''=207.3$  ( $M_q'' = m_\rho/2=387.6\text{ MeV}$ ) are close to the lepton ratio  $L=m_\mu/m_e=207=16\times 13-1$ . This can be considered together with other symmetry motivated relations, including a 16:1 ratio between the period  $\delta = 16m_e$  and  $m_e = 3 \cdot (m_e/3)$ , with  $m_e$  observed directly as a shift in the nucleon mass corresponding to a shift of  $3(m_e/3)$  in the mass of each of three baryon quarks. Number 16 (for  $N=16$  in Table 2) could be assigned to particle-hole configuration, schematically,  $16=16-1+1$  [3-5].

**Table 2.** Comparison of numbers of fermions in the central field (top line) with ratios between the masses  $m_e/M_q, m_\mu/M_Z, f_\pi/((2/3)m_t = M'_H)$  (with  $m_t$  and  $M'_H$  - masses of top quark and unconfirmed scalar [1,3-5]),  $\Delta M_\Delta/M_{H^0}$  and QED parameter  $\alpha/2\pi$ . Boxed in the bottom line are the hole configuration in  $1p$  shell (configuration  $1s_{1/2}^4, 1p_{3/2}^8, 1p_{1/2}$ ) and the valence fermion configuration as a fermion with the new principal quantum number over the filled shells (configuration  $1s_{1/2}^4, 1p_{3/2}^8, 1p_{1/2}^4$ ).

$N^{ferm}$	N = 1	N=16	<span style="border: 1px solid black;">16-13-1=L</span>	16-16	<span style="border: 1px solid black;">16-17+1</span>	16-18
Const. quark				$M_q'' = 3f_\pi$		$M_q = 3\Delta M_\Delta$
Particle mass	$m_e$	$\delta$	$m_\mu$	$f_\pi$	$m_{\pi^\pm}$	$\Delta M_\Delta$
Particle/param.	$m_e/M_q$		$m_\mu/M_Z$	$f_\pi/((2/3)m_t)$		$\Delta M_\Delta/M_{H^0}$
Ratio	$115.96\cdot 10^{-5}$		$115.87\cdot 10^{-5}$	$114\cdot 10^{-5}$		$117\cdot 10^{-5}$
Comments			<span style="border: 1px solid black;">hole in <math>1p</math></span>	filled shells	<span style="border: 1px solid black;">valence</span>	

To check the periodicity with the parameter  $\delta$ , all existing data from the PDG compilation were used, and distributions of differences between the masses of all particles known with an uncertainty of less than 8 MeV were plotted ( $\Delta M$  in Fig. 2). The maximum at  $\Delta M=m_\pi=142\text{ MeV}$  in this distribution (Fig. 2), the doublet of maxima at  $\Delta M=1671-1687\text{ MeV}$  (including  $12m_\pi = m_\Omega$ ) and the maximum at  $\Delta M=3370\text{ MeV}=24m_\pi$  correspond to distinguished stability of intervals with  $N=17$  (numbers of the period  $\delta = 16m_e$ ). The period  $\delta = 16m_e$  manifested also as stable splittings of  $17\text{ MeV}=2\delta$  and  $48\text{ MeV}=6\delta$  in the same Fig. 2 (top). Stable intervals with  $\Delta M=445\text{ MeV}$  and  $462\text{ MeV}$  are close to  $M_q=441\text{ MeV}$ , the main parameter of NRCQM model. The doublet at  $\Delta M=3940-3959\text{ MeV}$  is close to  $9M_q=3963\text{ MeV}$ . The value of  $932\text{ MeV}=6f_\pi+\Delta M_\Delta$  coincides with the nucleon mass in nuclear media (the final stage of nucleon mass evolution). The doublet at  $1671-1687\text{ MeV} = 12m_\pi$  and the maximum at exactly two-fold energy  $3370\text{ MeV} = 24m_\pi$  corresponds to the observed empirical periodicity (with the interval  $m_\pi$ ) in masses of  $\Lambda-, \Xi-, \Omega$ -hyperons and the charmed quark mass  $m_c$  ( $k=1, 8, 9, 11, 12$  of the period  $m_\pi$  [3-6,14-16]). Splitting in all doublets observed in Fig. 2 is about  $17\text{ MeV}=2\delta$

including the doublets at  $\Delta M=3959 \text{ MeV}=9M_q$  and  $4425 \text{ MeV}=10M_q$ . This means the existence of small splitting with a common value  $2\delta=17 \text{ MeV}$  and long-range correlations with the parameter  $M_q = 3\Delta M_\Delta$  ( $k=1, 9, 10$ , with  $\Delta M_\Delta = 18\delta$ ) and the pion mass  $m_\pi=142 \text{ MeV}=17\delta$ .

The direct manifestation of the pion mass ( $m_{\pi^\pm}=139.57 \text{ MeV}$ ) in the spectrum of charmed hadrons was noticed by G. Mac Gregor [17]: three values coincide within 1 MeV, namely,  $D^{*\pm}-D^\pm=140.7 \text{ MeV}$ ,  $D_s^{*\pm}-D_s^\pm=141.6 \text{ MeV}$  and  $\chi_{C2}(1P)-\chi_{C0}(1P)=141.2 \text{ MeV}$ . The ratios  $1:12:24=m_\pi:12m_\pi:24m_\pi$  between the positions of the maxima in the  $\Delta M$  distribution are in agreement with the coincidence of the charmed quark  $m_c=1275(25) \text{ MeV}$  with  $9m_\pi=1255 \text{ MeV}$  (shown in Fig. 1 as  $m_c$  on the straight line  $k \cdot m_\pi$ ).

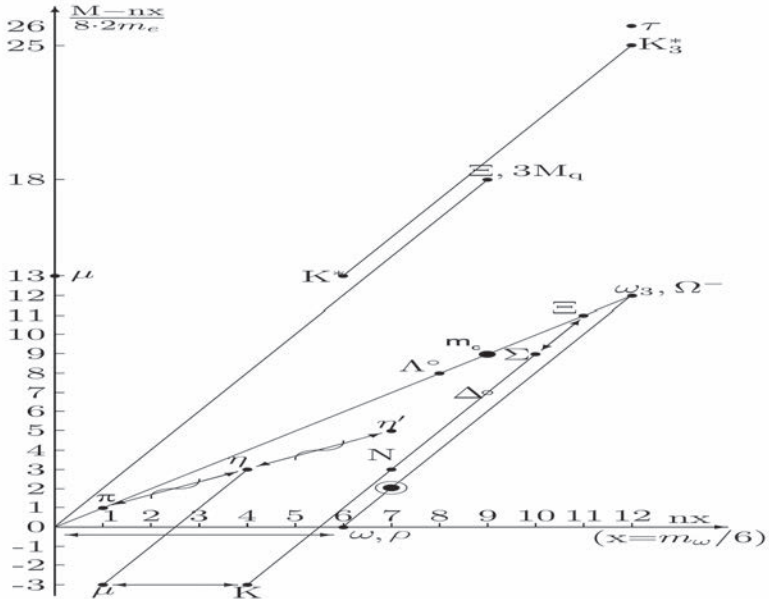


**Fig. 1.** Evolution of the baryon mass from  $3M_q$  to nucleon mass  $M_N$  is shown in two-dimensional presentation: values in the horizontal direction are in units  $16 \cdot 16m_e = f_\pi=130.7 \text{ MeV}$ , remainders  $M_i-n(16 \cdot 16m_e)$  are plotted along the vertical axis in units of  $16m_e$ . Nucleon mass in nuclear medium (circled point) is close to the sum  $\Delta M_\Delta+6f_\pi$ . Both parameters,  $f_\pi = M_q''/3 = M_w/3L$  and  $\Delta M_\Delta = M_q/3 = M_Z/3L$ , are connected with the fundamental fields and with the CODATA period  $\delta = 16m_e$  ( $N=16$  and  $N=18$ , see text).

Three different slopes correspond to three pion parameters:  $f_\pi = 16\delta$ ,  $m_{\pi^\pm} = 17\delta$  and  $\Delta M_\Delta = 18\delta$ . Line with the slope  $m_\pi=140 \text{ MeV}=f_\pi+\delta$  ( $N=16+1$ ) goes through  $\Lambda$ -,  $\Xi$ -,  $\Omega$ -hyperons and the charmed quark  $m_c = 9m_\pi$ .

Lines with  $\omega$ - and  $K^*$ -mesons correspond to stable mass intervals  $\Delta M = 2M_q = 6\Delta M_\Delta$ ,  $\Delta J=2$ . Mass of the  $\tau$  lepton is close to  $2m_\mu + 2M_q''$  (top). Stable interval in pseudoscalar mesons is  $50\delta$ .

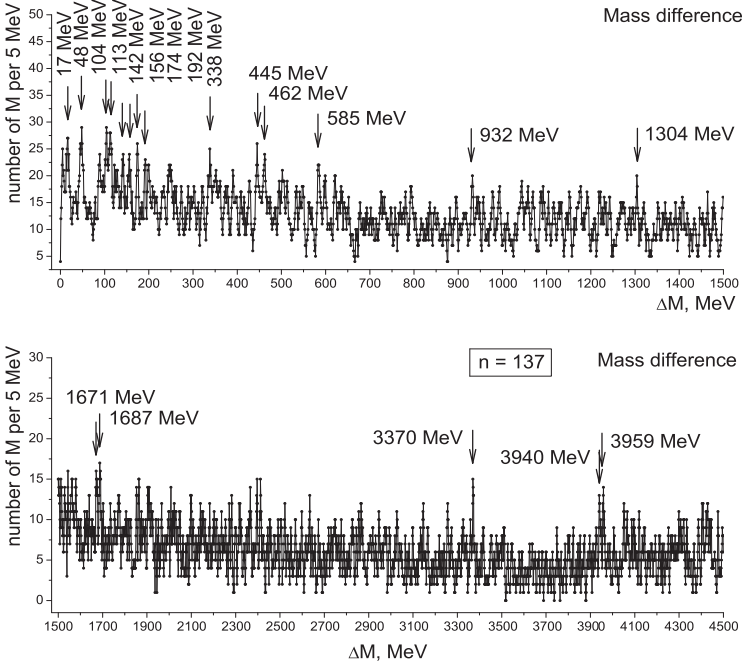


**Fig. 2.** Distribution of differences between particle masses  $\Delta M$  in regions 0–1500 MeV–4500 MeV, averaging interval of 5 MeV. Maxima at 16 MeV–48 MeV–104 MeV–141 MeV and doublets at 445–462 MeV, 1671–1687 MeV and 3940–3959 MeV correspond to integers  $k=2, 6, 13, 17, 54, 12 \times 17$  and  $9 \times 54$  of the period  $\delta = 16m_e$  in CODATA relations (2).

The observation of exact integer relation between different parts of expression (2), namely, 16:1 in units  $m_e$  and 1:9 in units  $(1/8)\delta m_N$ , is a very important aspect of the recent state of SM-development. The presence of two systems of fine structures based on two well-known electromagnetic mass differences (periods  $170 \text{ keV} = m_e/3$  and  $161 \text{ keV} = \delta m_N/8$ ) means that such fundamental parameters (which are complimentary to integer numbers of the period  $\delta = 16m_e$ , common to the particle mass spectrum) should be observed in many effects in nuclear data. A direct reflection of these fine structure intervals can be expected. The fundamental character of QED radiative correction [9,10] and the generally accepted large role of scalar fields, corresponding to the important empirical relation

$$m_e = 3\Delta M_\Delta \cdot (\alpha/2\pi) = 3M_{H^0} \cdot (\alpha/2\pi)^2, \quad (3)$$

should be directly observed in nuclear excitation  $E^*$  and binding energies  $E_B$  (or  $S_n$ ), as well as in the differences of these nuclear characteristics observed as positions of neutron resonances. The high energy resolution achieved by modern time-of-flight neutron resonance spectrometers can be used to study the fine and superfine structure effects. Existed data on low-lying and highly excited states confirm the CODATA relations. Nuclear spectroscopy has a unique opportunity to contribute to the SM development, based on the CODATA relations and the role of the electron and its symmetry.

## 2. Superfine structure in neutron resonance spectra

In neutron resonance spectroscopy, the properties of highly excited states are studied with a very high energy resolution, as can be seen in Figs. 3-4, where there are sharp maxima in the position of neutron resonances [14-16,19], and in the  $D$ -distributions of the resonances in  $^{233}\text{Th}$ ,  $^{124}\text{Sb}$ ,  $^{80}\text{Br}$ ,  $^{104}\text{Rh}$ ,  $^{105}\text{Pd}$  and  $^{179}\text{Hf}$ . The superfine structure in the  $D$ -distribution of neutron resonances, noticed by W. Havens [20] in data for Th (Fig. 3, top) with  $D_{ij}=22\text{eV}=16\times\varepsilon''=2\delta''$  in all resonances and  $D_{ij}=572\text{eV}=1\text{e}\times 4\delta''$  in strong resonances (*right*) was confirmed by many authors [6,14-16]. The periodicity in the positions of the resonances  $^{124}\text{Sb}$ , noticed by K. Ideno (Fig. 3, bottom), is in agreement with the grouping effect in heavy nuclei [19,21-24] (*left*).

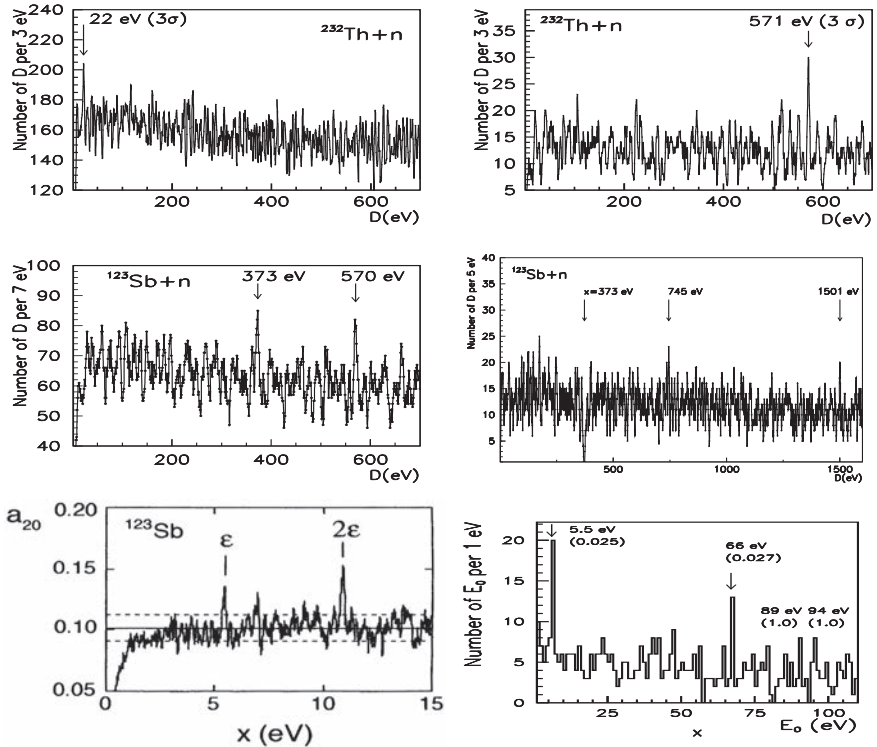


**Fig. 3.** *Top:*  $D$ -distributions of resonances in  $^{233}\text{Th}$  (*left*) and the same for resonances with  $\Gamma_n^0 > 1\text{ MeV}$  [12]. *Center left:*  $D$ -distribution in neutron resonances of the compound nucleus  $^{124}\text{Sb}$ . *Center right:*  $D^{AIM}$ -distribution for  $x=373\text{ eV}$  with maxima at  $745\text{ eV}=4.17\delta''$  and  $1501\text{ eV}=8.17\delta''$ . *Bottom left:* The period  $5.5\text{ eV}$  in the positions of  $^{124}\text{Sb}$  resonances was found by K. Ideno using a special program [23] for analyzing the grouping in resonance positions. *Bottom right:* Distribution of resonance positions known in the 1966 [19]. The selection of one strongest resonance in the interval  $10\text{ eV}$  was used (in parentheses is a random probability).

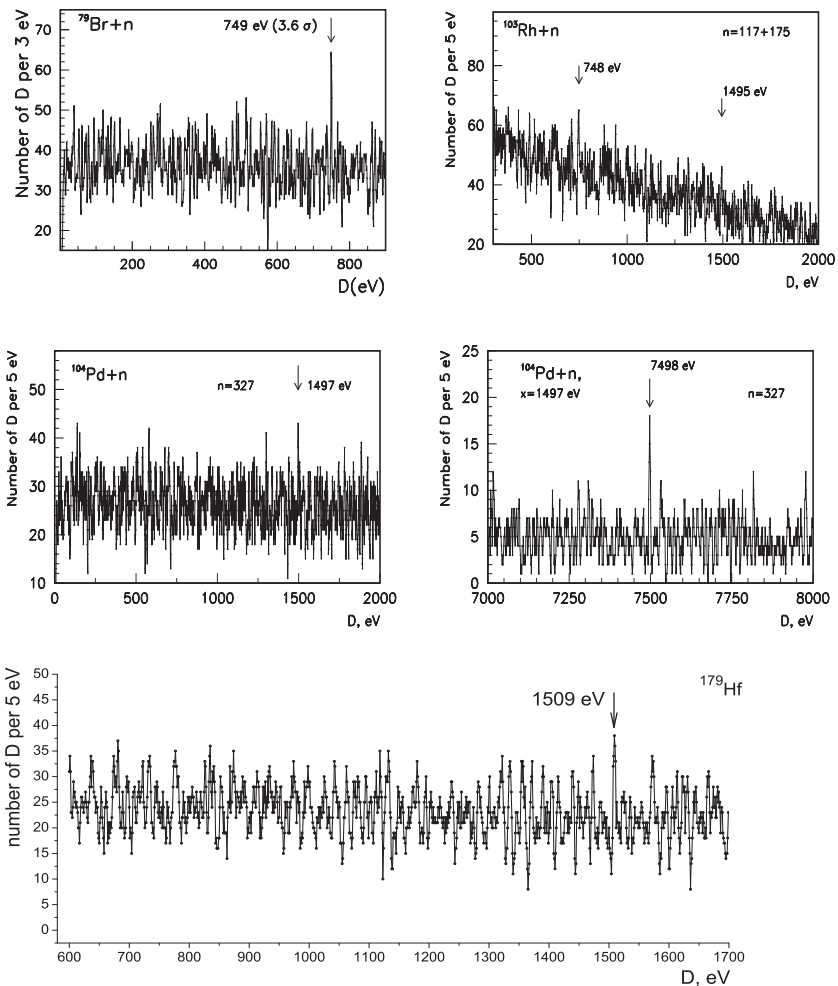


**Fig. 4.** *Top:* Spacing distribution of neutron resonances in the compound nuclei  $^{80}\text{Br}$  (left) and  $^{104}\text{Rh}$  (right), sum of distributions for s- and p-resonances. *Center left:* The same for  $^{106}\text{Pd}$ . *Center right:*  $D^{AIM}$ -distribution in  $^{106}\text{Pd}$  for  $x=1497$  eV (ratio  $7498$  eV/ $1497$  eV=5.009). *Bottom:*  $D$ -distribution in neutron resonances of the compound nuclei  $^{179}\text{Hf}$  with maxima at  $1509$  eV= $8 \cdot 17\delta''$  (without a small recoil correction  $A/A+1$ ).

The intervals  $D^{AIM}=745\text{ eV}=17\times 4\delta''=2x$  and  $1501\text{ eV}=17\times 8\delta''=4x$  found in  $^{124}\text{Sb}$  using the AIM method (Fig. 3) demonstrate the stability of the interval of the superfine structure with  $N=17$  ( $E_n=k\cdot\delta''$ ). The fine structure with  $k=17$  and the ratio  $\alpha/2\pi$  between the intervals in neutron resonances and low-lying levels are shown in Table 3.

In Fig. 5 and Table 3 manifestation of the fine structure interval  $161\text{ keV}=\delta m_N/8=\Delta^{TF}$  is shown as a linear dependence of the excitation energies in the sequence  $^{odd}\text{Sb}$  with  $N=70-82$ , where the large neutron shell  $1h_{11/2}$  is filling in, and the tensor force effect is expected [7,8]. This interval is also observed as a maximum in the sum spacing distribution of  $^{122,124}\text{Sb}$  (Fig. 5, top right,  $160\text{ keV}=17\times\delta'$  together with  $D=530\text{ keV}=4\times 14\delta'$ ). The same combination of  $k=14$  and  $17$  is observed in sum  $D$ -distribution for  $^{97,98}\text{Pd}$  (Fig. 5).

**Table 3.** Comparison of excitations  $E^*$  (in keV) in  $Z=51$  A-odd nuclei with integers of  $\Delta^{TF}=161\text{ keV}=(\delta m_N=1293\text{ keV})/8$  and close to  $\delta m_N$  intervals in  $0^+$ ,  $2^+$ ,  $1^+$  levels of  $^{116}\text{Sn}$ .

AZ	$^{123}\text{Sb}$	$^{125}\text{Sb}$	$^{127}\text{Sb}$	$^{129}\text{Sb}$	$^{131}\text{Sb}$	$^{133}\text{Sb}$	$^{119}\text{Sb}$	$^{116}\text{Sn}$	$^{116}\text{Sn}$
(N-70)/2	1	2	3	4	5	6		N=	66
$E^*$ , keV	160.3	332.1	491.2	645.2	798.4	962.0	644	1294	1292
$E^*-k\frac{\delta m_N}{8}$	-1	-9	+7	-1	-10	-7	-2	1	-1
$k\frac{\delta m_N}{8}$	161	323	484	646	808	969	646	1293	1293
$D$ , eV		373	570						
ratio $D/E^*$		$114\cdot 10^{-5}$	$116\cdot 10^{-5}$						

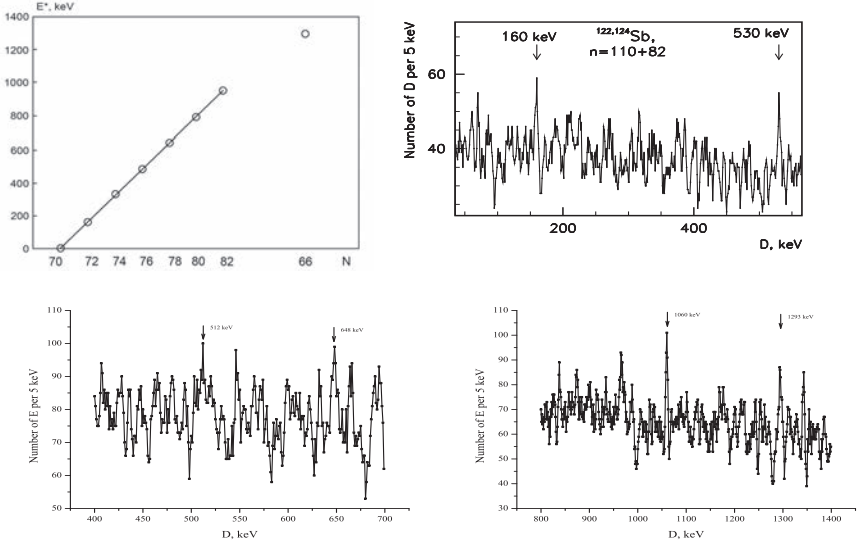


**Fig. 5.** *Top left:* Linear trend of  $E^*$  in  $^{odd}\text{Sb}$  with a slope  $\Delta^{TF}=161\text{ keV}=\delta m_N/8$  (Table 2). A point at right corresponds to stable equidistant  $E^*$  in  $^{116}\text{Sn}$  ( $J^\pi=0^+$ ,  $2^+$ ,  $1^+$ , boxed at right). *Top right:* Sum  $D$ -distribution in low-lying levels  $^{122,124}\text{Sb}$  (numbers of states  $n=110+82$ ). *Bottom:* Sum  $D$ -distribution in  $^{97,98}\text{Pd}$  in energy region 400-1400 keV. Maxima at  $512\text{ keV}=m_e=3\times 18\delta'$ ,  $648\text{ keV}=4\times 17\delta'$ ,  $1060\text{ keV}=8\times 14\delta'$  and  $1293\text{ keV}=8\times 17\delta'$  are discussed in the text.

### 3. Fine structure in neutron resonance spectra

The grouping of the neutron resonance positions in near-magic isotopes with N around 82 with periods  $k \times \varepsilon' = 1.16(1)$  keV and  $k=1, 4, 8$  and 18 are given in Fig. 6 and Table 4 together with the  $D$ -distributions of resonances in  $^{61}\text{Ni}$  and  $^{141}\text{Ce}$  (Fig. 6).

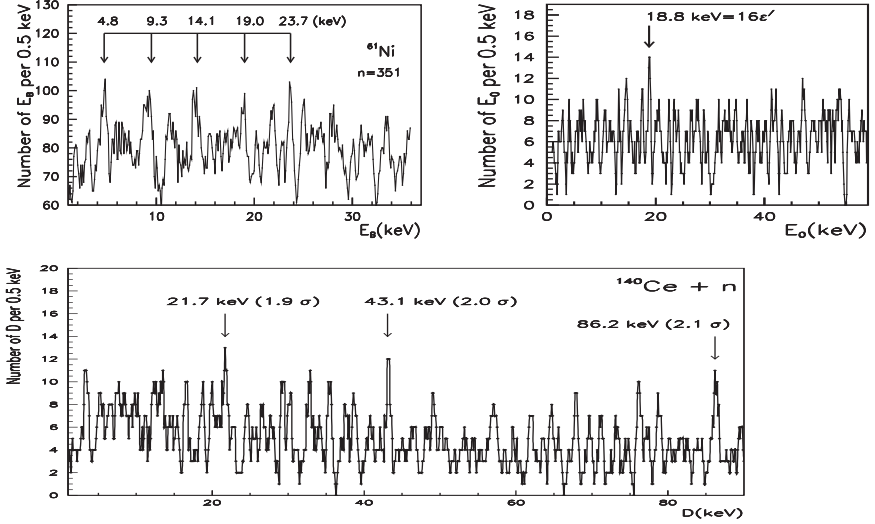


**Fig. 6.** *Top:*  $D$ -distribution of all 351 neutron resonances in the target nucleus  $^{60}\text{Ni}$  [14-16]. *Top right:* Distribution of resonance positions in all N-even light nuclei [14-16]. *Bottom:*  $D$ -distribution in resonances in  $^{141}\text{Ce}$  (period 21.7 keV double-boxed in Table 5).

**Table 4.** *Top:* Positions of strong neutron resonances in isotopes with N=83 compared with the integer number of the period  $9.5 \text{ keV} = 8(\varepsilon' = 1.188 \text{ keV}) = \delta'$ . *Bottom:* Positions of strong resonances in isotopes with Z=35-39 compared with  $k \times (\varepsilon' = 1.188 \text{ keV} = 9.505 \text{ keV}/8)$  (left), and excitations  $E^*$   $^{143}\text{Ce}$  (boxed are  $\varepsilon' = 1.188 \text{ keV}$  and  $18.9 \text{ keV} = 2\delta'$ ).

Nucl.	$^{141}\text{Ce}$	$^{141}\text{Ce}$	$^{142}\text{Pr}$	$^{141}\text{Ce}$	$^{141}\text{Ce}$	$^{141}\text{Ce}$	Comments
$J_i^\pi$	$1/2^+$	$1/2^+$	$(5/2^-)$	$D$	$D$	$D$	
$\Gamma_n^o, \text{meV}$	660	3060	160	$D$	$D$	$D$	
$E_n$	9.573	21.570	9.598	21.7	43.1	86.2	Ratio 9/4
$E^*, E'_n$	<span style="border: 1px solid black;">9.505</span>	<span style="border: 1px solid black;">21.418</span>	<span style="border: 1px solid black;">9.530</span>				was noticed
$k(8\varepsilon')$	1	9/4	1	9/4	9/2	9	by M. Ohkubo
$k \times 8\varepsilon'$	<span style="border: 1px solid black;">9.504</span>	21.384	<span style="border: 1px solid black;">9.504</span>	21.4	42.5	85	[22,24]
Nucl.	$^{140}\text{La}$	$^{80}\text{Br}$	$^{82}\text{Br}$	$^{86}\text{Rb}$	$^{143}\text{Ce}$	$J_o^\pi = 3/2^-$	
$J_i^\pi$	$3^+$	$l_n=0$	$l_n=0$	$l_n=0$	$7/2^-$	$5/2^-$	
$\Gamma_n^o, \text{meV}$	54	72.0	120	159	$E^*$	$E^*$	
$E_n$	1.179	1.201	1.209	2.398			
$E^*, E'_n$	<span style="border: 1px solid black;">1.170</span>	<span style="border: 1px solid black;">1.186</span>	<span style="border: 1px solid black;">1.194</span>	2.370	<span style="border: 1px solid black;">18.9</span>	42.3	
$k(8\varepsilon')$	1/8	1	1	2	2	9/2	
$k \times 8\varepsilon'$	1.188	1.188	1.188	2.376	19.0	42.77	

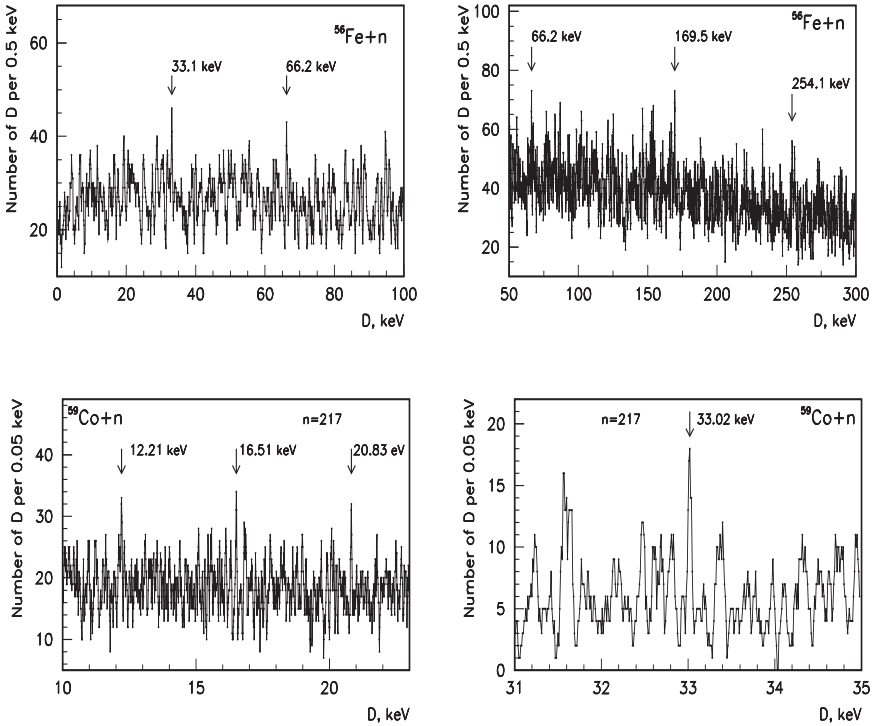


**Fig. 7.** *Top:*  $D$ -distribution in resonances of  $^{57}\text{Fe}$  in regions  $E_n=0$ -100-300 keV. *Bottom:*  $D$ -distribution in neutron resonances of  $^{60}\text{Co}$  in regions  $E_n=18$ -23-35 keV.

$D$ -distributions in the neutron resonances of  $^{57}\text{Fe}$  and  $^{60}\text{Co}$  in the regions  $E_n=0$ -300 keV and  $E_n=18$ -35 keV are shown in Fig. 7. The stable interval 33 keV is common for  $^{60}\text{Co}$  and  $^{57}\text{Fe}$ . In the spacing distribution of all 345 levels of  $^{60}\text{Co}$  with the excitation energy  $E^*$  smaller than the neutron separation energy  $S_n$  (Fig. 9, top), the maxima at  $D=399\text{ keV}=6\times 66\text{ keV}$  and  $D=534\text{ keV}=8\times 66\text{ keV}$  correspond to the same system of stable intervals  $D = k \times 7\delta'$  observed in the neutron resonance spectrum (Table 5, column  $n=14$ ). The same fine structure was observed as maxima in the  $D$ -distributions in the near-magic Sb and Pd (Fig. 5) and in the sum distribution of excitations of low-lying levels of a broad scope of nuclei with  $Z=61$ -73 (exact 1:2 ratio in the positions of the maxima at  $531\text{ keV}=4\times 14\delta$  and  $1059\text{ keV}=8\times 14\delta$  in Fig. 8, bottom).

The third maximum in this  $E^*$ -distribution at  $1294\text{ keV}=8\times 17\delta$  coincides with the maximum at  $1291\text{ keV}$  in a similar distribution for light nuclei with  $Z\leq 29$  (Fig. 8, top). Two nearby maxima located at a distance of  $144\text{ keV}$  correspond to a shift between  $483\text{ keV}=3\times 17\delta$  and  $340\text{ keV}=2\times 18\delta$ . Stable excitation with a value of  $1024\text{ keV}=6\times 18\delta$  is observed in nuclei with  $Z=32-37$  (center line in Fig. 8). Stable excitation in heavy nuclei (around  $Z=84$ ) correspond to a maximum close to  $683\text{ keV}=4\times 18\delta$ . All these maxima are presented in the top part of Table 5 together with CODATA parameters  $161\text{ keV}=17\delta$  and  $170\text{ keV}=1i\delta$ , with the pion parameters and the masses of NRCQM constituent quarks, and the fundamental fields considered in Introduction.

For an independent check of the fine structure with a period of  $\delta'$  observed in neutron resonances (Figs. 6, 7 and Table 4), and an indirect check of the CODATA relations (2), data on all excitations of light nuclei with  $Z=20-28$  were additionally analyzed [18].

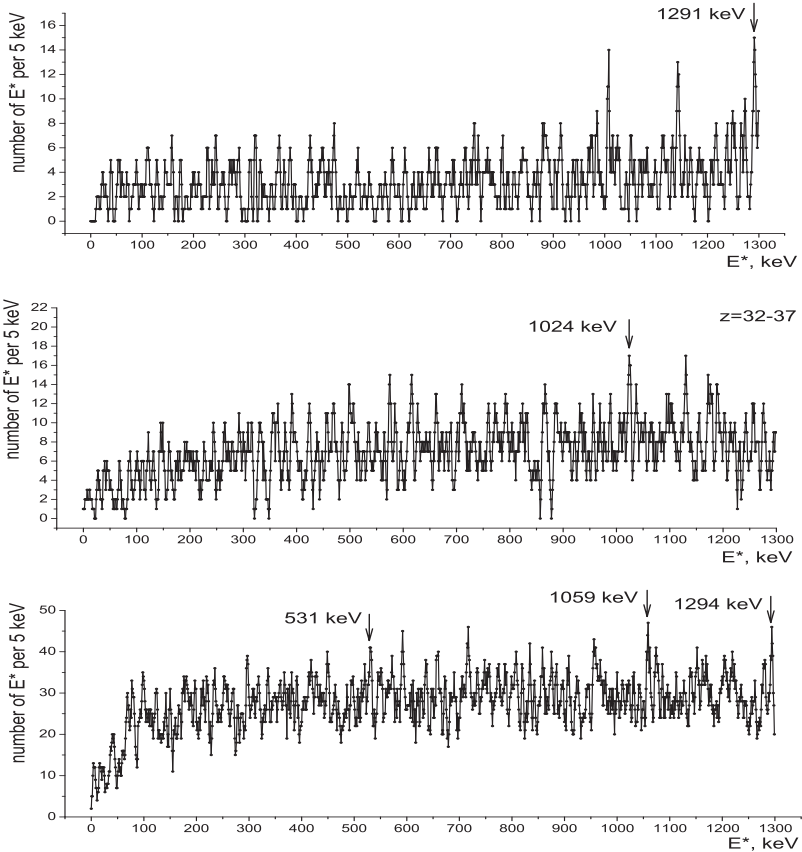


Fig. 8. Sum energy distributions of levels in all nuclei with  $Z=2-29$ ,  $32-37$  and  $61-73$ .

**Table 5.** Stable intervals  $D = k \times n \times 9.5 \text{ keV}$  ( $n=13, 14, 16, 17, 18$ , period  $\delta' = (\alpha/2\pi)16m_e$ ) reported in Vol. I/25E L-B Springer, are given together with values found in this work (double-boxed). Boxed in top section are intervals with  $k=1, n=17, 18$  corresponding to the fine structure in nucleon masses (CODATA) and parameters of NRCQM and Standard Model. Values  $\Sigma E^*$  and  $\Sigma E_B$  are sum effects in distributions of nuclear excitation and binding energies obtained for large groups of nuclei [14-16]. Factor  $k = 10^3 \approx (\alpha/2\pi)^{-1}$  is considered in [3-6].

$k$	n=13	n=14	n=16	n=17	n=18
1	CODATA		—	161 keV= $\delta m_N/8$	170 keV= $m_e/3$
8,6	$\Sigma E^*$	1059, 531	1212	1291, 1294= $\delta m_N$	1024 $\approx 2m_e$
$10^3$	$\Sigma E_B$		130 MeV	140 MeV, $\Lambda_{QCD}$	147 MeV
$10^3$	$m_\mu$	NRCQM	$f_\pi=131 \text{ MeV}$	$m_\pi=140 \text{ MeV}$	$\Delta M_\Delta=147 \text{ MeV}$
$3 \cdot 10^3$		NRCQM	$M_q''=390 \text{ MeV}$		$M_q=441 \text{ MeV}$
$10^6$	$M_Z=91 \text{ GeV}$	SM-param.	$M_H'=115 \text{ GeV}$		$M_H^\circ=125 \text{ GeV}$
1/8-1/2		$33 \text{ }^{60}\text{Co}$	$19 \text{ }^{51}\text{V}, \text{}^{53}\text{Mn}$		$21.7 \text{ }^{141}\text{Ce}$
1/2		$67 \text{ }^{40}\text{Ca}$	$76 \text{ }^{46}\text{Sc}$	$82 \text{ }^{56}\text{Co}$ $81 \text{ }^{49}\text{V}$	$85 \text{ }^{65}\text{Cu}$ $85 \text{ }^{68}\text{Cu}$
1/2		$66 \text{ }^{57}\text{Fe}$		$79 \text{ }^{53}\text{Mn}$ Fig. 6	$84 \text{ }^{55}\text{Co}$ $85 \text{ }^{40}\text{Ca}$
1		$133 \text{ }^{53}\text{Mn}$	$151 \text{ }^{62}\text{Cu}$	$159 \text{ }^{62}\text{Cu}$	$171 \text{ }^{63}\text{Cu}$ $170 \text{ }^{57}\text{Fe}$
1,3/2			$148 \text{ }^{59}\text{Cu}$	$240 \text{ }^{66}\text{Cu}$	$251 \text{ }^{69}\text{Cu}$ $254 \text{ }^{57}\text{Fe}$
2		$265 \text{ }^{46}\text{Sc}$	$305 \text{ }^{62}\text{Cu}$	$316 \text{ }^{56}\text{Co}$ $321 \text{ }^{46}\text{Sc}$	$339 \text{ }^{64}\text{Cu}$ $338 \text{ }^{46}\text{Sc}$
2				$323 \text{ }^{40}\text{Ca}$ $322 \text{ }^{33}\text{S}$	$341 \text{ }^{57}\text{Ni}$ $339 \text{ }^{19}\text{F}$
2,5/2		$399 \text{ }^{60}\text{Co}$ Fig. 9		$322 \text{ }^{32}\text{S}$	$340 \text{ }^{65}\text{Cu}$ $428 \text{ }^{23}\text{Na}$
3	$368 \text{ }^{69}\text{Cu}$	$399 \text{ }^{49}\text{V}$	$453 \text{ }^{59}\text{Cu}$		$511 \text{ }^{42}\text{Ca}$ $514 \text{ }^{23}\text{Na}$
3		$398 \text{ }^{51}\text{V}$			$512 \text{ }^{55}\text{Co}$ $511 \text{ }^{49}\text{V}$
4	$491 \text{ }^{46}\text{Sc}$	$531 \text{ }^{49}\text{V}$		$637 \text{ }^{22}\text{Na}$ $637 \text{ }^{18}\text{F}$	$682 \text{ }^{55}\text{Co}$
4	$490 \text{ }^{20}\text{F}$	$534 \text{ }^{60}\text{Co}$ Fig. 9		$645 \text{ }^{40}\text{Ca}$ $639 \text{ }^{65}\text{Cu}$	
4,5	$493,614 \text{ }^{18,19}\text{F}$			$646 \text{ }^{37}\text{S}$ $649 \text{ }^{53}\text{Mn}$	
6,8	$736 \text{ }^{42}\text{Ca}$	$797 \text{ }^{49}\text{V}$	$1211 \text{ }^{69}\text{Cu}$	$1294 \text{ }^{41}\text{K}$ $1295 \text{ }^{47}\text{V}$	$1017 \text{ }^{53}\text{Mn}$
6,8		$1065 \text{ }^{60}\text{Co}$	$1204 \text{ }^{59}\text{Cu}$	$1292 \text{ }^{38}\text{S}$ $1290 \text{ }^{53}\text{Mn}$	$1021 \text{ }^{49}\text{V}$ Fig. 10
8	$1060 \text{ }^{47}\text{V}$		$1217 \text{ }^{60}\text{Co}$	$1292 \text{ }^{55}\text{Mn}$ $1301 \text{ }^{59}\text{Mn}$	
8-10	$1228 \text{ }^{19}\text{F}$			$1291 \text{ }^{59}\text{Co}$ , $1454 \text{ }^{42}\text{Ca}$	
12	$1476 \text{ }^{38}\text{Ar}$	$1587 \text{ }^{46}\text{Sc}$		$1931 \text{ }^{18}\text{F}$ $1943 \text{ }^{41}\text{Ca}$	
12,16	$1967 \text{ }^{33}\text{S}, \text{}^{36}\text{Ar}$			$1942 \text{ }^{32}\text{Si}$ , $2577 \text{ }^{18}\text{F}$	

#### 4. Fine structure in excitations of nuclei with $Z=23,25,27$

The results obtained in the additional analysis for isotopes with  $Z=23, 25, 27$  are presented in Figs. 9, 10. In Table 6, where all low-lying levels of  $^{60}\text{Co}$  are given, it is shown that in this near-magic nucleus there are many stable intervals in the spectrum (maxima in the spacing distribution for all 345 levels, see Fig. 9, top and center) with energies close to the excitation of low-lying states (a large number ( $n$ ) of intervals  $D_{ij}=544, 1005, 1015, 1217$  keV in Table 6, bottom). By fixing  $x$  at real low-lying excitation levels  $E^*$  in the AIM analysis, we check the behavior of these well known  $E^*$  (stability of the relations between them) at higher excitation energies. In Fig. 7 (bottom) five intervals close to  $E^*$ , demonstrate such an unexpected effect in the case of  $x = E^* = 1217$  keV in  $^{60}\text{Co}$ . Fixing the interval  $x=1066 \approx 8 \times 14\delta'$  in  $^{60}\text{Co}$  (Fig. 9, bottom), we observe in the  $D^{AIM}$ -distribution (Fig. 10, top) a maximum at  $x/2=532$  keV.

**Table 6.** Excitations  $E^*$  (in keV),  $J^\pi$  and maxima in spacing distribution of  $^{60}\text{Co}$ .

$E^*$	0.0	58.6	277	288	436	506	543	1004	1006	1016	1208	1216	1217
$J^\pi$	$5^+$	$2^+$	$4^+$	$3^+$	$5^+$	$3^+$	$2^+$	(3,4)	4		$5^+$	$6^+$	4
$D_{ij}$		59		288			544		1005	1015			1217
$n(D_{ij})$							74		73	75			79

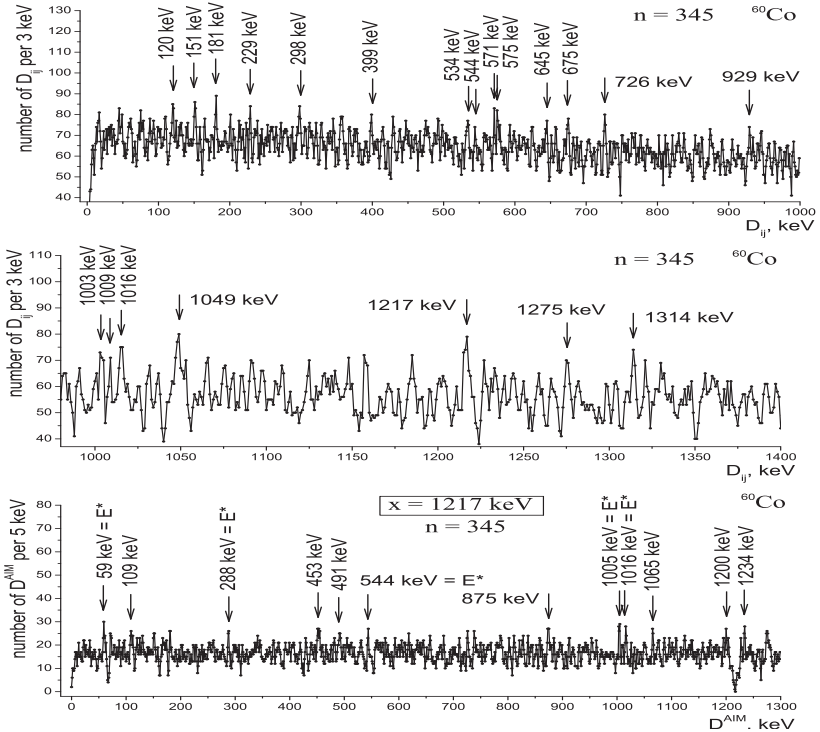


**Fig. 9.** *Top and center:* Spacing distributions in  $^{60}\text{Co}$  for energies 0-1000-1400 keV. *Bottom:*  $D^{AIM}$ -distribution for  $x=1217$  keV in  $^{60}\text{Co}$  with maxima at excitation energies  $E^*$ .

The intervals 1060 keV and 1294 keV= $E^*$  appear together in the  $^{47}\text{V}$  spectrum (Fig. 10, center). Similar small intervals 79-81 keV= $(17/2)\delta'$  in  $^{49}\text{V}$ - $^{53}\text{Mn}$ , stable excitations and intervals close to 1293 keV= $\delta m_N$  are shown in Table 5 ( $k=17$ , which also contain the second parameter of the CODATA relations). This means that the presence of fine and superfine structures in nuclear data provides confirmation of the common fundamental dynamics based on the electron.

In the case of  $^{49}\text{V}$ , fixing the intervals equal to the low-lying excitation  $E^*=1021\text{ keV}=6\times 18\delta'$  (Fig. 10, bottom) leads to intervals equal to its half  $x/2=511\text{ keV}$  and  $x/2=339\text{ keV}=2\times 18\delta'$ . Simultaneously, the above considered interval 399 keV (maximum with a deviation of about  $6\sigma$ ) and the intervals at 531 keV= $4\times 14\delta'$  and at the doubled value  $D^{AIM}=797\text{ keV}=6\times \delta'$  confirm the reality of the system of stable intervals 33 keV and 66 keV= $14\delta'$ , observed in neutron resonance spacing (Fig. 7 and double-boxed values in Table 5). In this table, the results obtained here are presented together with the results considered in Volume I/25E of the Landolt-Boernstein Library, Springer. The interval  $D=67\text{ keV}$  was assigned to the nucleus  $^{40}\text{Ca}$ , located at the beginning of the large subshell  $1f_{7/2}$ . The results considered here are usually compared with model calculations performed for nucleons in this subshell. Thus, the observed systems of stable intervals can appear in the correlations in the data for all other nuclei with N, Z after 20.

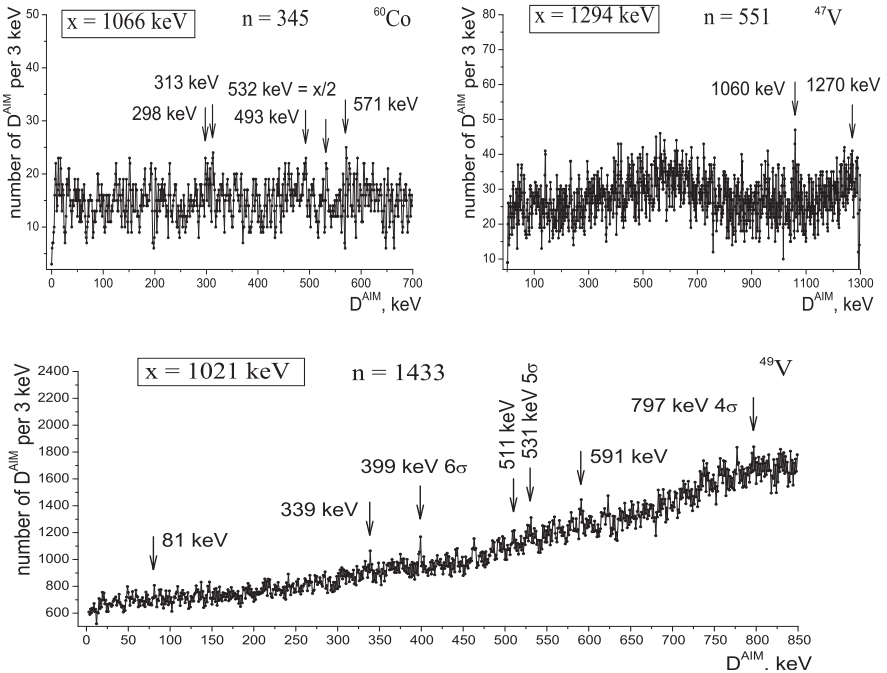


**Fig. 10.** *Top left:*  $D^{AIM}$ -distributions in  $^{60}\text{Co}$  for  $x=1066\text{ keV}$ , maximum at  $532\text{ keV}=x/2$ . *Top right:*  $D^{AIM}$ -distribution in  $^{47}\text{V}$  for  $x=1294\text{ keV}$ , maximum at  $1060\text{ keV}=8\times 14\delta'$ . *Bottom:*  $D^{AIM}$ -distribution in  $^{49}\text{V}$  for  $x=1021\text{ keV}=6\times 18\delta'$  with maxima at  $339\text{ keV}=2\times 18\delta'$ ,  $511\text{ keV}=3\times 18\delta'$ , as well as at 399, 541 and 797 keV equal to  $k\times 14\delta'$ ,  $k=3, 4, 6$ .

In case of  $^{53}\text{Mn}$ , the sum effect of 5 AIM-distributions with different  $x = E^*$  (Fig. 11, top) contains strong maxima at 379 keV and 2449 keV, which coincide with a real  $E^*$  not included in AIM analysis, and with the maximum at 133 keV= $14\delta'$ . In the total spacing distribution of  $^{53}\text{Mn}$  (Fig. 11, bottom right), two clearly observed maxima at  $10\delta'=187$  keV and  $20\delta'=377$  keV (ratio 2.02) correspond to  $k=10$  in the same fine structure systematics. The interconnection of this discreteness with the number of protons ( $n=5$ ) in the shell should be checked.

In both near-magic nuclei with  $N=28$  total spacing distributions ( $n=546$  and 1127 for  $^{51}\text{V}$  and  $^{53}\text{Mn}$ ) contain the same stable value  $D=19$  keV, exactly corresponding to  $2\delta = 2 \times 9.5$  keV, introduced from the grouping of neutron resonances in light and heavy near-magic nuclei (Fig. 6, right, Table 4). An important similarity between the discreteness ( $\delta'=9.5$  keV) in nuclear excitations (and the positions of neutron resonances) and the discreteness in CODATA parameters with a period  $(161 \text{ keV} + 170 \text{ keV}) : (17 + 18) = 9.46$  keV should be checked in other nuclear regions.

Analyzes of nuclear spectroscopic data and neutron data were performed separately. It is necessary to avoid inclusion of arrays of resonance energies (in ENSDF) in the analysis of the density of nuclear states. Such a nonstatistical effect from modulation with neutron threshold energies was observed in [25] (the correlation in the separation energies [6] was assigned to  $E^*$ ).

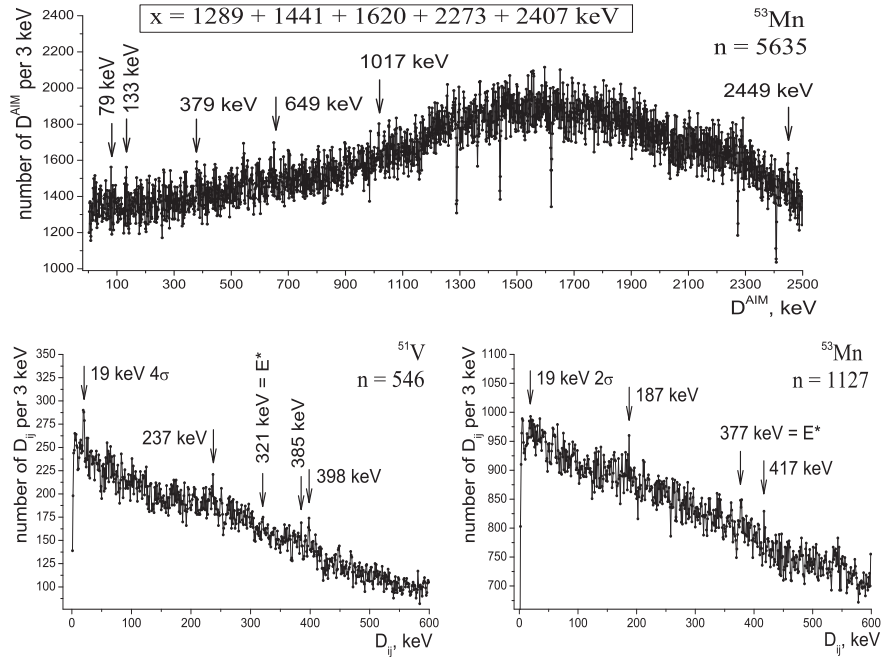


**Fig. 11.** *Top:* Sum of 5  $D^{AIM}$ -distributions in  $^{53}\text{Mn}$  ( $n=5635=5 \times 1127$  for 5 values  $x$ ). The maxima at  $E^*=379$  keV ( $5\sigma$ ) and 2449 keV ( $6\sigma$ ), as well as  $D=79, 133, 649, 1017$  keV are marked. 5 strong minima correspond to the positions  $x = E^*$  in the AIM analysis.

*Bottom left:* Spacing distribution in  $^{53}\text{Mn}$ , maximum at 19 keV= $2\delta'$  (deviation of about  $4\sigma$ ).

*Bottom right:* Spacing distribution in  $^{51}\text{V}$  with maxima at 19 keV= $2\delta'$ , 187 keV= $10\delta'$ , 377 keV= $20\delta'$ .

## 5. Conclusions

The analysis of neutron resonances performed here shows the inclusion of the observed fine and superfine structures (in positions and spacing distributions) in the fine structures observed in the charged-particle resonances and in low-lying excitations. The parameters of these common fine structures overlap with the parameters of the fine structure in the particle masses. This means that nuclear data can be used in indirect but independent check of the fundamental properties of matter.

According to F. Wilczek [26], a new aspect of nuclear spectroscopy ("nuclear chemistry" with very accurate results for nuclear states energies) can be used in several important applications, for example, in laser technologies.

Modern nuclear spectroscopy will take part in the unification of interactions based on CO-DATA relations. For strong interactions, this can be connected with the expression  $\alpha_s = 2/17$  (for the distance  $1/M_Z$  [2]), which contains a pion mass close to  $\Lambda_{QCD}$ . The particle mass spectrum extends from  $m_e$  to the scalar boson mass  $M_{H^0} = \Delta M_{\Delta}(\alpha/2\pi)^{-1} = (m_e/3)(\alpha/2\pi)^{-2}$  and from the muon mass to the vector boson mass  $M_Z = m_{\nu}(\alpha/2\pi)^{-1}$ , which are interconnected by QED corrections and symmetry motivated relations.

The creation of modern nuclear models based on fundamental aspects of nuclear spectroscopic data and neutron resonance data is an important step in the development of the Standard Model.

## References

1. M. Tanabashi *et al.* (Part. Data Group), Phys. Rev. D **98** (2018) 030001.
2. P. Mohr, D.B. Newell, B.N. Taylor, Rev. Mod. Phys. **88** (2016) 035009.
3. S.I. Sukhoruchkin, Nucl. Part. Phys. Proc. **300-302** (2018) 75.
4. S.I. Sukhoruchkin, IOP Conf. Series: J. Phys. Conf. Ser. (in press).
5. S.I. Sukhoruchkin, Nucl. Part. Phys. Proc. **294-296** (2018) 129.
6. S.I. Sukhoruchkin, *Statistical Prop. of Nuclei*, ed. G. Garg. Pl. Press, 1972, p. 215.
7. T. Otsuka, T. Suzuku, Y. Utsino, Nucl. Phys. A **805** (2008) 127c.
8. I. Tanihata, Mod. Phys. Lett. A **25** (2010) 1886 (and priv. commun.).
9. R. Feynman, *QED-Strange Theory of Light/Matter*, 1986. Princ. Univ. Press.
10. V.V. Belokurov, D.V. Shirkov, *Theory of Part. Inter.* AIP, 1991; M. Nauka, 1986.
11. Ya.B. Zeldovich, A.D. Sakharov, Yad. Fiz. **4** 1966 395; Sov. J. Nucl. Phys. **4** (1967) 283.
12. C. Itoh *et al.*, Phys. Rev. D **40** (1989) 3660.
13. L.A. Glozman, Nucl. Phys. A **629** (1998) 121c.
14. S. Sukhoruchkin, *Discr. part. masses* Lambert Ac. Publ. 2017. ISBN 978-620-2-02258-3.
15. S.I. Sukhoruchkin, *Proc. LI Winter School of PNPI*, pp. 43–139, SPb., 2018.
16. S.I. Sukhoruchkin, *Proc. L Winter School of PNPI*, pp. 45–119. SPb., 2017.
17. M.H. Mac Gregor, Nuovo Cimento A **103** (1990) 983.
18. S.I. Sukhoruchkin, Z.N. Soroko, D.S. Sukhoruchkin, these Proceedings.
19. S.I. Sukhoruchkin, *Proc. Conf. Nucl. Data for Reactors*, Paris, Vol. 1, p. 159 (1967).
20. W.W. Havens Jr., *Progr. Fast Neutron Phys.* Univ. Chicago Press, 1963, p. 215.
21. K. Ideno, M. Ohkubo, J. Phys. Soc. Jpn. **30** (1971) 620.
22. M. Ohkubo *et al.*, Rept. JAERIM93112, 1993.
23. K. Ideno, Proc. Conf. Neutr. Research, SPIE Proc. Ser. Vol. **2867**, 1997, p. 398.
24. M. Ohkubo, J. Nucl. Sci. Techn. (Tokyo) **19** (1981) 745.
25. S.L. Saharov, Izv. Rus. Acad. Sci. Phys. **64** (2000) 930; Bull. Rus. Acad. Sci. Phys. **64** (2000) 743.
26. F. Wilczek, Nature **520** (2015) 303.

# Problems and Possibilities of a Study of the Cascade Gamma-Decay of a Nucleus Excited below the Neutron Binding Energy

A.M. Sukhovej<sup>1</sup>, L.V. Mitsyna<sup>1</sup>, D.C. Vu<sup>1,2</sup>, N. Jovančević<sup>3</sup>, D. Knežević<sup>3,4</sup>,  
M. Krmar<sup>3</sup>, A. Dragić<sup>4</sup>

<sup>1</sup>*Joint Institute for Nuclear Research, Dubna, 141980, Russia*

<sup>2</sup>*Vietnam Academy of Science and Technology, Institute of Physics, Hanoi, Vietnam*

<sup>3</sup>*University of Novi Sad, Faculty of Science, Department of Physics, Trg Dositeja Obradovica 3,  
21000 Novi Sad, Serbia*

<sup>4</sup>*Institute of Physics Belgrade, Pregrevica 118, 11080 Zemun, Serbia*

## 1. Introduction

In modern experiment, in which technologically advanced equipment is used for investigation a cascade gamma-decay of excited nucleus, a determination of the parameters of excited nuclear levels (spin, parity, lifetime, excitation energy) is of less importance than an obtaining of fundamental data about intranuclear processes (interaction of nucleons).

Precisely for this reason, it is necessary to determine, first of all, a sequence of gamma-quanta in the cascades of different multiplicities  $M$ . There are  $M!$  variants of arrangement for any primary cascade-transition in the gamma-ray spectrum (in the decay scheme). If the two-step gamma-cascade (TSC) can be placed in the decay scheme by only two ways (one of them is false), then primary transition of the cascade with  $M=5$ , for example, have 120 variants of probable arrangement.

A task of determination of primary-transition spectra is solving in various indirect experiments differently:

- using a difference of total gamma-spectra for different excitation energies of the same nuclear reaction [Oslo];
- by calorimeter of total energy of the gamma-spectrum [Los-Alamos];
- by decomposition of the two-step gamma-cascade to two spectra of only primary and only secondary transitions with the use of both spectrometric information and shape difference of spectra of energy-resolved gamma-transitions and of continuum of unresolved transitions [Dubna].

Each of these ways without doubt has problems of analysis of indirect experiment which lead to inevitability of unknown sizeable systematical errors. Minimization of these errors is possible only by using potentials of these three methods.

An experimental obtaining of the reliable parameters of the cascade gamma-decay of any compound-states is exclusively important to understand processes which take place in an excited nucleus. The ground state of even-even nucleus, in terms of theorists, is “quasi-particle vacuum”, in which free fermions appear at an excitation energy  $E_{ex}$  (not just at  $E_{ex} > B_n$ , but also at  $E_{ex} < B_n$ , where  $B_n$  is the neutron binding energy in the nucleus). While the representation remained in being that the nucleus is a system of non-interactive Fermi-particles, a possibility for nucleons to form Cooper pairs could not be ruled out, and such pairs can break at any excitation energy. A process of breaking of Cooper pairs has not been experimentally investigated until now, as there are no high-aperture spectrometers of gammas with an electron-volt resolution.

When the  $B_n$  values compared with the nucleons' pairing energy  $\Delta$  [1], it is reasonable to expect that 3–4 breaks of Cooper pairs of nucleons below the neutron binding energy must occur, at least, in investigated by us nuclei from mass region of  $28 \leq A \leq 200$ . To form a clear picture of intranuclear processes, it is necessary to determine in experiment the parameters of the cascade gamma-decay (the partial radiative widths  $\Gamma$  or the strength functions  $k = \Gamma/(A^{2/3} \cdot E_\gamma^3 \cdot D_\lambda)$ , where  $A$  is the nuclear mass number,  $E_\gamma$  is the energy of  $\gamma$ -quantum,  $D_\lambda$  is an average space between nuclear compound states, and the nuclear level density  $\rho$ ) simultaneously

For the first time a technique of simultaneous determination of the nuclear level density  $\rho$  and partial widths  $\Gamma$  of emission of primary transitions from a total TSC spectrum was proposed and realized in Dubna, at LNP JINR in 1984 [2–4]. The first experiments with recording of the cascades of two quanta emitted sequentially, which have summarized energy of 5–10 MeV, were carried out with two Ge(Li)-detectors and statistics was amounted to several thousands of events of full absorption of cascade energy. From 2000 we began to use in our experiments HPGe-detectors, efficiency of which is essentially greater. By now, using this developed technique, the parameters of gamma decay for 44 nuclei [5, 6] have been determined from measured TSC intensity spectra.

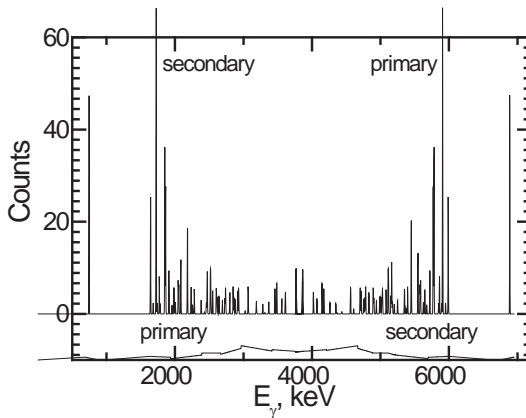


Fig.1. Quanta-energy dependence of the intensity of TSC to the first excited level with the energy  $E_f = 73$  keV of  $^{164}\text{Dy}$  nucleus. On top: the intensity of primary and secondary energy-resolved gamma-transitions; below: continuous distribution of unresolved transitions and small background.

Detectors with even tempered efficiency ( $\sim 10\%$ ) allow from a lot of coincidences to extract events of simultaneous recording of two (and more) quanta, if their total energy is equal to total energy of decaying compound state or  $\sim 0.5$ – $1$  MeV less than this energy. Experimental spectra are composed of isolated energy-resolved (intense) gamma-transitions and continuum of unresolved ones. Latest transitions represent a continuous distribution with zero average and small amplitude [7]. A center of the distribution is at the energy of  $0.5(E_1 + E_2)$  in the quanta-energy scale, where  $E_1$  and  $E_2$  are energies of primary and secondary quanta of the cascade, correspondingly. A typical quanta-energy dependence of intensity of

TSC is shown in Fig.1 with an example of the intensity distribution of the cascade with the total quanta energy  $E_1+E_2=7585$  keV to the first excited level of  $^{164}\text{Dy}$  nucleus.

Let's compare two experiments, in which the cascade gamma-decay at radiative capture of neutrons by  $^{163}\text{Dy}$  nucleus was investigated. Both experiments with different approaches to the data analysis have problems of the alternative ways of obtaining of the nuclear parameters.

- 1) In Dubna experiment reaction of the radiative capture of thermal neutrons by  $^{163}\text{Dy}$  nucleus has been investigated using two Ge(Li)-detectors placed in close geometry (opposite to each other and perpendicularly to the beam line). By the likelihood method (using some of appropriate models of the nuclear level density and partial widths) from the intensity of measured TSC the most probable nuclear level density and radiative strength functions were obtained in the energy range below  $B_n$ .
- 2) In Los-Alamos the same reaction for idem nucleus has been studied in the experiment with  $4\pi$ -calorimeter of the cascade gammas [8]. Analysis of measured total gamma-spectra of the decay of neutron resonances of  $^{164}\text{Dy}$  has been done using developed in Praha algorithm DICEBOX [9] for a simulation of the cascades of gamma-transitions of all possible multiplicities [10].

## 2. Problems of extracting of the nuclear parameters from gamma-spectrum

When analyzing the total gamma-spectrum, information about the nuclear parameters ( $\Gamma$  (or  $k$ ) and  $\rho$  values) is always extracted from the data of *indirect* experiment. In order to obtain the parameters of the investigated nucleus approximating the experimental gamma-spectrum it is always required to use model representations about  $\Gamma(E_\gamma)$  and  $\rho(E_{\text{ex}})$  functions. And a transfer of errors of the experimental spectra to the errors of the determined parameters has to be carefully examined. At a difference between relative errors of experimental spectra  $\delta S/S$  and of the required nuclear parameters,  $\delta\rho/\rho$  and  $\delta\Gamma/\Gamma$ , in  $\sim 1.5-2$  times, the absolute errors  $\delta\rho$  and  $\delta\Gamma$  can exceed  $\delta S$  in 5–10 times and more. We established that, in the detectors used by us, a difference between areas of the experimental and approximating spectra is usually not more than  $\sim 1\%$  when spectra of gamma-cascades are averaged over 200–250 keV.

In spite of the fact that the different types of spectrometers are used in various experiments to measure the intensities of multiple gamma-cascades, for the same investigated nucleus a certain part of TSC intensity  $I_{\gamma\gamma}$  at any measured spectrum is changeless. Therefore, a qualitative normalization of measured gamma-spectra per a decay of the nuclear compound state (neutron resonance) is necessary both in analysis with the use of simulation and in analysis by likelihood method.

### 2.1. Normalization of the cascade intensity

Collected to now and presented in files [11] and [12] data about spectra of the radiative capture of thermal neutrons allow determination of absolute intensity of the TSC  $i_{\gamma\gamma}$  (in percent per one decay) with a good accuracy.

For all nuclei investigated in Dubna [5, 6] the normalization of the two-step cascades was carried out using absolute intensity of strong primary gamma-transitions from [11, 12]. For this to be done, from the experimental results the branching coefficients  $b_r$  for excited intermediate levels of nuclei were accurately determined offline as well as the intensities of primary transitions of the compound-states decay. Intensity of the decay of individual cascades,  $i_{\gamma\gamma}=i_\lambda \cdot b_r$ , where  $i_\lambda$  is compound-state decay intensity per one decay, allows to obtain

a value of sum of all possible (both intense resolved and continuum of weak unresolved) cascades between initial level  $E_\lambda$ , intermediate levels  $E_i$  and final ones  $E_f$ . Result sum ( $I_{\gamma\gamma} = \sum i_{\gamma\gamma}$ ) is enough for a determination of the nuclear level density and partial widths of primary cascade transitions in iteration process of solving the system of equations (1), which connect experimental intensities of the TSC gamma-transitions  $I_{\gamma\gamma}$  with used parametrical functions  $\rho(E_{ex})$  and  $\Gamma(E_\gamma)$ . The shape and area of measured spectra  $I_{\gamma\gamma}$  are determined by a convolution of the required functions  $\rho(E_{ex})$  and  $\Gamma(E_\gamma)$ .

Experimental distribution  $I_{\gamma\gamma}(E_1, E_2)$  of the total intensity of the TSC can be fairly accurately described by infinite number of essentially different functions  $\rho(E_{ex})$  and  $\Gamma(E_\gamma)$  because of nonlinearity of the system of equations (1), which connect these strong correlated functions with  $I_{\gamma\gamma}(E_1, E_2)$ . And determination of the intensities  $I_{\gamma\gamma}(E_1)$  of only primary transitions of the cascades limits a set of solutions of foresaid system of equations, so established sequence of cascade gamma-quanta is a necessity of simultaneous determination of reliable nuclear parameters using likelihood method.

In order to obtain the  $I_{\gamma\gamma}(E_1)$  spectrum, which is wanted for further approximation, from the total spectrum  $I_{\gamma\gamma}(E_1, E_2)$ , it is necessary to establish the sequence of the gamma-quanta in the cascades. It is possible only when there is additional experimental information. In the Dubna technique, by means of the procedure described in [7], spectroscopic information was used thereto. Any TSC (after the procedure of numerical improvement of resolution [13]) is a mirror-symmetrical energy distribution of the intensities of primary and secondary gamma-transitions. Taking into account zero average and dispersion smallness of a noise line of a continuous distribution (see Fig.1) its subtraction from isolated peaks isn't a problem. Procedure [7] allows to determine a part of primary transitions of the cascades,  $I_{\gamma\gamma}(E_1)$ , with relative accuracy not worse than 10–20% in any energy interval, practically without a distortion of normalization of TSC intensity. For  $^{164}\text{Dy}$  we obtained  $I_{\gamma\gamma}(E_1) = 45.9\%$  per one decay [14].

In analysis of the experiment with scintillation detectors [8] there is no possibility to use the  $^{164}\text{Dy}$  decay scheme from [14] and the files [11, 12] for spectra normalization, as insufficient resolution of these detectors does not allow identification of individual intense transitions. In the paper [8] a normalization of the intensities of the two-step gamma-cascades per a decay is absent. It must be note that experimental intensity of the cascades with multiplicity of  $M = 2$  in experiment with  $4\pi$ -calorimeter ( $4\pi$ -C experiment) was, most likely, underrate because of existent irremovable transfer of annihilation gamma-quanta between detectors' crystals at bad resolution of the spectrometer at low energies (at 1 and 6 MeV the resolution is about 16% and 7%, respectively). In energy region near  $B_n$  a cross-section of pair production is, by order of magnitude, greater than it is at the energy of gamma-transition of 1–2 MeV. Such "inter-scattering" increases areas of spectrum components with multiplicities of  $M \geq 3$  and distorts (decreases) an area of TSC-component.

## 2.2. Possibility of determination of quanta sequence in the cascades

The cascades' quanta at a neutron capture are emitted sequentially but there is no possibility to determine experimentally their quanta sequence. If the cascade of two emitted quanta has only two variants of quanta placing in the decay scheme, then for three quanta there are  $3! = 6$  variants of replacement, i.e. it is impossible to obtain reliable information about gamma-decay from spectra with multiplicity of  $M \geq 3$ .

When the data of  $4\pi$ -C experiment analyzing, an objective information about  $\Gamma$  and  $\rho$  values can be extracted only from a spectrum with multiplicity of  $M = 2$ . But one should take

into account that one of possible variants of quanta sequence for the decay scheme is *false* and must be excluded from analysis.

On a base of investigated TSC of more than four tens of nuclei [5, 6], it was experimentally established that at a statistics of ~5000 (or more) of recorded events of total cascade-energy absorption

- ✓ about 2/3 of the intensity of all primary transitions accounts for energy-resolved ones (Fig.1, on top), and gamma-quanta of resolved primary transitions, as a rule, have energy  $E_1 > 0.5B_n$ , i.e. the levels excited by them are in the “lower” half of the decay scheme with  $E_{ex} < 0.5B_n$ ;
- ✓ about 1/3 of the intensity of all primary transitions accounts for a continuum of unresolved transitions with the energies  $E_1 < 0.5B_n$  and excite levels at  $E_{ex} \geq 0.5B_n$  (Fig.1, below), where tenth part of all intensity are transitions into energy region near  $E_1 \approx 0.5B_n$ , in which weak primary and weak secondary transitions are mixed.

To obtain the best values of  $\rho$  and  $\Gamma$ , iteration process of approximation in our analysis is repeated many times with different initial parameters of required functions  $\Gamma(E_\gamma)$  and  $\rho(E_{ex})$  varying a correction-vector value. In DICEBOX simulation [9] used by the authors of [8], for three functions of the level density the most suitable radiative strengths are chosen from few variants from [15].

It must be noted that the level-density model of Strutinsky [16], which is used by us and not taken into account by the authors of [8], can be included to the analysis in any experiment on a study of the cascade gamma-decay. This model is successfully used in practice for a description of pre-equilibrium reactions [15], and an existence in a nucleus of the collective levels (vibrational and rotation ones) [17] is a basis of modern representations about gamma-decay.

### 3. The possibilities of indirect experiment

In Dubna technique, for determination of  $\rho$  and  $\Gamma$  values the standard likelihood method is used. When solving the system of equations (1), which connect in small intervals of primary transitions with unknown numbers of intermediate cascade levels  $n_j$ , where  $M_{\lambda j}$  is the number of  $\gamma$ -transitions from level  $\lambda$  to intermediate levels  $n_j$  and  $m_{jf}$  is the number of secondary transitions to final level  $f$  of the cascade, corresponded unknown partial widths  $\Gamma$  and the experimental cascade intensities

$$I_{\gamma\gamma}(E_1) = \sum_{\lambda,f} \sum_i \frac{\Gamma_{\lambda i}}{\Gamma_\lambda} \frac{\Gamma_{if}}{\Gamma_i} = \sum_{\lambda,f} \sum_j \frac{\Gamma_{\lambda j}}{\langle \Gamma_{\lambda j} \rangle M_{\lambda j}} n_j \frac{\Gamma_{jf}}{\langle \Gamma_{jf} \rangle m_{jf}}, \quad (1)$$

the results of each successful iteration (trajectories of changing of the best  $\rho$  and  $\Gamma$  values and approximated  $I_{\gamma\gamma}$  intensities) are presented graphically by approximation program. It allows monitoring the search process of the absolute minimum

$$\chi^2 = \sum_{n_j} \frac{(I_{\gamma\gamma}^{cal}(E_1) - I_{\gamma\gamma}^{exp}(E_1))^2}{\sigma^2}, \quad (2)$$

where  $I_{\gamma\gamma}^{cal}(E_1)$  and  $I_{\gamma\gamma}^{exp}(E_1)$  are model-parametrized and experimental intensities, and  $\sigma^2$  is a dispersion of their difference. At  $\chi^2$ -redundancy recognition the initial parameters of iteration process are corrected.

As determination of the nuclear parameters surely demands a usage of parametrical functions  $\rho(E_{ex})$  and  $\Gamma(E_\gamma)$ , so there are no problem of degeneracy of the system (1). Usually, for a given model there is the only solution.

In Dubna technique there is no need to use any hypothesis untested experimentally. Now our analysis of the experiment is carried out on a base of a modern model of density of  $n$ -quasi-particle levels [16], on balance between an entropy change and a change of the energy of quasi-particle states [18] and on tested representations [19] about a shape of energy dependence of the radiative strength functions. Of course, our results (the nuclear parameters obtained simultaneously) have a systematic error connected with inaccuracy of used models, and only by improvement of these models it is possible to decrease the error. A comparison of the results obtained using different modern models would promote a clarification of intranuclear processes.

The other sources of systematic errors of  $\rho(E_{ex})$  and  $\Gamma(E_\gamma)$  functions are limited interval of spins of excited levels for TSCs (this interval is determined by spins of initial and final levels and dipole type of gammas) and incomplete number of energy-resolved transitions considered in the experiment.

#### 4. Results of reanalysis of $4\pi$ -C experiment

To evaluate an influence of all possible errors on a value and a shape of the experimental distribution  $I_{\gamma\gamma}$ , which was obtained for  $^{164}\text{Dy}$  nucleus with a calorimeter [8], we analyzed the Los-Alamos data for  $M=2$  using likelihood method taking into account anti-correlation between required nuclear parameters,  $\rho$  and  $\Gamma$ .

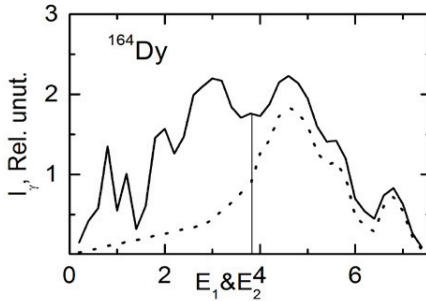


Fig. 2. Intensity distribution  $I_{\gamma\gamma}(E_\gamma)$  of the TSCs in  $^{164}\text{Dy}$ . Solid line – experimental-intensity distribution of all transitions for  $M=2$  from [8]; dashed line – intensity distribution of only primary transitions estimated according to the spectroscopy data from [14].

The shape of  $I_\gamma(E_1)$ -distribution shown in Fig.2 by dashed line was obtained using spectroscopy data from [14]. As we have no experimental and theoretical bases for identification of the parameters (the number of quantum in the cascade, the level life-time) for primary and secondary gamma-transitions in  $4\pi$ -C experiment, we cannot determine the quanta sequence in the framework of our procedure. Nevertheless, evaluating (on a base of the results from [14]) the part of intensity contained mainly primary gamma-transitions and keeping an equality  $I_{\gamma\gamma}(E_1) = I_{\gamma\gamma}(E_2)$  (an area under dash line is equal to a difference of areas under solid line and dash line) we can minimize an error of our analysis of  $4\pi$ -C experiment.

As there are no published values of the intensities for TSC spectra per one decay in [8], so analyzing the experimental spectra of  $4\pi$ -C experiment we made calculations for the intensity  $I_{\gamma\gamma} = 45\%$ , which correspond to the value from Dubna [14] experiment for the same nucleus, and, for a comparison, for an underrated value  $I_{\gamma\gamma} = 22\%$  (see. Fig. 3).

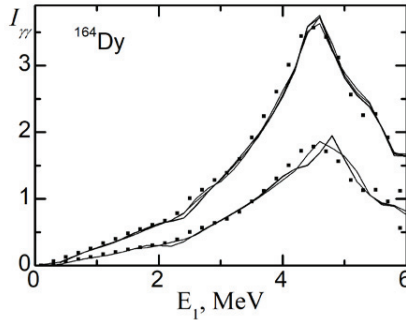


Fig.3. Intensity distributions of part of primary transitions of the TSCs in  $^{164}\text{Dy}$ : upper solid line and points are the best fit and a shape of expected distribution for a sum intensity  $I_{\gamma\gamma}(E_1)=45\%$  per one decay, bottom line and points – the same for  $I_{\gamma\gamma}(E_1)=22\%$  per a decay (the energy bin is 200 keV).

From the experimental two-step gamma-spectra of [8], after its division according to procedure [7] into two parts (of mostly primary or secondary transitions of the cascades), the part of secondary transitions was eliminated (see. Fig. 1).

Results of analysis of the  $4\pi$ -C experiment carried out by our technique are shown in Figs. 3–7, and they distinguish from the data of analysis of our experiment [20] (see Figs. 8, 9). In our reanalysis of  $4\pi$ -C experiment the breaking thresholds of the second and the third Cooper pairs of nucleons in  $^{164}\text{Dy}$  were obtained at the energies of 3.05(6) and 5.0(1) MeV. In Dubna experiment [20] with a capture of thermal neutrons, the breaks of the same pairs are happened at 2.57(1) and 5.48(5) MeV, correspondingly. It is seen in Figs. 3–7 that a difference in the intensities of primary transitions (Fig. 3), which are approximated by strong-correlated functions  $\rho(E_{\text{ex}})$  and  $\Gamma(E_1)$ , has a various influence on the obtained nuclear parameters: a step-wise level-density distribution changes much less (Figs. 4, 5) than an energy dependences of the strength functions of electrical and magnet dipole transitions (Figs. 6, 7).

As just  $\rho(E_{\text{ex}})$ -function has mainly influence on description of the spectrum of the cascades intensity, it seems reasonable to conclude that, without taking into account anti-correlation between the nuclear parameters, approximating data by smooth functions the authors of [8] lose a possibility to discover a dependence of the nuclear parameters on the structure of wave functions of excited levels of nucleus.

Modern theoretical representations both about a co-existence in a nucleus of quasi-particle and vibrational levels [15] and about a fragmentation of states [22] of a certain type at increasing of the excitation energy of nucleus point to a presence of various structure of the wave-functions of excited nuclear levels, which eliminates a smooth energy dependence of the level density and radiative strengths.

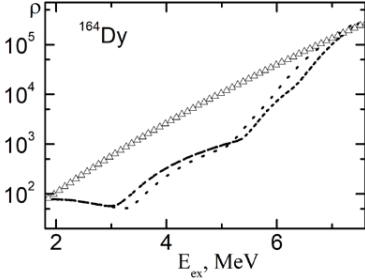


Fig.4. The most probable level density for  $^{164}\text{Dy}$  (spin  $J=2$ ). Lines are different approximations at  $I_{\gamma\gamma}(E_1)=22\%$ . Triangles is a calculation using the model [21].

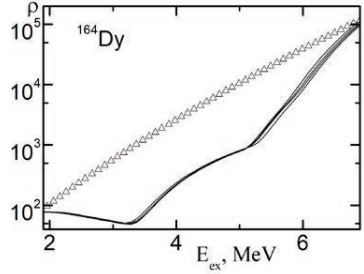


Fig.5. The most probable level density for  $^{164}\text{Dy}$  (spin  $J=2$ ). Lines are different approximations at  $I_{\gamma\gamma}(E_1)=45\%$ . Triangles is a calculation using the model [21].

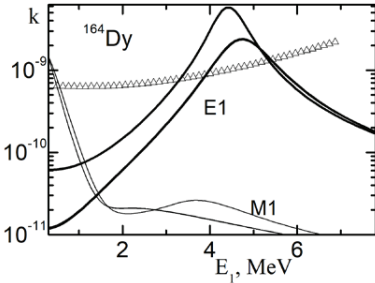


Fig.6. The most probable values of radiative strength functions of  $E1$ - and  $M1$ -transitions for cascades of  $M=2$  in  $^{164}\text{Dy}$  at  $I_{\gamma\gamma}(E_1)=22\%$  (lines). Triangles is a calculation using the model [19] in a sum with  $k(M1)=\text{const}$ .

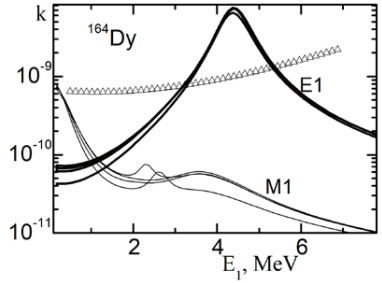


Fig.7. The most probable values of radiative strength functions of  $E1$ - and  $M1$ -transitions for cascades of  $M=2$  in  $^{164}\text{Dy}$  at  $I_{\gamma\gamma}(E_1)=45\%$  (lines). Triangles is a calculation using the model [19] in a sum with  $k(M1)=\text{const}$ .

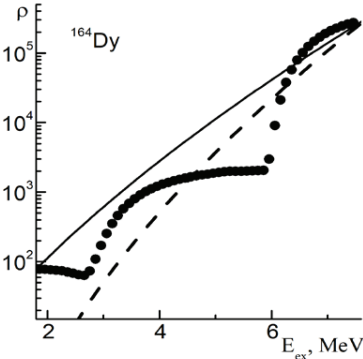


Fig.8. Distribution of  $^{164}\text{Dy}$  level density from our analysis of the data of [20]. Points is the best fit, solid and dotted lines are calculations using the model [21] without taking into account a correction on the shell inhomogeneities and with this correction, correspondingly.

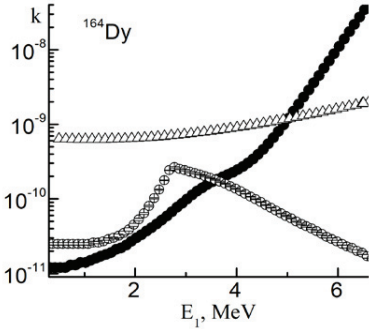


Fig.9. Dependences of the radiative strength functions on the energy of primary transitions of cascades in  $^{164}\text{Dy}$  (analysis of the data of [20]): for  $E1$ -transitions – close points, for  $M1$ -transitions – open points. Triangles is calculation using the model [19] in a sum with  $k(M1)=\text{const}$ .

## 5. Gamma-spectrum simulation

There is good reason to think that in the analysis using a technique with spectra simulation [8], just as in the paper [10] of the same experimenters' group, the criterion was used:

$$\chi^2 = \sum_{i=1}^N \frac{(\bar{A}_{\text{exp}}(E_i) - \bar{A}_{\text{sim}}(E_i))^2}{\varepsilon_{\text{exp}}^2(E_i) + \varepsilon_{\text{sim}}^2(E_i)}, \quad (3)$$

where  $\bar{A}_{\text{exp}}(E_i)$  and  $\bar{A}_{\text{sim}}(E_i)$  are the counts in  $E_i$  energy bin of measured and simulated spectra, and  $\varepsilon_{\text{exp}}^2$  and  $\varepsilon_{\text{sim}}^2$  are corresponding variances. The spectra consisted of  $N$  bins.

When gamma-spectrum simulation using, determining  $\rho(E_{\text{ex}})$  and  $\Gamma(E_1)$  it is necessary to distinguish primary transitions in TSC spectrum which isn't done by the authors in the analysis of  $4\pi\text{-C}$  experiment. Emission widths of second and the followed transitions are unknown in the considered experiment. In the experiment with  $^{164}\text{Dy}$  nucleus presented in [23], the partial widths of secondary transitions were obtained only for decay of 44 levels in excitation-energy region of 1675 – 3984 keV (these data are not considered in the simulation [8]), and the experimental data for the rest levels are absent. Unknown secondary gamma-transitions and the cascades with multiplicity  $M \geq 3$  are useless for a search of the most probable values of the level density and partial widths.

Authors of [8] suppose that energy distribution for the level density is «a priori known», so they attempt to find the radiative strengths  $k$ , which are acceptable for measured gamma-spectrum, calculating  $k$  in simulation under different existent models. But testing of different radiative strength functions makes sense to do only at simultaneous testing of used models for the level density.

## Conclusion

By the technique developed in Dubna it is possible to approximate precisely any experimental gamma-spectrum of TSC intensities by functions  $\rho(E_{\text{ex}})$  and  $\Gamma(E_1)$  parametrized with the help of models of the required nuclear parameters [16–19], without using Porter-Tomas distribution and Axel-Brink hypothesis. In such analysis the nuclear parameters are obtained from the experiment simultaneously. By now the best approximation of the experimental data was obtained with the use of the model of density of  $n$ -quasi-particle levels [16].

The best  $\chi^2$  value from a set of ones obtained solving the system (1) using the Dubna technique guarantees a maximal accuracy of the nuclear parameters extracted in the

experiment if to compare with alone  $\chi^2$  (3) from the model with gamma-spectrum simulation [8].

The step-wise structure which are observed in the obtained energy dependence  $\rho(E_{\text{ex}})$ , at a distance between “steps” in the energy scale of about  $2\Delta$ , where  $\Delta$  is the pairing energy of the last nuclear nucleon, can be explained as points of breaks of the Cooper pairs of nucleons.

Approximation of experimental TSC-intensities using a smooth function  $\rho(E_{\text{ex}})$  postulated by the authors of [8], which excludes step-wise effect, results in appreciable increase in  $\chi^2$ .

Because of an absence of the data of the intensities of individual primary transitions of the cascades for a spectrum of quanta multiplicity of  $M=2$  (and a large number of possible quanta arrangements for cascades with  $M \geq 3$ ), in the considered 4 $\pi$ -C experiment there is no possibility to study intranuclear processes at nuclear excitations as well as to test existing models of the nuclear parameters.

## References

1. V.A. Kravtsov, *Atomic Masses and Nuclear Binding Energies* (Atomizdat, Moscow, 1965) [in Russian].
2. Yu.P. Popov, A.M. Sukhovoij, V.A. Khitrov, Yu.S.Yazvitsky, *Izv. Acad. Nauk SSSR, Ser. Fiz.* **48**, 1830 (1984).
3. S.T. Boneva et al., *Sov. J. Part. Nucl.* **22**, 232 (1991).
4. S.T. Boneva et al., *Sov. J. Part. Nucl.* **22**, 698 (1991).
5. D.C. Vu, A.M. Sukhovoij, L.V. Mitsyna, Sh. Zeinalov, N. Jovancevic, D. Knezevic, M. Krmar, A. Dragic, *Phys. Atom. Nucl.* **80**, 113 (2017).
6. N.A. Nguyen et al., *Phys. Atom. Nucl.* **81**, 296 (2018).
7. S.T. Boneva, A.M. Sukhovoij, V.A. Khitrov, and A.V. Voinov, *Nucl. Phys.* **589**, 293 (1995).
8. S. Valenta et al., *Phys. Rev.* **C96**, 54315 (2017).
9. F. Becvar, *NIM A* **417**, 434 (1998).
10. G. Rusev et al., *Phys. Rev.* **C87**, 054603 (3013).
11. <http://www-nds.iaea.org/ENDSF>
12. <http://www-nds.iaea.org/pgaa/egaf.html>
13. A.M. Sukhovoij and V.A. Khitrov, *Instrum. Exp. Fiz.* **27**, 1017 (1984).
14. E.V. Vasilieva, A.V. Voinov, O.D. Kestarcova, V.D. Kulik, A.M. Sukhovoy, V.A. Khitrov, Yu.V. Kholnov, V.N. Shilin, *Bull. Rus. Acad. Sci. Phys.* **57**, 1758 (1993).
15. *Reference Input Parameter Library RIPL-2, Handbook for calculations of nuclear reaction data*, IAEA-TECDOC (2002).
16. V.M. Strutinsky, in *Proceedings of the International Congress on Nuclear Physics, Paris, France, 1958*, p. 617.
17. V.A. Plujko, O.V. Gorbachenko, E.P. Povenskykh, and V.A. Zheltonzhskii, *Nucl. Data Sheets*, **237** (2014).
18. A.V. Ignatyuk, Report INDC-233(L), IAEA (Vienna, 1985).
19. S.G. Kadomensky, V.P. Markushev, V.I. Furman, *Sov. J. Nucl. Phys.* **37**, 165 (1983).
20. A.M. Sukhovoij, L.V. Mitsyna, N. Jovancevich, *Phys. Atom. Nucl.* **79**, 313 (2016).
21. W. Dilg, W. Schantl, H. Vonach, and M. Uhl, *Nucl. Phys.* **A217**, 269 (1973).
22. L.A. Malov, V.G. Soloviev, *Sov. J. Nucl. Phys.* **26**, 384 (1977).
23. J. Margraf, T. Eckert, M. Rittner, I. Bauske, O. Beck, U. Kneissl, H. Maser, H.H. Pitz, A. Schiller, P. von Brentano *et al.*, *Phys.Rev. C* **52**, 2429 (1995).

# Experimental Study of the Gamma-Decay of Compound-States of $^{56}\text{Mn}$ and $^{94}\text{Nb}$ Nuclei in the $(n_{\text{th}}, 2\gamma)$ -Reaction

Anatoly M. Sukhovej<sup>1</sup>, Liudmila V. Mitsyna<sup>1</sup>, Nikola Jovančević<sup>2</sup>, David Knežević<sup>3</sup>, Aleksandar Dragić<sup>3</sup>, László Szentmiklósi<sup>4</sup>, Tamás Belgya<sup>4</sup>, Zsolt Revay<sup>5</sup>, Christian Stieghorst<sup>5</sup>, Stephan Oberstedt<sup>6</sup>, Miodrag Krmar<sup>2</sup>, Dimitrije Maletić<sup>3</sup>, and Dejan Joković<sup>3</sup>

<sup>1</sup>Joint Institute for Nuclear Research, 141980 Moscow region, Dubna, Russia

<sup>2</sup>University of Novi Sad, Faculty of Science, Department of Physics, Trg Dositeja Obradovica 3, 21000, Novi Sad, Serbia

<sup>3</sup>University of Belgrade, Institute of Physics Belgrade, Pregrevica 118, 11080 Zemun, Serbia

<sup>4</sup>Centre for Energy Research, Hungarian Academy of Sciences, Budapest, Hungary

<sup>5</sup>Technische Universität München, Forschungsneutronenquelle Heinz Maier-Leibnitz (FRM II), Lichtenbergstr.1, D-85747 Garching, Germany

<sup>6</sup>European Commission, Joint Research Centre, Directorate G Nuclear Safety and Security

When the results obtained from the reactions  $^{55}\text{Mn}(n_{\text{th}}, 2\gamma)$  and  $^{93}\text{Nb}(n_{\text{th}}, 2\gamma)$  [1, 2] analyzing, the experimental-data array on the intensities of two-step gamma-cascades (TSC) at a decay of compound-nuclei  $^{56}\text{Mn}$  and  $^{94}\text{Nb}$  after radiative capture of thermal neutrons was enlarged, which already contain the data of for 44 nuclei in mass region  $28 \leq A \leq 200$ . The experimental analysis was carried out with the use of the empirical Dubna model of the cascade gamma-decay, approximating of the  $I_{\gamma\gamma}(E_1)$ -intensities by parametrical functions of the nuclear level density,  $\rho = \phi(p_1, p_2\dots)$ , and partial radiative widths,  $\Gamma = \psi(q_1, q_2\dots)$ , when the most probable nuclear parameters were fitted simultaneously. The Dubna model provides a high precision of experimental-data description.

## 1. Introduction

The basic parameters of any nucleus at a changing of its excitation energy can be determined only if spectra of products of investigated nuclear reactions are experimentally measured. And the spectrum of total gammas at the decay of any high-lying nuclear level (compound-state) is one of the most convenient for the nuclear-parameters extracting. But such spectrum cannot be completely separated into individual  $\gamma$ -transitions because the level density in the absolute majority of nuclei is too high for modern-spectrometers' resolution. Therefore, in spite of an existence of the complete system of equations, which connect the nuclear level density,  $\rho$ , and partial widths,  $\Gamma$ , of the  $\gamma$ -decay of excited nuclear states in each point of the excitation energy,  $E_{\text{ex}}$ ,  $\rho$  and  $\Gamma$  values cannot be calculated exactly. Thus, the nuclear parameters ( $\rho$  and  $\Gamma$  or radiative strength functions  $k = \Gamma / (A^{2/3} \cdot E_{\gamma}^3 \cdot D_{\lambda})$ , where  $A$  is a mass of nucleus,  $D_{\lambda}$  is an average space between its levels, and  $E_{\gamma}$  is an energy of emitted  $\gamma$ -quantum) are always determined from the experiment indirectly.

For indirect experiments, situation is always strongly hindered by a inevitability of large coefficients of transfer of errors of the experimental spectrum to the errors of the

required nuclear parameters – relative errors of extracted  $\rho$  and  $k$  values can be several orders greater than the relative error of measured TSC intensity,  $I_{\gamma\gamma}$ .

For  $\gamma$ -transition identification in the measured total gamma-spectrum, it is necessary to determine the sequence of  $\gamma$ -quanta in the cascade, the excitation energy of nucleus, the number of decaying levels for each interval of excitation energy, etc. In other words, there are too many values, which must be extracted in experiment directly. Because of a deficiency of experimental information, a simultaneous determination of  $\rho$  and  $\Gamma$  values from the experimental data is possible only using different appropriate model representations about  $\rho(E_{\text{ex}})$ - and  $\Gamma(E_{\gamma})$ -functions when different acceptable models of the gamma-process are tested.

One should take into account that the partial widths and nuclear level density are strong anti-correlated values, so they cannot be determined independently. This fact is practically disregarded when the modern models of these parameters are tested. With the regard for this anti-correlation, in the experiment with recording of total-cascades energy (if a difference between the summarized energy of the cascade quanta and the energy of decaying compound-state isn't more than 0.5–1 MeV), the Fermi-gas model of the level density [3] and a representation that a nucleus is a system of non-interactive particles are not apparent for using.

A development of realistic models of a nucleus, as, for example, “generalized model of superfluid nucleus” created in Obninsk [4] and a fact of an existence of a collective-excitation spectrum in any nuclei (with excitations of both vibrational and rotation types) also demand to develop representations about nucleus which would be alternative to the statistical model. First of all, it is need to establish a set of models which take into account the data of modern experiments.

This way was just proposed in Dubna [5, 6, 7], where, for the first time, a possibility was shown to use experimental data on the TSCs of  $\gamma$ -transitions recorded by Ge-detectors for simultaneous obtaining of the gamma-decay parameters. The experiment gives a spectrum of primary transitions, but principally different spectrum of secondary transitions is unknown – only branching coefficients are obtained experimentally.

In order to reduce an absolute anti-correlation between required nuclear parameters,  $\rho$  and  $\Gamma$  (or  $k$ ), in the Dubna analysis we transform the experimental mirror-symmetrical quanta-energy dependences of the TSCs,  $I_{\gamma\gamma}(E_1, E_2)$ , where  $E_1$  and  $E_2$  are energies of primary and secondary quanta of the cascades, to two energy dependencies  $I_{\gamma\gamma}(E_1)$  and  $I_{\gamma\gamma}(E_2)$ . And only the  $I_{\gamma\gamma}(E_1)$  distribution is described with the use of the maximum likelihood method by appropriate parametrized functions  $\rho = \varphi(p_1, p_2, \dots)$  and  $\Gamma = \psi(q_1, q_2, \dots)$  at all excitation energies of nucleus. Fitted parameters  $p$  and  $q$  of the most probable functions  $\rho = \varphi(p_1, p_2, \dots)$  and  $\Gamma = \psi(q_1, q_2, \dots)$  were determined fitting the model description of the cascade intensity  $I_{\gamma\gamma}(E_1)$  to the experimental one. A necessity of description of just the  $I_{\gamma\gamma}(E_1)$ -distribution and a procedure of its separation from the mirror-symmetrical  $I_{\gamma\gamma}(E_1, E_1)$  distribution, which composed of isolated energy-resolved intense gamma-transitions and continuum of unresolved ones with zero average and small dispersion, are described in [8].

The reliable information about the nucleus can be obtained when comparing several model representations. The maximum likelihood method excludes using of Porter-Thomas and Axel-Brink hypothesis. An accuracy of approximation of the experimental distributions of the cascades intensities is determined by a total error of the  $I_{\gamma\gamma}(E_1)$ -distribution and varied shapes of functions  $\rho = \varphi(p_1, p_2, \dots)$  and  $\Gamma = \psi(q_1, q_2, \dots)$ , which are explicitly defined for different ways of iteration process at small variations of  $p$  and  $q$  parameters.

As in coincidence experiments the energies of initial state and of final levels of the cascade are unambiguously defined, it allows a determination (using additional spectroscopic data) of the energies of intermediate levels with a not great systematic error in the energy region near the center of  $I_{\gamma\gamma}(E_1, E_2)$ -distribution, where the energies of primary and secondary transitions are preliminary equal [8]. It means that the use of a technique of decay-scheme constructing [5] gives a possibility to include in analysis all accumulated spectroscopic data [9].

Moreover, a simultaneous determination of the nuclear parameters promotes an understanding of the intranuclear processes. Thanks to the fact that the TSCs connect low-lying weakly-fragmented nuclear levels and high-lying energy region of levels with strong fragmentation, a possibility to study nuclear superfluidity appears. The principal problem for a study of superfluidity in the excited nucleus is a choice of model representations for reliable description of the investigated process. In a majority of the world's experiments, in order to obtain the level density and the partial widths of the products of the nuclear reaction, the models are used which are based on the calculations of different spectra and cross-sections at the large excitation energies [3, 10, 11]. But experiments on many nuclei [12, 13] showed that the intensities of the  $\gamma$ -cascades cannot be exactly described by energy dependences of the nuclear parameters if they are represented with the use of predictions of the conventional models [14]. Most probably, this is because of unremovable difference in the wave-functions structures of excited levels of various nuclei.

## 2. Representation of the nuclear parameters in empirical Dubna model

In order to extract reliable experimental information about a behavior of a superfluid phase of the nuclear matter it is necessary:

- 1) to measure an intensity of gamma-cascades to the low-lying levels of investigated nucleus (both the ground state and a group of levels with small energies);
- 2) to ensure the best description of measured spectra at a simultaneous fitting of the parameters of both the level density and the partial radiative widths.

In the absence of credible theoretical models we created our empirical model, inclusive of the different realistic phenomenological representations, without even generally-accepted representations, which are not tested experimentally.

For the level-density description in the present analysis, the model of density of  $n$ -quasi-particle nuclear excitations [3, 15], which is commonly used in a study of the pre-equilibrium reactions, was parameterized. The density  $\rho_l$  of levels of fermion type above the expected breaking threshold of the  $l$ th Cooper pair of nucleons in nucleus was written as:

$$\rho_l = \frac{(2J+1) \cdot \exp(-(J+1/2)^2 / 2\sigma^2)}{2\sqrt{2\pi}\sigma^3} \Omega_n(E_{ex}),$$

$$\Omega_n(E_{ex}) = \frac{g^n (E_{ex} - U_l)^{n-1}}{((n/2)!)^2 (n-1)!}. \quad (1)$$

Here  $\Omega_n$  is a density of  $n$ -quasi-particle states,  $\sigma$  is a spin cutoff-factor parameter,  $J$  is a spin of the compound-state of nucleus,  $g$  is a density of single-particle states near Fermi-surface, and  $U_l$  is the breaking energy of the  $l$ th Cooper pair of nucleons (or the energy of an excitation of pair of quasi-particles).

For a description of the coefficient  $C_{coll}$  of an increase in a density of collective levels, a phenomenological relation between entropies of phases of the nuclear matter was used [10] with taking into account a cyclical break of Cooper pairs:

$$C_{col} = A_l \exp(\sqrt{(E_{ex} - U_l)/E_u} - (E_{ex} - U_l)/E_u) + \beta. \quad (2)$$

Here  $A_l$  are fitting parameters of vibrational level density above the breaking point of each  $l$ th Cooper pair, parameter  $\beta \geq 0$  can differ from 0 for deformed nuclei. It turned out, that parameter  $E_u$  (a rate of a change in densities of quasi-particle and phonon levels) is practically equal to the average pairing energy of the last nucleon in the majority of investigated nuclei [12, 13, 16].

As was experimentally determined earlier [17], a closest fit to the intensities of the TSCs is possible only if to add one or two peaks to the smooth energy dependence of the radiative strength functions of  $E1$ - and  $M1$ -transitions. The smooth parts of the energy dependences  $k(E1, E_\gamma)$  and  $k(M1, E_\gamma)$  were described just as in the model [11], but with addition fitted parameters of weight  $w_E$  (or  $w_M$ ) and of a change of derivatives of the strength function  $\kappa_E$  (or  $\kappa_M$ ), where indexes  $E$  and  $M$  refer to  $E1$ - or  $M1$ -transitions, correspondingly. And in order to take into account the local peaks, one or two summands were added to the smooth parts of the strength functions. And at a description of the shape of each local peak by the asymmetric Lorentzian curve,  $k(E1, E_\gamma)$  and  $k(M1, E_\gamma)$  strength functions were expressed similarly as:

$$k(E1, E_\gamma) = w_E \frac{\Gamma_{GE}^2 (E_\gamma^2 + \kappa_E 4\pi^2 T_E^2)}{(E_\gamma^2 - E_{GE}^2)^2 + E_{GE}^2 \Gamma_{GE}^2} + \sum_i W_{Ei} \frac{(E_\gamma^2 + (\alpha_{Ei}(E_{Ei} - E_\gamma)/E_\gamma)) \Gamma_{Ei}^2}{(E_\gamma^2 - E_{Ei}^2)^2 + E_\gamma^2 \Gamma_{Ei}^2}, \quad (3)$$

$$k(M1, E_\gamma) = w_M \frac{\Gamma_{GM}^2 (E_\gamma^2 + \kappa_M 4\pi^2 T_M^2)}{(E_\gamma^2 - E_{GM}^2)^2 + E_{GM}^2 \Gamma_{GM}^2} + \sum_i W_{Mi} \frac{(E_\gamma^2 + (\alpha_{Mi}(E_{Mi} - E_\gamma)/E_\gamma)) \Gamma_{Mi}^2}{(E_\gamma^2 - E_{Mi}^2)^2 + E_\gamma^2 \Gamma_{Mi}^2}. \quad (4)$$

Here  $E_{GE}$  (or  $E_{GM}$ ) and  $\Gamma_{GE}$  (or  $\Gamma_{GM}$ ) are location of the center and width of the maximum of the giant dipole resonance,  $T_E$  (or  $T_M$ ) is varied nuclear thermodynamic temperature, for  $E1$ - (or  $M1$ -) transitions. And for each  $i$ th peak ( $i \leq 2$ ) of the strength functions of  $E1$ - (or  $M1$ -) transition:  $E_{Ei}$  (or  $E_{Mi}$ ) is a center position,  $\Gamma_{Ei}$  (or  $\Gamma_{Mi}$ ) – width,  $W_{Ei}$  (or  $W_{Mi}$ ) – amplitude, and  $\alpha_{Ei}$  (or  $\alpha_{Mi}$ )  $\sim T^2$  is an asymmetry parameter. A necessity of taking into account a local-peak asymmetry in the radiative strengths follows from theoretical analysis of features of the fragmentation of single-particle states in the nuclear potential [18]. In the fitting process the functions (3) and (4) vary in wide range of parameters.

The shell inhomogeneties of a single-partial spectrum were also taken into account in our analysis (see detailed description in [10]).

### 3. Analysis of the experimental data

In fig. 1 the spectra of sums of amplitudes of coincident pulses are shown for the cascade gamma-decay of compound-nuclei  $^{56}\text{Mn}$  (left picture) and  $^{94}\text{Nb}$  (right picture). For  $^{56}\text{Mn}$  nucleus, 5 cascades were recorded at  $E_1 + E_2 = 6930, 7057, 7157, 7243,$  and  $7270$  keV. The rest of peaks in this spectrum corresponds to recording of energy sums of primary  $\gamma$ -quanta and third (or fourth, etc.) cascade quanta as well as to recording of primary quanta of the cascades in their single-escape modes. And for  $^{94}\text{Nb}$  compound-nucleus, 7 two-step cascades were recorded with total energies of  $6831, 6916, 7087, 7114, 7168, 7186,$  and  $7227$  keV.

Absolute intensities of all cascades were determined with the use of experimental data from the cites [9, 19] on intense primary gamma-transitions to low-lying levels of investigated nuclei, and branching coefficients for intermediate levels were obtained from experimental data array of collected coincidences. Procedure [20] of resolution improvement of intense cascade gamma-transitions essentially increases an accuracy of determination of their intensities.

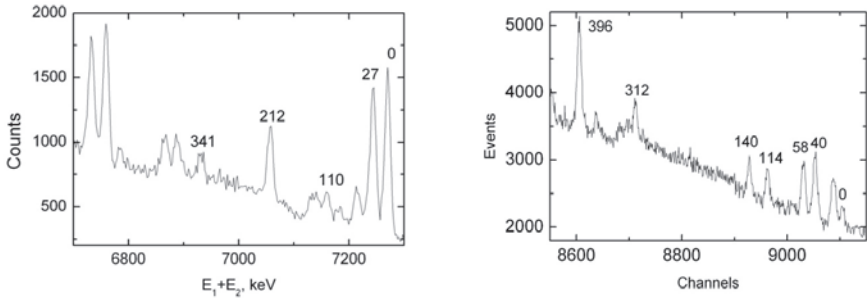


Fig. 1. The spectra of the cascades intensity at radiative capture of thermal neutrons by  $^{55}\text{Mn}$  (left picture) and  $^{93}\text{Nb}$  (right picture) nuclei. Peaks of the full capture of the TSC energy are marked by energies of their final levels.

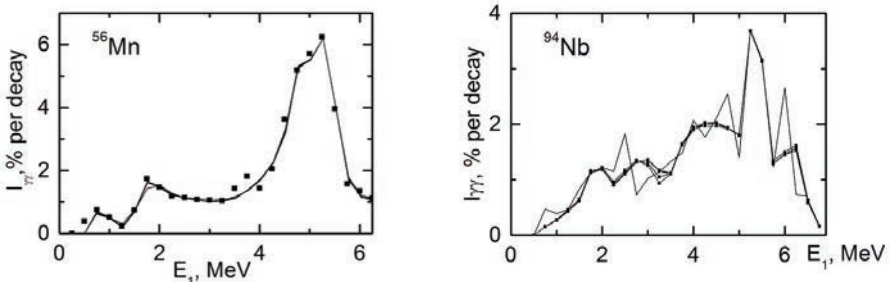


Fig. 2. Intensity distributions for the TSCs to final levels with the energies  $E_f \leq 341$  keV for  $^{56}\text{Mn}$  and  $E_f \leq 396$  keV for  $^{94}\text{Nb}$  as a function of energy of primary transitions. Solid lines – several fits for  $I_{\gamma}(E_1)$  summarized over energy intervals  $\Delta E = 250$  keV.

The total intensity of abovementioned TSCs of  $^{56}\text{Mn}$  is 50.9(18)%, and for  $^{94}\text{Nb}$  nucleus it is 35.2(40)% per a capture. The parts of intense energy-resolved peaks of  $\gamma$ -transitions for the cascades of these nuclei are 0.597 and 0.56.

Error of normalization of the experimental  $I_{\gamma}(E_1)$  spectra are 4% for  $^{56}\text{Mn}$  and 10% for  $^{94}\text{Nb}$  [9]. And in each energy bin of  $I_{\gamma}(E_1)$  distributions, a difference between experimental and approximated values is a few times less. In spite of an uncertainties of the  $I_{\gamma}(E_1)$ -distributions for a majority of nuclear cascades are largish with respect to modern nuclear-data requirements, such accuracy is acceptable for obtaining of the reliable nuclear parameter. An accuracy of bipartition of the total spectrum of the TSC intensity, on spectra of

primary and secondary transitions, increase with increasing in statistics of recorded coincidence events.

As for investigated earlier light spherical nuclei ( $^{40}\text{K}$ ,  $^{52}\text{V}$ ,  $^{60}\text{Co}$ ,  $^{64}\text{Cu}$ ) [13],  $I_{\gamma\gamma}(E_1)$ -distributions for nuclei  $^{56}\text{Mn}$  and  $^{94}\text{Nb}$  decrease at low energies of primary transitions and increase at their bigger energies. Functions  $I_{\gamma\gamma}(E_1)$  for nuclei  $^{56}\text{Mn}$  and  $^{94}\text{Nb}$  have similar general trend and mostly vary from each other in energy region near  $0.5B_n$  due to a difference in the intensities of their cascades there. At the same time, these  $I_{\gamma\gamma}(E_1)$ -distributions nothing like ones for heavy odd-odd nuclei in the energy region of 2–4 MeV [13], i.e. there is a certain factor, which provides a principal difference of the cascade-decay spectra for light and heavy nuclei.

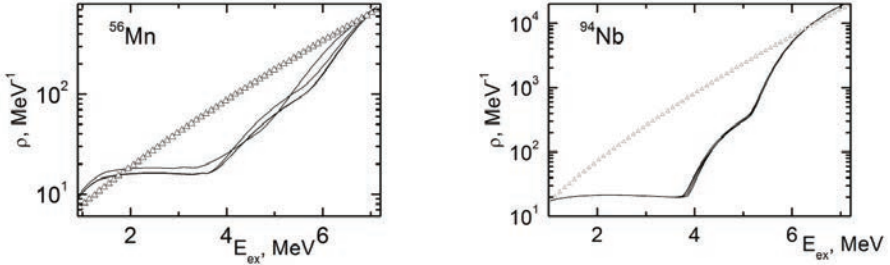


Fig. 3. Dependences of the level densities on the excitation energy of  $^{56}\text{Mn}$  and  $^{94}\text{Nb}$  nuclei. Lines are several fits, triangles are calculations using the back-shift Fermi-gas model [3].

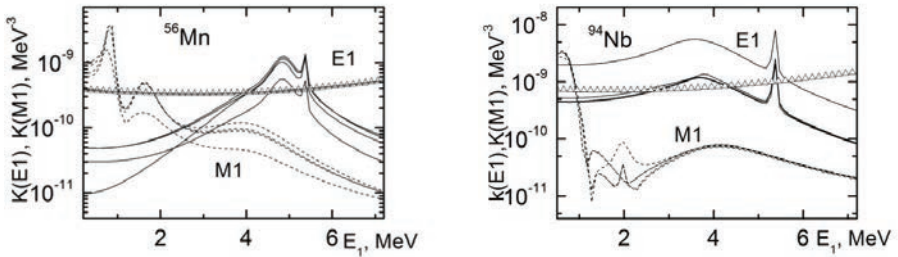


Fig. 4. The radiative strengths as functions of the energies of primary cascade quanta obtained for  $^{56}\text{Mn}$  and  $^{94}\text{Nb}$  nuclei. Solid and dotted lines are the best fits for  $E1$ - and  $M1$ -transitions, correspondingly. Triangles are expected values calculated using the model [11] for electrical transitions in a sum with a constant radiative strength for magnet transitions.

As for all investigated earlier light odd-odd nuclei, in  $^{56}\text{Mn}$  and  $^{94}\text{Nb}$  nuclei the  $\rho(E_{\text{ex}})$ -distributions have the very strong deviations from their calculations using the model of [3] at excitation energies  $E_{\text{ex}} \approx 4$  MeV (for investigated heavy odd-odd nuclei it is at  $E_{\text{ex}} \approx 3$  MeV) [13]. And like the other light odd-odd nuclei, a step-wise behavior of the fitted parametrical  $\rho(E_{\text{ex}})$ -functions was also discovered for  $^{56}\text{Mn}$  and  $^{94}\text{Nb}$  nuclei which can be explained by a decrease of the density of the levels of vibrational type between the breaking thresholds of Cooper pairs of nucleons.

The probable values of  $E1$ - and  $M1$ -radiative strength functions for  $^{56}\text{Mn}$  and  $^{94}\text{Nb}$  nuclei in dependence on the energies of primary transitions of the cascades are presented separately in fig. 4. A noticeable difference in the radiative strengths for  $E1$ - and  $M1$ -transitions for various energies of primary transitions can be qualitatively explained by diverse structures of their wave-functions. An existence of fluctuations (appearance of some sharp deviations) in the best fits of functions  $k(E1)$  and  $k(M1)$  can be explained by residual anti-correlation of these functions with  $\rho(E_{\text{ex}})$ -functions.

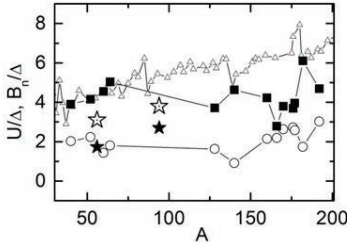


Fig. 5. The breaking thresholds  $U_2$  and  $U_3$  of the second (circles) and the third (squares) Cooper pairs of nucleons obtained for odd-odd nuclei [13]. Black and open stars – obtained in present analysis  $U_2$  and  $U_3$  for  $^{56}\text{Mn}$  and  $^{94}\text{Nb}$ , correspondingly. Triangles – the neutron binding energy in units of pairing energy  $\Delta_0$ .

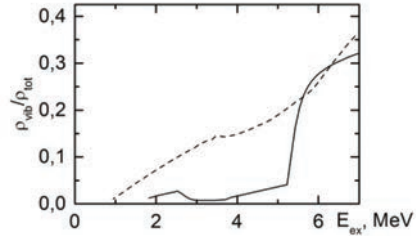


Fig. 6. The ratio of the density of vibrational levels to the total density of nuclear levels in  $^{56}\text{Mn}$  (dashed line) and in  $^{94}\text{Nb}$  (solid line).

The obtained in the analysis ratios  $U_2/\Delta_0$  and  $U_3/\Delta_0$  for  $^{56}\text{Mn}$  and  $^{94}\text{Nb}$  are shown in fig.5 among these ratios for all investigated earlier odd-odd nuclei, and in fig. 6 the ratios  $\rho_{\text{vib}}/\rho_{\text{tot}}$  of the density of vibrational levels to the total density of nuclear levels in  $^{56}\text{Mn}$  and in  $^{94}\text{Nb}$  are also presented. Like the others investigated light odd-odd nuclei ( $^{40}\text{K}$ ,  $^{52}\text{V}$ ,  $^{60}\text{Co}$ ,  $^{64}\text{Cu}$ ), the  $^{56}\text{Mn}$  and  $^{94}\text{Nb}$  nuclei differ from odd-odd heavy and near-magic odd-odd nuclei by a smaller number of Cooper pairs which break below the neutron binding energy. A part of vibrational levels in  $^{56}\text{Mn}$  and  $^{94}\text{Nb}$  nuclei in the region of the neutron binding energy is close to its average [13].

## Conclusion

In the analysis of experimental data on the intensity of the TSCs in  $^{56}\text{Mn}$  and  $^{94}\text{Nb}$  nuclei, any principal difference of the gamma-decay process, which occurs in them and in the others light nuclei ( $^{40}\text{K}$ ,  $^{52}\text{V}$ ,  $^{60}\text{Co}$ ,  $^{64}\text{Cu}$ ) investigated earlier, is not discovered.

The gamma-decay process is really determined by two dipole strength functions. As for all investigated nuclei, quadruple transitions were observed neither in  $^{56}\text{Mn}$  nor in  $^{94}\text{Nb}$ .

A noticeable difference in the radiative strengths for  $E1$ - and  $M1$ -transitions for various energies of primary transitions cannot be described by a model of the strength functions with the same parameters for all investigated nuclei.

The best fits of the level densities contradict completely the representation about an excitations of non-interacted Fermi-particles in nuclear.

The reliable information about the nucleus can be obtained when comparing several model representations of the required nuclear parameters.

## References

1. L. Szentmiklósi, T. Belgya, Z. Révay, Z. Kis, *Journal of Radioanalytical and Nuclear Chemistry* **286** (2), 501 (2010).
2. L. Szentmiklósi, Z. Kasztovszky, T. Belgya, Z. Révay, Z. Kis, B. Maróti, K. Gméling, V. Szilágyi, *Journal of Radioanalytical and Nuclear Chemistry* **309** (1), 71 (2016).
3. W. Dilg, W. Schantl, H. Vonach, and M. Uhl, *Nucl. Phys. A* **217**, 269 (1973).
4. A. V. Ignatyuk, G.N. Smirenkin and A.S. Tishin, *Yad. Fiz.* **21**, 485 (1975).
5. Yu. P. Popov et al., *Izv. Acad. Nauk SSSR, Ser. Fiz.*, **48**, 1830 (1984).
6. S.T. Boneva et al., *Sov. J. Part. Nucl.* **22**, 232 (1991).
7. S.T. Boneva et al., *Sov. J. Part. Nucl.* **22**, 698 (1991).
8. S.T. Boneva, A.M. Sukhovoj, V.A. Khitrov, and A.V. Voinov, *Nucl. Phys.* **589**, 293 (1995).
9. <http://www-nds.iaea.org/ENDSF>.
10. A.V. Ignatyuk, Report INDC-233(L), IAEA (Vienna, 1985).
11. S.G. Kadenskij, V.P. Markushev and W.I. Furman, *Sov. J. Nucl. Phys.* **37**, 165 (1983).
12. A.M. Sukhovoj and L.V. Mitsyna, in *Proceedings of XXII International Seminar on Interaction of Neutrons with Nuclei, Dubna, May 2014*, Preprint № E3-2015-13 (Dubna, 2015), p. 245; <http://isinn.jinr.ru/past-isinns.html>.
13. D.C. Vu et al., *Phys. Atom. Nucl.* **80**, 237 (2017).
14. *RIPL Reference Input Parameter Library RIPL-2, Handbook for calculations of nuclear reaction data*, IAEA-TECDOC (2002).
15. V.M. Strutinsky, in *Proceedings of the International Congress on Nuclear Physics, Paris, France, 1958*, p. 617.
16. A.M. Sukhovoj, L.V. Mitsyna, N. Jovancevich, *Phys. Atom. Nucl.* **79**, 313 (2016).
17. A.M. Sukhovoj, W.I. Furman, V.A. Khitrov, *Phys. Atom. Nucl.* **71**, 982 (2008)
18. L.A. Malov, V.G. Soloviev, *Sov. J. Nucl. Phys.* **26**, 384 (1977).
19. <http://www-nds.iaea.org/EGAF>.
20. A.M. Sukhovoj, V.A. Khitrov, *Instrum. Exp. Tech.*, **27**, 1071 (1984).

# Neutroneum — Applications of the Half-Phenomenological Approach

Yu. L. Ratis

*Institute of Power Engineering for Special Applications, Samara, Russia*

## Abstract

The formalism of the half-phenomenological theory of the exotic electroweak processes is described. The unusual aspects of exonuclear reaction and its application to biophysics are discussed.

## 1. Introduction

The existence of the metastable quasi-bound (unbound) state of the electron and proton (so called neutroneum - neutrinos exoatom) as a result of the underthreshold induced electrons capture in the inelastic  $eu \rightarrow \nu d$  quantum transition was proved in [1].

The aim of this paper is to formulate the adequate half-phenomenological formalism, which one can use to calculate lifetime of the neutroneum and its creation cross-section at the low-energy region and use it to explain the bionucleosynthesis phenomena in the framework of the theory of the exotic electroweak processes and exonuclear reactions.

## 2. Main formalism

The Hamiltonian of the self-consistent neutrino atoms includes weak lepton and weak nucleon currents [1]

$$\begin{cases} j_l^\lambda(\vec{r}, t) = (\bar{\psi}_e(\vec{r})\gamma^\lambda(1 - \gamma_5)\psi_{j,w}^k(\vec{r})) \cdot \exp(-i(\varepsilon_\nu - \varepsilon_e)t) \\ j_N^\mu(\vec{r}, t) = (\bar{\psi}_n(\vec{r})[\tilde{f}_1 + \tilde{g}_1\mathbf{\Upsilon}_5]\mathbf{\Upsilon}^\mu\psi_p(\vec{r})) \cdot \exp(-i(\varepsilon_p - \varepsilon_n)t) \end{cases}, \quad (1)$$

where

$$\psi_{j,w}^k(\vec{r}) = \begin{pmatrix} g_k(r) \chi_{j,w}^k \\ if_{-k}(r) \chi_{j,w}^{-k} \end{pmatrix}, \quad (2)$$

where  $g$  and  $f$  are the Dirac radial wave function (WF) of the discrete spectrum of the leptons. More detail see in [1].

Change the ideology and system of designations of the relativistic quantum theory of the field to the formalism and a conceptual framework used for the description  $\beta$ - processes in the low energies nuclear physics, is as follows.

- 1) Time integration of the Hamiltonian  $\hat{h}_{e+p \rightarrow n+\nu}$  [1] instead of the Hamiltonian

$\hat{h}_{p+e \rightarrow n+\nu}$  leads to change the final expressions for probability of neutroneum decay and creation cross-section reactions. Thus matrix elements for  $p + e \rightarrow n + \nu$  reaction contains  $\delta$ - functions  $\delta(\varepsilon_e + \varepsilon_p - \varepsilon_n - \varepsilon_\nu)$ . It means that the energy conservation law is carried out automatically. In our case  $|in\rangle$  or  $\langle out|$  states designate as neutroneum – the real particle lying on the mass surface. If to treat it as the quasi-bound state of two quasi-particles, than in the energy conservation law

in expressions for probabilities of decay and creation cross-sections appear  $\delta$ -function  $\delta(\varepsilon_e + \varepsilon_p - \varepsilon_{n_\nu})$ .

- 2) The Hamiltonian of creation and decay of the neutroneum is the sum of two Hermite-conjugated terms:

$$h_{e+p \rightarrow n_\nu} = h_{e+p \rightarrow n_\nu} + h_{n_\nu \rightarrow e+p}, \quad (3)$$

where

$$h_{e+p \rightarrow n_\nu} = [h_{n_\nu \rightarrow e+p}]^\dagger. \quad (4)$$

- 3) In the framework of  $\delta$ - forces approximation, traditionally used in the low energies nuclear physics, the Hamiltonian (4) has a form

$$h_{n_\nu \rightarrow e+p} = \frac{G}{\sqrt{2}} \gamma_\lambda (1 - \gamma_5) [(\vec{f}_1 + \vec{g}_1 \boldsymbol{\gamma}_5) \boldsymbol{\gamma}^\lambda]^\dagger \tau_+ \delta(\vec{r}_\nu - \vec{r}_n) \delta(\vec{r}_e - \vec{r}_p) \delta(\vec{r}_p - \vec{r}_n). \quad (5)$$

The isospin operators  $\tau_\pm$  are defined by ratios

$$\begin{cases} \tau_+ = (\tau_1 + i\tau_2) / 2 = -\tau_{+1} / \sqrt{2} \\ \tau_- = (\tau_1 - i\tau_2) / 2 = \tau_{-1} / \sqrt{2} \end{cases} \Rightarrow \begin{cases} \tau_+ \chi_{1/2} = 0; \tau_+ \chi_{-1/2} = \chi_{1/2} \\ \tau_- \chi_{-1/2} = 0; \tau_- \chi_{1/2} = \chi_{-1/2} \end{cases}, \quad (6)$$

where  $\chi_{1/2}(\vec{T})$  ( $\chi_{-1/2}(\vec{T})$ ) - isospin WF of a proton (quasi-neutron), and operators  $\tau_\pm$  are expressed through Pauli matrixes  $\tau_1$  and  $\tau_2$  ( $\tau_{+1}, \tau_{-1}$ ) [2].

- 4) The states  $|in\rangle$ , and  $|out\rangle$  for a Hamiltonian (5) are:

$$\begin{cases} |in\rangle = |n_\nu\rangle = \sum_{\substack{m_n, m_\nu \\ m_p, m_e}} C_{1/2 m_n, 1/2 m_\nu}^{j_{n_\nu} m_{n_\nu}} |\hat{p}_e\rangle \otimes |\hat{n}\rangle \\ |out\rangle = |H^*\rangle = |e\rangle \otimes |p\rangle \end{cases}, \quad (7)$$

where  $|\hat{p}_e\rangle$  and  $|\hat{n}\rangle$ - WF of a quasi-neutrino and quasi-neutron, respectively. Further "hat"  $\hat{\ } over WF we omit as it cannot result in ambiguity of interpretation of the text. Neutroneum has whole spin  $j_{n_\nu} = 0$  or  $j_{n_\nu} = 1$ , i.e. is a boson.$

- 5) In a coordinate representation the lepton WF-s are

$$\begin{cases} \psi_e(\vec{r}_e) = \frac{1}{\sqrt{V}} \cdot \exp(i\vec{k}_e \vec{r}_e) u_e(\vec{k}_e) \\ \psi_\nu(\vec{r}) = \begin{pmatrix} g_k(r) \chi_{jm_j}^k \\ if_{-k}(r) \chi_{jm_j}^{-k} \end{pmatrix} \end{cases}, \quad (8)$$

and nucleon WF-s are

$$\begin{cases} \psi_p(\vec{r}_p) = V^{-1/2} \cdot \exp(i\vec{k}_p \vec{r}_p) u_p(\vec{k}_p) \chi_{1/2}(\vec{T}) \\ \psi_n(\vec{r}_n) = V^{-1/2} \cdot \exp(i\vec{k}_n \vec{r}_n) u_n(\vec{k}_n) \chi_{-1/2}(\vec{T}) \end{cases}. \quad (9)$$

- 6) The Dirac - conjugated electron WF in matrix elements (ME) of  $n_\nu \rightarrow e + p$  - transition is

$$\bar{\psi}_e(\vec{r}_e) = V^{-1/2} \cdot [\exp(i\vec{k}_e \vec{r}_e) u_e(\vec{k}_e)]^\dagger \gamma^0. \quad (10)$$

- 7) The nonrelativistic limit in the nucleon's space is reduced to neglecting small components of bispinor  $u(\vec{k})$ . At the same time bispinor  $u(\vec{k})$  are replaced with Pauli spinor  $\chi$ :

$$u(\vec{k}) \rightarrow \chi_m(\vec{s}), \quad (11)$$

where  $\vec{s}$  - spin of the corresponding nucleon, and  $m$  - projection of the spin.

- 8) At substitution (11) Dirac matrix  $\gamma^0$  it is replaced by the Pauli matrix  $\sigma_0 = 1$ , and Dirac matrix  $\vec{\gamma}$  are replaced by the Pauli matrixes  $\vec{\sigma}$ .

Isospin ME of a Hamiltonian (5) is

$$M_{isospin} \equiv \left\langle out \left| h_{n_e \rightarrow e+p} \right| in \right\rangle_{isospin} = \left\langle \chi_{1/2}(\vec{T}) \left| \tau_+ \right| \chi_{-1/2}(\vec{T}) \right\rangle = 1. \quad (12)$$

Spatial ME of the Hamiltonian (5) is equal

$$M_{space} = V^{-3/2} \cdot \int d\vec{r}_e d\vec{r}_p d\vec{r}_\nu d\vec{r}_n e^{-ik_e \vec{r}_e - ik_p \vec{r}_p + ik_n \vec{r}_n + ik_\nu \vec{r}_\nu} \times \\ \times \delta(\vec{r}_\nu - \vec{r}_n) \delta(\vec{r}_e - \vec{r}_p) \delta(\vec{r}_p - \vec{r}_n) b_\lambda(\vec{r}_\nu - \vec{r}_n). \quad (13)$$

The value of radius  $\vec{r} = \vec{r}_\nu - \vec{r}_n = 0$  in (13) is fixed by translation invariance of the Hamiltonian (5). It allows us to get the general multiplier in spatial ME  $(2\pi)^3 \delta(\vec{k}_{n_\nu} - \vec{k}_e - \vec{k}_p)$ :

$$M_{space} = V^{-3/2} \cdot (2\pi)^3 \delta(\vec{k}_{n_\nu} - \vec{k}_e - \vec{k}_p) b_\lambda(\vec{r} \approx 0), \quad (14)$$

where  $\vec{k}_{n_\nu} = \vec{k}_n + \vec{k}_\nu$ . At the same time momentum conservation law, and  $\vec{r}$  - dependence of  $b_\lambda(\vec{r})$  is absent; ME  $b_\lambda$  depend only on the spin projections of an electron and a quasi-neutrino.

The components of 4- vector of spin ME  $b_\lambda$  in the lepton sector are:

$$\left\langle out \left| (h_{n_e \rightarrow e+p})_\lambda^l \right| in \right\rangle_{spin} \equiv b_\lambda(\underline{m}_e, \underline{m}_\nu) = (\bar{u}_e \gamma_\lambda (1 - \gamma_5) u_\nu), \quad (15)$$

where  $\underline{m}_e, \underline{m}_\nu$  - are the electron and neutrino spin projections. These ME in cyclic basis at the low energies limit are equal

$$\left\{ \begin{aligned} b_0(\underline{m}_e, \underline{m}_\nu) &\approx g_{-1}(r_N) (4\pi)^{-1/2} \delta_{\underline{m}_e \underline{m}_\nu} - if_1(r_N) \sum_{m_1} C_{1m_1, 1/2 \underline{m}_e}^{1/2 \underline{m}_\nu} Y_{1m_1}(\vartheta, \varphi) \\ b_k(\underline{m}_e, \underline{m}_\nu) &\approx \sqrt{3} \left[ g_{-1}(r_N) (4\pi)^{-1/2} C_{1k, 1/2 \underline{m}_e}^{1/2 \underline{m}_\nu} - if_1(r_N) \sum_{m_1, \sigma} C_{1m_1, 1/2 \sigma}^{1/2 \underline{m}_e} C_{1k, 1/2 \sigma}^{1/2 \underline{m}_\nu} Y_{1m_1}(\vartheta, \varphi) \right], \end{aligned} \right. \quad (16)$$

where  $\underline{m}_p, \underline{m}_n$  - are the proton and quasi- neutron spin projections, channel radius  $r_N \approx 0.86 \text{ fm}$ . The components of the spin ME in the nucleons space are similar:

$$\left\langle out \left| (h_{n_e \rightarrow e+p})_\lambda^N \right| in \right\rangle_{spin} \equiv d^\lambda(\underline{m}_p, \underline{m}_n). \quad (17)$$

The full transition  $n_e \rightarrow e + p$  ME in the spin space is the linear combination of scalar products of the two 4- vectors

$$M_{spin} = \sum_{\underline{m}_p, \underline{m}_n} C_{1/2 \underline{m}_p, 1/2 \underline{m}_n}^{j_{n_e} \underline{m}_{n_e}} b_\lambda(\underline{m}_e, \underline{m}_\nu) \cdot d^\lambda(\underline{m}_p, \underline{m}_n). \quad (18)$$

As a result we receive ME of the Hamiltonian (5):

$$\langle out | \hat{h}_{n_e \rightarrow e+p} | in \rangle = \frac{\hat{G}_\beta}{\sqrt{2}} \cdot V^{-3/2} \cdot (2\pi)^3 \delta(\vec{k}_{n_\nu} - \vec{k}_e - \vec{k}_p) \cdot M_{spin}, \quad (19)$$

where  $G_\beta = f_1 G$  ( $G_\beta$  - constant for nuclear  $\beta$  - processes), and spin ME is equal

$$M_{spin} = \sum_{m_n, m_p} C_{1/2 m_n, 1/2 m_p}^{j_{n_\nu}, m_{n_\nu}} \langle \chi_{m_p} | b_0(\vec{m}_e, \vec{m}_\nu) + \lambda \cdot (\vec{b}(\vec{m}_e, \vec{m}_\nu) \cdot \vec{\sigma}) | \chi_{m_n} \rangle, \quad (20)$$

where  $\lambda = g_1 / f_1 \approx 1.23$ .

### 3. Biophysics

The nuclear transmutation in biological systems was discovered by C.L. Kervran [4]. He investigated the potassium transmutation into calcium in the biological system containing hydrogen (see fig. 1). For more details and references see [5].

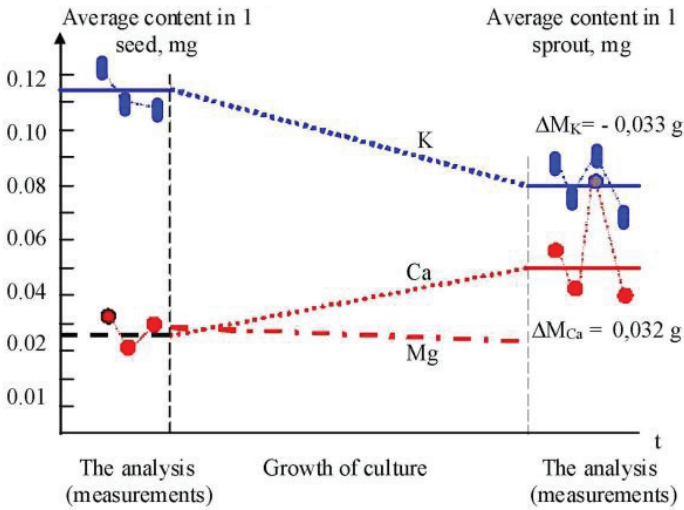


**Fig. 1.** The left and the right parts of figure show the measurement results by three series and average results. There are the decrease of potassium  $K$  and the increase of calcium  $Ca$  ( $\Delta M_{Ca} = 0.032$  g) [4].

Evidently that exonuclear reactions in the biological objects takes place only in the presence of the heavy water ( $D_2O$ ) because of the extremely low threshold of the reaction



where symbol  $D_\nu$  designates the dineutroneum (the bound state of the neutron and neutroneum). The charge conservation law is valid according to  ${}^2_1H$  and  $D_\nu$  in (21) are the

neutral atoms [1]. The threshold of the reaction (21) is about 0.1 eV and abundance of the deuterium ( $a \sim 1.5 \cdot 10^{-4}$ ) is enough to realize Kervran's reaction.

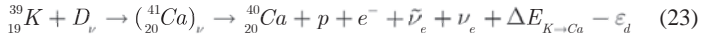
Thus the exit channel of the simplest exonuclear reaction with dineutroneum and carbon is open



This result says: we need to check out our knowledge on the radiocarbon analysis.

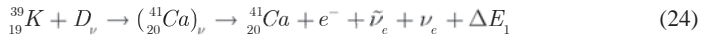
Let's consider another extremely interesting example – so-called radio-calcium analysis.

One of the more probable reactions inside the cells is



with the free proton in the continuous spectrum. According to (21) transformation deuteron – dineutroneum is possible and reaction (23) is not forbidden.

Alternative reaction is



with proton bound in calcium. The branching ratio for the reaction (23) and (24) is

$${}^{39}_{19}K + D_\nu \rightarrow ({}^{41}_{20}Ca)_\nu \rightarrow \left\{ \frac{{}^{40}_{20}Ca + p + e^- + \tilde{\nu}_e + \nu_e}{{}^{41}_{20}Ca + e^- + \tilde{\nu}_e + \nu_e} \right\} \approx 1.4 \cdot 10^5. \quad (25)$$

The nucleus  ${}^{41}_{20}Ca$  is unstable. As a result the comparison of the calcium isotope abundances from the reactions (23) and (24) in the ancient bones permits one to find the age of the bones. This fact could be extremely useful for archeologists.

Hypothetical reactions (22)-(24) are supported by the data of A.A. Kornilova [5]. In the works of the Kornilova's group the hypothetical reaction in the biological objects



was investigated. Isotope barium-137 was found.

But we have to remember, that

$$\varepsilon_b({}^{137}_{55}Cs) = 1149.286072 \text{ MeV}; \quad \varepsilon_b({}^{137}_{56}Ba) = 1149.680299 \text{ MeV}. \quad (27)$$

As a result

$$\varepsilon_b({}^{137}_{56}Ba) - \varepsilon_b({}^{137}_{55}Cs) < m_n - m_p = 1.3 \text{ MeV} \quad (28)$$

and charge-exchange reaction (26) forbidden, i.e. reaction (26) has the threshold. Thus we have to search alternative mechanisms of nuclear reactions in the living cells (see (22) – (24)).

#### 4. Conclusion

- The early lifetime calculation [3] for the neutroneum was essentially improved.
- The short description of the formalism [1] may be useful as a base of the theory of bionucleosynthesis.
- The new explanation of the calcium method of the age measurements in the archeology is given.
- New and very promising mechanism of the radiocarbon synthesis is proposed.
- We can consider the results of this paper as a way to explain the dominance of the abundance of the odd-odd isotope  ${}^{14}_7N$  in Nature instead of odd-even isotope  ${}^{15}_7N$ .

### **Acknowledgments**

I would thank S.G. Kadmsky, V.I. Furman and A.V. Strelkov for many fruitful discussions and L.S. Yaguzhinsky for his proposal to use this formalism in biophysics.

### **References**

1. Ratis Yu.L. *Neutrino's atom "neutroneum". Hypothesis or reality?* Applied physics and mathematics (rus), 2017. No. 1. page 28-73.
2. Varshalovich D.A., Moskalyov A.N., Khersonsky V.K., *Quantum theory of angular momentum.* (Science, Leningrad, 1975), 439 pages.
3. Ratis Yu.L. *Controlled thermonuclear synthesis or cold fusion? Drama of ideas.* (SSC RAS, Samara, 2009), 92 pages.
4. Kervran C.L. *Biological transmutations,* Happiness press, USA (Magalia, California, 1999).
5. Vysotskii V.I., Kornilova A.A. *Nuclear fusion and transmutation of isotopes in biological systems,* M.: MIR, 2003, 161 p.

# **Neutron Induced Reactions**

# Statistical Model Analysis of (n,t) Cross Sections for 14–15 MeV Neutrons

G. Khuukhenkhuu, J. Munkhsaikhan, M. Odsuren, Ch. Saikhanbayar,  
and B. Batchimeg

*Nuclear Research Center, National University of Mongolia, Ulaanbaatar, Mongolia*

Yu.M. Gledenov, E. Sansarbayar, and M.V. Sedysheva

*Frank Laboratory of Neutron Physics, JINR, Dubna, Russia*

## 1. Introduction

Fast neutron induced (n,t) reaction data analysis is of important for nuclear reaction study and fusion reactor technology, particularly to evaluate three nucleons clustering effect and enhancing tritium in the structural materials. However, experimental data base of the (n,t) reaction is very scarce due to small cross sections and their available values for the same isotopes are varied in the wide range. So, theoretical model calculations and systematical analysis of available data are useful to estimate unmeasured (n,t) cross sections and to conclude which value is a probably correct.

A few attempts of compilation, systematical analysis and evaluation for the (n,t) cross sections were carried out using different approaches [1–10] and some systematical regularities were observed. But, the results of these studies are not consistent and up to now a common explanation of the observed regularities are not available.

In past years we have been analyzing the (n, $\alpha$ ) and (n,p) cross sections for fast neutrons using a unified method, namely the statistical model, and some regular behaviours in known experimental data were observed [11–14] for wide energy range of 2 to 20 MeV. Moreover, in the framework of the statistical model, alpha clustering factors (or probabilities) for slow and fast neutron induced (n, $\alpha$ ) reactions were obtained [13,14].

In this work we carried out a systematical analysis of known (n,t) cross sections around 14–15 MeV neutrons using the statistical model and determined the triton clustering factor.

## 2. Theoretical background

In the framework of the statistical model based upon Bohr's assumption of compound mechanism the (n,t) cross section can be expressed as following:

$$\sigma(n,t) = \sigma_c(n)G(t). \quad (1)$$

Here:

$$\sigma_c(n) = \pi(R + \tilde{\lambda}_n)^2 \quad (2)$$

is the compound nucleus formation cross section, where  $R = r_0 A^{1/3}$  is the target nucleus radius,  $r_0 = 1.3 \cdot 10^{-13}$  cm and  $A$  is target nucleus mass number;

$$\tilde{\lambda}_n = \frac{4.55 \cdot 10^{-13}}{\sqrt{E_n(\text{MeV})}} (\text{cm}) \quad (3)$$

is the wavelength of the incident neutrons divided by  $2\pi$ , where  $E_n$  is the neutron energy. The triton decay probability of the compound nucleus is given by

$$G(t) = \frac{\Gamma_t}{\Gamma} = \sum_i \frac{\Gamma_t}{\Gamma_i}, \quad (4)$$

where  $\Gamma_t$  and  $\Gamma$  are the triton and total level widths.

Using the detailed balancing principle and Weisskopf-Ewing's evaporation model [15,16] the triton width of level,  $\Gamma_t$ , is determined as following:

$$\Gamma_t = \frac{2S_t + 1}{\pi^2 \hbar^2 \rho_c(E_c)} M_t \int_{V_t}^{E_t^{\max}} E_t \sigma_c(E_t) \rho_y(U_t) \rho_y(U_t) dE_t. \quad (5)$$

Here:  $S_t$ ,  $M_t$ ,  $E_t$ , and  $V_t$  are the spin, mass, energy and the Coulomb potential energy for the outgoing triton, respectively;  $\rho_c(E_c)$  and  $\rho_y(U_t)$  are the level densities of the compound and residual nuclei, respectively;  $U_t$  is the excitation energy of the residual nuclei;  $\sigma_c(E_t)$  is the inverse reaction cross section which is determined in the semiclassical approximation [16] as follows:

$$\sigma_c(E_t) = \begin{cases} \pi R^2 \left(1 - \frac{V_t}{E_t}\right) & \text{for } E_t > V_t \\ 0 & \text{for } E_t < V_t \end{cases}. \quad (6)$$

Using the nuclear entropy [17] and constant temperature approximation [16] we can get from (1), (2) and (4)–(6) the following simple formula for fast neutron induced (n,t) reaction cross section:

$$\sigma_{(n,t)} = \pi (R + \lambda_n)^2 \frac{2S_t + 1}{2S_n + 1} \cdot \frac{M_t}{M_n} e^{-\frac{Q_m - V_t}{\theta}}. \quad (7)$$

The (n,t) reaction energy,  $Q_m$ , can be obtained using Weizsäcker's formula [18] for binding energy as:

$$Q_m = -\alpha A + \alpha(A-2) + \beta \left[ A^{2/3} - (A-2)^{2/3} \right] + \gamma \left[ \frac{Z^2}{A^{1/3}} - \frac{(Z-1)^2}{(A-2)^{1/3}} \right] + \xi \left\{ \frac{(A-2Z)^2}{A} - \frac{[(A-2)-2(Z-1)]^2}{A-2} \right\} \pm \left[ \frac{\delta_f}{(A-2)^{3/4}} - \frac{\delta_t}{A^{3/4}} \right] + \varepsilon_t. \quad (8)$$

Here:  $\varepsilon_t = 8.48$  MeV is the internal binding energy of triton;  $\alpha = 15.7$  MeV,  $\beta = 17.8$  MeV,  $\gamma = 0.71$  MeV,  $\xi = 23.7$  MeV and  $|\delta| = 34$  MeV or 0 are the Weizsäcker's constants;  $Z$  is the proton number. For medium mass and heavy nuclei approximation  $A \gg 2$  can be used. Then, the reaction energy is found from (8) as follows:

$$Q_m = \gamma \frac{2Z-1}{A^{1/3}} - 4\xi \frac{N-Z+1}{A} + \varepsilon_t. \quad (9)$$

The Coulomb potential energy of triton can be written [19] in the form:

$$V_i = 1.029 \frac{(Z-1)}{A^{1/3} + 3^{1/3}}. \quad (10)$$

If we use Fermi gas model for level density parameter [20], the nuclear thermodynamic temperature [13] is expressed as:

$$\Theta = \sqrt{\frac{13.5(E_n + Q_m)}{A}}. \quad (11)$$

So, from (7), (9) and (10) the (n,t) cross section can be obtained as follows:

$$\sigma(n,t) = C\pi(R + \lambda_n)^2 e^{-\frac{K(N-Z+1)}{A}}, \quad (12)$$

where:  $N$  is the neutron number of the target nucleus; The parameters  $C$  and  $K$  are expressed as follows:

$$C = 3 \exp \left\{ \frac{\gamma \frac{2Z-1}{A^{1/3}} + \varepsilon_i - 1.029 \frac{(Z-1)}{A^{1/3} + 3^{1/3}}}{\Theta} \right\} \quad (13)$$

and

$$K = \frac{4\varepsilon}{\Theta}. \quad (14)$$

Here the thermodynamic temperature,  $\theta$ , is determined by formula (11) and reaction energy,  $Q_m$ , is obtained by expression (9). The parameters  $C$  and  $K$  can be, also, obtained by fitting of theoretical (n,t) cross sections to experimental data as constants for all isotopes. Formulas (7) and (11)–(14) are used in the systematical analysis of the fast neutron induced (n,t) cross sections.

### 3. Results and Discussion

From formula (12) can be found a reduced (n,t) cross section as:

$$\frac{\sigma(n,t)}{\pi(R + \lambda_n)^2} = C e^{-\frac{K(N-Z+1)}{A}}. \quad (15)$$

The dependence of the reduced (n,t) cross sections on the relative neutron excess parameter  $(N-Z+1)/A$  in the target nuclei, for which experimental data are available, is shown in Fig.1. Some regular dependence of the reduced (n,t) cross sections on the parameter  $(N-Z+1)/A$  is seen from Fig.1 except light nuclei with mass number  $A=6-18$  which perhaps have a cluster structure and strong resonances in the cross sections. Systematical behaviour of the reduced (n,t) cross sections for odd-even and even-even nuclei are separately and satisfactorily described by formula (15) with fitting parameters  $C$  and  $K$  which are given in Fig.1, also. Using the approximation  $A \gg 2$ , the absolute value of the (n,t) cross section can be obtained by formulae (11)–(14). Results of such calculations in comparison with experimental data for odd-even and even-even nuclei are shown in Fig.2.

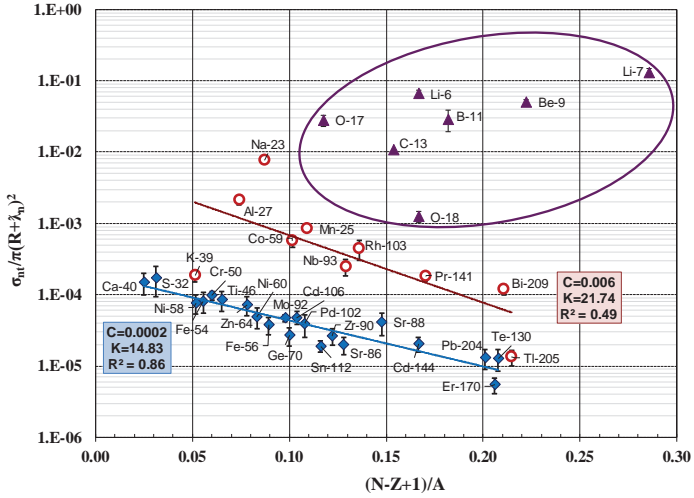


Fig.1. Experimental data for the reduced (n,t) cross sections:  
 ▲ -light nuclei; ○ -odd-even nuclei; ◆ -even-even nuclei.

Theoretical lines were drawn by formula (15) with fitted parameters C and K.

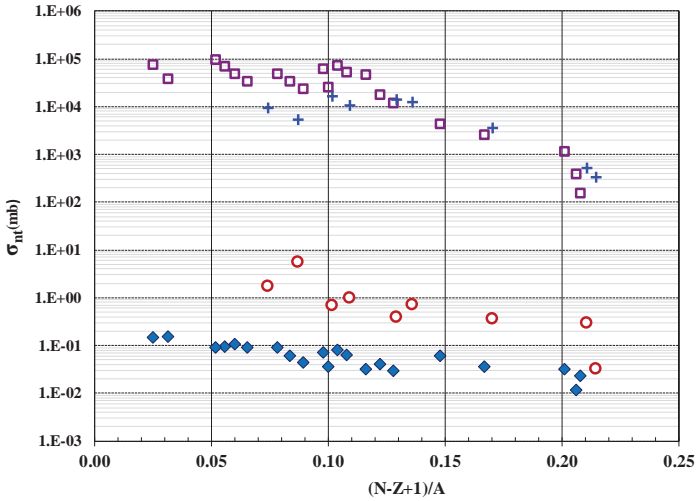


Fig.2. Experimental data and calculated by formulae (11)–(14) (n,t) cross sections:  
 □ and + -theoretical cross sections for even-even and odd-even nuclei, respectively;  
 ◆ and ○ -experimental data for even-even and odd-even nuclei without  $^{39}\text{K}$ , respectively;

It is seen from Fig.2 that the statistical model formulas give overestimated values of the (n,t) cross sections for fast neutrons. We assume that this fact is probably caused by three nucleons (or triton) clustering effect that is not considered in the above deduced formulae.

So, the triton clustering factor (or probability), by analogy with the spectroscopic factor [21] and alpha-clustering probability [13,22], can be obtained as a ratio of experimental (n,t) cross sections to theoretical ones as:

$$\phi_t = \frac{\sigma_{(n,t)}^{\text{exp}}}{\sigma_{(n,t)}^{\text{theor}}} \quad (16)$$

Results of such calculations are given in Fig.3.

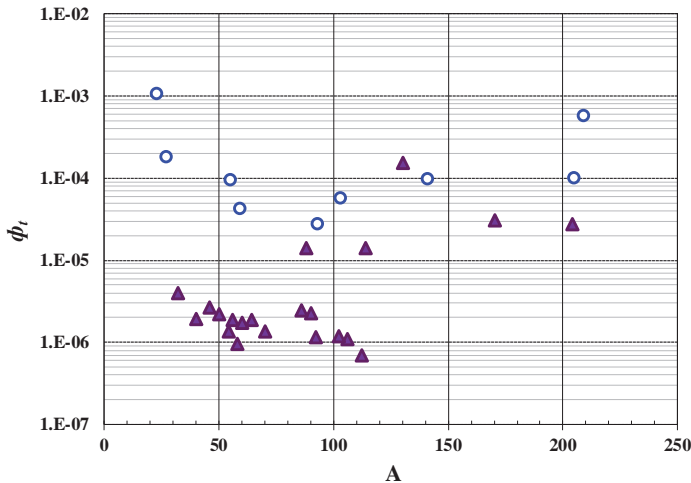


Fig.3. The triton clustering factor versus mass number of target nuclei:  
 ▲-even-even nuclei and ○-odd-even nuclei.

It is seen from Fig.3 that the triton clustering factors for even-even nuclei are on average lower by factor around 10–100 than ones for odd-even nuclei.

The values of the triton clustering factor ( $\phi_t \approx 10^{-3} - 10^{-6}$ ) obtained in this work are much lower than  $\alpha$ -clustering (four nucleons) probability ( $\phi_r \approx 0.28$ ) for 14.5 MeV neutrons determined by the same method in our previous work [10].

#### 4. Conclusions

1. Simple formulae for systematical analysis of the fast neutron induced (n,t) reaction cross sections were deduced using the statistical model.
2. The systematical analysis of known (n,t) cross sections for 14–15 MeV neutrons shows that general regularity of experimental data for medium mass and heavy nuclei are satisfactorily described by the statistical model which, however, gives overestimated values for absolute (n,t) cross sections. We assume that this fact is, probably, caused by three nucleons (triton) clustering effect which was not considered in the above mentioned approach.

3. The triton clustering factor (or probability) was obtained, by analogy with the spectroscopic factor, as a ratio of experimental (n,t) cross sections to theoretical ones.
4. The values of the triton clustering factor ( $\phi_t \approx 10^{-3} - 10^{-6}$ ) obtained in this work are much lower than  $\alpha$ -clustering probability ( $\phi_t \approx 0.28$ ) for 14.5 MeV neutrons determined by the same method in our previous work.

## 5. Acknowledgement

The present work was performed in the framework of the project “Nuclear Cluster Structure and Reaction Study” supported by the Mongolian Science and Technology Foundation (Contract: No.ShuSs-2019/6).

## REFERENCES

1. S.M. Qaim and G. Stöcklin, Nucl. Phys., v.**257A**, 1976, p.233.
2. Z.T. Bödy and K. Mihaly. In book: Neutron Physics (Proceedings of the 6-th All Union Conference on Neutron Physics, October 2–6, 1983, Kiev), v.**3**, Moscow, 1984, p.245 (in Russian).
3. Z.T. Bödy *et al.*, Proceedings of the International Conference on Nuclear Data for Science and Technology, Sept.6–10, 1982, Antwerp, Brussels and Luxemburg, 1983, p.368.
4. Z.T. Bödy and K. Mihaly. Report IAEA, INDC(HUN)-22/L, Vienna, 1985.
5. Yao Lishan, Communication of Nuclear Data Progress, China Nuclear Information Center. No.7, 1992, p.85.
6. A.Yu. Konobeyev, Yu.A. Korovin and P.E. Pereslavl'tsev, Communication of Higher Schools: Nuclear Power Engineering, No.1, 1993, p.70 (in Russian).
7. A.Yu. Konobeyev, Yu.A. Korovin and P.E. Pereslavl'tsev, Nucl. Instr. Meth. in Phys. Res., v.**93B**, 1994, p.409.
8. M. Belgaid, T. Segueni, F. Kadem and M. Asghar, Nucl. Instr. Meth. in Phys. Res., v.**201B**, 2003, p.545.
9. E. Tel, A. Aydin, A. Kaplan and B. Sarer, J. Fusion Energy, v.**27**, 2008, p.188.
10. E. Tel *et al.*, J. Fusion Energy, v.**28**, 2009, p.377.
11. G. Khuukhenkhuu *et al.*, Communication of the JINR, E3-2007-25, Dubna, 2007.
12. G. Khuukhenkhuu *et al.*, Physics of Elementary Particles and Atomic Nuclei, Letters, v.**11**, No.6 (190), 2014, p.1159.
13. G. Khuukhenkhuu *et al.*, Proceedings of the XXIV International Seminar on Interaction of Neutrons with Nuclei, JINR, Dubna, 2017, p.166.
14. G. Khuukhenkhuu *et al.*, Acta Phys. Pol., v.**49B**, No.3, 2018, p.325.
15. V.F. Weisskopf and D.H. Ewing, Phys. Rev., v.**57**, No.6, 1940, p.472.
16. J.M. Blatt and V.F. Weisskopf, Theoretical Nuclear Physics, John Wiley and Sons, New York, 1952.
17. L.D. Landau and Ya. Smorodinsky, Lectures on Nuclear Theory, Translated from Russian, Plenum Press, Inc., New York, 1959.
18. C.F. Weizsäcker, Z. Phys., v.**96A**, No.7–8, 1935, p.431.
19. D.G. Gardner and S. Rosenblum, Nucl. Phys., v.**96A**, No.1, 1967, p.121.
20. A. Bohr and B.R. Mottelson, Nuclear Structure, W.A. Benjamin Inc., New York, Amsterdam, 1969.
21. L. Scherck and E.W. Vogt, Can. Jour. Phys., v.**46**, No.9, 1968, p.1119.
22. S.G. Kadmsky and V.I. Furman, Alpha Decay and Related Nuclear Reactions, EnergoAtomIzdat, Moscow, 1985 (in Russian).

# Fast Neutrons Processes on Molybdenum Isotopes

C. Oprea, A.I. Oprea

*Joint Institute for Nuclear Research, Frank Laboratory of Neutron Physics,  
Joliot-Curie 6, 141980 Dubna, Russian Federation*

**Abstract.** Molybdenum nucleus has many natural and artificial isotopes important for fundamental and applicative researches. Cross sections, angular correlations and isomer ratios in fast neutrons induced reactions up to 25-30 MeV were evaluated using codes realized by authors as well as dedicated software. Contributions of different nuclear reaction mechanisms in the cross sections were also determined. Parameters of nuclear optical potential, density levels and radius channels were extracted. Theoretical evaluations were compared with existing experimental data. The results of present work were realized in the frame of the fast neutrons scientific program at FLNP basic facilities (IREN and EG5) and are necessary for future experiment preparation.

## INTRODUCTION

The Molybdenum nucleus, (protons numbers  $Z=42$  and mass  $A= 83-115$ ) has 33 isotopes of which 7 are natural ( $A=92, 94, 95, 96, 98, 100$ ) and four isomers. The first 6 natural isotopes are stable but the nucleus with  $A=100$  is unstable with the time of life of  $7.8 \cdot 10^{18}$  y. The isotopes with  $A=100$  is a fission product and it is used in medicine [1].

Nuclear reactions induced by fast neutrons are of great interest for fundamental and applicative researches. For fundamental investigations fast neutrons reactions are a source of new data on nuclear reactions mechanism and structure of nuclei. For applications these reactions provide precise nuclear data for reactors technology (fission and fusion), processing of long live nuclear waste, reprocessing of *U* and *Th* for transmutation and energy projects, accelerated driven systems (ADS) etc. [2-4]. Fast neutrons cross sections data for charged particles emission are of interest also because, the accumulation of Hydrogen and Helium in the walls and vessels of nuclear facilities lead to the modification of their physical properties [5].

Neutrons are neutral elementary particles and therefore they have high penetrability power in the matter. This property is very useful in neutrons activation analysis because it is possible to analyze large solid samples. Furthermore, the emitted gamma quanta resulted in the neutron capture process emerging from the samples can be also registered. Instrumental Neutron Activation Analysis (INAA) performed with slow neutrons is a powerful tool for elemental analysis. Complementary to INAA is Fast Neutrons Activation Analysis (FNAA) method which allows to obtain better gamma emitters [6].

The following reactions  $^{94}\text{Mo}(n,p)^{94}\text{Nb}$  and  $^{95}\text{Mo}(n,np)^{94}\text{Nb}$  induced by fast neutrons were analyzed. Cross sections, isomers ratios, parameters of nuclear optical potentials were also evaluated. The  $^{94}\text{Nb}$  isotope can be found in the radioactive wastes. This nucleus is unstable, has a very large time of life ( $T_{1/2} = 20300$  y) and contributes to the low level geological activity of the environment due the buried wastes [7, 8].

## THEORETICAL BACKGROUND

Cross sections of  $^{94}\text{Mo}(n,p)^{94}\text{Nb}$  and  $^{95}\text{Mo}(n,np)^{94}\text{Nb}$  and of some concurrent processes which may influence the measurements were evaluated with Talys computer codes. In the calculations the contribution of all reactions mechanism (compound, direct and pre-equilibrium) were taken into account. In the case of compound processes the Hauser-

Feshbach approach of statistical model of nuclear reaction was considered [9]. Direct processes were described the Distorted Wave Born Approximation (DWBA) [10] and a two-component exciton model for pre-equilibrium processes was used [11].

Density levels were described by the constant temperature Fermi gas model [12]. The optical nuclear potential is of Woods–Saxon type, with real and imaginary part of volume, surface and spin-orbit components using locals and global parameters [13].

In the exit channels of mentioned reactions many isomer states are formed and from here it follows that will be of interest to evaluate in the experiment the corresponding isomer ratios. The expression of isomer ratio (neglecting the loss of charged particles in the target), used in the measurements, has the form:

$$R = Y_m \cdot Y_g^{-1} = \left( \int_{E_{thr}}^{E_{max}} N_0 \phi(E) \sigma_m(E) dE \right) \cdot \left( \int_{E_{thr}}^{E_{max}} N_0 \phi(E) \sigma_g(E) dE \right)^{-1} \quad (1)$$

where:  $Y_{m,g}$  are the yields of isotope in isomer ( $m$ ) and ground ( $g$ ) states;  $N_0$  is the number of nuclei in the target;  $\phi$  is the flux of incident beam;  $\sigma_{m,g}$  are the production cross section of  $m$  and  $g$  states respectively;  $E_{thr}$  is the threshold energy of emergent particle emission;  $E_{max}$  is the maximum energy of incident beam.

Talys is a freeware soft working under Linux, dedicated to nuclear reaction and structure of nuclei calculations with a friendly user interface. In these codes are implemented all models of nuclear reactions, density levels, optical potentials and related parameters to almost all nuclei and their isotopes. Parameters of Woods–Saxon nuclear potentials are obtained from processing of existing nuclear data for a large number of nuclei and isotopes. In the case when for some nuclides the parameters are not given then they are defined globally according with the approach described in [13]. Incident particles in Talys can be neutrons, protons, deuterons, tritium,  $^3He$  and alpha particles with energy up to 1000 MeV. This software is in development by free contribution of many users.

Talys gives the possibility to evaluate inclusive and exclusive cross sections. Lets consider a binary nuclear reaction of type  $A(a,b)B$ . The cross section is considered inclusive when in the final state are measured emergent “ $b$ ” particle from all possible open channels. The exclusive cross section is characterized by the situation when particles in the emergent channel “ $b+B$ ” are in a well defined states of spin, parity, energy levels etc.

A comprehensive description of Talys, with models, formalisms and approaches, possibilities and limits can be found in codes documentation and reference [14].

## RESULTS AND DISCUSSIONS

The  $^{94}Nb$  isotope in isomer and ground states can be obtained in the  $^{94}Mo(n,p)^{94}Nb$  and  $^{95}Mo(n,np)^{94}Nb$  reactions for incident neutrons energy starting from emergent particles threshold up to 25 MeV. For both processes the cross sections and isomer ratios were evaluated. In the given incident neutrons energy range other channels are open. Some of them are concurring with the reactions of interest because they have the cross sections of the same order of magnitude. Inclusive and exclusive cross sections with default Talys input parameters of optical potential and levels’ density are evaluated. In the exit channels 10 discrete levels of residual nucleus were considered. The main properties of investigated reactions and of concurrent ones are given in the Table 1. The spin and parity of  $^{94}Mo$  and  $^{95}Mo$  in fundamental state are  $0^+$  and  $(5/2)^+$  respectively.

**Table 1.**  $Q$  is heat of reaction;  $J_{m,g}^{\Pi}$ ,  $\tau_{m,g}$  are spin, parity and time of life of isomer and ground states;  $E_{\gamma}$  is gamma transition energy; 1, 3 – reaction of interest ; 2, 4 – concurrent reactions ( $M$ = main,  $C$  = concurrent)

	Reaction	Q[MeV]	$J_m^{\Pi}$	$J_g^{\Pi}$	$\tau_m$	$\tau_g$	$E_{\gamma}$ [MeV]	Obs
1	$^{94}\text{Mo}(n,p)^{94}\text{Nb}$	-1.262	$3^+$	$6^+$	6.263 m	$2.03 \times 10^3$ y	0.041	M
2	$^{94}\text{Mo}(n,np)^{93}\text{Nb}$	-8.49	$(1/2^-)$	$(9/2^+)$	16.13 y	stable	0.308	C
3	$^{95}\text{Mo}(n,np)^{94}\text{Nb}$	-8.631	$3^+$	$6^+$	6.263 m	$2.03 \times 10^3$ y	0.041	M
4	$^{95}\text{Mo}(n,p)^{95}\text{Nb}$	-0.143	$(1/2^-)$	$(9/2^+)$	80.60 h	34.975 d	0.236	C

First the inclusive reactions stated in lines 1, 2, 3, 4 of Table 1 were evaluated. The contribution of all reaction mechanisms, given by discrete and continuum states of the residual nuclei are separated. In the Figure 1 are shown the results of inclusive reaction of  $^{94}\text{Mo}(n,p)$  process.

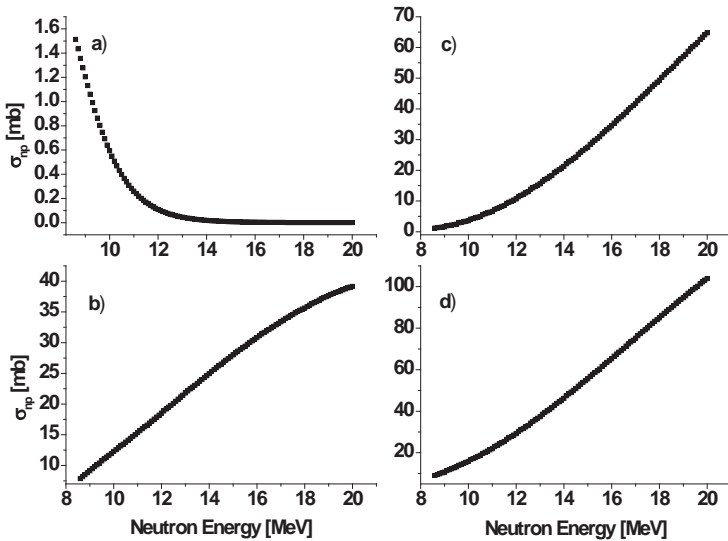


**Figure 1.** Inclusive cross section (XS) of  $^{94}\text{Mo}(n,p)$  reaction. a) Compound processes on discrete states b) Compound on continuum c) Direct on continuum d) Total XS.

Discrete states, for both compound and direct processes have a very small influence on the cross sections in comparison with the continuum ones. The contribution to the cross section of compound processes on discrete states (shown in Fig.1a) are with order of magnitude greater than the contribution of direct processes on discrete states and therefore the last are not represented in Fig.1. From Figs. 1b) and 1c) the main contribution to the cross section are given by continuum states of the residual nuclei and in the given incident neutron energy interval the compound and direct processes are of the same order of magnitude and competing with each other. The shape of the cross sections is in accordance with theory in each analyzed cases. At low energies the cross sections are increasing until to a maximum

value and followed after by a decreasing. From Fig. 1b) it is observing that the compound processes will reach the maximum faster than the direct ones (Fig. 1c)). From here results that the contribution of direct processes on the cross section are higher in comparison with compound processes and with the increasing of the energy the direct processes will become dominant. Talys calculations indicate that the compound and direct processes represented in Fig.1 are generated by the pre-equilibrium mechanism. In Fig. 1d) the total inclusive cross section for  $^{94}\text{Mo}(n,p)$  reaction is represented taking into account all type of processes and states of residual nuclei. Same inclusive cross sections evaluations for all reactions from Table 1 are done but are not shown here. It is very interesting to mention that for all analyzed reactions from Table 1 there are the following common elements: the direct processes on continuum states of residual nuclei are higher in comparison with compound processes and the cross sections values have the same order of magnitude for all cases.

Production of  $^{94}\text{Nb}$  nucleus in different states can be evaluated using exclusive cross sections. The results of  $^{94}\text{Mo}(n,p)^{93m,g}\text{Nb}$  are represented in Fig. 2a). Cross sections of ground and isomer states production are designated by numbers 1) and 2). Total production of  $^{94}\text{Nb}$  isotopes represented by the dependence 3, is compared with existing experimental data (Fig. 2a), curve 4) [15–17]. Description of experimental data, applying default Talys input can be considered satisfactory. Mainly the results on production of  $^{41}\text{Nb}$  were obtained by activation methods, which are very difficult for elements with a very long time of life [15–17]. Furthermore, for neutrons energy up to 20 MeV many channels are open and they are in competition with the first analyzed reaction ( $^{94}\text{Mo}(n,p)^{93m,g}\text{Nb}$ ) from Table 1. The following concurrent channels,  $^{94}\text{Mo}(n,np)^{93}\text{Nb}$  (number 2 from Table 1) and  $^{94}\text{Mo}(n,2n)^{93}\text{Mo}$  ( $Q=-9.67$  MeV), must be taken into account for future measurements. In the Fig. 2. b. are represented the results for  $^{93}\text{Nb}$  nucleus production in  $^{94}\text{Mo}(n,np)^{93m,g}\text{Nb}$  reaction.

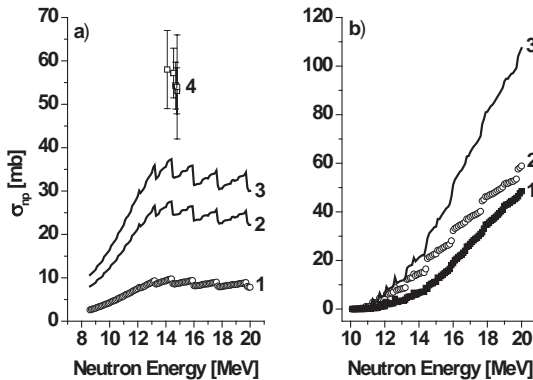


**Figure 2.** Exclusive XS. a)  $^{94}\text{Mo}(n,p)^{93m,g}\text{Nb}$  for states: 1) ground, 2) isomer respectively, 3) total (1+2), 4) comparison with experimental data; b)  $^{94}\text{Mo}(n,np)^{93m,g}\text{Nb}$  for 1) isomer, 2) ground, 3) total (1+2).

The cross section of  $(n,np)$  process from Fig. 2b) has a greater value than the  $(n,p)$  reaction from Fig. 2a) but however the authors had not found experimental data. In the given incident neutrons energy range it is difficult, in the measurements, to separate neutrons and protons of  $(n,np)$  process from neutrons and protons coming from other open channels.

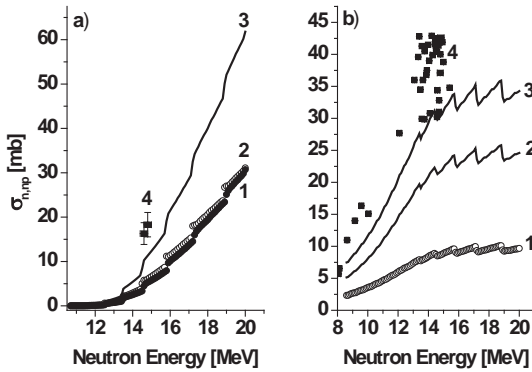


**Figure 3.** Exclusive XS. a)  $^{95}\text{Mo}(n,np)^{94m.g}\text{Nb}$  reaction for 1) isomer, 2) ground, 3) total (1+2), 4) comparison with experimental data; b)  $^{95}\text{Mo}(n,p)^{95m.g}\text{Nb}$  reaction for 1) isomer, 2) ground, 3) total (1+2), 4) comparison with experimental data.

The  $^{94}\text{Nb}$  isotope can be obtained in  $^{95}\text{Mo}(n,np)^{94}\text{Nb}$  reaction. Main properties of this process are shown in the row 3 of Table 1. For this reaction were evaluated also the inclusive cross section with a separation of different contribution of compound and direct processes on discrete and continuum states. Like in the case of  $^{94}\text{Mo}(n,p)^{94}\text{Nb}$  reaction, the main contribution to the cross section is given by continuum states. Moreover, cross section given by direct processes are, higher than those of compound ones and both, direct and compound, are coming from pre-equilibrium mechanism. Inclusive processes for the  $^{95}\text{Mo}(n,np)^{94}\text{Nb}$  and corresponding competing channels were not represented.

For  $^{95}\text{Mo}(n,np)^{94}\text{Nb}$  process also were considered possible competing channels and they are:  $^{95}\text{Mo}(n,p)^{95}\text{Nb}$  (number 4 from Table 1) and  $^{95}\text{Mo}(n,2np)^{93}\text{Nb}$  ( $Q=-15.857\text{ MeV}$ ). In the Figure 3.a. are shown the cross section production of the reaction of interest  $^{95}\text{Mo}(n,np)^{94}\text{Nb}$ . In the Figure 3b) exclusive cross sections of  $^{95}\text{Mo}(n,p)^{95}\text{Nb}$  concurrent process are represented also. The results of other competing process are not given because their cross sections are lower and the threshold particle production is higher than in the investigated cases.

Fig. 3a) shows the experimental data taken from [15]. In Fig. 3b) are represented experimental data in a wide energy interval up 16–18 MeV [15, 18, 19]. Experimental data follows qualitatively the theoretical evaluations and a satisfactory agreement can be considered. The cross sections of investigated reaction (Fig. 3a) and of competing process (Fig. 3b)) are of the same order of magnitude and must be considered in future measurements. Taking into account the theoretical values of isomer and ground states production and the satisfactory agreement between theory and experiment it is possible to evaluate the isomer ratios of the processes from Fig. 2 and Fig. 3 using relation (1). Two types of neutrons sources were considered. In the first case has the flux is equal with unity. In the second case the flux is much closer to reality and is proportional with  $1/E^{0.9}$  ( $E$  is the neutron energy) like in the case of pulsed neutrons sources like IREN and IBR2 reactor from LNF. Results of evaluated isomer ratios for all reactions from Table 1 are given in Table 2.

**Table 2.** Isomer ratios obtained for investigated (I) and concurrent (C) processes in the case of neutrons source with incident flux 1)  $\phi = I$ ; 2)  $\phi \sim 1/E^{0.9}$ ;  $E_\gamma =$  gamma transition energy

	Reaction	$E_\gamma$ [MeV]	$R_1 \pm \Delta R_1$	$R_2 \pm \Delta R_2$	Obs
1	$^{94}\text{Mo}(n,p)^{94}\text{Nb}$	0.041	$2.852 \pm 0.013$	$2.860 \pm 0.013$	I
2	$^{94}\text{Mo}(n,np)^{93}\text{Nb}$	0.308	$1.426 \pm 0.015$	$1.511 \pm 0.025$	C
3	$^{95}\text{Mo}(n,np)^{94}\text{Nb}$	0.041	$0.927 \pm 0.019$	$0.923 \pm 0.018$	I
4	$^{95}\text{Mo}(n,p)^{95}\text{Nb}$	0.236	$0.402 \pm 0.025$	$0.393 \pm 0.028$	C

The neutron energy interval taken into account in the evaluation of isomer ratios is starting from about 8 MeV up to 20 MeV. The  $R$  values are very close in the both cases, but the absolute error  $\Delta R$  is higher in the second case, because with the increasing of the energy the number of incident neutrons is slowly decreasing. In the relations (1) it is necessary to calculate the integrals. Cross sections were evaluated numerically with a step of 0.1 MeV and therefore the integrals are approximated by sums, which are the origin of absolute errors  $\Delta R$ .

All calculations of cross sections and isomer ratios are done with default Talys input of Woods–Saxon (WS) potential parameters and densities states. In the Table 3 are extracted optical potential parameters that are influencing in a higher degree the cross sections.

**Table 3.** WS parameters. Real and imaginary VWS. Real SO.  $V$ ,  $W$ ,  $V_{SO}$  = potential depth;  $r$  = radius;  $a$  = diffuseness; Channel (row): 1), 3) incident and 2), 4) emergent

	Channel	Volume WS (VWS)						Spin Orbit (SO)		
		Real Part			Imaginary Part			Real Part		
		$V$ [MeV]	$r_V$ [fm]	$a_V$ [fm]	$W$ [MeV]	$r_W$ [fm]	$a_W$ [fm]	$V_{SO}$ [MeV]	$r_{SO}$ [fm]	$a_{SO}$ [fm]
1	n+ $^{94}\text{Mo}$	50.99	1.22	0.658	0.16	1.22	0.658	5.99	1.05	0.58
2	p+ $^{94}\text{Nb}$	61.94	1.21	0.664	0.13	1.21	0.664	6.03	1.041	0.59
3	n+ $^{95}\text{Mo}$	51.27	1.21	0.664	0.16	1.21	0.664	5.99	1.044	0.59
4	p+ $^{94}\text{Nb}$	62.10	1.21	0.664	0.13	1.21	0.664	6.03	1.044	0.59

The evaluations have demonstrated that the most significant part of potential is the VWS parameters with real and imaginary part. In a lower degree the cross sections are influenced by the real part of SO components. The imaginary part of SO potential depth is taken zero in the default Talys calculations. The surface and other parameters of WS components are not shown here. The extracted parameters have the values in the general accepted range of magnitude.

## CONCLUSIONS

Cross sections, isomer ratios and activities, of the nuclear processes indicated in the Table 1 were evaluated. Inclusive and exclusive cross sections were obtained with Talys computer codes using the default parameters input. From inclusive cross sections, the contributions of each nuclear-reaction mechanism on discrete and continuum states of residuals nuclei were obtained. For the given incident neutrons energy interval the direct processes, coming from pre-equilibrium mechanism, are giving the main contribution to the cross sections.

Exclusive cross sections allow to calculate the production of an isotope in a well defined states and therefore isomer ratios for different pairs of isomer – ground states were obtained.

For many presented theoretical results on cross sections and isomer ratios in the nuclear reactions with fast neutrons on *Mo* isotopes there are no experimental data. There will be of interest for fundamental and applicative researches to plan some future measurements for obtaining new nuclear data.

The present work is a part of nuclear data and isotopes production programs realized at IREN and IBR2 facilities of LNF JINR Dubna.

**Acknowledgement.** The work was supported by Cooperation Program between JINR Dubna and Romanian Research Institutes coordinated by JINR Dubna Plenipotentiary Representative of 2018–2019 years and FLNP Thematic Plan.

## REFERENCES

1. J. Meija, T.B. Coplen, M. Berglund, W.A. Brand, P.D. Bièvre, M. Gröning, N.E. Holden, J. Irrgeher, R.D. Loss, T. Walczyk, T. Prohaska, *Pure Appl. Chem.*, **88**(3), (2016) 265–291.
2. M. Salvatores, I. Slessarev, A. Tchistiakov, *Nucl. Sci. Eng. P.*, **130**, (1998) 309–319.
3. M. Salvatores, A. Zaetta, C. Girard, M. Delpuch, I. Slessarev, J. Tomassi, *Appl. Radiat. Isot.*, **46** (6), (1995) 681–687.
4. C. Rubbia, J. A. Rubio, S. Buono, F. Carmine, N. Fieter, J. Galvez, C. Geles, Y. Kadi, R. Klapisch, P. Mandrillon, J.P. Revol, and C. Roche, Report CERN/AT/95-44(ET) (1995); [http://cern.web.cern.ch/CERN/Divisions/SL/EER/Energy Amplifier/PDF/95-44.pdf](http://cern.web.cern.ch/CERN/Divisions/SL/EER/Energy%20Amplifier/PDF/95-44.pdf)
5. G. Khuukhenkhuu, Yu.M. Gledenov, M.V. Sedysheva, M. Odsuren, J. Munkhsaikhan, T. Delgersaikhan, *Journal Physics of Elementary Particles and Atomic Nuclei (PEPAN) Letters*, **11** (6), (2014) 1159–1168.
6. G. Berri, F. Mezzeti, A. Da Re, A. Bortolotti, L. Rapezzi, V.A. Grybkov, *Nucleonika*, **45** (3), (2000) 189–191.
7. Y. Ikeda, C. Konno, IAEA Vienna, INDC(NDS)-286, (1993), p. 27–31.
8. L. R. Greenwood, D. G. Doran, H. L. Heinisch, *Phys. Rev.*, **C 35** (1), (1987) 76.
9. W. Hauser, H. Feshbach, *Phys. Rev.*, **87**, 2, (1952) 366.
10. G.R. Satchler, *Direct Nuclear Reactions*, Oxford University Press, New York (1983).
11. A.J. Koning, M.C. Duijvestijn, *Nucl. Phys.*, **A 744**, (2004) 15.
12. Amos de Shalit, Herman Feshbach, *Theoretical Nuclear Physics*, John Wiley and Sons, ISBN13: 9780471203858 (1974).
13. A.J. Koning, J.P. Delaroche, *Nucl. Phys.*, **A 713**, (2003) 231.
14. A.J. Koning, S. Hilaire and M.C. Duijvestijn, TALYS-1.0., Proceedings of the International Conference on Nuclear Data for Science and Technology, April 22–27, 2007, Nice, France, editors O.Bersillon, F. Gunsing, E. Bauge, R. Jacqmin, S. Leray, EDP Sciences, (2008) 211.
15. L.R. Greenwood, D.G. Doran, H.L. Heinisch, *Phys. Rev.*, **C 35**, (1987) 76.
16. Y. Ikeda, C. Konno, A. Kumar, Y. Kasugai, IAEA Vienna, INDC(NDS)-342, (1996), 19.
17. Xiangzhong Kong, Yongchang Wang, Junquan Yuan, Jingkang Yang, *Journal of Radioanalytical and Nuclear Chemistry*, **V. 227**, (1998) 15.
18. P. Reimer, V. Avrigeanu, S.V. Chuvaev, A.A. Filatenkov, T. Glodariu, A. Koning, A.J. M. Plompen, S.M. Qaim, D.L. Smith, H. Weigmann, *Phys. Rev. C* **71**, (2005) 044617.

# Asymmetry and Spatial Symmetry Breaking Effects Modeling in $(n,p)$ Reactions

C. Oprea, A.I. Oprea

*Frank Laboratory of Neutron Physics, Joint Institute for Nuclear Research,  
Joliot Curie 6, 141980 Dubna, Moscow Region, Russian Federation*

**Abstract.** Asymmetry and spatial parity breaking effects in nuclear reaction induced by slow and resonant neutrons on  $^{35}\text{Cl}$  nucleus followed by protons emission were analyzed. Effects were obtained applying Flambaum-Sushkov formalism using two-levels approximation. In the computer simulation, different types of target and neutrons incident flux were considered. Obtained results are compared with existing experimental data. Differences between theoretical evaluation, computer modeling and experimental data are explained considering contributions of other open channels.

## INTRODUCTION

After the discovery of parity non-conservation phenomena (PNC) of neutrons, protons it was supposed universal characteristic of weak interaction [1]. Later, theoretically was evidenced the non-leptonic characteristic of weak forces which can be observed in the interactions between nucleons [2]. The constant of weak non-leptonic interactions is of order of  $10^{-7}$  in comparison with nuclear strong interactions which is parity conserving (PC). Weak non-leptonic interaction is acting together with nuclear force and therefore is very difficult to measure it in the experiments. First experimental proof of the existence of weak non-leptonic interaction between nucleons was evidenced at FLNP, in the measurement of the asymmetry of emitted gamma quanta in capture process of slow neutrons by  $^{113}\text{Cd}$  nuclei. The nonzero value of measured asymmetry was interpreted as effect of weak interaction between nucleons [3]. Analogue phenomena in other neutrons reactions on light medium and heavy nuclei (including fission), were observed at FLNP basic facilities [4,5]. Parity breaking effects observed in slow neutrons processes were very well explained by in the frame of the model of the mixing states of compound nucleus with the same spins and opposite parities [6,7].

Authors had analyzed, using the resonance-resonance approach, asymmetry and spatial parity breaking effects in  $^{35}\text{Cl}(n,p)^{35}\text{S}$  reaction with slow and resonance neutrons. Forward-backward (FB), left-right PC effects, together with PNC one were obtained and compared with experimental data. From experimental data and theoretical evaluations of asymmetry coefficients, weak matrix element was extracted [8,9].

In the present work a mathematical modeling of FB asymmetry coefficient measurement, in the  $^{35}\text{Cl}(n,p)^{35}\text{S}$  reaction was realized. The asymmetry coefficient was obtained using resonant-resonant approach, considering an incident neutrons flux on a target with a given thickness. Results are analyzed and compared with measurements obtained at FLNP basic facility.

## THEORY AND FORMULAS

In the resonant-resonant formalism it is supposed that asymmetry and parity violation (PV) effects are manifesting in the presence of resonance of compound nucleus with the same spins and opposite parities. In addition resonances enhance the effects mainly due to amplification mechanisms (cinematic, dynamic and structural) [6,7]. In  $(n,p)$  reaction induced by neutrons with orbital momentum  $l=0, 1$  ( $s, p$  neutrons) compound nucleus in the  $S$  and  $P$

states can be formed. Amplitudes of  $(n,p)$  process corresponding to parity PC interaction are [6,7]:

$$f_{np}^{S(P)}(E_n) \sim \sqrt{\Gamma_n^{S(P)}\Gamma_p^{S(P)}} \left[ (E - E_{S(P)}) + 0.5 \cdot i \cdot \Gamma_{S(P)} \right]^{-1} \text{Exp}(\Delta\phi_{np}^S), \quad (1)$$

where  $E_n$  is neutron energy;  $\Gamma_n^S, \Gamma_p^S, \Gamma_n^P, \Gamma_p^P$  = neutron and proton widths corresponding to  $S$  and  $P$  states of compound nucleus, respectively;  $\Gamma_{S,P} = \Gamma_n^{S,P} + \Gamma_p^{S,P} + \Gamma_\gamma^{S,P} + \Gamma_\alpha^{S,P} + \dots =$  total widths in  $S$  and  $P$  states as sum of neutron, proton, gamma, alpha and other particles widths in the given channel;  $E_{S,P}$  = energy of  $S$  and  $P$  resonances;  $\Delta\phi_{np}^{S,P} = \phi_n^{S,P} - \phi_p^{S,P}$  = difference of neutron and proton phases in  $S$  and  $P$  states.

Amplitudes form (1) represents the capture of an  $s$ -neutron ( $p$ -neutron) with formation of an  $S$ -resonance ( $P$ -resonance) of compound nucleus followed by emission of protons with orbital momentum necessary for parity conservation. If the weak interaction between nucleons are considered then the corresponding amplitudes can be written as [6,7]:

$$f_{np}^{SP(PS)}(E_n) \sim W_{PNC} \sqrt{\Gamma_n^{S(P)}\Gamma_p^{P(S)}} \left\{ \left[ (E - E_S) + 0.5 \cdot i \cdot \Gamma_S \right] \left[ (E - E_P) + 0.5 \cdot i \cdot \Gamma_P \right] \right\}^{-1} \text{Exp}(\phi_n^S - \phi_p^P), \quad (2)$$

where  $W_{PNC}$  = weak matrix element;  $W_{PNC} \ll W_{PC}$ ;  $W_{PC}$  = matrix element of nuclear interaction.

Relations (2) describe the capture of an  $s$ -neutron ( $p$ -neutron) with formation of compound nucleus in  $S$  state ( $P$ -state). Due to the weak non-leptonic interaction between nucleons in the intermediate state, compound nucleus is changing the spatial parity going from  $S$ -state ( $P$ -state) to  $P$ -state ( $S$ -state) followed by protons emission. In formulas (1), (2) sum over Clebsh-Gordan coefficients and spherical functions are omitted for a better understanding of the processes. Detailed calculations can be found in [6–9]. If the  $(n,p)$  reactions is going with formation of a compound nucleus characterized only by  $S$  and  $P$  resonances with participation of weak interaction then total amplitude is:

$$f_{np} = f_{np}^S + f_{np}^P + f_{np}^{SP} + f_{np}^{PS}. \quad (3)$$

Differential cross section, angular correlation and cross section are calculated as following:

$$\begin{aligned} [d\sigma/d\Omega](E_n, \theta, \phi) &= |f|^2 \sim W(\theta, \phi), \quad \sigma(E_n) = \int [d\sigma/d\Omega](E_n, \theta, \phi) d\Omega, \\ \int_{(\Omega)} W(\theta, \phi) \sin(\theta) d\theta d\phi &= 1, \end{aligned} \quad (4)$$

where  $W(\theta, \phi)$  = angular correlation;  $\theta, \phi$  = polar and azimuth angles.

Using angular correlations, asymmetry and PV effects can be obtained. Forward-backward effect is defined as:

$$\alpha_{FB}(E_n) = (W(\theta = 0) - W(\theta = \pi)) \cdot (W(\theta = 0) + W(\theta = \pi))^{-1}. \quad (5)$$

## RESULTS AND DISCUSSIONS

The  $^{35}\text{Cl}$  nucleus, in fundamental state has the spin and parity  $J^\Pi = (3/2)^+$ . In  $^{35}\text{Cl}(n,p)^{35}\text{S}$  reaction induced by  $s$  and  $p$  neutrons with energies up to 1000 eV,  $^{36}\text{Cl}$  compound nucleus is formed which can be characterized by  $S$  and  $P$  resonance with following energies, spins and parity:  $E_S = -180\text{eV}$ ,  $E_P = 398\text{eV}$ ,  $J_S = 2^+$ ,  $J_P = 2^-$ . Residual nucleus  $^{35}\text{S}$  is in fundamental state with the following spin and parity,  $J^\Pi = (3/2)^+$ . Neutrons resonance parameters of  $^{36}\text{Cl}$  compound nucleus are taken from [10]. For incident neutrons energy interval up to 1000 eV the influence of other resonances can be neglected. If the incident neutrons are unpolarized then the PNC components of the amplitudes are zero, therefore the amplitude of  $(n,p)$  process is:

$$f_{np} = f_{np}^S + f_{np}^P. \quad (6)$$

Using relations (4), angular correlations can be written as:

$$W(E_n, \theta) = \left( |f_{np}^S|^2 + |f_{np}^P|^2 + 2\text{Re} f_{np}^S f_{np}^{P*} \right) \left[ \sigma_{np}(E_n) \right]^{-1} = \left[ 1 + \alpha(E_n) \cos(\theta) + \beta(E_n) \cos^2(\theta) \right] [4\pi]^{-1}. \quad (7)$$

Applying (5) the FB asymmetry effect is:

$$\alpha_{FB}(E_n) = \frac{2\text{Re} f_{np}^S f_{np}^{P*}}{|f_{np}^S|^2 + |f_{np}^P|^2} \Bigg|_{\theta=0} = \pm \frac{\sqrt{\Gamma_n^S \Gamma_p^S \Gamma_n^P \Gamma_p^P}}{\Gamma_n^S \Gamma_p^P [P] + \Gamma_n^P \Gamma_p^P [S]} u_{FB}(E_n) (X_n - Y_n) (X_p - Y_p), \quad (8)$$

$$u_{FB}(E_n) = \left[ (E - E_S)(E - E_P) + 0.25 \Gamma_S \Gamma_P \right] \cos(\Delta\phi) - \left[ 0.5(E - E_S) \Gamma_p - 0.5(E - E_P) \Gamma_S \right] \sin(\Delta\phi), \quad (8.1)$$

$$[S] = (E - E_S)^2 + 0.25 \cdot \Gamma_S^2, \quad [P] = (E - E_P)^2 + 0.25 \cdot \Gamma_P^2, \quad (8.2)$$

$$X_n^2 + Y_n^2 = 1, \quad X_p^2 + Y_p^2 = 1, \quad (8.3)$$

where  $X_n, Y_n, X_p, Y_p$  are reduced partial neutron and proton widths;  $k$  is wave number;  $Z, Z'$  are charge of target and residual nuclei respectively;  $e$  is elementary charge;  $h$  is Planck constant.

Also,  $\alpha$  and  $\beta$  coefficients from (7) were evaluated and they have the following form:

$$\alpha = \pm \sqrt{\Gamma_n^S \Gamma_p^S \Gamma_n^P \Gamma_p^P} \left[ \Gamma_n^S \Gamma_p^S [P] + \Gamma_n^P \Gamma_p^P [S] \right]^{-1} u_{FB}(E_n) (X_n - Y_n) (X_p - Y_p), \quad (9)$$

$$\beta = \mp 0.35 X_n X_p Y_n Y_p \Gamma_n^S \Gamma_p^P [S] \left[ \Gamma_n^S \Gamma_p^S [P] + \Gamma_n^P \Gamma_p^P [S] \right]^{-1}. \quad (10)$$

From relation (8) FB effect can be interpreted as the result of interference between  $S$  and  $P$  states of compound nucleus. This confirms the main assumptions of the formalism of mixing states of compound nucleus with the same spins and opposite parities that asymmetry and PV effects can be observed in the presence of at least a pair of  $S$  and  $P$  resonances. The “ $\pm$ ” sign in relations (8), (9), (10) appears due to the determination of phases sign cannot. Further, if  $\alpha$  is positive then  $\beta$  will be negative, and vice-versa. Coefficient  $\beta$  is important in the investigation of differential cross section anisotropy. It is easy to observe that if  $\beta=0$  then  $\alpha_{FB} = \alpha$ . Coefficients  $\alpha$  and  $\beta$  determine completely the angular correlation which allows

to generate polar and azimuth angles necessary in the computer modeling of FB measurement. Polar angle  $\theta$  can be determined by direct Monte Carlo method [11] applying the relations:

$$\int_0^{\theta c < \pi} W(\theta) \sin(\theta) d\theta = r < 1 \Rightarrow \theta = \pm \text{ArcCos} \left[ \frac{-2 + \beta}{2(\alpha + \beta)} \left( 1 \pm \sqrt{\frac{(-2 + \beta)^2}{4(\alpha + \beta)^2} \pm \frac{2 + \alpha - 4r}{\alpha + \beta}} \right) \right], \quad (11)$$

$$\varphi = 2\pi r, r \in [0,1), \quad (12)$$

where  $r$  is random number.

If  $\beta=0$  then the generator for polar angle  $\theta$  is simplifying and takes the form:

$$\theta c = \text{ArcCos} \left\{ \left( \sqrt{1 + 2\alpha_{FB} + \alpha_{FB}^2 - 4\alpha_{FB}r} - 1 \right) (\alpha_{FB})^{-1} \right\}. \quad (13)$$

Experimental FB coefficient differs from theoretical definition and can be written as:

$$\alpha_{FB}^{\text{exp}} = (N_F - N_B) \cdot (N_F + N_B)^{-1}, \quad (14)$$

where  $N_F, N_B$  = number of protons in the forward and backward directions.

In the experiment, forward direction means all protons emitted from the target in the solid angle  $0 \leq \theta < \pi/2, \varphi \in [0, 2\pi]$  and correspondingly backward directions represents the solid angle  $\pi/2 \leq \theta < \pi, \varphi \in [0, 2\pi]$ . For a point target, forward (F) and backward (B) events, are:

$$N_F = \int_0^{\pi/2} \Phi_n(E_n) W(\theta, \varphi) \sin(\theta) d\theta d\varphi, \quad N_B = \int_{\pi/2}^{\pi} \Phi_n(E_n) W(\theta, \varphi) \sin(\theta) d\theta d\varphi, \quad (15)$$

where  $\Phi_n(E_n)$  = flux of incident neutrons.

Applying (15), FB asymmetry coefficient is:

$$\alpha_{FB}^{\text{exp}} = (\alpha/2) \cdot [3(1 + \cos \theta_{\max})] \cdot (3 + \beta + \beta \cdot \cos \theta_{\max} + \beta \cdot \cos^2 \theta_{\max})^{-1} \text{ or if } \beta = 0, \alpha_{FB}^{\text{exp}} = \alpha_{FB}/2, \quad (16)$$

where  $\theta_{\max}$  = maximal angle of protons emerging from the target.

Due to the geometry and thickness of the target polar angle in expression (15) is lower than  $\pi/2$ . Passing through the target protons lose their energy and maximal path depends on initial protons energy material type. Stopping power data are taken from [12]. Cross section of  $^{35}\text{Cl}(n,p)^{35}\text{S}$  process is represented in Fig. 1a). Theoretical evaluation describes well existing experimental data. Results from Fig. 1a) are calculated using the expression [9]:

$$\sigma_{np}(E_n) = g\pi\hat{\lambda}_n^2 \left( \Gamma_S^n \Gamma_S^p / [S] + \Gamma_P^n \Gamma_P^p / [P] \right), \quad (17)$$

where  $\hat{\lambda}_n$  = neutron wave number;  $g = (2J + 1) / [(2I + 1)(2s + 1)]$  = statistical factor;  $J, I, s$  = spin of compound nucleus, target nucleus and neutron, respectively.

Fig. 1 shows the dependence on incident neutrons energy up to 1000 eV of  $\alpha$ ,  $\beta$  coefficients according to relations (8), (9), (10).

In the  $^{35}\text{Cl}(n,p)^{35}\text{S}$  reaction with neutrons energy up to 1000 eV cross section is well described by compound nucleus mechanism and the main contribution is given by the first 2 resonances ( $S$  and  $P$ ). Influence of higher resonance interferences and interferences can be neglected [9]. Comparing Figs. 1a) and 1b) result that when FB effect has high values, cross section is very low and vice versa. This is an important feature not only for FB effect but also for other PV and asymmetry coefficients. From Fig. 1b), in the given energy interval results, the influence of  $\beta$  on FB effect is not so large. As is expected  $\alpha$  and  $\beta$  have opposite sign. For resonance energy,  $E_p=398$  eV,  $\alpha_{FB}=0$  but  $\beta\cong 0.08$ . This fact is of interest in the measurement of differential cross section in the resonance. Coefficient  $\beta$  reduces with few percent  $\alpha_{FB}$  coefficient. In the evaluations, neutron resonance parameters, phases for neutron and proton widths are taken from [10].

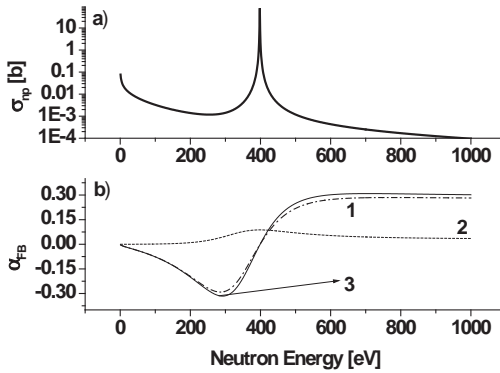


**Figure 1.** Neutron energy dependences of cross section and angular correlation coefficients (7). a)  $^{35}\text{Cl}(n,p)^{35}\text{S}$  cross section b) Coefficients. 1 –  $\alpha_{FB}$  (8); 2 –  $\beta$  (10); 3 –  $\alpha$  (9).

Results obtained above will be applied in the mathematical modeling of experimental evaluation of FB coefficient. A constant flux of incident neutrons interact with a rectangular  $\text{NaCl}$  target with different thickness and dimensions were tested (see Fig. 1). In the target a  $^{35}\text{Cl}(n,p)^{35}\text{S}$  process takes place. Part of emitted protons with initial energy  $E_p \cong Q_{np} = 0.62 \text{ MeV}$  by losing their energy can get out from the target. If the maximum protons path is larger than thickness than the FB effect can be observed [8]. Polar and azimuth angle were generated using (11) and (12). Angular distribution coefficients,  $\alpha$  and  $\beta$ , were calculated applying relations (9) and (10). Reduced neutrons and protons widths have the following values:  $X_n = X_p = -Y_n = -Y_p = 1/\sqrt{2}$ . Spectra of emitted protons in forward and backward directions are simulated. Further  $N_F, N_B$  were determined and simulated  $\alpha_{FB}^{sim}$  are calculate. Forward and backward protons spectra obtained in the mathematical modeling are shown in Fig. 2.

Protons spectra from Fig. 2 were obtained for a target with a square like transversal surface with 1 cm side length. Incident neutrons energy was chose from 150 up to 260 eV. In this energy interval it is expected to have a large FB effect and advantageous experimental conditions [8]. For target with  $0.25 \text{ mg/cm}^2$  thickness about 15% of protons are not getting

out from the target. If thickness is  $5 \text{ mg/cm}^2$  than almost 15% of protons are getting out from the target. Table 1 with FB effect results with simulated FB coefficient are shown in Table 1.

For a point target, ratio between measured (or modeled) and theoretical effect is equal with 2 (see relation (16)). If the target is rectangular then with the increasing of the thickness the ratio of simulated and averaged FB coefficient is decreasing. Thickness is an important parameter and must be chosen in an optimal way in order to not lose the FB effect and to have necessary statistics in the measurements.

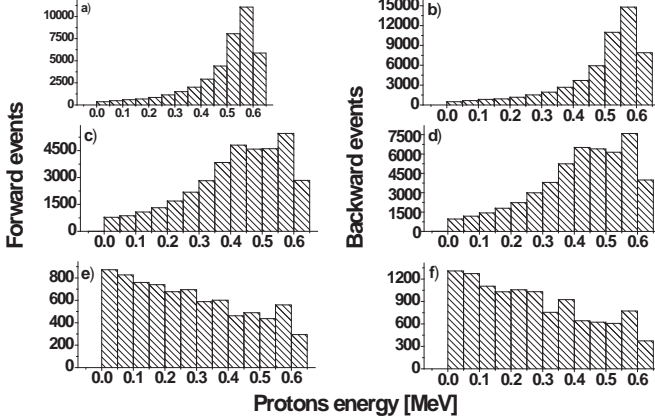


**Figure 2.** Forward, backward protons spectra for different target thickness. Generated events – 100 000. Target thickness: a) and b) –  $0.25 \text{ mg/cm}^2$ ; c) and d) –  $0.5 \text{ mg/cm}^2$ ; e) and f) –  $5 \text{ mg/cm}^2$ .

**Table 1.** Simulated FB effect for different thickness. Flux of incident neutrons is constant with energy from 150 up to 260 eV.  $g$  = target thickness

$g \text{ [mg/cm}^2\text{]}$	$\alpha_{FB}^{sim}$	$\overline{\alpha}_{FB}$	$\overline{\alpha}_{FB}/\alpha_{FB}^{sim}$
0.25	-0.146	-0.274	1.92
0.5	-0.155	-0.274	1.77
5	-0.179	-0.274	1.53

Averaged FB asymmetry coefficient for neutrons with energy from 150 up to 260 eV was calculated using the following formula:

$$\overline{\alpha}_{FB} = (E_{\max} - E_{\min})^{-1} \int_{E_{\min}}^{E_{\max}} \alpha_{FB}(E_n) dE_n, E_n \in [E_{\min}, E_{\max}]; E_{\min} = 150 \text{ eV}; E_{\max} = 260 \text{ eV}. \quad (18)$$

For the same neutrons energy interval is  $\alpha_{FB}^{exp} = 0.23 \pm 0.05$  [8] which is higher than results obtained from simulation. This fact can be explained in many ways. First reason could be that the measurements are difficult because they are affected by high background and the effect has maximum value where the cross section is very low. A second and uninvestigated reason can come from the fact that in  $^{35}\text{Cl}(n,p)^{35}\text{S}$  reaction alpha channel is also open. Energy of emitted alpha particles is about 0.94 MeV and close to the value protons energy. It is of interest therefore to investigate FB effect in the case of  $(n,\alpha)$  reaction on  $^{35}\text{Cl}$ . Another aspect which can affect measured proton spectra and must be analyzed in the future is related to the heating of the target due to the interaction with neutrons and energy loss of charged particles.

Theoretical and experimental investigations of FB effect in  $^{35}\text{Cl}(n,p)^{35}\text{S}$  reaction with slow and resonance neutrons is very important because correlated with other effects allow us to extract the matrix element of weak non-leptonic interaction between neutrons [9].

## CONCLUSIONS

Forward-backward effect in  $^{35}\text{Cl}(n,p)^{35}\text{S}$  nuclear reaction with neutrons up to 1000 eV was investigated. In the frame of the model of the mixing state of the compound nucleus with the same spin and opposite parities cross section, angular correlation and FB effect were calculated. Results were used in the mathematical modeling of FB effect on a target with finite dimensions. Using angular correlation, distribution of polar and azimuth angles were obtained. For different experimental condition (target thickness, area of transversal surface, flux and energy of incident neutrons etc.) protons spectra and FB asymmetry coefficient were simulated. Modeled FB effect is lower than existing experimental data. Were evidenced few reasons that could explain the difference between real measurement and mathematical modeling which represents a subject for future investigations.

The results of present studies represent a proposal for asymmetry and PV effects for slow and resonant neutrons induced reaction followed by charged particles emission at FLNP basic facilities.

**Acknowledgements.** The present work was realized in the frame of the Annual Program of Cooperation between Romanian research institutes and Joint Institute for Nuclear Research led by Plenipotentiary Representative of Romanian Government to JINR Dubna and 1128 Theme Plan of FLNP at 2018–2019 years.

## REFERENCES

1. R.P. Feynmann, M Gell-Mann, *Phys. Rev.* **109**, (1957) 193.
2. N. Tanner, *Phys. Rev.* **107**, (1957) 1203.
3. Yu.G. Abov, P.A. Krupchitsky, Yu.A. Oratovsky, *Phys. Lett.*, **12**, № **1**, (1964) 25.
4. G.E. Mitchel, J.D. Bowman, S.E. Pentilla, E.I. Sharapov, *Physics Reports*, **354**, (2001) 157.
5. V.R. Alfimenkov, A.N. Chernikov, L. Lason, Yu.D. Mareev, V.V. Novitski, L.B. Pikelner, V.R. Skoy, M.I. Tsulaya, A.M. Gagarski, I.S. Guseva, S.E. Golosovskaya, I.A. Krasnoschokova, A.M. Morozov, G.A. Petrov, V.I. Petrova, A.K. Petukhov, Yu.S. Pleva, V.E. Sokolov, G.V. Val'ski, S.M. Soloviev, *Nucl. Phys A* **645**, (1999) 31.
6. V.V. Flambaum, G.F. Gribakin, *Prog. Part. Nucl. Phys.* **35**, (1995) 423.
7. V.E. Bunakov, L.B. Pikelner, *Progr. Part. Nucl. Phys.* **39**, (1997) 337.
8. Yu.M. Gledenov, R. Machrafi, A.I. Oprea, V.I. Salatski, P.V. Sedyshev, P.I. Szalanski, V.A. Vesna, I.S. Okunev, *Nucl. Phys. A* **654**, (1999) 943.
9. A.I. Oprea, C. Oprea, Yu.M. Gledenov, P.V. Sedyshev, C. Pirvutoiu, D. Vladioiu, *Romanian Reports in Physics*, ISSN 1221-1451, **63**, № **2**, (2011) 357.
10. Mughabghab S.F., Divadeenam M., Holden N.E. – *Neutron Cross Sections*. NY, Academic Press, **1** (1981).
11. O. Sima, *Monte Carlo Simulation of Transport of Radiations*, Editura All, Bucuresti, 1994 (in Romanian).
12. Stopping Power Data. <http://www-nds.iaea.org/stopping/>.

# Angular Distribution of 1.368 MeV Gamma-Rays from Inelastic Scattering of 14.1 MeV Neutrons on $^{24}\text{Mg}$

I.N. Ruskov<sup>1,4,\*</sup>, Yu.N. Kopatch<sup>1</sup>, V.M. Bystritsky<sup>1</sup>, D.N. Grozdanov<sup>1,4</sup>,  
N.A. Fedorov<sup>1,2</sup>, T.Yu. Tretyakova<sup>3</sup>, V.R. Skoy<sup>1</sup>, S. Dabylova<sup>1,5</sup>, F.A. Aliyev<sup>1,6</sup>,  
C. Hramco<sup>1,7</sup>, A. Kumar<sup>8</sup>, A. Gandhi<sup>7</sup>, D. Wang<sup>9</sup>, E.P. Bogolyubov<sup>10</sup>,  
Yu.N. Barmakov<sup>10</sup>, and TANGRA Collaboration

<sup>1</sup>*Joint Institute for Nuclear Research (JINR), Dubna, Russia*

<sup>2</sup>*Faculty of Physics, Lomonosov Moscow State University (MSU), Moscow, Russia*

<sup>3</sup>*Skobel'syn Institute of Nuclear Physics (SINP), MSU, Moscow, Russia*

<sup>4</sup>*Institute for Nuclear Research and Nuclear Energy of Bulgarian Academy of Sciences (INRNE-BAS), Sofia, Bulgaria*

<sup>5</sup>*L.N. Gumilyov Eurasian National University (ENU), Nur-Sultan, Kazakhstan*

<sup>6</sup>*Institute of Geology and Geophysics (IGG), Baku, Azerbaijan*

<sup>7</sup>*Institute of Chemistry, Academy of Sciences of Moldova, Chisinau, Republic of Moldova*

<sup>8</sup>*Banaras Hindu University, Varanasi, India*

<sup>9</sup>*Xi'an Jiao Tong University, Xi'an, China*

<sup>10</sup>*All-Russia Research Institute of Automatics (VNIIA), Moscow, Russia*

## Abstract

In the frame of TANGRA-project at JINR-FLNP (Dubna) we measured the gamma-rays resulting from the inelastic scattering of 14.1 MeV neutrons on magnesium. As a source of neutrons we used ING-27 portable neutron generator of VNIIA (Moscow) where the neutrons are produced in a d-t fusion-fission nuclear reaction,  $^3\text{H}(d,n)^4\text{He}$ . The  $\alpha$ -particles were registered by a 64-pixel Si charge particle detector embedded in ING-27 vacuum chamber.

The sample tested was a 10cm-thick plastic cube filled with MgO powder. The gamma-rays from the interaction of neutrons with the sample we registered by a Romashka-type Fe-protected array, consisted of 22 hexagonal NaI(Tl) scintillator prisms. The analog signals from all the  $\alpha$ - and  $\gamma$ -detectors were collected in list-mode, simultaneously, by a computerized 32-channel data acquisition system (DAQ) from JINR AFI-electronics, which was used, also, for digitizing and storing the waveforms on the computer hard-drive for further off-line analysis with CERN-ROOT modular scientific software toolkit.

Using the time-correlated associated particle method (TCAPM), also known as tagged neutron method (TNM), the influence of the background radiation on the collected gamma-ray spectra was drastic reduced.

We obtained the angular distribution of 1.368 MeV gamma-rays from  $^{24}\text{Mg}(n, n'\gamma)$ -reaction in the range from  $\sim 15^\circ$  to  $\sim 165^\circ$  with a good statistical accuracy.

Here we report the results from our first experiment in comparison with the available data from the other authors. Further experiments are foreseen.

**Keywords:** ING-27; 14 MeV tagged neutrons; tagged neutron method; inelastic neutron scattering; gamma-rays angular distribution; NaI(Tl) multi-detector system

---

\* Corresponding author tel.: + 359-979-2-54-57  
email: : [ivan.n.ruskov@gmail.com](mailto:ivan.n.ruskov@gmail.com); [ivan@inrne.bas.bg](mailto:ivan@inrne.bas.bg).

## Introduction

Magnesium (Mg) is one of the most important elements together with C, N, O, B, Al, Si, from fundamental and application (practical) points of view. That is why it is an object of investigation in different branches of physics: geophysics, planetology, astrophysics, nuclear physics. Magnesium is a fundamental building block of the terrestrial planets, constituting ~15% of Earth's mass. Compared to the 'solar' composition of the primordial disk, it is well established that the Earth is depleted in Mg by ~20%, relative to more Cosmo chemically refractory elements as Al, consistent with increasing terrestrial depletions of elements with higher volatility [1]. The atomic weights and isotopic compositions for Magnesium are shown in Table 1.

Table 1. Atomic weights and Isotopic compositions for Magnesium

Isotope	Relative (to $^{12}\text{C}$ )	Isotopic	Standard
	Atomic Mass	Composition	Atomic Weight
12 Mg	24 23.985041697(14)	0.7899(4)	[24.304, 24.307]
	25 24.985836976(50)	0.1000(1)	
	36 25.982592968(31)	0.1101(3)	

Accurate determination of the Magnesium isotopic composition of the Moon, rocky planets and achondrites is important for Mg isotope studies of surface processes on Earth,

as well as, for using Mg-isotope data to understand evaporation and condensation effects in the solar nebula, the behavior of Mg-isotopes during magmatic differentiation processes in different planetary bodies, and to evaluate the extent of Mg isotopic heterogeneity in the solar system. High-precision Mg-isotope measurements of terrestrial and extraterrestrial (asteroids, Lunar) material by different methods are used for determining the relative and absolute Mg-isotope compositions of the bulk samples from the oceanic mantle. Magnesium isotopes are also used as Tracer of Crustal materials in volcanic arc Magmas.

**Magnesium** is used in flashlight photography, flares and pyrotechnics, including incendiary bombs. It is one third lighter than aluminum, and in alloys is essential for airplane and missile construction. The metal improves the mechanical, fabrication, and welding characteristics of aluminum when used as an alloying agent. Magnesium is used in producing nodular graphite in cast iron, and is used as an additive to conventional propellants.

For modern nuclear science and applications there is need from more precise and detailed neutron-nuclear data [2–4]. In this field Magnesium and its substances play an important role.

**Magnox** is an alloy, mainly of Magnesium with small amounts of Aluminum and other metals, used in cladding unenriched uranium metal fuel with a non-oxidizing covering, to contain fission products in nuclear reactors. Magnox is short for Magnesium non-oxidizing. This material has the advantage of a low neutron capture cross-section, but has two major disadvantages: it limits the maximum temperature (to about 415°C), and hence the thermal efficiency of the plant and it reacts with water, preventing long-term storage of spent-fuel under water in spent-fuel pools. The Magnox alloy Al80 has a composition of 0.8% Aluminum and 0.004% Beryllium.

**MgO** is prized as a refractory material, i.e. a solid that is physically and chemically stable at high temperatures. It is while used in dry process plants (as one of the components in Portland cement), in medicine (for relief of heartburn and dyspepsia, as an antacid, magnesium supplement, and as a short-term laxative), in nutrition as a food additive (known as E530), animal feed, in agriculture as a commercial plant fertilizer, in radio-electronics as an insulator in heat-resistant electrical cable and a protective coating in plasma displays, etc. It is also used as a reducing agent in the production of pure uranium and other metals from their salts. In nuclear industry MgO is packed around transuranic waste at the waste isolation plants, to control the solubility of radionuclides.

Mg presents as ingredient of the core in the conceptual design of European Facility for Industrial Transmutation (EFIT) of U-free waste, Pu and minor actinides (MA). It can be a pure-lead cooled reactor, working at thermal power of about several MW power, aiming at high-performance and flattening of the radial power distributions in fuel elements with different MgO matrix content and suitable pin diameter, provided considerable burning of Pu and MA.

High-quality nuclear data are required for reliable design calculations of fusion and Generation IV neutron-nuclear reactors as well as analyses related to their safety, licensing, waste management, and decommissioning issues. The Generation IV Roadmap selected the sodium fast reactor (SFR) concept as one of the six technologies for further development under Generation IV. The Mg-isotope  $^{24}\text{Mg}$  is produced in SFR coolant, as sodium (Na) is activated by neutron capture (the activation product  $^{24}\text{Na}$  is short-lived with 15 h half-life and decays in the stable  $^{24}\text{Mg}$  that influence  $k_{\text{eff}}$  of the reactor).

The study of the inelastic scattering (INS) of fast neutrons is of considerable theoretical and practical importance. From theoretical point of view such studies provide information about the level structure of stable nuclei. Information concerning inelastic scattering cross sections (CS) of neutrons can be obtained also by registering the gamma-ray spectra. This method is widely used, because it gives the possibility not only of establishing a scheme for nuclear energy levels, but also of determining the value of the excitation cross-sections of the individual levels. The use of pure isotopic targets (scatterers) permits unambiguously to interpret the experimental results.

The scheme of  $n$ -scattering on an  $A$ -nucleus via forming and decay of a compound nucleus system (CN) is shown in Fig. 1. Because the probability for emission of gamma-ray of multipolarity  $l$  is proportional to its energy as  $\sim E^{2l}$ , the probability for CN-decay directly to the ground state (GS) is  $\sim 10^3$  times higher than the preliminary emission of gamma-ray, Fig.1(a). That is why it is assumed that the inelastic scattering follows the scheme of Fig.1(b), and that the loss of energy of the neutron, measured in the coordinate system in which the center-of-mass (CM) is at rest, is equal to the excitation energy of the residual nucleus. The practical value of these studies is due to the importance of the inelastically scattered neutrons in the operation of the fast-neutron reactors and the new reactor concepts. Knowledge of the Neutron Inelastic Cross-Section and spectra of the inelastically scattered neutrons and gamma-rays is essential to the provision of a sound theory of the fast reactors.

Most gamma rays, produced by fast neutrons, are made by inelastic-scattering reactions, e.g.,  $^{12}\text{C}(n,n'\gamma)^{12}\text{C}$ ,  $^{14}\text{N}(n,n'\gamma)^{14}\text{N}$ ,  $^{16}\text{O}(n,n'\gamma)^{16}\text{O}$ ,  $^{24}\text{Mg}(n,n'\gamma)^{24}\text{Mg}$ , with the gamma-ray emitted from an excited level of the target nucleus.

The  $\gamma$ -production cross-sections from neutron inelastic scattering on  $^{24}\text{Mg}$  were measured for neutron energies up to 18 MeV at GELINA (Geel Linear Accelerator) [6]. They used GAINS (Gamma Array for Inelastic Neutron Scattering) spectrometer with seven large-

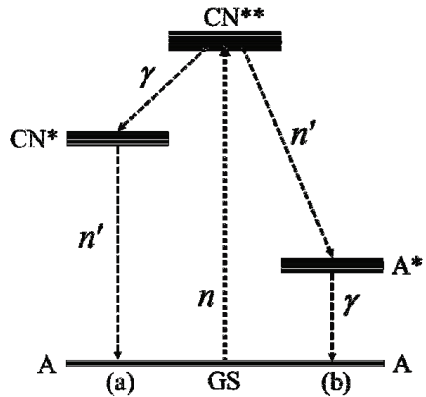


Fig.1. The scheme of  $n$ -scattering. A—scattering nucleus, CN—compound nucleus ( $A+n$ ).

volume high-purity germanium (HPGe) detectors placed at  $110^\circ$  and  $150^\circ$  with respect to the beam direction. Their results for  $^{24}\text{Mg}(n,n'\gamma)^{24}\text{Mg}$  reaction is shown in Fig. 2.

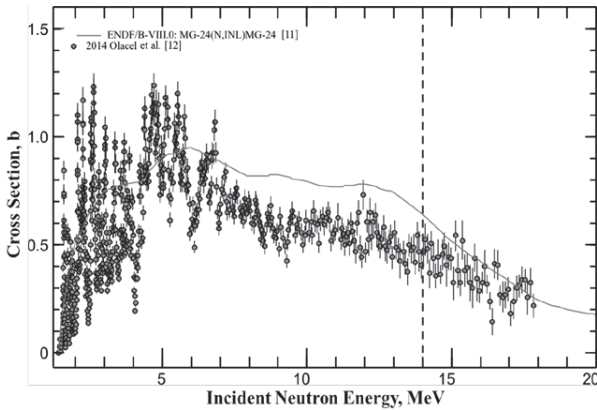


Fig. 2. Total inelastic cross-section for the  $^{24}\text{Mg}(n,n'\gamma)^{24}\text{Mg}$  reaction. The line displays the evaluated values from ENDF/B-VIII.0 [5]. The full-circles with error-bars represent the result of the experiment by Olacel et al. [6].

The measurement of angular distributions (differential cross-sections) of gamma-rays, produced in the inelastic scattering of neutrons with nuclei, is one of the important experimental means of studying the nuclear level schemes. A systematic study over nuclei of different elements can lead to an insight into the nuclear reaction mechanisms. A comparison of the experimental excitation functions and angular distributions with the Hauser-Feshbach and Satchler formalisms, checks the validity of the statistical

assumption in the compound nucleus formation. In this direction, the study of nucleon interactions with light nuclei is of great interest from early 60s till now.

In nuclear spectroscopy, the analysis of angular distribution is an important tool to determine the spins of states and the  $\gamma$ -ray intensity. Angle-differential  $(n,n')$  nuclear data is notoriously difficult to measure due to the difficulties involved in measuring the neutron energy and the absence of facilities supplying intense neutron beams of fast neutrons. An alternate approach to determine  $(n,n'\gamma)$  cross-sections involves measuring the prompt  $\gamma$ -rays emitted from the excited states populated via inelastic scattering, e.g.  $(n,n')$ . These data can be used to improve modelling for non-destructive assay of materials using active neutron interrogation. The 14-MeV neutron capture cross-section, as is well known, is quite small, and its contribution can be neglected. The reaction  $(n, 2n)$  has a threshold of 17 MeV, while the cross-sections of the  $(n, \alpha)$  and  $(n, np)$  reactions have not been measured. The neutrons of different energies are used to test and validate materials suitable for harsh neutron environments, such as a fusion reactor, Fusion technology, Electronics and its application, Material science, Fundamental physics, Industrial applications, Metrology, Neutron radiation biology, therapy and pharmaceuticals, Training and neutron science testing. Having 14-MeV kinetic energy, the incident neutron can excite the Mg-nucleus to higher excited state. After an incident neutron forms a compound nucleus, the excited  $\text{Mg}^*$  decays to the ground state after some time by releasing a gamma-quantum of exactly the excitation energy.

### Time-Related Associated Particle Method (TCAPM)

The TCAPM, also known as Associated Particle Technique (APT) or Imaging (API), as well as Tagged Neutron Method (TNM), is based on the advantage given by the kinematics of the binary  $(d-t)$ -fusion reaction, in which the reaction products, namely, neutron and alpha-particle are irradiated in opposite direction, in center-of-mass frame (CM) (Fig. 3).

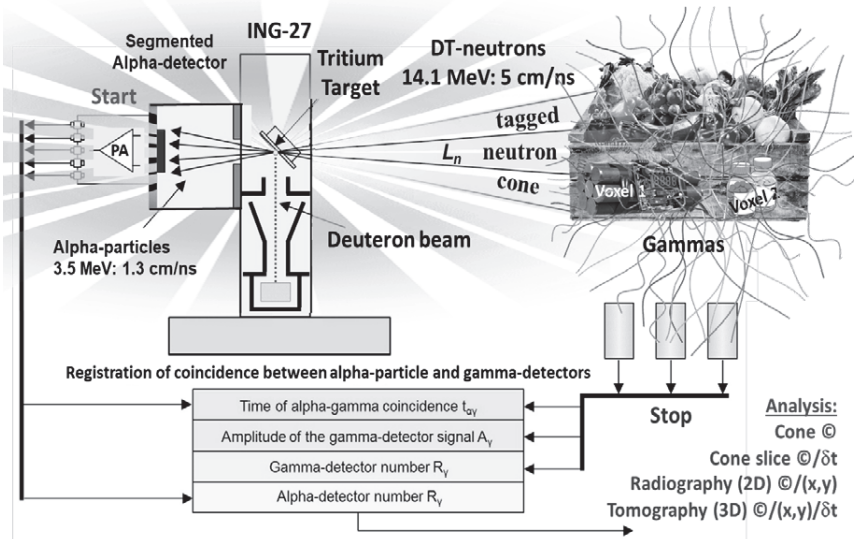


Fig. 3. TCAPM: The 14-MeV neutron is tagged in time and direction by detecting the associated  $\alpha$ -particle, emitted in opposite direction, by a 64-pixel Si  $\alpha$ -detector. Recording the coincided pulses from the  $\alpha$ -particle and  $\gamma$ -ray detectors in different time-windows, one can investigate the content of any voxel of the target object [7].

The well-established associated-particle technique is distinguished by the source neutrons being tagged in time and direction by the particles, which are simultaneously emitted in the nuclear reaction generating the neutrons. Associated Particle Imaging (API) has been applied to bulk sample analysis due to the emergence of the associated-particle sealed-tube neutron generator (APSTNG), making use of the  ${}^3\text{H}(d,n){}^4\text{He}$  reaction. In the APSTNG, deuterons are accelerated to 100 keV, producing 14.1-MeV neutrons and 3.5 MeV alpha-particles, which are emitted in opposite directions, as illustrated in Fig. 3 [7]. Each alpha-particle, which is detected in the position-sensitive detector, tags the direction of the associated neutron. These neutrons then scatter inelastically on nuclei in the interrogated material, producing characteristic  $\gamma$ -rays in a similar fashion to the available fast-neutron techniques (FNA, PFNA and PFTNA). Knowledge of the direction and speed (5.2cm/ns) of the neutron and the speed of the  $\gamma$ -rays (30 cm/ns) allow the position of the scattering nuclide to be located in space. The main advantage of this approach is that the interrogating neutron beam does not need to be pulsed, allowing the use of cheaper sealed-tube neutron generators. However, these generators do have a finite lifetime and typically need to be replaced after  $\sim 800$ -900 hours, if operated to produce  $\sim 10^7$  neutrons per second.

### Experiment Setup Model Simulation

In the framework of TANGRA project [8], using GEANT4 simulation toolkit we modelled the geometry of the experimental setup and determined the timing and energy characteristics of gamma-rays from  ${}^{24}\text{Mg}(n,n'\gamma){}^{24}\text{Mg}$  for “Romashka” gamma-ray detector system. This multi-detector  $\gamma$ -ray detecting system consists of 22 hexagonal NaI(Tl) radiation detectors,

situated around the target-sample (Fig. 4, left). This geometry allows measuring the angular distribution of characteristic gamma-rays (CGR) from the INS of 14-MeV neutrons on  $^{24}\text{Mg}$  with a good angular resolution, while preserving an optimal efficiency of their registration.

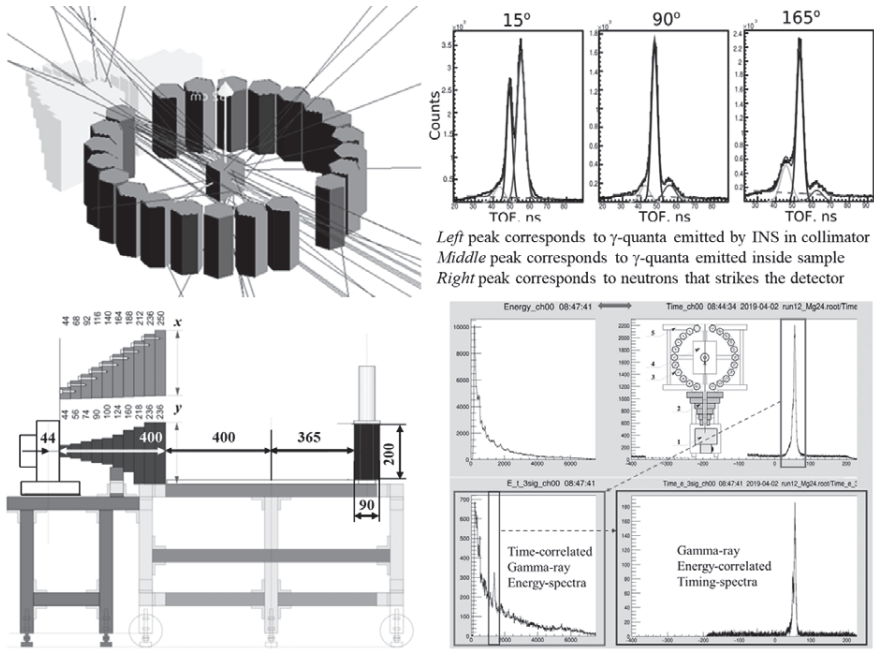


Fig. 4. GEANT4 simulation of TANGRA NaI(Tl) “Romashka” setup (left), the gamma-ray timing spectra (top right), the time- and energy- correlated timing- and energy- spectra (bottom right).

The expected time-resolution function of the system, as well as the timing- and energy- spectra at 3 angles ( $15^\circ$ ,  $90^\circ$ ,  $165^\circ$ ) of registration of CGR, relative to the direction of the incident neutrons, are shown in Fig. 4, top-right. The contribution from the gamma-rays, originating from different parts of the model setup, is clearly seen and can be distinguish by using the time-correlated associated particle method and analyzing the data in time- and energy- windows (ToF-Energy gating).

### Experimental Setup

For investigating the energy spectra and angular distribution of gamma-rays from INS of 14-MeV neutrons on the nuclei of  $^{24}\text{Mg}$  we designed, constructed and used 3 multi-detector, multi-purpose, multi-functional, mobile TANGRA system setups [9]. They consist of ING-27 portable generator of ‘tagged’ neutrons with energies of  $\sim 14.1$  MeV, with or without an iron shield-collimator, 2D fast-neutron beam profilometer [10], arrays of neutron-gamma detectors in geometry of daisy-flower (“Romashka”, “Romasha”, HPGe), and a 32-channel computerized system for data acquisition and analysis (DAQ).

The Portable Neutron Generator ING-27 is a D-T Neutron Generator, manufactured by VNIIA (Moscow, Russia) that utilizes  ${}^3\text{H}(d, n){}^4\text{He}$  reaction to produce 14-MeV neutrons and has a pixelated charge-particle detector, embedded in its sealed-tube vacuum chamber. The main characteristics of ING-27 are listed in Table 1. The beam of deuterons is accelerated up to  $\sim 120$  keV (in Lab-frame) and bombards a tritiated Ti-target (TiT) in the generator assembly. The generator has a rated 14-MeV neutron output of up to  $10^8$  n/s in  $4\pi$ . The main advantages of a D-T neutron generator with built-in position-sensitive detector of accompanying  $\alpha$ -particles over an isotopic sources like  ${}^{252}\text{Cf}$ ,  ${}^{210}\text{Po}$ -,  ${}^{241}\text{Am}$ -,  ${}^{238,239}\text{Pu}$ -Be are: 1) neutrons with higher energies, produced in D-T fusion reaction, having higher cross-sections of inelastic scattering on nuclei of light chemical elements; 2) position sensitivity, which provides information about which area of space is actually being investigated, helping to extract events coming from small objects, “hidden” inside a large volume of “parasitic” material; 3) neutron generator can be switched off, making it safe during transportation and storage; 4) the activation of the investigated objects and the generator’s constructive materials is negligible.

The TANGRA NaI(Tl) setup, consisted of ING-27 and “Romashka” gamma-ray spectrometer, built according to GEANT4 simulation studies, is shown in Fig. 5, where some important information on the DAQ and main counting and spectrometric characteristics of the experimental system is given, also. The analogue signals from the  $\alpha$ -particle and  $\gamma$ -ray detectors are fed to a 32-channels computerised data-acquisition (DAQ) system, where after digitizing the waveform are saved in list-mode (consequently one-by-one) by ADCM-software. List-mode files contain energy (ADC number) of each event detected along with a time-stamp when the event happened. Offline, the saved waveforms are analysed with ROMANA software, by which are determined the time-of-registration and the amplitude of each digitized signal, and the timing and amplitude (energy) spectra histograms are constructed. The procedure is depicted in Fig. 4, bottom right.

The gamma-ray efficiency of every NaI(Tl) detector (gamma-ray full-energy peak) was determined at various gamma-ray energies, using standard point-like gamma-ray sources  ${}^{137}\text{Cs}$  (661.8 keV),  ${}^{60}\text{Co}$  (1173 keV, 1332 keV) and a  ${}^{238}\text{PuBe}$  neutron-gamma source (the shape of its gamma-ray energy distribution is dominated by the 4.44-MeV gamma-ray, associated with the decay of the first excited  $2^+$ -state of  ${}^{12}\text{C}$  ( $\alpha + {}^9\text{Be} \rightarrow n + {}^{12}\text{C}^*$ ) with a 4.44-MeV gamma-quantum). The results from the measurements were in very good agreement with those obtained by GEANT4 software.

Table 1. Main characteristics of ING-27

	
Characteristic	Value
TiT-to-front distance	$44.0 \pm 1.4$ mm
TiT-to- $\alpha$ -detector distance	$100 \pm 2$ mm
Power supply voltage	$200 \pm 5$ V
Max Power Supply Current	$300 \pm 30$ mA
Consumed Power	$< 40$ W
Continuous Mode, n-energy	14-MeV neutrons
Initial Intensity	$> 5.0 \times 10^7$ n/s/4 $\pi$
Final Intensity	$> 2.5 \times 10^7$ n/s/4 $\pi$
Double-side Si $\alpha$ -particles detector	
Number of pixels	64 (8x8 strips)
Pixel area	$6 \times 6$ mm <sup>2</sup>
Distance between strips	0.5 mm
Voltage bias	$\sim 250$ V DC
Dark current	$< 5$ $\mu\text{A}$
n-tube life-time	$> 800$ h
ING-27 <Duty time>	$> 18$ months
Weight: ING-27	$7.5 \pm 0.5$ kg
Power and Operation Unit	$2.7 \pm 0.3$ kg

Two Mg-contain samples of different type and shape were used: a plastic box (10×10×10cm) filled with high-purity MgO and an Al-box (6×6×14cm) filled with fine metallic Mg-chips. The sizes of the samples were optimized by GEANT4 simulations to minimize the fast neutron attenuation and gamma-ray absorption.

In the measurements only one tagged neutron beam (one  $\alpha$ -pixel detector) was used to avoid the correction of the angular distributions of the gammas, caused by INS of neutrons from the nearby tagged neutron beams that touched the samples at average angles  $\sim 4^\circ$ , relative to the used one. A photo of TANGRA “Romashka” setup, together with some important characteristics (and details) of its basic components, are shown in Fig. 5.

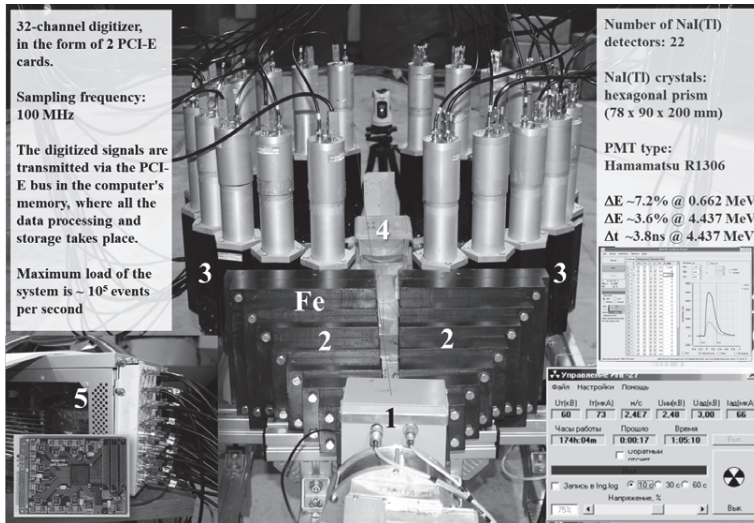


Fig. 5. Experimental setup: 1 – ING-27, 2 – 40cm-thick Fe shielding-collimator, 3 – NaI(Tl) probes, 4 – target, 5 – computerized AFI Electronics ADCM DAQ.

## Experimental Results Analysis and Interpretation

A typical gamma-ray energy spectrum, measured with this setup, is shown in Fig. 6. This energy spectrum is of the gamma-rays from a time-interval of 6 ns (T-window {54-60} ns, Fig. 4, top right) and corresponds mainly to the interactions of neutrons with the nuclei of the sample, because for this time-interval the 14-MeV neutrons, covering a distance of  $\sim 30$ cm, can inelastically scatter mainly on the nuclei of Al support. The contribution of random coincided pulses (uncorrelated background) can be estimated from a time-interval of the same length taken outside the true-coincidence window. The correlated radiation background can be reduced by taking narrower true-coincidence time-windows or can be subtracted from the energy spectrum by approximating it with a spline function (dashed line in Fig. 6). Because of the moderate energy resolution of NaI(Tl) not many gamma-lines can be resolved. Particularly it can be said for gamma-line at  $\sim 3866$  keV from  $3^+ \rightarrow 2^+$  transition in  $^{24}\text{Mg}^*$ , as well as, for the gamma-lines from  $^{16}\text{O}(n,n'\gamma)$ -reaction above 5 MeV, where the efficiency of registration of gamma-rays with these energies is also smaller.

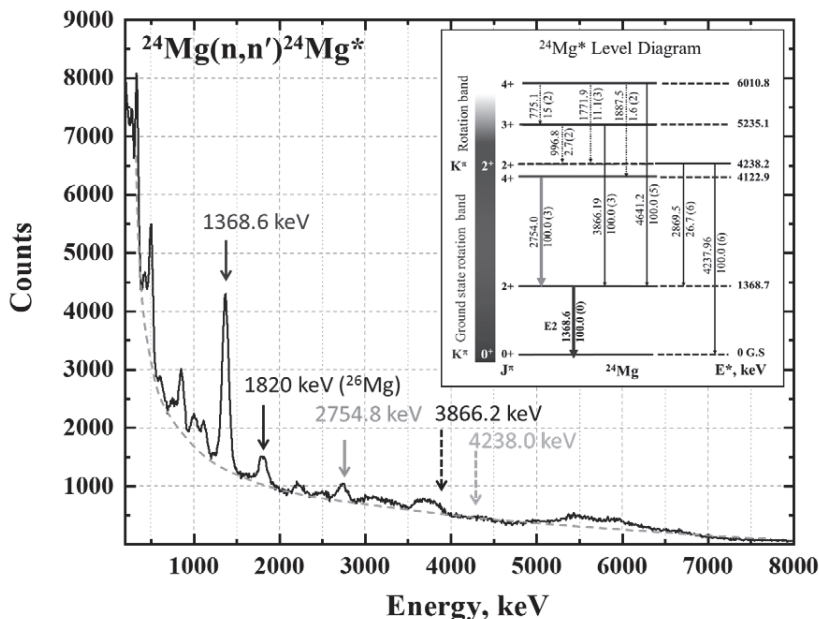


Fig. 6. Gamma-ray energy spectrum, measured with “Romashka” NaI(Tl) system and the decay scheme of  $^{24}\text{Mg}^*$ , exited by INS of 14.1-MeV neutrons.

The weaker peaks at  $\sim (1014, 2211, 3004)$  keV are from  $^{27}\text{Al}(n,n'\gamma)$ -reaction, those at  $\sim (847, 1038, 1238)$  keV are from INS-reactions in the Fe shielding-collimator:  $^{56}\text{Fe}(n,n'\gamma)$ -reaction. The strongest line produced by inelastic reactions on  $^{24}\text{Mg}$  is at  $\sim 1369$  keV, resulting from transitions from the first excited state to the ground state:  $2^+ \rightarrow 0$ , the small peak at  $\sim 2755$  keV can be from transition  $4^+ \rightarrow 2^+$ . After subtracting the background contribution, the peak at  $\sim 1369$  keV was approximated by a Gauss function and its parameters (the peak energy, area and standard deviation) were determined by least-square fit procedure. It was done for the energy spectra from all 22 NaI(Tl) gamma-spectrometers. The full-energy peak area values were corrected for different intrinsic and geometrical efficiencies of the gamma-detectors. The corresponding values in the intervals  $[15^\circ, 135^\circ]$  and  $[-15^\circ, -135^\circ]$  (the angles are related to the tagged neutron beam axis) with a step of  $15^\circ$  were averaged and the mean values were used to plot the angular distributions of gamma-rays from INS-reaction on some light elements [11–12]. The results for Mg were normalized to the A-value at  $90^\circ$  in order to compare them with the data from other authors [13–19], which is shown in Fig. 7. It is seen that our experimentally determined anisotropy (A) of irradiation of gamma-rays with energy of  $\sim 1369$  keV from first  $2^+$  state of  $^{24}\text{Mg}^*$  nucleus, in the interval of angles between  $\sim 45^\circ$  and  $\sim 135^\circ$ , and in the limits of the shown experimental uncertainties, are in reasonable agreement with the data of the cited authors for  $^{24}\text{Mg}(n,n'\gamma)$ -reaction for neutrons with energies between  $\sim 2.6$  MeV and  $\sim 14.7$  MeV (the INS-reaction threshold energy  $E_n^{\text{thr}} = 1.4$  MeV, Tab. 2). Below  $\sim 45^\circ$  and above  $\sim 135^\circ$  a decreasing of the anisotropy is revealed. The A-values at  $15^\circ (\pm 4^\circ)$  and  $165^\circ (\pm 4^\circ)$ , measured for the first time, keep this tendency.

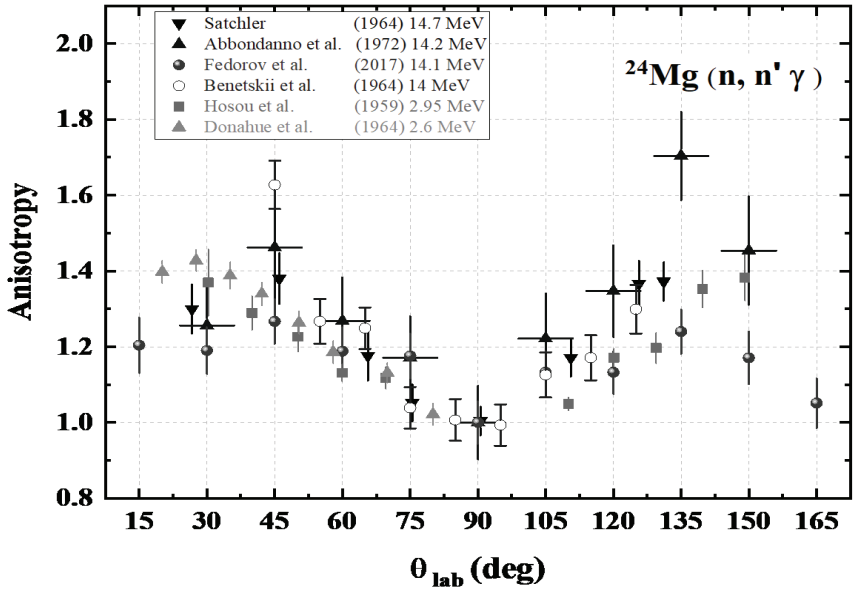


Fig. 7. Comparison of the anisotropy of irradiation of  $\gamma$ -rays during INS-reactions of 14.1-MeV neutrons with  $^{24}\text{Mg}$  ( $2^+$ , 1368.67 keV level), obtained in different experiments.

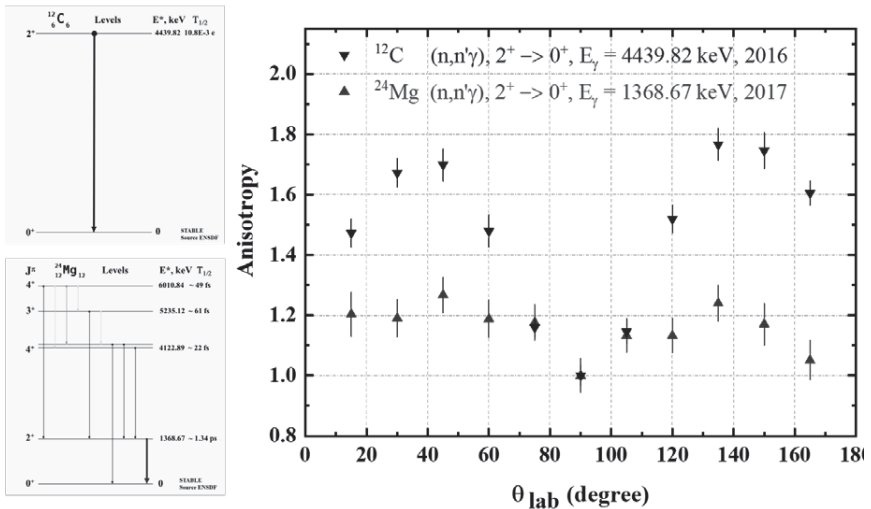


Fig. 8. Anisotropy of irradiation of  $\gamma$ -rays during INS-reactions of 14.1-MeV neutrons with  $^{12}\text{C}$  ( $2^+$ , 4439.82 keV level) and  $^{24}\text{Mg}$  ( $2^+$ , 1368.67 keV level).

Table 2. Main characteristics of the 1<sup>st</sup> excited state of the nucleus formed by INS-reaction.

Reaction	$E_n^{\text{thr}}$ , MeV	$\sigma_{\gamma}$ , mb	$J^{\pi} \rightarrow 0$	$T_{1/2}$	$E_{\gamma}$ , keV	$I_{\gamma}$ , %	$M_{\gamma}$
$^{12}\text{C} (n,n'\gamma)$	4.8	450	$2^+ \rightarrow 0$	10.8 meV	4438.94	100	E2
$^{16}\text{O} (n,n'\gamma)$	6.6	265	$3^- \rightarrow 0$	18.4 ps	6128.63	100	E3
$^{24}\text{Mg} (n,n'\gamma)$	1.4	600	$2^+ \rightarrow 0$	1.33 ps	1368.63	100	E2
$^{27}\text{Al} (n,n'\gamma)$	4.8	220	$7/2^+ \rightarrow 5/2^+$	26.6 fs	2212.01	100	M1+E2

In (Fig. 8, left) are shown the gamma-decay scheme of excited nucleus  $^{12}\text{C}^*$  (the only one level) and  $^{24}\text{Mg}^*$  (only levels build on the base rotation band with  $K^{\pi}=0^+$  are shown).

In (Fig. 8, right) we show the anisotropy coefficient as function of the angle of irradiation of the gamma-rays during the decay of 1368.67 keV  $2^+$  level of  $^{24}\text{Mg}^*$  to the 0-level (ground state, g.s.) in comparison with the A-values for 4.439.82 keV  $2^+$  level of  $^{12}\text{C}^*$ , obtained by us with the same experimental setup [11]. It is well known that the angular distribution of the first  $\gamma$ -ray from the decaying cascade is less isotropic than that of the following  $\gamma$ -rays because each successive gamma-emission causes a spread in the direction of the CN-spin. The feeding of low-lying levels from higher lying also attenuates the angular distribution, as can be seen in Fig. 8 for the anisotropy of the first  $\gamma$ -ray from  $2^+$  excited states of  $^{12}\text{C}^*$  and  $^{24}\text{Mg}^*$  in  $^{12}\text{C}(n,n'\gamma)$  and  $^{24}\text{Mg}(n,n'\gamma)$  reactions.

## Conclusions and Outlook

Using ING-27 portable generator of 14-MeV “tagged” neutrons, 22 NaI(Tl) gamma-ray spectrometer “Romashka” and time-correlated associated particle method (TCAPM), we measured the angular distribution of gamma-rays from the first excited state  $2^+$  of  $^{24}\text{Mg}$  formed by inelastic scattering (INS) of 14.1 MeV neutrons on the nuclei of this isotope,  $^{24}\text{Mg}(n,n'\gamma)$ -reaction. Our results agree with the data from the literature in the range of their experimental uncertainties. The anisotropy values at  $\sim 15^\circ$  and  $\sim 165^\circ$  are measured for the first time. Meanwhile, we measured the timing- and energy- spectra of gamma-rays from this reaction by a HPGe gamma-ray spectrometer, in order to determine the angle-integrated gamma-ray production cross-sections for each observable transition. A comparison of recorded gamma-ray energy spectra is shown in Fig. 9. Recently, by means of the new constructed 18 BGO array “Romasha” we have measured the angular distributions of gamma-rays from 6 excited states of  $^{24}\text{Mg}$  in the angular range from  $14^\circ$  to  $136^\circ$  (step of  $14^\circ$ ) with a good accuracy and precision.

The angular distributions for discrete reactions are conventionally given in the Center-of-Mass (CM) frame, while the energy-angular distributions for continuum reactions are conventionally given in the Laboratory (Lab) frame. However, the energy-angular distributions are often given in the CM frame in ENDF. The high-order Legendre polynomials are commonly used to describe the anisotropy of angular distributions.

Because the gamma-ray angular distributions are symmetric about  $90^\circ$  they can be expressed as a series of even order Legendre polynomials (0, 2, and 4) and their coefficient  $a_0$ ,  $a_2$  and  $a_4$  can be determined. The coefficients of the Legendre polynomials are obtained by a least-squares fit of the measured angular-distribution data. Angle-integrated gamma-ray production cross-sections are obtained by integrating the angular distribution over the full  $4\pi$ -solid angle. Using the orthonormal condition of the Legendre polynomials, the integrated cross-section becomes  $\sigma_{\text{tot}} = 4\pi a_0$ . The results from the last experiments will be published elsewhere [20].

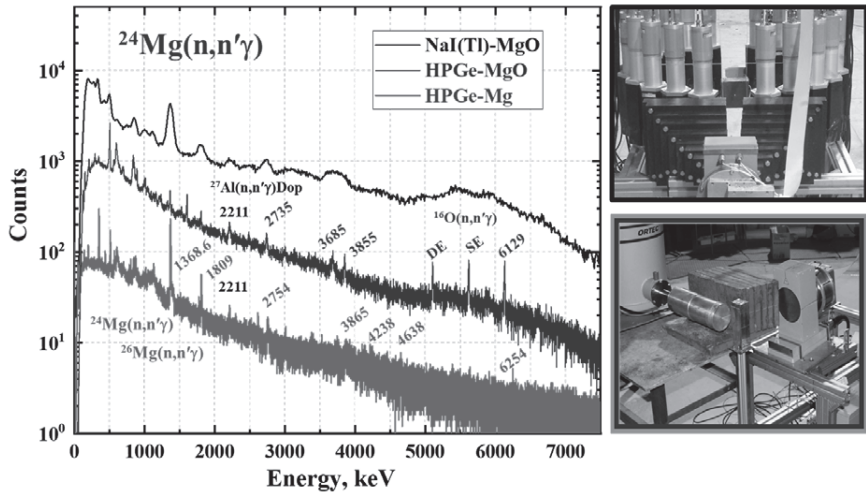


Fig. 9. The energy spectra of  $\gamma$ -rays from INS-reaction of 14.1-MeV tagged neutrons on  $^{24}\text{Mg}$  ( $2^+$ , 1368.67 keV) by “Romashka” (MgO, top), HPGe (MgO, middle) and HPGe (Mg, bottom).

## References

1. Remco C. Hin, Christopher D. Coath, Philip J. Carter, Francis Nimmo, Yi-Jen Lai, Philip A.E. Pogge von Strandmann, Matthias Willbold, Zoë M. Leinhardt, Michael J. Walter, and Tim Elliott, Magnesium isotope evidence that accretional vapor loss shapes planetary compositions, *Nature* **549** (2017) 511–515, <https://doi.org/10.1038/nature23899>
2. Nuclear Data Needs and Capabilities for Applications, white paper edited by Shamsuzzoha Basunia, Lee Bernstein, David Brown, Aaron Hurst, Toshihiko Kawano, John Kelley, Filip Kondev, Elizabeth McCutchan, Caroline Nesaraja, Rachel Slaybaugh, and Alejandro Sonzogni, LLNL Report LLNL-CONF-676585 (2015); <http://bang.berkeley.edu/events/ndnca/whitepaper>
3. The Generation IV International Forum, online: <http://www.gen-4.org/>
4. L.A. Sonzogni, National Nuclear Data Center, Brookhaven National Laboratory, <https://www.nndc.bnl.gov/nudat2/>
5. ENDF/B-VIII, 2018, <https://www.nndc.bnl.gov/exfor/servlet/E4sMakeE4>.
6. A. Olacel, C. Borcea, P. Dessagne, M. Kerveno, A. Negret, and A. J. M. Plompen, Neutron inelastic cross-section measurements for  $^{24}\text{Mg}$ , *Phys. Rev. C* **90** (2014) 034603, <https://doi.org/10.1103/PhysRevC.90.034603>
7. E.P. Bogolyubov, A.V. Gavryuchenkov, M.D. Karetnikov, D.I. Yurkov, V.I. Ryzhkov, V.I. Zverev, Neutron generators and DAQ systems for tagged neutron technology, Proceedings of the XXVI International Symposium on Nucl. Electronics & Computing (NEC'2017), Becici, Budva, Montenegro, September 25–29, (2017)176–181, <http://ceur-ws.org/Vol-2023/176-181-paper-27.pdf>
8. JINR-FLNP TANGRA project, <http://flnph.jinr.ru/en/facilities/tangra-project>.
9. Ivan Ruskov, Yury Kopatch, Vyacheslav Bystritsky, Vadim Skoy, Valery Shvetsov, Franz-Josef Hamsch, Stephan Oberstedt, Roberto Capote Noy, Dimitar Grozdanov, Artem Zontikov, Yury Rogov, Nikolay Zamyatin, Mikhail Sapozhnikov, Vyacheslav

- Slepnev, Evgeny Bogolyubov, Andrey Sadovsky, Yury Barmakov, Valentin Ryzhkov, Dimitry Yurkov, Vladivoj Valković, Jasmina Obhodaš, and Fuad Aliyev, TANGRA – an experimental setup for basic and applied nuclear research by means of 14.1 MeV neutrons, *European Physics Journal (EPJ) Web of Conferences* **146**, 03024 (2017), <https://doi.org/10.1051/epjconf/201714603024>
10. Zamyatin, N.I., Bystritsky, V.M., Kopach, Y.N., Aliev, F., Grozdanov, D.N., Fedorov, N.A., Hramko, C., Ruskov, I.N., Skoy, V.R., Slepnev, V.M., Wang, D., Zubarev, E.V., Neutron beam profilometer on the base of double-sided silicon strip detectors, *Nuclear Instruments and Methods A* **898**, 2018, 46–52, <https://doi.org/10.1016/j.nima.2018.04.031>
  11. N.A. Fedorov, T.Yu. Tretyakova, Yu.N. Kopatch, V.M. Bystritsky, D.N. Grozdanov, F.A. Aliyev, I.N. Ruskov, V.R. Skoy, C. Hramco, E.P. Bogolyubov, Yu.N. Barmakov and TANGRA collaboration, Angular distribution of gamma rays from the inelastic scattering of 14 MeV neutrons on light nuclei, XXV<sup>th</sup> Int. Seminar on Interaction of Neutrons with Nuclei, ISINN-25, 2017, Dubna., <http://isinn.jinr.ru/past-isinns/isinn-25/25/Fedorov.pdf>
  12. N.A. Fedorov, T.Yu. Tretyakova, Yu.N. Kopatch, V.M. Bystritsky, D.N., Grozdanov, F.A. Aliyev, I.N. Ruskov, V.R. Skoy, C. Hramco, E.P., Bogolyubov, Yu.N. Barmakov and TANGRA collaboration, Angular distribution of gamma rays from the inelastic scattering of 14-MeV neutrons on light nuclei, <http://isinn.jinr.ru/proceedings/isinn-25/pdf/fedorov.pdf>
  13. S.C. Mathur, W.E. Tucker, R.W. Benjamin, I.L. Morgan, Angular distributions of gamma rays produced by neutron bombardment of Al, Mg and Si, *Nuclear Physics* **73/3** (1965) 561–578, [https://doi.org/10.1016/0029-5582\(65\)90701-7](https://doi.org/10.1016/0029-5582(65)90701-7)
  14. K. Nyberg-Ponnert, B. Jönsson and I. Bergqvist, Gamma Rays Produced by the Interaction of 15 MeV Neutrons in N, O, Mg and Al, *Physica Scripta*. Vol. **4**, 165–173, 1971, <https://doi.org/10.1088/0031-8949/4/4-5/004>
  15. D.T. Stewart, P.W. Martin. Gamma Rays From the Interaction of 14 MeV Neutrons with C<sup>12</sup> and Mg<sup>24</sup>, *Nuclear Physics* **60/2** (1964) 349–352, [https://doi.org/10.1016/0029-5582\(64\)90669-8](https://doi.org/10.1016/0029-5582(64)90669-8)
  16. U. Abbondanno, R. Giacomich, M. Lagonegro and G. Pauli, Gamma rays resulting from nonelastic processes of 14.2 MeV neutrons with sodium, magnesium, silicon, sulphur, titanium, chromium and iron, *Journal of Nuclear Energy* **27/4** (1973) 227–239, [https://doi.org/10.1016/0022-3107\(73\)90058-0](https://doi.org/10.1016/0022-3107(73)90058-0)
  17. B.A. Benetskii, Yu. P. Betin, Ya. Gonzatko, Inelastic Scattering of 14 MeV Neutrons on Mg<sup>24</sup>, *Journal of Experimental and Theoretical Physics (JETP)*, 1964, Vol. **18**, No. 3, p. 640, [http://www.jetp.ac.ru/cgi-bin/dn/e\\_018\\_03\\_0640.pdf](http://www.jetp.ac.ru/cgi-bin/dn/e_018_03_0640.pdf)
  18. Masanao Hosoe, Shoji Suzuki, Gamma Rays from Neutron Inelastic Scattering of Magnesium, Aluminum, Iron and Bismuth, *Journal of the Physical Society of Japan* **14/6** (1959) 699–707, <https://doi.org/10.1143/JPSJ.14.699>
  19. D.J. Donahue, R.D. Roberts, Angular distributions of gamma-rays from (n, n'γ) reactions in Mg<sup>24</sup> and Fe<sup>56</sup>, *Nuclear Physics* **50** (1964) 641–647, [https://doi.org/10.1016/0029-5582\(64\)90236-6](https://doi.org/10.1016/0029-5582(64)90236-6)
  20. N.A. Fedorov, D.N. Grozdanov, Yu.N. Kopach, V.M. Bystritsky, T.Yu. Tretyakova, I.N. Ruskov, V.R. Skoy, S. Dabylova, F.A. Aliev, C. Hramko, N.A. Gundorin, I.D. Dashkov, E.P. Bogolyubov, D.I. Yurkov, A. Gandhi, A. Kumar, Measurement of yields and angular distributions of γ-quanta generated during the interaction of 14.1 MeV neutrons with magnesium nuclei, to be published in *Bulletin of the Russian Academy of Sciences*, (in Russian), <http://www.izv-fiz.ru/>

**Applied and Methodical  
Aspects of Neutron Physics,  
Calculations**

# Comparison of Artificial Neural Network Architectures by the Separation Quality of Signals from a Digital Neutron Spectrometer

T. Bobrovsky, P. Prusachenko, V. Khryachkov

*Institute for Physics and Power Engineering, Obninsk, Russia*

## ABSTRACT

Machine learning is one of the popular methods for analyzing and processing complex data. Despite shown good accuracy, Applying it in the scientific field is hindered by the unpredictable neural networks behavior. Thus, incorrect results can be able caused by applying neural networks to separate particles in scintillator. Therefore, it was necessary to compare series different neural networks architectures and to find out the feasibility of their application to the task of separating particles according to the shape of the pulse.

## 1. INTRODUCTION

Mostly, gamma radiation goes with neutron radiation. For this reason, ability of most organic scintillators to separate signals by pulse shape is very important. At nowadays, to separate the signals by pulse shape uses both digital and analog methods. At the same time, there is the possibility of using artificial neural networks (ANN). A number of studies have shown good results of using ANNs to solve this problem [1–3, 5–6]. However, in the most works published on this topic, there are no sound estimates of the quality of the separation of signals in relation light output. Comparison of different architectures has not done.

The purpose of this work was to train several types of ANNs, to obtain a reasonable estimate of the recoil protons false count rate and the efficiency of registration of recoil protons.

## 2. MATERIALS AND METHODS

In this work, we had used early-obtained in [6] data. In [6] neutrons spectrum of  $^{252}\text{Cf}$  spontaneous fission was measured by using time-of-flight method. To detect neutrons we used crystal stilbene with size  $2 \times 2$  cm. This scintillator was paired with PMT EQ Enterprise 9813 QB. An offset voltage of 1150 V was applied to it. Thin  $^{252}\text{Cf}$  layer was placed on flat parallel ionizing chamber cathode. Chamber inter electrode gap was 2 mm. Signals form ionizing chamber gained in charge sensitive amplifier. PMT signals and chamber signals digitized with Ultraview AD14-500MHz and wrote together. Last dynode was source of trigger signal accumulated about 3.8 million events.

Supervised learning is main method to train ANN. In a few words, ANN takes sample of data and configures inherent state to produce required data, for example, event class. For this training method is necessary to obtain training data set which, in our case, represented as labeling signals set. Signals labeling was performed by correlation analysis [6]. The separation parameter R is determined from eq.1:

$$R = \frac{\text{Max}(\sum_{j=-inf}^{inf} f_j * g_{i-j})}{A}, \quad (1)$$

where A – signal area,  $f$  – analyzed signal,  $g$  – averaged electron signal.

For low light-output region separation curve was calculated by rule that false recoil protons number was less than 1%. For higher energy region, separation curve was passed through the intersection point of the particles distributions. The signals had length of 200 channels. Label “0” corresponded to recoil protons, “1” – electrons. Each signal was normalized to the maximum amplitude. Besides, for MICNN were calculated three additional signals: smoothed, differentiated, cumulative sum for each sample.

Table 1. Train set composition.

Energy window, keVee	Recoil protons	Electrons
45 – 124	1000	1000
124 – 520	1000	1000
520 – 915	500	500
915 – 1311	500	500

ANNs was performed by using the Python libraries Keras and Tensorflow [5, 9]. The following neural networks (fig.1) were investigated: single-layer perceptron (Per), multilayer perceptron (MLP), convolutional neural network (CNN), multi-input convolutional neural network (MICNN) [10], recurrent neural network (RNN). All layers in ANNs had activation function “ReLU”, besides LSTM [4] layer and output layer. Output layer of each ANN have sigmoid activation function. To avoid overfitting was used random weight zeroing (Dropout). Adam (adaptive moment estimation) optimizer we used to train ANNs. The loss function was mean squared error.

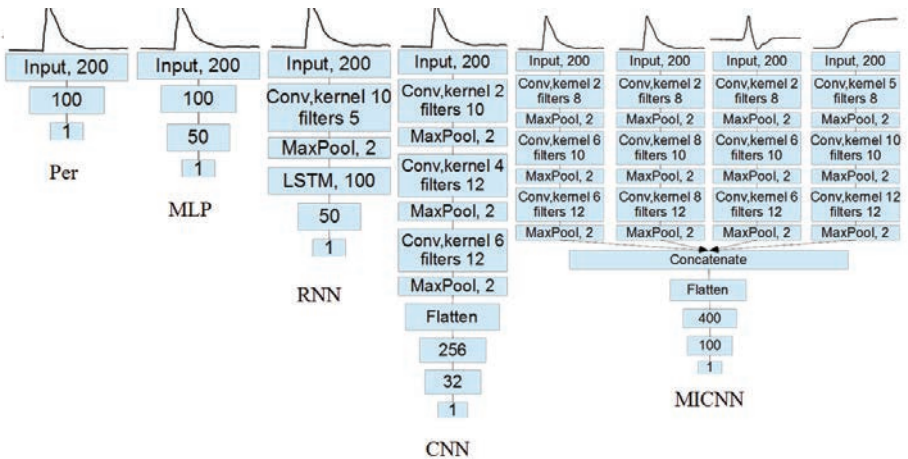


Figure 1. ANNs architectures.

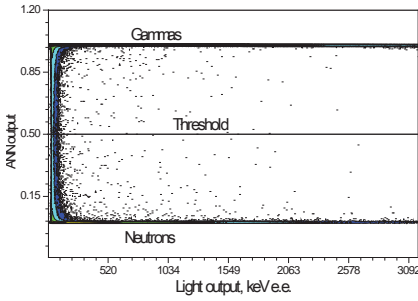


Figure 2. Example of two-dimensional spectra for MICNN.

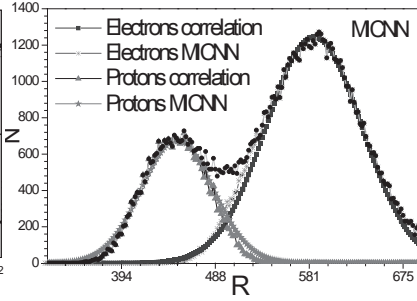


Figure 3. Correlation analysis for separated by MICNN particles at 45 keVee.

## 2.1 Separation quality

To calculate false count rate of recoil protons (Fig. 4) were used “clear” signals from electrons obtained using information about time-of-flight. The proportion of background neutrons in the instant gamma peak was about  $4.5 \cdot 10^{-5}$ .

False count rate is:

$$f = \frac{N_{FP}}{N_{TE} + N_{FP}}, \quad (2)$$

$N_{FP}$  – number of false identify protons,  $N_{TE}$  – number of true identify electrons.

Registration error of recoil protons was founded by eq. 3:

$$e = \frac{(A_{p,ap} - (A_{p,NN} - f * A_{e,ap}))}{A_{p,ap}}, \quad (3)$$

$f$  – false count rate of recoil protons,  $A_{p,ap}$  – number of recoil protons obtained from approximation of cuts two-dimensional spectrum for correlation analysis,  $A_{e,ap}$  – number of electrons obtained from approximation of cuts two-dimensional spectrum for correlation analysis,  $A_{p,NN}$  – number of recoil protons obtained by ANN.

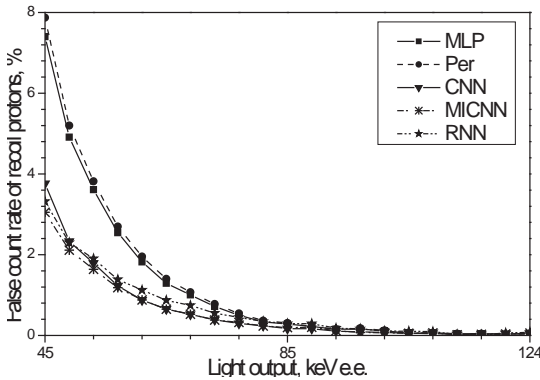


Figure 4. False count rate for ANNs.

All neural networks have similar values of false protons count rate and lost protons above 85 keVee (Figs. 4, 5). However, in low energy range the situation is changing. Complicated neural networks much less fault in definition particle type according to simple neural networks that mostly used in the earlier studies. At the same time registration efficiency of neutrons for complicated neural networks worse than for simple neural networks.

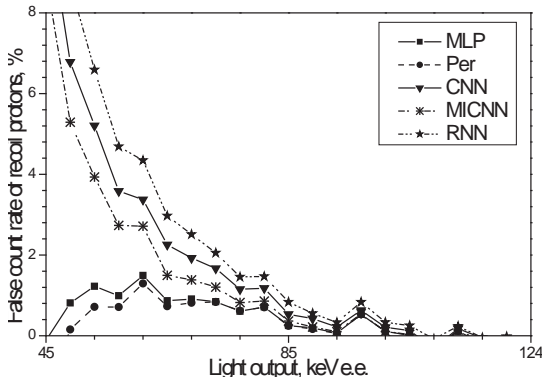


Figure 5. Proportion of lost recoil protons.

### 2.3 Performance

Processing speed was measured for kernels of each algorithm. For neural network was measured time for front propagation, CI – integrals calculation, correlation analysis – parameter R (eq.1) calculation. The test was carried out on PC that had the following characteristic: four-threaded Intel core i3-3220 3.3 GHz processor, DDR3 4 GB RAM, windows 7x64.

Table 2. Processing time for 1000 samples.

Algorithm	time, ms
Correlation analysis	37.8
Charge integration	1.3
Per	3.9
MLP	6.6
CNN	65.5
MICNN	181.7
RNN	374.8

### CONCLUSION

A reasonable estimate of the false identification of neutrons by neural networks has been obtained. Was compared the several neural network architectures. The comparison was made of the operation speed of some standard digital algorithms for separating signals according to the pulse shape and the presented artificial neural networks. By the level of false

classification, convolutional neural networks showed better results, but the calculations take longer than classical methods.

#### REFERENCES

1. Doucet E. et al., NIM A, available online 24 Sep. 2018.
2. Fu C. and all. Annals of Nuclear Energy, Volume **120** (2018) 410–421.
3. Griffiths J. et al., physics.ins-det, 19 July 2018.
4. Hochreiter Sepp and all. Neural Computation **9**(8), (1997) 1735–1780.
5. Keras: The Python Deep Learning library.
6. P.S. Prusachenko et al., NIM A, Volume **905** (2018) 160–170.
7. Söderström P.-A. et al., NIM A, Volume **916** (2019) 238–245.
8. Tambouratzis T. et al., JAISCR. December 2014.
9. Tensorflow. An end-to-end open source machine learning platform.
10. Zhicheng Cui et al., cs.CV, 22 Mar 2016.

# SOME IMPROVEMENTS OF THE DATA PROCESSING ALGORITHMS IN THE TIME-OF-FLIGHT MASS-SPECTROMETRY OF HEAVY IONS

D.V. Kamanin<sup>1</sup>, Yu.V. Pyatkov<sup>1,2</sup>, Z.I. Goryainova<sup>1</sup>, V.E. Zhuchko<sup>1</sup>,  
A.A. Alexandrov<sup>1</sup>, I.A. Alexandrova<sup>1</sup>, P.Yu. Naumov<sup>2</sup>, R. Korsten<sup>3</sup>, V. Malaza<sup>3</sup>,  
E.A. Kuznetsova<sup>1</sup>, A.O. Strelakovsky<sup>1</sup>, O.V. Strelakovsky<sup>1,4</sup>

<sup>1</sup>*Joint Institute for Nuclear Research, Dubna, Russia*

<sup>2</sup>*National Nuclear Research University MEPhI (Moscow Engineering Physics Institute), Moscow, Russia*

<sup>3</sup>*University of Stellenbosch, Faculty of Military Science, Military Academy, Saldanha 7395, South Africa*

<sup>4</sup>*Dubna State University, 141980 Dubna, Russia*

## INTRODUCTION

The physical program implemented by the FOBOS group more than ten last years is dedicated to the study of different manifestations of clustering in heavy low excited nuclei [1, 2]. In the mass correlation distribution of fission fragments (FFs) from  $^{252}\text{Cf}$  (sf) and  $^{235}\text{U}(n_{\text{th}}, f)$  reaction a specific two-dimensional region of increased yields that is far from the loci of conventional binary fission has been revealed for the first time. In its projection onto the axis of light FFs, there are two peaks corresponding to the magic isotopes  $^{68}\text{Ni}$  and  $^{72}\text{Ni}$ , which is why we dubbed the region the “Ni-bump”. The experimental yield of the events that make up the bump does not exceed  $4 \cdot 10^{-3}$  per binary fission.

The Ni-bump is one of the most clear manifestations of a new type of ternary decay of heavy nuclei, called by us collinear cluster tri-partition (CCT) due to the specific features of the decay, namely the decay partners fly apart almost collinearly, and at least one of them shows magic nucleon composition.

In addition, for the first time we have observed the binary break-up of the fission fragment due to inelastic scattering in the metal foil with a thickness close to the total range of fission fragments [3]. The residual energy of the fragment does not exceed several MeV. Based on the obtained results we suppose that the fragments directly after scission of the mother system look like a di-nuclear system consisting of the magic core and the light cluster.

Four features of the processes under study essential for the experimental method to be used should be underlined: a relatively low yield of the events to be searched for ( $10^{-5}$ – $10^{-3}$  per binary fission); a large range of the masses (4–210 u) and energies (2–110 MeV) of the decay products; very small,  $\sim 1^\circ$ , open angle between the partners flying in the same direction; and short, up to a zero, time interval between the sequential hits of the PIN-diode by these fragments.

Most of the results were obtained using the “missing mass” approach which means that two decay products (fragments) are detected in coincidence using a double armed time-of-flight (TOF) spectrometer, while the significant difference between their total mass  $M_s = M_1 + M_2$  and the mass of a mother system serves as a sign of at least ternary decay. A fragment mass is calculated by the energy  $E$  and the velocity  $V$  using time-of-flight spectrometers based on the mosaics of PIN-diodes.

The use of semiconductor detectors for measuring ion's energy and for obtaining time stamp has two methodological issues that are necessary to address. First of them is the pulse-height defect (PHD) that manifests itself in a form of seemingly less energies than particles actually have. The second is the plasma delay effect (PD) that prevents precise measurement of the fragment TOF. Our experimental method provides solution of the both these problems. The method was presented in Refs [6, 7]. At the first stage, the digital images of all the detector signals are obtained using CAEN Switched Capacitor Digitizer DT5742, while all subsequent signal processing is performed off-line. The FFs mass and energy reconstruction procedure is based on the PHD parameterization proposed in Ref. [8]. To avoid the influence of the PD effect, an original time-pickoff "sewing-parabola" method proposed in Ref. [7] is used.

In this work:

- an analytical justification is given for the method of measuring the energy of a heavy ion with an arbitrary response function of the preamplifier of the PIN diode signal (previously, the correctness of the method was confirmed only empirically and only for FFs [8]);
- pulse-height defect parametrization for registration of fission fragments of PIN diode is refined;
- the results of testing the time-pickoff "sewing-parabola" method in a differential experiment are presented.

## ION ENERGY SPECTROMETRY AT HIGH COUNTING RATE OF THE SPECTROMETER

In the classical approach, to estimate the charge  $q$  created by an ion in the detector volume, the area under the input current graph  $i(t)$  is calculated:

$$E \sim q = \int_{-\infty}^{\infty} i(t)dt \quad (1)$$

In its turn,  $q$  is proportional to the ion energy  $E$  in the absence of PHD. In practice, it means that the current  $i(t)$  is integrated with the time constant much larger than the current duration, and corresponding voltage impulse looks like a long (tens microseconds) stair-step, while time interval between the sequential hits of two CCT products of a PIN-diode could lie in the nanosecond range. For independent registration of such signals (so called "double hit" mode) they must be short shaped. In order to avoid overlap, a similar requirement for the signal duration arises when the spectrometer is operating in conditions of high counting rate.

Let us show that with an arbitrary response  $h(t)$  of the spectrometric electronic circuit connected to the detector the area of the output signal  $S$  stays proportional to the charge  $q$ . Given the linearity of the system at the output of this external circuit, a response  $U(t)$  to the current  $i(t)$  can be calculated as follows:

$$U(t) = \int_0^t i(r)h(t-r)dr \quad (2)$$

That is, the convolution of the function describing the input current  $i(t)$  with the response function of the subsequent electronic path  $h(t)$ .

According to the meaning of the problem,  $U(t)$  is the shape of the pulse supplied to the input of the digitizer. The area  $S$  of the pulse  $U(t)$  is determined by the expression:

$$S = \int_0^{\infty} U(t) dt = \int_0^{\infty} \left\{ \int_0^t i(r) h(t-r) dr \right\} dt \quad (3)$$

This double integral could be reduced to two repeated ones (Fubini's theorem [9]):

$$S = \int_0^{\infty} U(t) dt = \int_0^{\infty} \left\{ \int_0^t i(r) h(t-r) dr \right\} dt = \int_0^{\infty} i(r) dr \int_r^{\infty} h(t-r) dt \quad (4)$$

Let us make a change of variables in the internal integral:

$$t \rightarrow z = t - r$$

Then  $z$  varies between  $0-\infty$  and:

$$S = \int_0^{\infty} i(r) dr \int_r^{\infty} h(t-r) dt = \int_0^{\infty} i(r) dr \int_0^{\infty} h(z) dz = C \int_0^{\infty} i(r) dr = Cq \quad (5)$$

where  $C = \text{const}$  is the area of the response function, and  $q$  is the charge created by the fragment in the detector. The constant  $C$  is calculated during calibration using alpha particles, under the assumption that there is no PHD for them.

The algorithm for estimating the charge created by a particle in the detector by finding its area avoids the ballistic error inherent to estimating  $q$  from the pulse amplitude [10]. The ballistic error is caused by the dependence of the amplitude of the pulse on its shape for any finite constant of integration of the current pulse  $i(t)$ . In the presence of a plasma delay, which depends on the mass and energy of the fragment, the presence of a ballistic error is guaranteed, which determines the relevance of the approach to measure the energy of CCT products based on formula (5).

The example of registration of the FFs in the double hit mode is presented in figure 1. As can be inferred from the figure, two FFs were detected in PIN diode during 200 ns registration gate. Each fragment also hits the start detector.

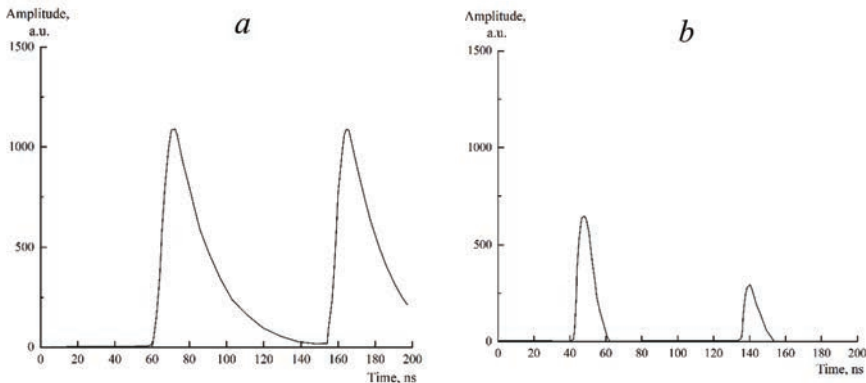


**FIGURE 1.** Example of registration of the FFs in the “double hit” mode. Signals from the same event at two different exits of the multichannel DT5742 digitizer are shown:  $a$  – signals from one of the PIN diodes of the mosaic;  $b$  – signals from the start detector.

## MODERNIZATION OF THE PHD PARAMETRIZATION

In order to take into account the FF pulse height defect  $R(M, E)$ , the following parameterization was proposed in Ref. [8]:

$$R(M, E) = \frac{\lambda E}{1 + \frac{\varphi E}{M^c}} + \alpha M^d E + \beta M^f E \quad (6)$$

Here  $E$  and  $M$  are the FF energy and mass. The formula includes the vector of parameters  $\{\lambda, \varphi, \alpha, \beta, c, d, f\}$ . In order to determine the constants, the authors of Ref. [8] analyzed all known experimental data on  $R(M, E)$  within the least squares' method (the  $\chi^2$ -method) using MINUIT program [11]. They demonstrated that the minimum value of  $\chi^2$  is achieved with the power coefficients values slightly differing from the  $d = 1$  and  $f = 0$ , and the authors recommended to use those values for the sake of significant simplification of the formula. So far, we have used the revision of the formula for  $R(M, E)$  with the recommended integer values of  $d$  and  $f$  degrees:

$$R(M, E) = \frac{\lambda E}{1 + \frac{\varphi E}{M^2} + \alpha M E + \beta E} \quad (7)$$

In our FFs mass reconstruction procedure [5], the vector  $\{\lambda, \varphi, \alpha, \beta\}$  is calculated by fitting to the known FFs mass spectrum of  $^{252}\text{Cf}(\text{sf})$ . Usually the parameters  $\lambda$  and  $\varphi$  are set constant, as recommended in Ref. [8], or varied slightly, up to ten percent from the initial values.

To increase the robustness of the procedure in regard to the errors of the input variables [5], an attempt was made to use a more flexible parameterization for  $R(M, E)$ . For this, the last two terms in Eq. (7) were changed as follows:

$$\alpha M^{(1+\Delta d)} E + \beta M^{\Delta f} E \quad (8)$$

where  $\Delta d$  and  $\Delta f$  are corrections to the powers of  $d$  and  $f$  recommended in Ref. [8] (Eq. (6)).

**TABLE.** The FFs masses and velocities obtained using extended  $R(M, E)$  parameterization.

PIN №	$V_L, \text{sm}\cdot\text{ns}^{-1}$			$V_H, \text{sm}\cdot\text{ns}^{-1}$			$M_L, \text{u}$		
	$V_{\text{lit}}$	$V_{\text{exp}}$	$\Delta V$	$V_{\text{lit}}$	$V_{\text{exp}}$	$\Delta V$	$M_{\text{exp}}$	$M_{\text{lit}}$	$\Delta M$
1	1.34	1.32	0.02	1.003	0.988	0.015	107.25	106.6	0.65
2	1.34	1.32	0.02	1.003	0.983	0.02	107.25	106.6	0.65
3	1.34	1.316	0.024	1.003	0.983	0.02	107.25	106.4	0.85
	PIN №	$M_H, \text{u}$				$\Delta d$	$\Delta f$		
		$M_{\text{exp}}$	$M_{\text{lit}}$	$\Delta M$					
	1	141.28	141.7	-0.42	-0.35	0.47			
	2	141.28	141.9	-0.62	-0.69	0.49			
	3	141.28	140.8	0.48	-0.19	-0.15			

In Table  $V_L, V_H, M_L, M_H$  are the most probable velocities and masses for the FFs of the light and heavy mass peaks of  $^{252}\text{Cf}(\text{sf})$  respectively;  $\Delta V, \Delta M$  are the differences between the values known from the literature (lit) and those obtained in experiment (exp) [12];  $\Delta d, \Delta f$  – the power coefficients in Eq. (8).

The FFs mass reconstruction procedure similar to that described in Ref. [5] with the extended  $R(M, E)$  parameterization (8) was applied to the processing of the FFs mass spectra from  $^{252}\text{Cf}(\text{sf})$ . The results for three PIN diodes are presented in Table. As can be inferred

from the table the values of additional parameters  $\Delta d$  and  $\Delta f$  are significantly different from the previously adopted (7) values. It means that these parameters are significant for the adequate  $R(M, E)$  parameterization.

### VALIDATION OF THE SEWING-PARABOLA TIMESTAMP (SPT) METHOD

The idea of the SPT method is as follows. We search for the parabolic approximation of the initial part of the PIN diode signal under conditions that the parabola vertex lies on the mean value of the pulse's baseline, while parabolic and linear parts of the leading edge (figure 2) would sew together seamlessly (see [7] for details).

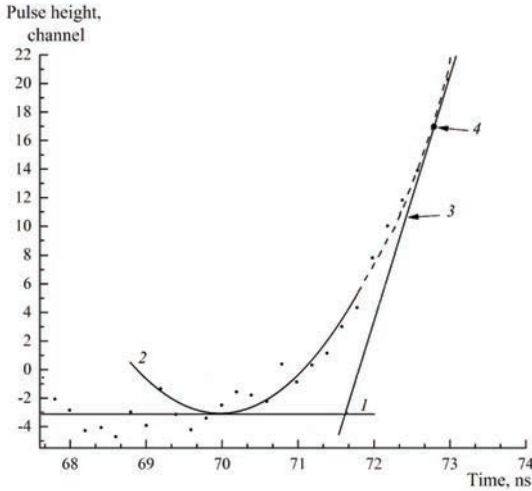


**FIGURE 2.** Stored waveform from the PIN diode. 1 – line corresponded to the mean value of the base-line, 2 – parabolic approximation of the initial part of the signal, 3 – linear part of the edge, 4 – sewing point.

The parabola vertex serves as a “true” timestamp. In other words, the STP algorithm allows the detection of a real point in time when the fragment hits the detector. Validation of the SPT method was performed at the time-of-flight spectrometer shown in figure 3. The fragment's TOF  $t_a$  on the segment  $a$  was measured using two microchannel plates based time detectors (MCP detectors) St1 and St2. There is no plasma delay for them, so the velocity  $V_1 = a/t_a$  can be considered the true velocity of the fragment. After passing detector St2, the fragment hits the PIN diode. The velocity  $V_2$  of the fission fragment was measured using the time stamps of the signals from the detector St2 and the PIN diode. The velocities  $V_1$  and  $V_2$  can be compared event by event (figure 4). It should be noted that the FF energies at the segments  $a$  and  $b$  differ by the amount of energy losses in the foil of the St2 detector (figure 3). The loss calculation was performed using the SRIM package [13], and the estimate is expected to have a systematic error. The expected calculated velocity difference is shown in figure 4 by dashed line 1. The deviation of line 1 from line 2 (dashed-dotted line in figure 4), which approximates the linear portion of the dependence  $\langle V_2 - V_1 \rangle$  on  $V_1$ , does not exceed  $0.01 \text{ cm}\cdot\text{ns}^{-1}$ , i.e.  $\approx 1\%$  FF's velocity. This deviation is also likely due only to a systematic error in the estimation of  $\Delta V_c$ . Indeed, a priori it can be assumed that the SPT algorithm could give a systematic shift in the estimation of the TOF, but this shift should depend on the velocity of the FF to reproduce the horizontal section in the experimental graph in Fig. 4.

When the parabola approximates the initial part of the signal's edge within the SPT algorithm, the TOF (FF's velocity) or the signal amplitude are not used in any way. Thus, the very presence of a horizontal section on the graph  $\langle V_2 - V_1 \rangle / V_1$  (figure 4) can serve as a criterion for the correctness of the sewing-parabola algorithm.

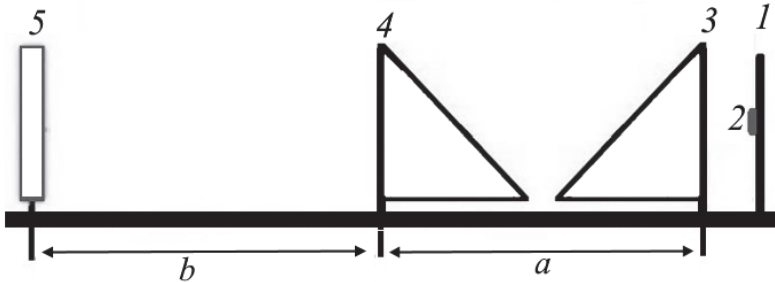


**FIGURE 3.** Time-of-flight spectrometer for testing SPT method using  $^{252}\text{Cf(sf)}$  source. 1 – target holder with the  $^{252}\text{Cf(sf)}$  source; 2, 3 – St1 micro-channel plates based timing detector; 4 – micro-channel plates based timing detector St2; 5 – PIN diode that provides the “stop” signal; flight-passes  $a = 14.2$  cm,  $b = 14.1$  cm.

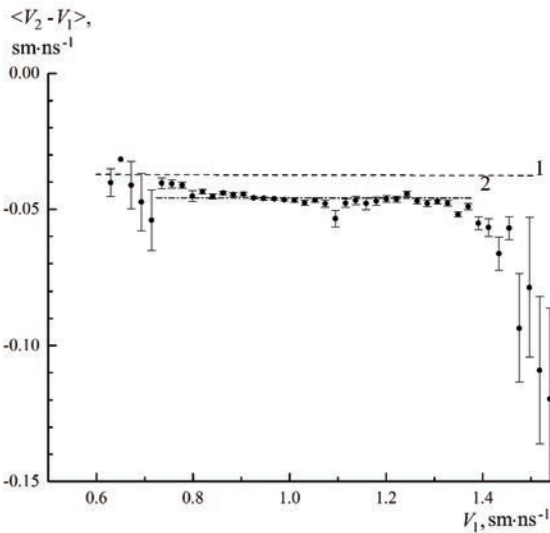


**FIGURE 4.** Mean difference  $\langle V_2 - V_1 \rangle$  as a function of  $V_1$  for the FFs from the  $^{252}\text{Cf(sf)}$  source measured at the “a” and “b” flight segments (figure 3), respectively, as a function of  $V_1$ . The horizontal dashed line 1 corresponds to the expected calculated value  $\langle V_2 - V_1 \rangle$ , taking into account the FF energy loss in the detector St2. The horizontal dash-dotted line 2 approximates a statistically significant linear portion of the experimental dependence.

### CONCLUSION

It has been analytically shown that for an arbitrary response  $h(t)$  of the electronic circuit connected to the detector, the area of the output signal  $S$  remains proportional to the charge  $q$  created by the ionizing particle in the detector. The  $q$  estimation algorithm by calculating the area  $S$  of the output signal avoids the ballistic error inherent in estimating  $q$  from the amplitude of the pulse.

To increase the stability of the procedure for calculating the ion mass with respect to the errors of the input variables, the parametrization of the amplitude defect  $R(M,E)$  has been modified. The significance of the introduced corrections is shown.

In a differential experiment for measuring FF's speed in  $^{252}\text{Cf}$  (sf) by using microchannel plates based detectors and sewing-parabola time pick-off method for the signals from PIN diodes it is shown that this algorithm gives an unbiased time reference corresponding to the moment of FF detection in the detector.

## ACKNOWLEDGMENTS

This work was supported by the research project № 18-32-00538 of the Russian Foundation for Basic Research (RFBR) and partially by the MEPhI Academic Excellence Project (Contract No. 02.a03.21.0005, 27.08.2013) of the Russian Science Foundation as well as by the Department of Science and Technology of the Republic of South Africa (RSA).

## REFERENCES

1. D.V. Kamanin, Yu. V. Pyatkov, "Clusters in Nuclei – Vol. 3" ed. by C. Beck, Lecture Notes in Physics 875, pp. 183–246 (2013).
2. D.V. Kamanin, Yu. V. Pyatkov, Nuclear Particle Correlations and Cluster Physics Part 4. Cluster Radioactivity, Fission and SHE. World Scientific, 2017. p. 339–370.
3. Yu.V. Pyatkov et al., FIAS Interdisciplinary Science Series. Nuclear Physics: Present and Future. 2015. pp.79–88.
4. Yu.V. Pyatkov et al., Eur. Phys. J. A **45** (2010) 29–37.
5. A.O. Strelakovsky et al., Yadernaya Fizika i Inzhiniring. Vol. **6**, No. 5–6, 2015, p. 290–296 (rus).
6. Yu.V. Pyatkov et al., J. Phys.: Conf. Ser. **675** (2016) 042018.
7. Yu.V. Pyatkov et al., Bull. Russ. Acad. Sci.: Phys. **82** (2018) 804.
8. S.I. Mulgin et al., NIM A **388** (1997) 254.
9. [http://edu.sernam.ru/book\\_sm\\_math2.php?id=111](http://edu.sernam.ru/book_sm_math2.php?id=111).
10. A.P. Tsitovich, Yadernaya elektronika. Moskva. Energoatomizdat. 1984. C. 408 (rus).
11. F. James, M. Roos, Comput. Phys. Commun. **10** (1975) 343.
12. H.W. Schmitt, W.E. Kiker, C.W. Williams, Phys. Rev. **137** (1965) B837.
13. J.F. Ziegler, M.D. Ziegler, J.P. Biersack, NIM B **268** (2010) 1818.

# Monte Carlo Simulation of Ions in the Radiative Neutron Decay Experiment

Khafizov R.U.<sup>a</sup>, Kolesnikov I.A.<sup>a</sup>, Nikolenko M.V.<sup>a</sup>, Tarnovitsky S.A.<sup>a</sup>,  
Tolokonnikov S.V.<sup>a</sup>, Torokhov V.D.<sup>a</sup>, Trifonov G.M.<sup>a</sup>, Solovei V.A.<sup>a</sup>,  
Kolkhidashvili M.R.<sup>a</sup>, Konorov I.V.<sup>b</sup>

<sup>a</sup>NRC «Kurchatov Institute», Russia

<sup>b</sup>Technical University of Munich, Munich, Germany

[khafizov\\_ru@nrcki.ru](mailto:khafizov_ru@nrcki.ru)

## Annotation

This report aims to research the influence of the ionic background on registration of radiative neutron decay events and the measurement of its branching ratio (B.R.). Our methodology is focused on measuring the spectra of triple coincidences of radiative gamma-quantum, beta electron, and recoil proton and double coincidences of beta electron and recoil proton. The peak on the spectrum of triple coincidences shows the number of radiative neutron decays, while the peak on the spectrum of double coincidences shows the number of regular neutron beta-decays. This methodology enabled us to become the first team to measure the branching ratio of radiative neutron decay  $B.R. = (3.2 \pm 1.6) \cdot 10^{-3}$  (where C.L. = 99.7% and gamma quanta energy exceeds 35 keV) in 2005 on our old experimental equipment.

We have now prepared a new experiment on radiative neutron decay with the aim of measuring B.R. with a high degree of precision. The precision of branching ratio measurement is determined using the value of the ion background. The spectrum of double coincidences obtained in our experiment shows a fairly significant ion background, the fluctuations of which indicate the precision of measurement for the number of recoil protons. Because the ion background specifically is quite significant, it appears even under super deep vacuum as beta electrons ionize the highly rarified air inside the chamber. The value of the ion background very slowly decreases with decreasing density of air inside the equipment. For example, our experimental data lead to the conclusion that the value of the ionic background is significant when compared with the value of the proton peak and on the other hand decreases only by 5–6 times if the pressure within the chamber goes down by 2 orders of magnitude. Besides, we discovered an additional wide peak on the spectrum of triple coincidences. This peak consists of delayed gamma quanta created during the ionization of rare gas by beta-electrons.

Thus, this experiment allows us to study another important phenomenon, the ionization of rarified gas by beta electrons with emission of gamma quanta. Our last experiment showed that these two phenomena, radiative neutron decay and ionization with gamma quanta emission, are distinguishable in the case of high time resolution and can be studied separately. This is another important result of our last experiment and in this report we mention that the authors of articles registered namely the ionization with gamma radiation events.

This report is dedicated to a discussion of the computer experiment we conducted using the well-known GEANT4 software package. As a result of these calculations, we demonstrated that the value of the ionic background is proportional to the cubic root of the

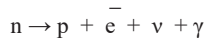
rarefied air density within the equipment, i.e. it changes very smoothly in relation to the pressure within the chamber. Besides, the report presents a comparison of our measurements of double coincidences and triple coincidences, with two other experimental groups.

## Introduction

Presently, the characteristics of the ordinary decay mode are measured with precision of tenths of a percentage point. Under these circumstances, the experimental data obtained by different groups of experimentalists can be reconciled only by taking into account the corrections calculated within the framework of the standard theory of electroweak interactions. This means that the experimental research of the ordinary mode of neutron decay have exhausted their usefulness for testing the standard model. To test the theory of electroweak interaction independently, it is necessary to move from the research of the ordinary branch of decay to the next step, namely, to the experimental research of the radiative decay branch.

The radiative decay branch of elementary particles, where an additional particle, a radiative gamma quantum is formed along with the regular decay products, has been discovered for practically all elementary particles. This has been facilitated by the fact that among the rare decay branches the radiative branch is the most intensive, as its value is proportional to the fine structure constant  $\alpha$  and is only several percent of the intensity of the regular decay mode (in other words, the relative intensity B.R. of the radiative decay branch has the value of several hundredths of a unit.)

However, for the neutron this decay branch had not been discovered until recently and considered theoretically only [1–4]. Our first attempt to register the radiative neutron decay events was made on intensive cold neutron beam at ILL [5]. But our experiment conducted in 2005 at the FRMII reactor of Munich Technical University became the first experiment to observe this elementary process [6]. We initially identified the events of radiative neutron decay by the triple coincidence, when along with the two regular particles, beta electron and recoil proton, we registered an additional particle, the radiative gamma quantum



and so could measure the relative intensity of the radiative branch of neutron decay B.R.=  $(3.2 \pm 1.6) \cdot 10^{-3}$  (with C.L.= 99.7% and gamma quanta energy over 35 keV; before this experiment we had measured only the upper limit on B.R. at ILL [5] ).

The main characteristic of any rare mode of elementary particle decay is its relative intensity, branching ratio (B.R.). By definition, B.R. is equal to the ratio between the intensity of the rare decay mode and the intensity of the ordinary mode. In the case of neutron, this intensity ratio can be reduced to the ratio between the number of triple coincidences between the registration of beta-electrons, radiative gamma-quantum and the delayed proton  $N_T$  to the number of double coincidences between the registration of the ordinary decay products, beta electron and recoil proton  $N_D$ :

$$B.R. = I(\text{radiative decay}) / I(\text{ordinary decay}) = N(e,p,\gamma) / N(e,p) = N_T / N_D.$$

These two values can be determined only from the analysis of double and triple coincidences spectra, which form corresponding peaks. Identifying these peaks and distinguishing them from the significant background is the central problem in the methodology of B.R. measurements for neutron radiative decay.

Further, this experimental B.R. value needs to be compared with the theoretical value, estimated within the framework of the electroweak model. Any difference between these two values would mean that we are observing a deviation from the electroweak interaction theory.

Our group calculated the neutron radiative spectrum in the framework of standard electroweak theory in the following papers [1–4]. The calculated branching ratio for this decay mode as a function of the gamma energy threshold was published in these papers. B.R. value for the energy region over 35 keV was calculated to be about  $2.1 \cdot 10^{-3}$ .

It follows that to measure the main characteristic of radiative neutron decay, it is necessary to obtain and analyze the spectra of double and triple coincidences. So, it is necessary to consider the main particularity of these spectra – the ion and gamma backgrounds.

Let us consider in detail the question around the value of ion background in the experiment on radiative neutron decay, namely, its value in the spectrum of double coincidences of electron and proton. Theory makes it clear that the number of ions created by an electron that spreads in the media of its path with length of  $L$  is equal to  $N_{\text{ion}} = L/\lambda$ . Here  $\lambda$  is the length of the electron's free path in media with molecular density  $n$ . If ionization cross section of media is  $\sigma_i$ , then the length of the free path is inversely proportional to the product of media density to the cross section  $\lambda = (n \cdot \sigma_i)^{-1}$ . On the other hand, if the probability of the one media atom ionization is  $P(n)$ , then the number of ions  $N_{\text{ion}}$  created when the electron cross the media equals the product of this probability to the total number  $N$  of atoms on the electron trajectory length  $L$ . This number is equal to the ratio of the trajectory length  $L$  to the average distance between nearest atoms of media  $\ell = n^{-1/3}$  with density  $n$ :  $N = L/\ell$ . Thus, we arrive at the following chain of equations:

$$N_{\text{ion}} = \frac{L}{\lambda} = Ln\sigma_i = P(n)N = P(n)\frac{L}{\ell} = P(n)Ln^{1/3}.$$

Thus, the classic probability of ion creation per one media atom with density  $n$  is equal to the ratio of the two areas – that of ionization cross section  $\sigma_i$  to area  $S = (n)^{-2/3}$ , the area per one media atom:  $P(n) = \sigma_i/S = \sigma_i n^{2/3}$ .

This formula occurs in the simplest model of a “perfectly black sphere”. Introducing a random value, aim distance  $\rho$ , leads to the probability of ionization dependent on that aim distance of  $P(\rho) = 1$  for all aim distances shorter than the atom radius  $a = (\sigma_i/\pi)^{1/2}$  while for greater aim distances probability of ionization is 0 (see Fig. 1).

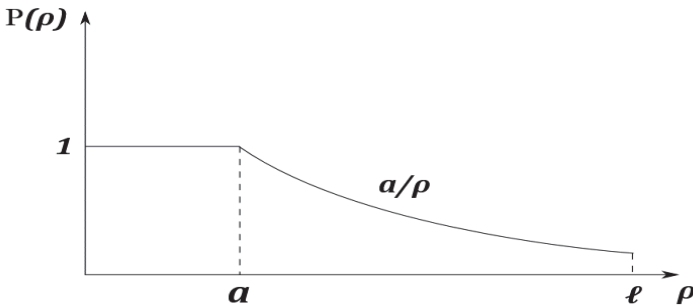


**Fig. 1.** The dependence of the ionization probability on  $\rho$ . For the usual model:  $P(\rho) = 1$  for  $\rho < a$  and  $P(\rho) = 0$  for  $a < \rho < \ell$ ; for Coulomb interaction model  $P(\rho) = 1$  and  $P(\rho) = a/\rho$  for  $a < \rho < \ell$ .

However, in the case of ionization process in highly rarefied media this simple model becomes inaccurate as it does not take into account Coulomb interaction, which may have a fairly long “Coulomb tail” inversely proportional to the aim distance. In this case, one must consider a more realistic model where probability  $P(\rho)$  is not zero, when the electron flies by the atom without touching it, i.e. at aim distances  $\rho$  greater than  $a$ . So, it is necessary to consider the long “Coulomb tail” of distribution  $P(\rho)$ , which falls inversely proportionally to the aim distance (see Fig. 1). Thus, the total ionization cross section will depend on density and have an additional term, inversely proportional to the cubic root of media density  $n$ :

$$\sigma_{tot} = \int_0^{2\pi} d\varphi \int_0^a \rho d\rho + \int_0^{2\pi} d\varphi \int_a^{\infty} \frac{1}{\rho} \rho d\rho = \pi a^2 + 2\pi a(l - a) = -\pi a^2 + 2\pi al = -\sigma_i + 2(\pi\sigma_i)^{1/2} n^{-1/3}$$

The probability of ionization per one atom will be:  $P(n) = \sigma_{tot} \cdot n^{2/3} = -\sigma_i \cdot n^{2/3} + 2(\pi\sigma_i)^{1/2} n^{1/3}$ .

It is evident that in extremely rarified media where  $\sigma_i \cdot n^{2/3}$  is significantly below 1, the second member of this formula leads and significantly exceeds the first. Thus, probability of ionization of one atom becomes proportional to the cubic root of density (pressure), i.e. depends on density in a very smooth way. This, in turn, leads to a gradual reducing of the ion background dependency on density and this background cannot be ignored even in highly rarefied media. For example, a fall in pressure within the experimental setup of two orders of magnitude leads to a fall in the ionic background equal to the cubic root of pressure, i.e. 4–5 times. Our experiment observed exactly this behavior of ionic background and, as we'll show later in this report, such smooth dependency on density is experimentally demonstrated when measuring spectra of double coincidences obtained by our and emiT groups.

## Analysis and comparison of double coincidences spectra

Here let's pause to analyze the spectra of double coincidences between beta-electron and recoil proton, and compare our spectrum with the results obtained by other authors. We have published the diagram of our experimental equipment in the past [5, 6]. Here we will simply note that in its sizes our equipment is comparable to the equipment used by the two other groups and the distance between the observed decay zone and the proton detector in our equipment is about 0.5 m. The accelerating potential of the electric field is also approximately the same in all three equipment sets, so all three experiments should lead to similarly forms of double and triple coincidences spectra.

Fig. 2 demonstrates the summary statistics on double e-p coincidences (coincidences of electron with delayed proton). Fig. 2 clearly shows two major peaks: one peak with a maximum in channels 99–100, which is the peak of zero or prompt coincidences [6]. The position of this peak marks the zero time count, namely the time when the electron detector registered the electron. This peak is not physics-related in its nature. Instead, it is a reaction of the detectors and the electronic system to the registration of the beta electron. It is namely the pulse from the electron channel that opens the time windows on spectra Fig. 2 for 2.5  $\mu$ s forward and backwards. The next peak visible in Fig. 2 has a maximum in channel 120 and is the peak of e-p coincidences of beta-electron with delayed proton.

An analogous situation was observed in experiments on the measurement of the correlation coefficients by two independent groups at ILL [9] and emiT group at NIST [10], and it was also mentioned at [11]. We would especially like to emphasize the correspondence of our spectrum of double coincidences with an analogous spectrum from the result obtained by the emiT group from NIST [10]. In Fig. 3 we present their spectrum and diagram for the

registration of the beta electron and the recoil proton. A comparison of our results with the results of the emiT group shows their unquestionable similarity. Moreover, the position of the second proton peak in Fig. 3 (emiT group), like in Fig. 2 (our result), corresponds well to the simple estimate obtained by dividing the length of a proton trajectory by its average speed.

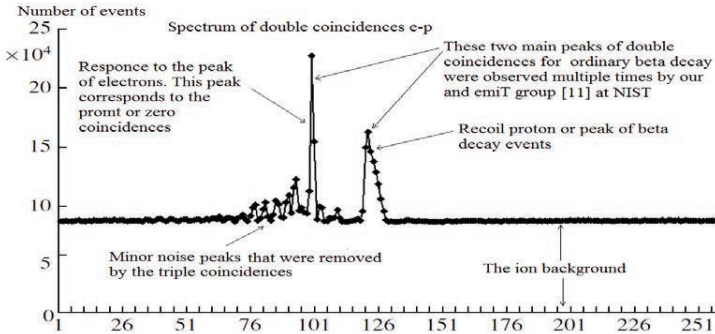


**Fig. 2.** Timing spectrum for e-p coincidences. Each channel corresponds to 25 ns. The peak at channel 99–100 corresponds to the prompt (or zero) coincidences. The coincidences between the decay electrons and delayed recoil protons (e-p coincidences) are contained in the large peak centered at channel 120.

Here we will also note the presence of a significant homogenous ionic background in Fig. 2 and Fig. 3. However, in both cases this background allows to easily distinguish the neutron decay peak. As we will shortly demonstrate, this ionic background will play a dominant role in the presence of a strong magnetic field and it will become impossible to distinguish events of ordinary neutron decay against it.

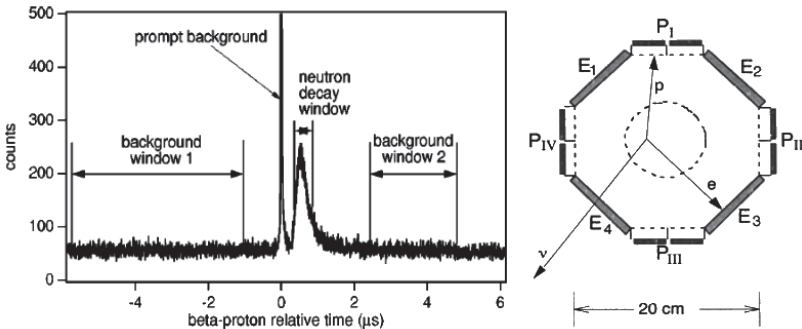


**Fig. 3.** Spectrum of double electron-proton coincidences obtained by emiT Group [10] with two peaks and ion background value comparable to the neutron decay peak; emiT group scheme for registering beta electron and recoil proton.

Following Avogadro's law, even in the case of a very deep vacuum under pressure of  $10^{-6}$ – $10^{-8}$  mbar, air molecule concentration remains very high. In fact, it is sufficient for beta-electrons produced in neutron decay to create a significantly high ionic background. Here one must note that the probability of ion creation along the trajectory of beta-electron is in inverse proportion to the average distance between neighboring ions, i.e. proportional not to the molecule concentration but to the cubic root of this value. From this observation it follows that the value of the ionic background does not significantly depend on the vacuum conditions inside the experimental chamber. In our case, pressure was two orders of magnitude greater than the pressure in the emiT experiment. However, we observed an ionic background of only 4–5 times their background. This estimate is confirmed when one compares the spectra in Fig. 2 and Fig.3. Our spectrum, presented in Fig. 2, has a 1:1 ratio of the value of e-p coincidences peak and the value of the background. The emiT group (Fig. 3) spectrum has a ratio of 4:1 – 5:1, i.e. only 4–5 times our number, that is equal to the cubic root of pressure ratio in both teams' work (see Introduction).

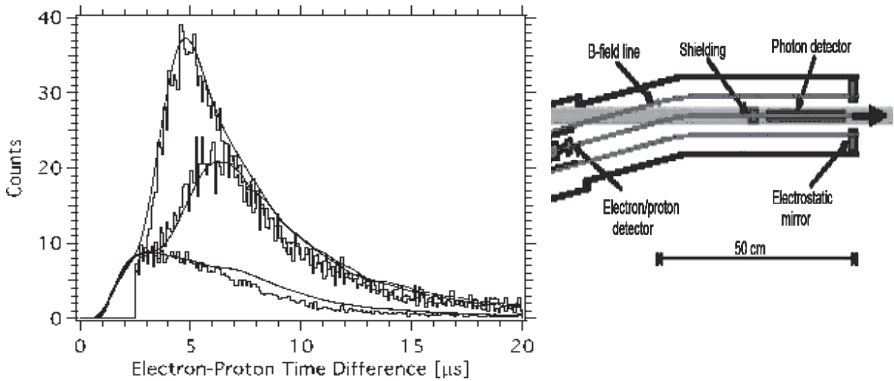
We will present the specific calculations using the GEANT4 package in a separate paper, where we will consider the ionization process in more detail. It is noteworthy that in our case it is impossible to isolate and track individual tracks of electrons ionizing the residual air in the chamber due to their multiple reflections and scattering on the walls of the chamber, the neutron guide and other structural elements of the installation. As shown by concrete calculations, in this case it makes more sense to talk about the steady-state electron density  $\rho_e$  inside the chamber and, accordingly, the ion density  $\rho_i$ . The density of ions  $\rho_i$  is proportional to the density of electrons  $\rho_e$ , with the proportionality factor being the probability of the formation of the ion  $P(n)$  (see Introduction):  $\rho_i = P(n) \cdot \rho_e = 2(\pi\sigma_i)^{1/2} \cdot n^{1/3} \rho_e$ . Thus, the ratio of the ionic background value to the proton peak value also decreases in proportion to the cube root of density or pressure.

Fig. 2 shows that the total number of events in e-p coincidences peak in our experiment equals  $N_D = 3.75 \cdot 10^5$ . This value exceeds the value we obtained in our previous experiment conducted on beam PF1 at ILL by two orders of magnitude. It was precisely because of the low statistics volume that we could not identify the events of radiative neutron decay in that experiment and instead defined only the upper B.R. limit [5]. It is very important to note that the peak of double coincidences between electron and the delayed proton is observed against a non-homogenous background (see Fig. 2 and Fig. 3): besides the homogenous ionic background, which has a value comparable to the value of the e-p coincidences peak, there is an obvious peak in channels 99–100. In essence, this peak is a response peak to the time spectrum of electron registration, which contains just one peak in channels 99–100, signifying the time when the electron detector registered the electron. We will shortly see that the radiative peak of triple coincidences appears against a non-homogenous background with not one, but two response peaks.

The remaining peaks in Fig. 2 are small, with just seven peaks distinct from the statistical fluctuations. These occurred because of the noise in the electric circuits of the FRMII neutron guide hall. There are no other physics-related reasons for their occurrence. These peaks appeared and disappeared depending on the time of day, reaching their maxima during the work day and disappearing over the weekends. Such behavior was observed throughout the experiment as we collected statistics. Since the nature of these seven small peaks is in no way related to radiative and ordinary decay, we did not emphasize them in our article.

The comparison conducted demonstrates that the spectra of double coincidences obtained in our experiment completely correspond with the results obtained by the emiT

group. Now we will compare these two spectra with the spectrum of double coincidences obtained by the third group. Unfortunately, the authors did not publish the spectrum of double coincidences in their original article [7], instead it was only published this year in paper [12]. Fig. 4 displays the spectrum of double coincidences and the diagram of their experimental equipment.



**Fig. 4.** Equipment diagram and the single peak of “electron-proton” coincidences, published in [12]. The lower curve corresponds to 0 volts, the middle curve corresponds to 300 volts and the highest curve corresponds to 500 volts in an electrostatic mirror. The location of the peak’s maximum and its significant width differ from our and the emiT results subsequently by one and two orders of magnitude. The location and the width of the peak also deviate by one and two orders of magnitude from the elementary estimates of delay times (see below).

The significant deviation obtained is explained by the fact that the peak in the NIST experiment consists not of beta-decay protons, but rather of ions. The density of gas molecules inside the equipment is proportional to pressure and according to the Avogadro’s law is at the order of  $10^7$  mol/cm<sup>3</sup> even at the pressure of  $10^{-8}$ – $10^{-9}$  mbar. This is a very significant number, which quite enough for creation the large ionic background in the presence of ionizing radiation. The energy of beta-electrons significantly exceeds the energy of ionization. Besides, the probability of ion creation by electrons is inverse proportional not to volume taken up by one molecule but to the average distance between molecules. It is precisely due to this reason that the ionic background falls proportionally to the cubic root of the pressure and not proportionally to pressure. In the emiT group experiment the pressure was the same as in the NIST experiment, so the ionic background should be the same too. The light ions, together with the beta protons, should have a delay time comparable to 1 μs. The pulses from these particles are simply not visible in the spectrum due to the NIST group’s use of combined electron-proton detector (see Fig. 5 with the shape of electron and ion pulses). The maximum of the “proton” peak in the NIST experiment, according to the delay times estimations (delay time is proportional to square root of ion mass), falls exactly to the air ions 4–6 μs.

Fig. 5 presents the pulse forms on the electron-proton detector. As was pointed out above, the significantly delayed pulses of low amplitude correspond to ion pulses, and the pulses from protons are simply invisible due to a presence of a wide electron pulse of high

amplitude. Namely this fact explains the dead zone around zero on the spectrum of electron coincidences in Fig. 4.

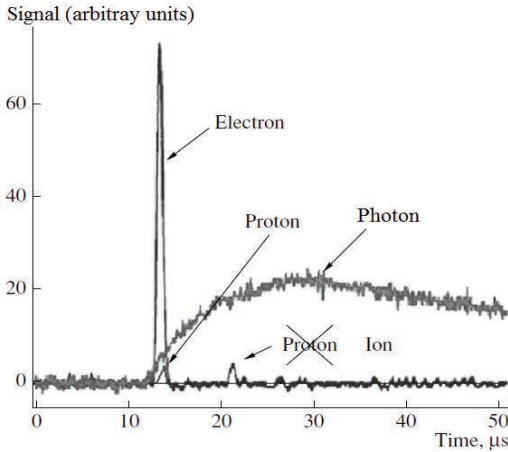


**Fig. 5.** The signal from the decay proton has to be delayed by less than one microsecond, which is why it is located at the base of the electron pulse (see line number 2) and so cannot be registered by the combined electron-proton detector. The pulses that are delayed by longer than 1 microsecond are pulses not from decay protons, as it was indicated in ref. [7], but rather from ions, formed in the decay zone. The line number 1 shows the shape of pulses from the gamma detector.

### Analysis and comparison of triple coincidences spectra

In paper [10] the emiT group researched only the ordinary decay mode, thus this comparison is limited to our spectrum of triple coincidences, presented in Fig. 5, and the only peak published by the NIST authors in Nature [7], presented in Fig. 7. Analysing the double coincidences spectra obtained by our and the emiT groups (both of which present two main peaks) shows that in the spectrum of triple coincidences we should observe not two but three peaks. Namely, along with the sought after radiative peak, the triple e-p-gamma coincidences spectrum should show two (not one!) response peaks to the registration of beta-electrons and the registration of protons. Fig. 5 of triple coincidences clearly shows three peaks, and the leftmost peak with the maximum in channel 103 is connected to the peak of the radiative gamma-quanta in question, as this gamma-quantum is registered by the gamma detectors in our equipment before the electron.

It is also important to note that while both teams' double coincidences spectra show the peaks at a distance from each other and easily distinguishable, in the spectrum of the triple coincidences the radiative peak is on the left slope of the response peak to electron registration. This means that we observe the peak of radioactive neutron decay events against a heterogeneous background. At the same time, both response peaks on the spectrum of triple coincidences are significantly wider and located closer to each other than in the original spectrum of double coincidences. As we demonstrate below, one must take into account such spectrum behavior (related to the presence of a response in the electron detector system of data collection) by introducing the non-local response function. Using this well-known

method it is possible to distinguish  $N_T$  the number of triple coincidences from the heterogeneous background, arriving at the experimental BR value.

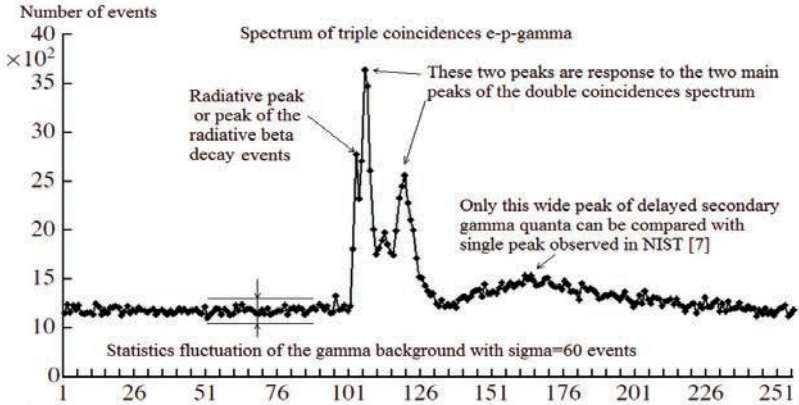


**Fig. 6.** Timing spectrum for triple e-p-g coincidences. Each channel corresponds to 25 ns. In this spectrum, three main peaks in channels 103, 106 and 120 can be distinguished. The leftmost peak in 103 channel among these three main peaks is connected with the peak of radiative decay events.

Comparing Figs. 2 and 6, it becomes clear that if we ignore the first leftmost peak with the maximum in channel 103 in Fig. 6, the spectrum of double e-p coincidences will resemble the spectrum of triple e-p- $\gamma$  coincidences in Fig. 2. The peak with the maximum in channel 106 in Fig. 6 is connected to the left peak of false coincidences in Fig. 2, and the peak with the maximum in channel 120 in Fig. 6 is connected to the right peak of e-p coincidences in Fig. 2. The emerging picture becomes obvious when one uses a standard procedure, introducing a response function for gamma channel  $R_\gamma(t,t')$  [6], which is also necessary for calculating the number of triple radiative coincidences  $N_T$  in radiative peak:

$$S_{out}(t) = \int S_{in}(t') R_\gamma(t,t') dt'$$

Using the method of response function, one can confidently define our double-humped background: the narrow peak with the maximum in channel 106 in Fig. 6 is the response to the narrow peak of zero coincidences (by other words this peak is response to beta-electron registration) in channels 99–100 in Fig. 2, and the second peak in this double-humped background in Fig. 5 is the response to the peak in channels 117–127 in Fig. 2 (or this peak is response to proton registration).

It must be noted that in our case we have to use the non-local response function, as the peaks on the original spectrum  $S_{in}(t)$  of double coincidences are significantly narrower than those in the spectrum  $S_{out}(t)$  of triple coincidences and also are shifted in their relative positions. In this case we use “functional” multiplication, however if we use the local response function, the triple coincidences spectrum is arrived at by simple multiplying the double coincidences spectrum by a number, in which case neither the width of the peaks nor

their position change. It is also evident that the local response function approach leads to an erroneous number of triple coincidences  $N_T$  and, therefore, the wrong B.R. value.

When discussing the similarities between the spectra in Fig. 2 and Fig. 6, it is important to note that the response peak in Fig. 6 with a maximum in channel 106 is shifted to the right or delayed in comparison to the peak responding to electron registration in channel 100 in Fig. 1. This is due to the fact that in our electron diagram we used a constant fraction discriminator (CFD). CFD has its own delay line and the location of the time-pickoff signal it generates is determined by the method of comparing the fraction of the original signal to the delayed (CFD method [13]). Thus, there is a shift in the first response peak with a maximum in channel 106 in Fig. 6 versus the first peak in Fig. 2 with the maximum in channel 100. The value of this delay is equal to the front duration of the gamma quantum signal and is on average 150 ns. The CFD method obviously also shifts the radiative peak, but it should be located to the left of the response peak, as is observed in Fig. 6.

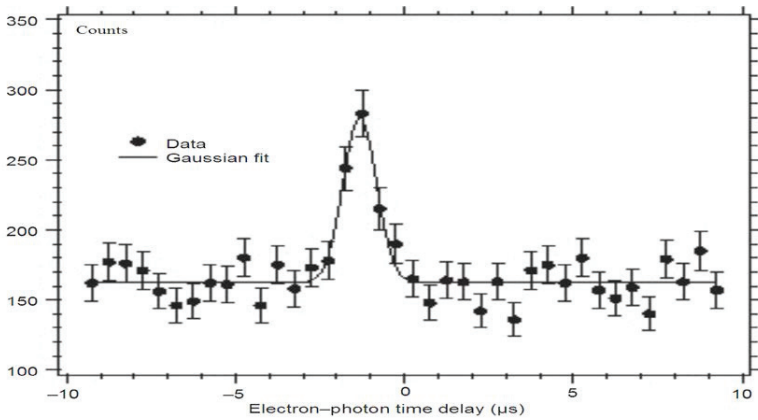


**Fig. 7.** Only peak of “electron-photon” coincidences, shifted to the left of 0 – the time of beta-electron registration – by 1.25 microseconds, published in [7, 10].

As for the wide, almost indistinguishable peak in channel 165 in Fig. 6, its influence on the radiative peak in channel 103 is negligible. Its nature is in no way related to the researched phenomenon, so we do not discuss it in our article. This peak is created by the radioactive gamma quanta delayed on average by 1.25  $\mu\text{s}$  and emitted by the radioactive medium within our experimental equipment. The medium is activated by registered beta-electrons. This event of artificial, induced radioactivity has been known for over 100 years and does not have anything in common with the new event of radiative neutron decay which is the subject of current research. As we will demonstrate below, only this 1 microsecond peak and delayed from the registration time by about the same time can be compared to the peak observed by the authors of paper [7] at NIST (see Fig. 7). Thus, the authors of this experiment observed not the events of radiative decay but rather the event of artificial radioactivity, already well known in the time of Joliot-Curie.

After analyzing the spectra with the help of the non-local response function  $R_{\gamma}(t, t')$  we finalize the average value for the number of radiative neutron decays  $N_T = 360$  with a statistics fluctuation of 60 events. B.R. can be expressed as a ratio of  $N_T$  to  $N_D$  as  $\text{B.R.} = k (N_T / N_D)$ ,

where coefficient  $k = 3.3$  is the geometrical factor that we can calculate by using anisotropic emission of radiative gamma-quanta [4]. With the number of observed double e-p coincidences  $N_D = 3.75 \cdot 10^5$  and triple e-p- $\gamma$  coincidences  $N_T = 360$ , one can deduce the value for radiative decay branching ratio of  $(3.2 \pm 1.6) \cdot 10^{-3}$  (99.7 % C.L.) with the threshold gamma energy  $\omega = 35$  keV. The average B.R. value we obtained deviates from the standard model, but because of the presence of a significant error (50%) we cannot make any definite conclusions. The measurements must be made with greater precision. According to our estimates, in the future experiment we will be able to make more definite conclusions about deviation from the standard electroweak theory with experimental error less than 10%.

The difference between the NIST experiment and our experiment becomes immediately apparent. First and foremost, it is the time scale: in our spectra, the scale is measured in nanoseconds, while in the other experiment the scale is in microseconds. Besides, we used three types of detectors, each of which registered its own particle: one detector for the electrons, one for the protons, and six identical detectors for the radiative gamma-quanta (see [6]). The duration of the front pulse from the electron and proton detectors is 10 nanoseconds in our experiment and 100 times greater than that in the NIST experiment, in the order of 1  $\mu$ s. The rise time of gamma signal from our gamma-detectors is on average 150 ns, and from avalanche diode on the NIST equipment greater than 10  $\mu$ s, besides that the diode pulse arrives with significant noise, which makes the thickness of the front pulse line equal to more than 0.5  $\mu$ s (see the photon line in Fig. 7 from [7]). All of this leads to our factual time resolution being two orders of magnitude better than the resolution achieved in the NIST experiment. However, as the two experiments used equipment which was practically the same in size and smaller than 1 meter, the choice of the time scale is a matter of principle. Given this geometry, it is impossible to get microsecond signal delays from all of the registered charged particles, i.e. electrons and protons. In this light, it is surprising that the peak identified by the authors of the NIST report [7] as the peak of radiative gamma-quanta, is shifted by 1.25 microseconds to the left. The expectation that magnetic fields of several tesla in magnitude delay all electrons and protons, are absolutely ungrounded.

Indeed, the magnetic field cannot change the speed of charged particles. It can only twist a line trajectory into a spiral. The length  $l$  of this spiral depends on angle  $\theta$  between particle velocity and magnetic field direction. In beta decay, electrons can fly out under any angle  $\theta$ , therefore the magnetic field can increase the time of delay by several orders of magnitude only for a negligible portion of the charged particles. Even this negligible number of particles that flew out at an almost 90 degree angle to the direction of the magnetic field that coincides with the direction of the narrow neutron guide (see Fig. 4) will most likely end up on the walls of the neutron guide rather than reach and hit the detector due to the presence of the strong electrostatic field. Because the distance between the point of decay and the detector is about 0.5 meter and electron velocity is comparable with speed of light, the electron time of delay should be less than a microsecond by two orders of magnitude.

Thus, both the 1 microsecond shift and the width of the only peak in Fig. 7 in the experiment conducted at NIST, is in sharp contradiction to elementary estimates. We, on the other hand, did not observe any wide peaks before electron registration and our gamma background is very even in this part of the spectrum (see Fig. 6). However, when we assume that the NIST experiment authors observed the wide peak, shifted by 1 microsecond, not before, but after the registration of beta-electrons. In that case, the wide peak on our spectrum in Fig. 6 completely corresponds to the wide peak in Fig. 7. However, as noted above, density of gas molecules remains high even with the pressure of  $10^{-8}$ – $10^{-9}$  mbar and this residual gas

is activated by beta-electrons. The wide peak in our spectrum is formed by the delayed gamma quanta from this induced artificial radioactivity.

**Conclusions.** The main result of our experiment is the discovery of the radiative peak namely in the location and of the width that we expected. The location and the width of the radiative peak correspond to both estimates and the detailed Monte Carlo simulation of the experiment. Thus, we can identify the events of radiative neutron decay and measure its relative intensity, which was found to be equal  $B.R. = (3.2 \pm 1.6) \cdot 10^{-3}$  (with C.L.= 99.7% and gamma quanta energy over 35 keV ).

At the same time, the average experimental B.R. value exceeds the theoretical value by 1.5 times. However, due to a significant error we cannot use this result to assert that we observe a deviation from the standard model. Therefore, our most immediate goal is to increase experiment precision, which we can improve by several percent according to estimates.

For last two years we were preparing this new experiment and conducted number of tests for our new electronics. We constructed multichannel generator what can generate the pulses with the same forms as our electron, proton and gamma detectors. During these tests we got the same responses as during our last experiment on real neutron beams at FRMII. It means that all additional peaks on our spectra have no any physics reasons and It proves once more that we were absolute correct when applied the response function method for explaining these peaks as response ones and for developing our experimental spectra.

We created and tested our new electronic system for obtaining experimental spectra. By using this new programmable electronics we can significantly reduce the influence of response peaks on peak with radiative decay events. Now we can get this peak almost isolated from responses. On our estimations all these allow us to reach accuracy for our new experiment about 1%. So, on the base of our new electronics we can confirm or refuse the deviation of our average experimental value of BR from the standard model one.

As concerning the comparison of our experimental results with others we can make the following two main conclusions. The main parameters of our spectrum of double electron-proton coincidences identifying the events of ordinary neutron decay fully coincide with an analogous spectrum published by emiT group in [10].

Unfortunately we cannot say same for another experiment measuring the radiative neutron decay published in [7]. Particularly vexing is the authors' unsubstantiated assertion that they observe their only wide peak of gamma quanta before the registration of beta-electrons. Both the position and the width of this peak are located in sharp contradiction to both the elementary estimates, and the results of our experiment. In the course of our entire experiment we did not observe such a wide peak in the triple coincidences spectrum, located before the arrival of electrons at a huge distance of 1.25  $\mu$ s. However, it is possible to reconcile our spectra of triple coincidences with the one isolated peak observed at NIST if we assume that at NIST, the gamma-quanta were registered after the beta electrons. Only in this case does the NIST peak almost completely coincide with the peak we observed in the spectra of triple coincidences with the maximum in channel 165, both in terms of the huge delay of 1.25  $\mu$ s and in terms of its huge width. This peak is created by the delayed secondary radioactive gamma-quanta, arising from the activation by beta electrons of the media inside experimental chamber, which was the real object of the NIST experimentalists' observation.

Despite the recent disagreements [14], which we consider to be subjective in nature [15], we acknowledge the contribution of our Western colleagues Profs. N. Severijns, O. Zimmer and Drs. H.-F. Wirth, D. Rich to our experiment conducted in 2005. Here it is

important to note that the authors of the article published in Nature [7] consciously misled first our Western colleagues and then the physics community at large by insisting that their only wide peak is removed by 1.25 microseconds to the left from the time of electron registration, when in reality this peak was formed by delayed gamma-quanta, emitted by the activated medium inside the experimental equipment, and corresponds to our wide peak with the maximum in channel 165 (refer to Fig. 6) [14, 15]. The authors would like to thank Profs. D. Dubbers and Drs. T. Soldner, G. Petzoldt and S. Mironov for valuable remarks and discussions. We are also grateful to the administration of the FRMII, especially Profs. K. Schreckenbach and W. Petry for organizing our work. We would especially like to thank RRC President Academician E.P. Velikhov and Prof. V.P. Martem'yanov for their support, without which we would not have been able to conduct this experiment. Financial support for this work was obtained from RFBR (Project N 014-02-00174).

## References

1. Gaponov Yu.V., Khafizov R.U., Phys. Lett. B **379** (1996) 7–12.
2. Yu.V. Gaponov, R.U. Khafizov. *Radiative neutron beta-decay and experimental neutron anomaly problem*. Weak and electromagnetic interactions in nuclei (WEIN '95): proceedings. Edited by H. Ejiri, T. Kishimoto, T. Sato. River Edge, NJ, World Scientific, 1995, 745p.
3. R.U. Khafizov, N. Severijns, *About the possibility of conducting an experiment on radiative neutron beta decay*, Proceedings of VIII International Seminar on Interaction of Neutrons with Nuclei (ISINN-8), Dubna, May 17–20, 2000, E3-2000-192, 185–195.
4. Khafizov R.U., Physics of Particles and Nuclei Letters, **108** (2001) 45–53.
5. M. Beck, J. Byrne, R.U. Khafizov, et al., JETP Letters, **76** (2002) 332.
6. R.U. Khafizov, N. Severijns, O. Zimmer et al., *Discovery of the neutron radiative decay*, JETP Letters, **83** (2006) 5.
7. J.S. Nico, et al. Nature, v. **444** (2006) 1059–1062.
8. B.G. Yerozolimsky, Yu. A. Mostovoi, V.P. Fedunin, et al., Yad. Fiz. **28** 98 (1978) 98; [Sov. J. Nucl. Phys. **28** (1978) 48].
9. I.A. Kuznetsov, A.P. Serebrov, I.V. Stepanenko, et al., Phys. Rev. Lett., **75** (1995) 794.
10. L.J. Lising, S.R. Hwang, J.M. Adams, et al., Phys. Rev. C, v. **6** (2000) 055501.
11. J. Byrne, R.U. Khafizov, Yu.A. Mostovoi, et al., J. Res. Natl. Inst. Stand. Technol. **110**, (2005) 415.
12. R.L. Cooper, T. E. Chupp, M. S. Dewey, et al, Phys. Rev. C, **81** (2010) 035503.
13. T.J. Paulus, IEEE Transactions on Nuclear Science, v.NS-32, no.3, June, p.1242, 1985.
14. N. Severijns, et al., e-print arXiv:nucl-ex/0607023; J. Nico, private communication.
15. R.U. Khafizov, V.A. Solovei, e-print arXiv:nucl-ex/0608038.

# Programs for the R-Matrix Description of Neutron Cross-Section Structure

A.B. Popov

*Frank Laboratory of Neutron Physics,*

*Joint Institute for Nuclear Research, Dubna, 141980, Russia*

popov\_ab@nf.jinr.ru

## Abstract

A study of neutron fission and non-fission cross sections, performed during many years in the Frank Laboratory of Neutron Physics, allowed to accumulate a significant experience in the analysis of resonance structure of the cross section as well as of correlation effects in fission using R-matrix formalism. We present a detailed description of the mathematical approach used for the analysis of experimental data with the help of least square method (FUMILI minimization) in order to extract the parameters of structure of cross section or correlation coefficients. The obtained results of the fits for the total, fission and capture cross sections of  $^{235}\text{U}$ , in the energy range up to 10 eV, and for the total cross section of  $^{181}\text{Ta}$ , in the energy range up to 50 eV, are presented.

The calculations were performed in Fortran-codes at JINR using the FLNP and LIT computer clusters.

In an initial stage of neutron cross-section investigations on a booster IBR-30+LUE-40 of Laboratory of neutron physics, JINR, in order to extract the neutron resonance parameters the experimental data was described in single-level Breit-Wigner approach using a program [1]. In a study of angular correlations of fragments at fission of the aligned nuclei of  $^{235}\text{U}$  an attraction of R-matrix description of observable effects [2–4] is demanded, within the limits of the theoretical approach developed by A. Barabanov and W. Furman [5, 6]. This approach has been used also for analysis of P-even and P-odd effects in angular distributions of fission fragments of  $^{235}\text{U}$  and  $^{239}\text{Pu}$  [7, 8]. Results of long-term investigations are presented in the review [9], and information about used programs can be discovered in [10]. In these programs the mathematical apparatus provided that several channels of K-projections of spin  $J$  of compound nucleus to a neutron axis are exhibited in fission.

Let's reduce the basic formulas used in the programs. Initial expression of a scattering matrix is of the form

$$S_{nc}^J = e^{-i(\phi_n + \phi_c)} \{ 2((I - K)^{-1})_{nc} - \delta_{nc} \},$$

where  $I$  is unit matrix,  $K_{ij} = -\frac{1}{4} \sum_{\lambda} \frac{\Gamma_{\gamma\lambda} \sqrt{\Gamma_{i\lambda} \Gamma_{j\lambda}}}{d_{\lambda}} + \frac{i}{2} \sum_{\lambda} \frac{(E_{\lambda} - E) \sqrt{\Gamma_{i\lambda} \Gamma_{j\lambda}}}{d_{\lambda}}$ ,  $d_{\lambda} = (E_{\lambda} - E)^2 + \Gamma_{\gamma\lambda}^2 / 4$ .

Taking into account that  $W_{nc}^J = ((I - K)^{-1})_{nc}$ , cross sections can be written in the following way:

the total cross-section

$$\sigma_{tot} = \frac{4\pi}{k^2} \sum_J g_J [\sin^2 \phi_n - \sin 2\phi_n \operatorname{Im} W_{nn}^J + \cos 2\phi_n (1 - \operatorname{Re} W_{nn}^J)],$$

the scattering cross section

$$\sigma_{sc} = \frac{4\pi}{k^2} \sum_J g_J [\cos^2 \phi_n (1 - 2 \operatorname{Re} W_{nn}^J) - \sin 2\phi_n \operatorname{Im} W_{nn}^J + \operatorname{Re}^2 W_{nn}^J + \operatorname{Im}^2 W_{nn}^J],$$

the absorption cross section

$$\sigma_{abs} = \frac{4\pi}{k^2} \sum_J g_J [\operatorname{Re} W_{nn}^J - \operatorname{Re}^2 W_{nn}^J - \operatorname{Im}^2 W_{nn}^J],$$

the fission cross section (here  $K$  - is the projection of a spin  $J$  to a nucleus axis)

$$\sigma_{fis} = \frac{4\pi}{k^2} \sum_J g_J \sum_K |W_{nJK}^J|^2,$$

and the capture cross-section

$$\sigma_{n\gamma} = \sigma_{abs} - \sigma_{fis}.$$

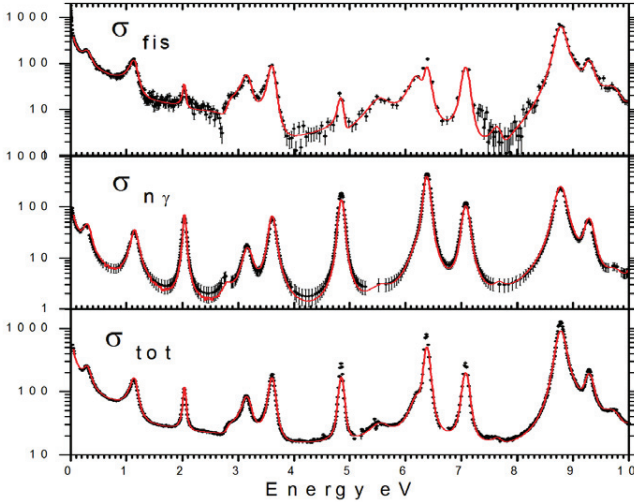


Fig. 1. Results of fitting for cross sections of  $^{235}\text{U}$ : points – experimental data (in barn), curves – calculations.

The analysis of angular correlations of fragments at fission of the aligned  $^{235}\text{U}$  nuclei was made with the use of FUMILI-code together with the known data on total neutron cross sections, total and spin-divided fission cross sections. In the present paper an adaptation of mentioned programs to the analysis of the cross-section data of fissionable and nonfissionable nuclei is made, without an attraction of data on the correlation effects. It would appear that for

this aim it is quite enough to use, instead of four-rank matrix, a two-rank matrix, when only contributions of neutron and fission channels are taken into account. However, trying to describe the total neutron cross section, fission cross section and capture cross section of  $^{235}\text{U}$  we ascertained again that these data are not fitted in a supposition of one (single) fission channel but, for a satisfactory description of the experimental data, it is required to introduce, at least, two fission channels. In fig. 1 the result of the fitting for cross-section data of  $^{235}\text{U}$  taken from EXFOR-bank, in the range of 0 – 10 eV, is shown.

Note that in the calculations a correction for the Doppler broadening of resonances was made. There are no difficulties to take into account an influence of resolution function of a spectrometer used in measurements, as appropriate. There is also a certain ambiguity in values of fitted parameters caused by a number of introduced negative resonances.

For the analysis of cross section of nonfissionable nuclei the similar *R*-matrix parametrization looks simpler and it is possible to use formulas from the paper of A. Lukjanov and N. Janeva [11]:

$$\sigma_{tot} = \frac{4\pi}{k^2} \sum_J g_J \{ \sin^2 \varphi_n + \text{Re} [ e^{-2i\varphi_n} \frac{-iK_m^J}{1 - iK_m^J} ] \},$$

$$\sigma_{abs} = \frac{4\pi}{k^2} \sum_J g_J \text{Re} \left\{ \frac{-iK_{nn}^J}{|1 - iK_{nn}^J|^2} \right\}.$$

Here  $\sigma_{abs}$  is simply the capture cross section. We have tested the modified program for description of the total neutron cross section using the data  $^{181}\text{Ta}$  from EXFOR. Results are presented in fig. 2.

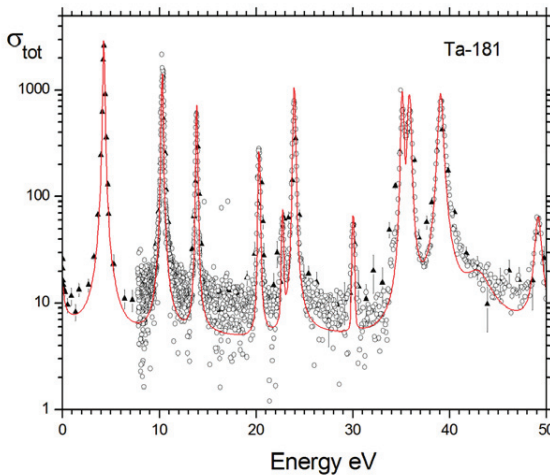


Fig. 2. The total neutron cross section of  $^{181}\text{Ta}$ : points are experimental Belanova, etc. data, triangles are Pohan data (barn), curves are calculations with taking into account of the account Doppler-effect.

Singularity of our programs, unlike SAMMY-code used extensively, is a simultaneous fitting of different types of cross sections, in the same iteration. Despite a multi-parameter character of a problem and a numerical evaluation of fitted-parameters derivatives, using a modern computer cluster of LIT JINR a counting time, for example for  $^{235}\text{U}$ , will be a few tens of minutes.

## References

1. A.B. Popov, I.I. Shelontsev, N.J. Shirikova, "Evaluation of parameters of neutron resonances", JINR, 3-9742, Dubna, 1976.
2. D.I. Tambovtsev, L.K. Kozlovsky, N.N. Gonin, N.S. Rabotnov, J.N. Kopach, A.B. Popov, V.I. Furman, J. Kliman, G. Postma, A.A. Bogdzal, M.A. Gusejnov, "Experimental researches of energy association of angular anisotropy of splinters at division of the oriented kerns  $^{235}\text{U}$  resonance neutrons", ЯФ, **60**, 981,(1997); Phys. Atom. Nucl., **60**, 877, (1997).
3. J.N. Kopach, A.B. Popov, V.I. Furman, N.N. Gonin, L.K. Kozlovsky, D.I. Tambovtsev, J. Kliman, "Examination of angular anisotropy of splinters of division of the drawn up kerns  $^{235}\text{U}$  resonance neutrons and a role of JK-channels", ЯФ, **62**, 900, (1999); Phys. Atom. Nucl., **62**, 840, (1999).
4. J.N. Kopach, A.B. Popov, V.I. Furman, V.P. Alfimenkov, L. Lason, L.B. Pikelner, N.N. Gonin, L.K. Kozlovsky, D.I. Tambovtsev, A.M. Gagarsky, G.A. Petrov, V.E. Sokolov, "Division of heavy kerns by resonance neutrons", PEPAN, **32**, issue 7, 204, (2001).
5. Barabanov A.L. and Furman W.I., "New theoretical possibilities of describing P-even and P-odd angular correlation of fission fragments from resonance neutron induced fission", Proc. of Int. Conf. on Nucl. Data for Science and Technology, (Gatlinburg, Tennessee, 1994, Ed. J.K. Dickens), v.1, p. 448.
6. Barabanov A.L. and W.I.Furman W.I., "Formal theory of neutron induced fission", Z. Phys. A, **357**, 411, (1997).
7. A. Barabanov, W. Furman, A. Popov, "Violation of fundamental symmetries in resonance neutron induced fission", in: Astrophysics, Symmetries, and Applied Physics at Spallation Neutron Sources, ORNL symposium, April 2002, World Scientific, 2003, p.184–193.
8. A.B. Popov, I.S. Guseva, A.L. Barabanov, W.I. Furman, G.A. Petrov. "A helicity approach description of the P-even and P-odd effects in the fission of  $^{239}\text{Pu}$  by resonance neutrons". In: Neutron spectroscopy, nuclear structure, related topics. XI Int. Seminar on Interaction of neutron with nuclei. Dubna, Russia, May 28–31, 2003, Dubna, JINR, 2004, p.304.
9. Gundorin N.A., Zeinalov Sh.S., Kopach Yu.N., Popov A.B., Furman W.I., "Investigations of fission characteristics and correlation effects", PEPAN, **47**, №4, 681–701, (2016); "Examinations of performances and correlative effects in division", PEPAN, **47**, issue 4, 1249–1287, (2016).
10. Popov A.B., Furman W.I., "Programs for calculations of neutron resonance parameters from neutron total and fission cross sections". XXIV International seminar on interaction of neutrons with nuclei, Dubna, May 24–27, 2016, JINR E3-2017-8, p. 291, Dubna, 2017.
11. A.A. Lukjanov, N. Janeva, "All-level parametrization of neutron resonance cross sections", PEPAN, **28**, issue 4, 847, (1997).

# Investigation of the Systematic Time Mark Shift for the Signals from the Organic Scintillator Based Neutron Spectrometer

Prusachenko P., Khryachkov V., Bobrovsky T., Ketlerov V., Bondarenko I.

*Institute for Physics and Power Engineering, Obninsk, Russia*

## 1. Introduction

Organic scintillators are widely used for fast neutron spectrometry. In most cases, the time-of-flight method is used. The accuracy of the neutron energy measurement depends on the accuracy of time mark determination. This is especially important for performing experiments on the measurement of the prompt fission neutron spectra, which are characterized by a rapid change in the neutron yield depending on their energy. Even the small shift in the time mark definition can lead to a serious error in determining the yields of fission neutrons [1]. It is usually in experimental practice that the correction to the time mark shift is determined only for events caused by the detection of gamma rays. Then this correction is applied to correct the time mark of both signals from neutrons and gamma rays [2–7]. The purpose of this work was to study the possible systematic time mark shifts for signals caused by the detection of both neutrons and gamma rays in an organic scintillator. Analysis of the time mark position was performed using the most widely used algorithms – software emulation of the constant-fraction discriminator and the leading edge discriminator. The comparison of the obtained results was made, depending on the algorithm used and its input parameters.

## 2. Experimental setup

The time mark position can be obtained by analyzing the time distributions corresponding to events with the fixed detection time. Using the signal area and the time-of-flight values, this analysis can be performed depending on the signal amplitude. In our case, we analyzed the prompt neutrons and gamma rays from the  $D(d,n)^3\text{He}$  reaction. The neutron detector was located in a special massive shielding at the 0 degrees angle relative to the ion beam axis. Both signals, the signal from the pick-up electrode of the accelerator chop-buncher system and the signal from the neutron detector were simultaneously digitized and stored on the disk for further processing. The main parameters of the experiment are shown in Table 1. The experimental setup is shown in Fig. 1.

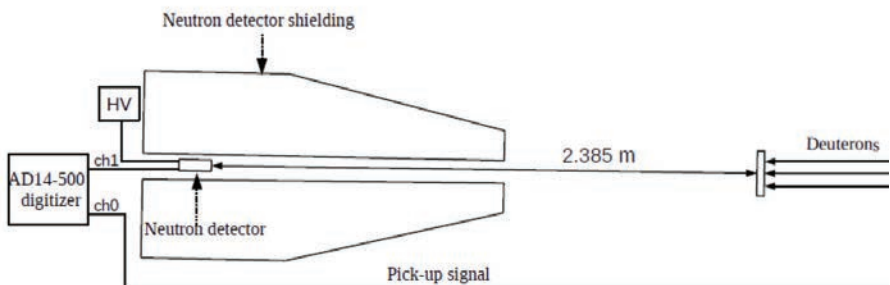


Fig. 1. Experimental setup.

Table 1. The main parameters of experimental setup.

Accelerator operation mode	Pulse mode, pulse width ~1.2 ns.
Accelerated ions type	deutrons
Ion energy	5.952 MeV
Average neutron energy (0 deg.)	9.112±0.005 MeV
Target	D-Ti, 1275±50 ug/cm <sup>2</sup>
Neutron detector	Stilbene, 40×40 mm PMT ET Enterpize 9813QB
Flight path	237.7±0.2 cm
Data acquisition system	AD14-500 waveform digitizer 500 MSamples per second 14 bit ADC resolution.

### 3. Digital Signal Processing

#### 3.1 $n/\gamma$ separation

To determine the type of particle that caused the event in the detector, correlation analysis of signals was used [8, 9]. The signal from gamma rays averaged over 5000 events was used as the target signal for the correlation function calculation. The separation quality obtained for the entire range of the pulse areas is shown in Fig. 2. The dynamic threshold on the separation parameter was used for selection events from neutrons and gamma rays [9].

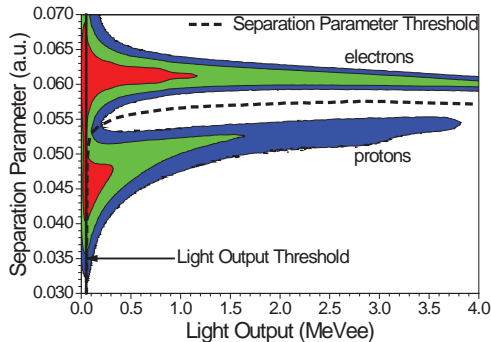


Fig. 2. Two-dimensional spectrum, the separation parameter vs. pulse area. Dotted line – the threshold for the separation parameter.

### 3.2 Time Mark Definition

The study of the systematic errors was carried out for the two most used algorithms for the time mark definition - algorithms that emulate the operation of the constant-fraction discriminator (CFD) and the leading edge discriminator (LED).

In the case of the constant-fraction discriminator algorithm, the operation of the classical CF discriminator was emulated [5, 10]. The time of the baseline crossing of the bipolar pulse formed by summing the main signal, delayed in time, and its copy, inverted and attenuated in 5 times, was used as the time mark (Fig. 3). The accurate time of the baseline crossing was determined by approximating three points near the zero by the parabola. A study of the time mark behavior was conducted for several values of the main signal delay: 8 (CFD # 1), 12 (CFD # 2) and 20 ns (CFD # 3). For the delays above and below these values, the time resolution deteriorated sharply.

The use of the leading-edge discriminator algorithms is associated with a strong amplitude dependence of the time mark position. In our work, we applied an improved algorithm. The time point when the signal reached the predetermined fraction of its pulse height was used as the time mark (Fig. 4). The accurate value of this time point was determined by linear interpolation. The algorithm was compared for several fraction values: 10 (LE#1), 25 (LE#2), and 50% (LE#3) of the pulse height.

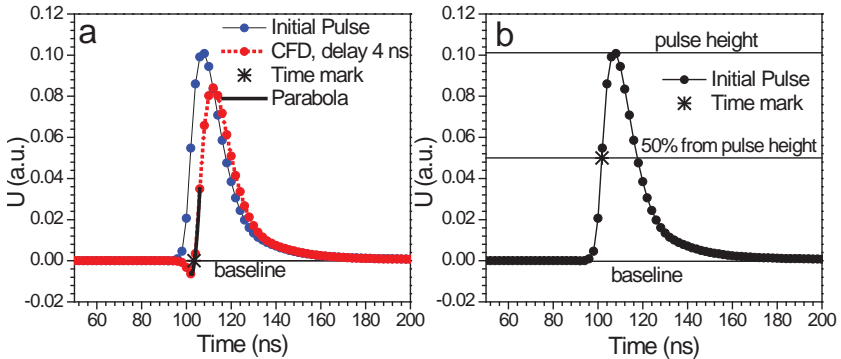


Fig. 3. Demonstration of digital algorithms CFD and LED.

### 4. Time distribution analysis

After the events selection on the separation parameter, time distributions were constructed for both gamma rays and neutrons. In both distributions, narrow peaks are observed, corresponding to the detection of prompt gamma rays and neutrons emitted from the target (Fig. 4).

The main contribution in the background for gamma rays time distribution was made the scattering on the accelerator target node and the random coincidences background, which practically not influenced on the distribution form (Fig. 5). The scattered neutron contribution in the neutrons time spectrum was more significant (Figs. 5, 6). The small amount of the high-energy neutrons was observed to the left of the main peak (Figs. 5, 6).

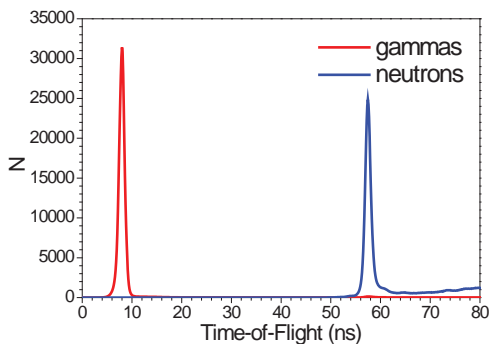


Fig. 4. The time distributions for gamma-rays and neutrons.

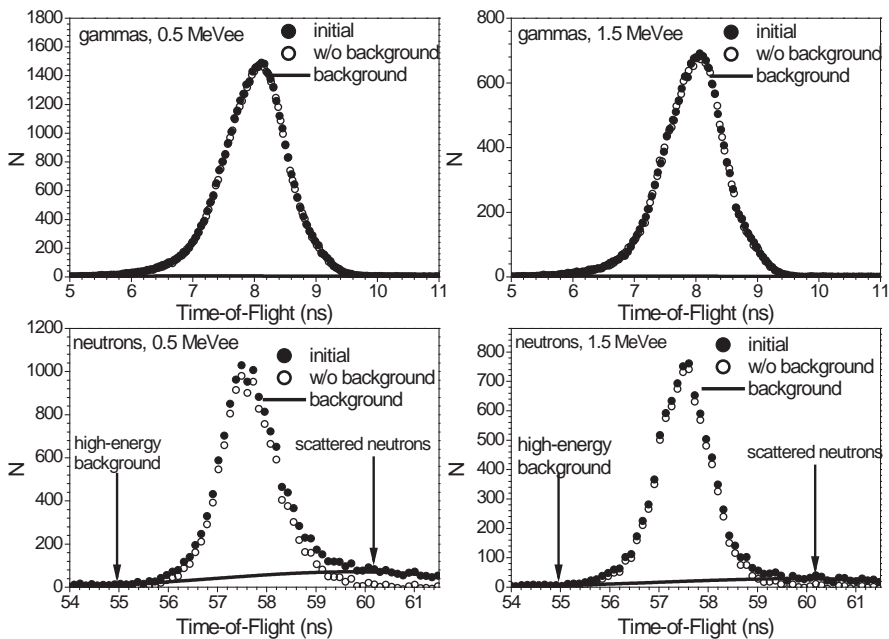


Fig. 5. The time distribution of gamma and neutron for the several fixed pulse area values.

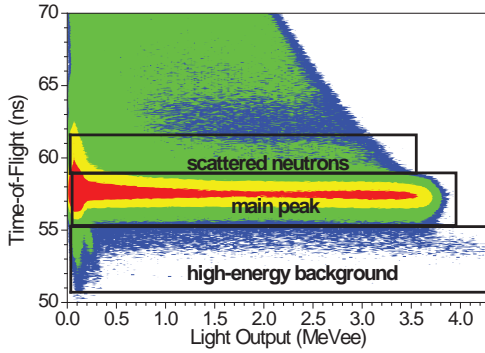


Fig. 6. The neutron two-dimensional spectrum – light output vs. time-of-flight.

The amplitude dependence of the time mark shift was determined by analyzing the position of the peaks of prompt gamma rays and neutrons for the different fixed pulse area values. The value of the peak's mathematical expectation after subtracting the background (Fig. 5) was taken as the estimation the peak position. In the gamma rays case, the average peak position  $M_{\gamma av}$  was calculated after the definition of the position of the prompt gamma rays peak for all values of the pulse area. The time mark shift for the fixed value of the pulse area  $\Delta t_{\gamma i}$  was determined as the difference between the peak position for this pulse area  $M_{\gamma i}$  and the average position of the prompt gamma rays peak for the all range of the pulse areas  $M_{\gamma av}$ :

$$\Delta t_{\gamma i} = M_{\gamma i} - M_{\gamma av} \quad (1)$$

In the neutron case, we determined the time mark shift for the fixed value of the pulse area  $\Delta t_{ni}$  as the difference between the expected neutron time-of-flight  $ToF_{ne}$  and the experimental value of the neutron time-of-flight for this pulse area value  $ToF_{ni}$ :

$$\Delta t_{ni} = ToF_{ne} - ToF_{ni} \quad (2)$$

The experimental time-of-flight value  $ToF_{ni}$  for the fixed pulse area was calculated using follow equation:

$$ToF_{ni} = M_{ni} - M_{\gamma av} + 3.335641d \quad (3)$$

where  $M_{ni}$  – mathematical expectation of neutron peak for fixed pulse area  $i$ ,  $M_{\gamma av}$  – the average position of the prompt gamma peak,  $d$  – the flight path in meters. The expected neutron time-of-flight value  $ToF_{ne}$  was calculated using the known value of the average neutron energy and the known flight path:

$$ToF_{ne} = 3.335641d \frac{E+A}{\sqrt{E(E+2A)}} \quad (4)$$

where  $A$  – neutron mass (939.565 MeV),  $E$  – neutron energy in MeV,  $d$  – flight path in meters.

## 5. Results of time distribution analysis

The results of the time distributions analysis are shown in Fig. 7. For all cases considered, the neutron peak centroids are systematically shifted relative to the expected value, calculated from the known neutron energy and the known flight path. The value of the systematic shift depends on the algorithm's type, its parameters and the pulse area. This indicates that the time mark definition using the most commonly used algorithms can lead to its systematic shift, and therefore to a shift in the neutron energy definition. For the CFD algorithm with the increase of the delay and for the LED algorithm with the increase of the threshold fraction, the value of the observed shift increases.

An analysis of the experimental results showed that for all the analyzed cases the shape of the curve for neutrons differs from that for gamma rays. The dependence of the peak centroid position on the pulse area is also observed for gamma rays, which also can be seen in the other author's works [2–7]. It can also be noted that the time mark quality obtained using the modified LED algorithm is insignificantly worse than that of the CFD algorithm.

The observed time mark position shift for neutrons and its difference from that for gamma rays can be explained by the difference in the pulse shapes from neutrons and gamma rays. In this case, it should be observed both for digital algorithms and when using analog electronics.

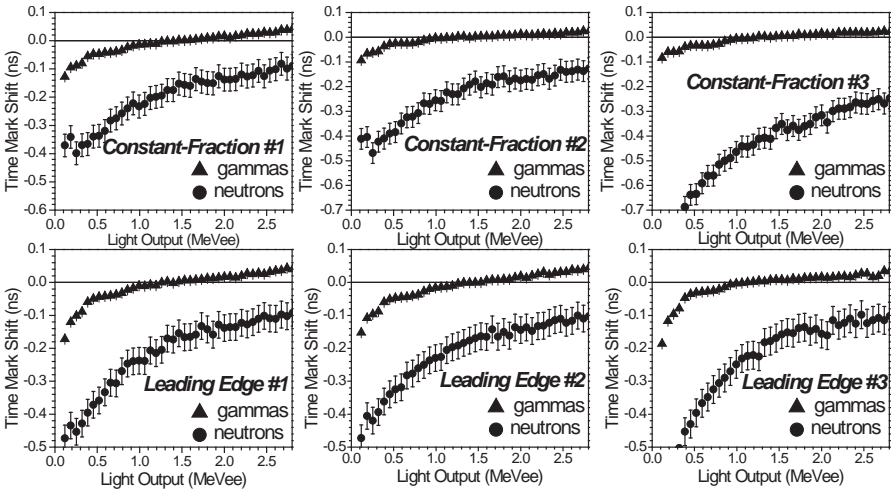


Fig. 7. The time mark shift for neutrons and gamma rays as the pulse area function. The results are given for all algorithms considered in the work.

## 6. Influence on the neutron spectrum measurements

The shift in the detected neutron energy will depend on the flight path. The larger the flight path, the smaller the error in determining the energy. Fig. 8 shows the energy dependence of the systematic shift in the neutron energy for the extreme cases considered in the work (CFD#1,3, LE#1,3). The value of the shift is given at the flight path of 1 meter. For large values of the flight path (more than 2.5–3 meters) the shift value will be negligible. Also, from the results it can be seen that the time mark shift will have the greatest influence at neutron energies above 6 MeV.

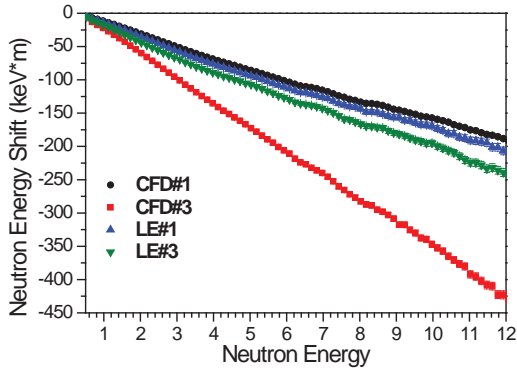


Fig. 8. The shift in the neutron energy definition as the neutron energy function for several algorithms.

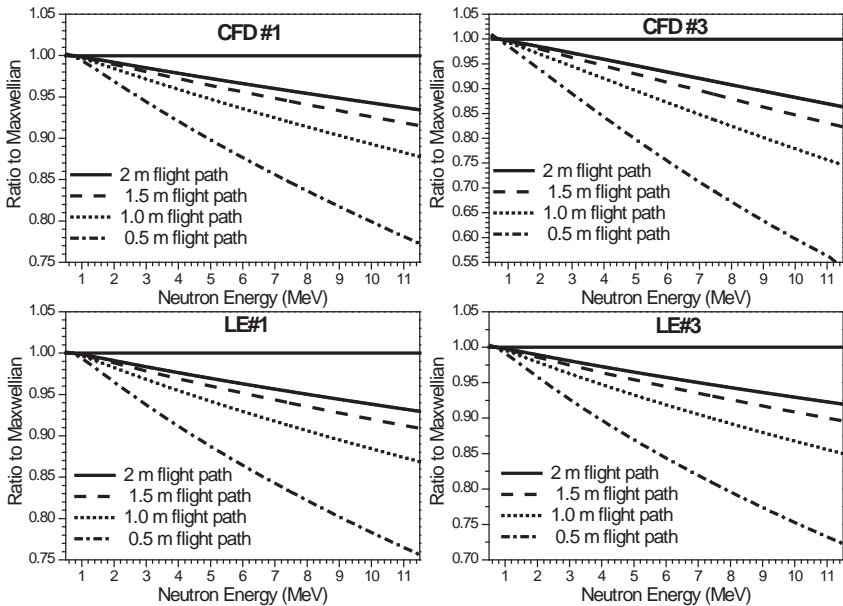


Fig. 9. The demonstration of the time mark shift influence on the prompt neutron yield measurements.

The prompt fission neutron spectra are characterized by a sharp change in the neutron yield with an increase in their energy. Therefore, even a small error in the determination of energy can lead to a serious error in determining the yield of fission neutrons. Fig. 9 shows the possible influence of the time mark shift on the measurements of the prompt fission neutron yield as the neutron energy function. The results were obtained by simulating the  $^{252}\text{Cf}$

prompt neutron spectrum (the Maxwell distribution with  $T=1.42$  MeV) using the neutron energy shift data (Fig. 8) for the different algorithms and flight path values.

It should be noted that most measurements of the prompt fission neutron spectra are carried out on the short flight path (0.5–2 m), so the observed effect can have a significant impact on the results of measurements of fission neutron yields at different energies. In turn, this may lead to an error in determining the average energy of the fission neutrons spectrum.

## 7. Conclusions

The analysis of systematic shifts in the time mark definition was carried out for the digital algorithms that emulate the operation of the constant-fraction discriminator and the leading edge discriminator. The influence of the algorithms input parameters of the shift value is studied.

For all cases considered, the neutron peak centroids are systematically shifted relative to the expected value, calculated from the known neutron energy and the known flight path. The value of the systematic shift depends on the algorithm's type, its parameters and the pulse area. For the CFD algorithm with the increase of the delay and for the LED algorithm with the increase of the threshold fraction from the signal pulse height, the value of the observed shift increases.

An analysis of the experimental results showed that for all the analyzed cases the shape of the curve for neutrons differs from that for gamma rays. Therefore, it is incorrect to use as an correction for the neutron signals the time mark shift value determined from the analysis of the prompt gamma rays peak. The correction for the time mark of the neutron signals must be determined separately.

It is shown that the observed systematic time mark shift for signals from neutrons will lead to a significant shift in the neutron energy value determined from their time-of-flight for short flight path (less than 2 meters). This is especially critical for experiments on the prompt fission neutron spectra measurements, since they are characterized by a rapid change in neutron yield with an increase in their energy. In turn, this may lead to an error in determining the average energy of the fission neutrons spectrum.

## References

1. R.C. Haight, H.Y. Lee, T.N. Taddeucci, et al., Nuclear Data Sheets **119** (2014) 205.
2. A.S. Vorobyev, O.A. Shcherbakov, Yu.S. Pleva et al., Nuclear Instruments and Methods in Physics Research A **598** (2009) 795.
3. E. Blain, A. Daskalakis, R. C. Block, et al., Physical Review C **95** (2017) 064615.
4. S. Noda, R. C. Haight, R. O. Nelson et al., Physical Review C **83** (2011) 034604.
5. A. Gook, F.-J. Hamsch, and M. Vidali, Physical Review C **90** (2014) 064611.
6. C. Matei, F.-J. Hamsch, S. Oberstedt, Nuclear Instruments and Methods in Physics Research A **676** (2012) 135.
7. N.V. Kornilov, I. Fabry, S. Oberstedt, F.-J. Hamsch, Nuclear Instruments and Methods in Physics Research A **599** (2009) 226
8. N.V. Kornilov, V.A. Khriatchkov, M. Dunaev, et al., Nuclear Instruments and Methods in Physics Research A **497** (2003) 467.
9. P.S. Prusachenko, V.A. Khryachkov, V.V. Ketlerov, et al., Nuclear Instruments and Methods in Physics Research A **905** (2018) 160.
10. Rudlevski P.D., Khriachkov V.A., Dunaev M.V., Proceeding of XII International Seminar on Interaction of neutrons with Nuclei (2004), 415.

# TySSA — A Set of Means for Building of Distributed Software Systems for the Automation of Experiments by the User

Shvetsov V.N., Salamatin K.M., Salamatin I.M., Tsulaia M.I.

*FLNP, JINR, Joliot Currie 6, Dubna, Moscow region, Russia*

Modification of software systems for automation of experiments requires time comparable to their development due to uniqueness. In this regard, methods and means that reduce these terms are relevant. The paper presents a set of tools designed to build distributed software systems for automation of experiments (SAE). Service-oriented architecture is used. The main means of the complex are multi-user programs. Each SAE, built by means of the complex **TySSA**, consists of independent components (programs in the format .exe). If the necessary services are available, their integration into the experiment automation system corresponding to the planned experiment technique is performed by the experimenter and requires 10-20 minutes. The complex **TySSA** is designed for use in experiments at the **IBR-2** research reactor [1], but can be used in other problem areas.

## 1. Architecture of the complex

The emergence of large neutron centers leads to the expansion of the research front and requires a quick response of developers of research automation systems. The possibilities of modern computer technology allowed to create a technology for the development and modification of software systems for the automation of experiments that meets this requirement.

The developed complex **TySSA** (Typical System for Spectrometry Automation) uses Service-Oriented Architecture (SOA), which provides effective approach to solving the problem.

### 1.1. Basic principles of the used architecture

1. **Publication of access interfaces.** Services are components of the automation system, they publish their interfaces and interact with each other and with support services through open, widely used standards. Interfaces do not depend on the platform, programming language, operating system and other technical features of the implementation.
2. **Separation of code.** The service included in the information system implements a separate function, which is a logically separate, repetitive task used in accordance with the experimental technique.
3. **Large-Block structure of services.** Services in SOA are components of a sufficiently high level, so that the interaction between them is reduced to a limited number of messages.
4. **Weak coupling.** Services can be implemented independently of other system services. Changes to the service implementation do not affect the control program that uses the service. Weak coupling provides a simple adaptation of the system to changes in the structure and composition of services.

These principles allowed to remove the most difficult problems of integration of components in SAE and to react to changes in a configuration and a technique dynamically and without difficult transformations at the level of integration of components. The architecture is aimed at supporting a process rather than a program. The components are integrated in such a way that their execution takes place in a certain sequence in accordance with the technique of the experiment. Each of the service components can participate in different automation systems.

## 1.2. Technological support of architecture

The following main components have been developed to support SOA technology:

1. **DiCME** module [2] (message bus), which provides guaranteed sending and receiving of messages.
2. **Database (DB)** - an electronic catalog where information about each component of the system is stored. The database management program provides customers with information about the components (services) that are currently available.
3. **Program for description of technique of work.**
4. **Experiment control program** - a component that controls the flow of work in accordance with a given technique. At the same time, data processing at separate stages is carried out in different independent components.
5. **Services** to ensure the implementation of the technique. The set of selected services, the specified sequence and parameters of their operation determine the technique of the experiment.
6. **Additional group of services**, whose task is to monitor emergency situations, ensure the viability of the system, etc.

## 2. PSJ support database management program

The database is implemented by means of **SQLite** and in 4 tables contains information about the characteristics of available services (**devices** and **SrvsProps**), experiment management programs (**JOBS**, **CurrentJob**) of all users and some current information. Figure 1 shows the database management interface and the contents of the devices table. The figure shows the names and ways of presenting data to control the operation of services. The data to update the devices table are provided by the developers of these programs.

There are 2 modes of filling the database: (1) editing by using the provided (figure 1) interface; (2) automatic, by reading the passport of the service in case of it change. Information from the devices table is used to describe the technique of the experiment and to prepare the experiment program.

## 3. PSJ program for description of the technique and preparation of the experiment program in JSON format

The PSJ program is designed to describe the technique of the experiment and prepare the text of the task for the experiment (experiment program) in JSON format. The technique is represented by a sequence of states of the experimental setup, in each state data registration is performed. The state of the instrument is formed by the sample environment devices, the composition of the devices and the parameters transmitted to them are determined by the

experimental technique. Each device is managed by a separate service. The number of devices and states is not limited.

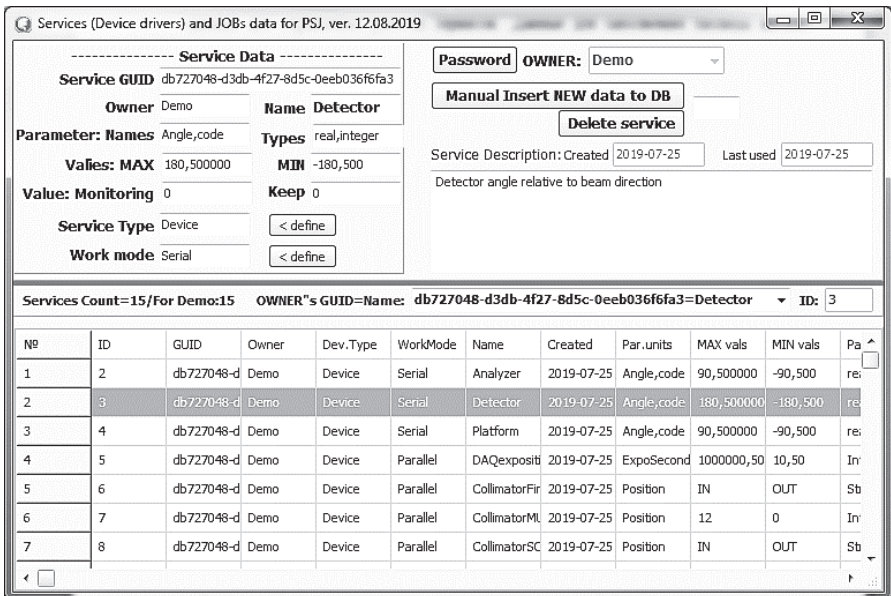


Figure 1. PSJ support database management program interface.

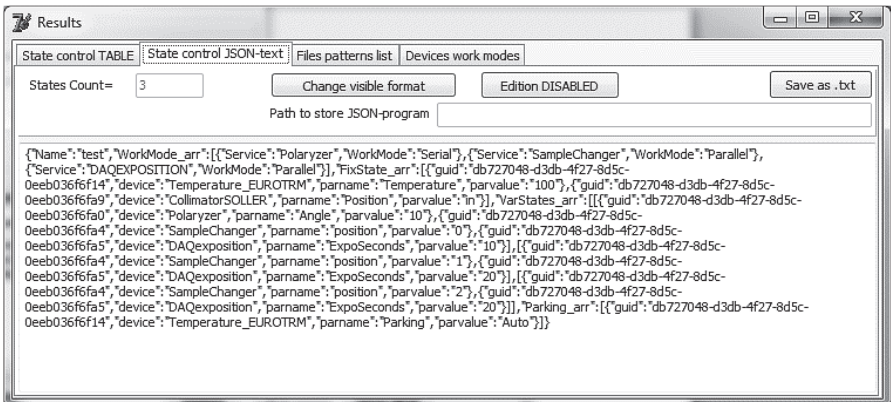


Figure 2. Text of the experiment program.

The PSJ program allows you to select the characteristics of the necessary services from the database in accordance with the planned technique of the experiment and make a task for the experiment.

The experiment program contains 3 main sections:

1. A section of fixed conditions that remain unchanged throughout the experiment.
2. A section of changeable conditions. This section describes all the instrument states in which you want to register data, as well as the parameters for recording and storing data. The number of implemented states and registration conditions are determined by the planned experiment technique.
3. A section providing parking of devices at the end of work.

Figure 2 shows the text of the experiment program prepared by the PSJ program. The PSJ program enters the results and intermediate data of the task preparation process into the database.

#### 4. Job Control program

The **Job Control** program performs the task for the experiment that was prepared using PSJ. Search for services in the network and interaction with them is performed by a specially designed module **DiCME**. The **Job Control** program is equipped with means of protection against loss of information in case of power failures and failures of experimental equipment.

#### 5. Services that manage sample environment devices

Within the framework of the considered technology, a special structure of services and a method of integration with the experiment management program were developed. Services are independent components in executable format (.exe) and are combined into a distributed system dynamically.

Each service manages one sample environment device. The set of devices determines a number of states of the experimental setup at which the registration of experimental data will be performed.

The structure of the service can be divided into the following parts:

1. A device **Passport** describing some program IDs, managed parameters and ranges of their values.
2. The **main function** of the service, forming the conditions on the device in accordance with the parameters transmitted to it.
3. A function that returns the **time required** to perform this operation.
4. The **Interface** part that provides interaction with the control program.

Figure 3 shows a fragment of the service program text containing an example of the Passport view. Different formats for parameters representing can be used.

The interface part of the service provides management of the service over the network, which includes:

1. The discovery of a service and determining of address for the interaction.
2. Transfer of control parameters to the service.
3. Receiving service responses about the duration of the operation completion.
4. Receiving service responses on completion of the operation.

```

{Passport Data}
const
  SRVC_NAME      = 'Polarizer';
  SRVC_GUID      = 'db727048-d3db-4f27-8d5c-0eeb036f6fa0';
  SRVC_TYPE      = 'device';
  SRVC_OWNER     = 'Demo';
  SRVC_WORK_MODE = 'serial';
  SRVC_PAR_NAMES = 'angle,code';
  SRVC_PAR_TYPES = 'real,integer';
  SRVC_PAR_MIN   = '-90,500';
  SRVC_PAR_MAX   = '90,10000';
  SRVC_HAVEMONITORING = false;
  SRVC_HAVEKEEPVALUE  = false;

```

Figure 3. Fragment of program text of service.

The text of the interface part is the same for all services in this technology. For the new service, only the text shown in figure 3 (Passport) and two functions are edited and combined with the interface part. The interaction of the experiment control program (**Job Control**) with the service is performed by the **DiCME** module, using open protocols **SLP**, **JSON-RPC**, **MQTT** [3]. These protocols, using **GUID**, provide search of the necessary service in a local network and management of its work.

All services that put the hardware system in a needed state can run simultaneously. The hardware part of the system may include several computers connected to a local network. In this case, the service is started on the corresponding computer and the control program searches for it automatically.

The same devices (e.g. collimators, filters, targets, DAQ controllers, etc.) can be used in different installations. If the software is created using this technology, it is possible to use the same services. To ensure that the characteristics of a particular instance of the service are found in DB the service passport contains the name of the installation (**Owner** field).

## 6. Example of DAQ subsystem parameterization for TOF-experiments

The **DAQ** subsystem differs from other services in the way it interacts with the experiment control program. The description of time encoder used in a number of experiments is presented in paper [4]. For this device, at the stage of describing the experimental technique, only the duration of exposition in each state of the experimental setup is determined. The command to start the registration is issued by **Job Control** automatically, when each installation of state is completed, the registration is stopped automatically by the **DAQ** subsystem when the specified exposition time expires. The operator commands **Pause**, **Continue** do not affect the actual exposition duration. Parameterization of the method of operation of the time encoder requires much more parameters, the values of which are determined by the requirements of the selected experimental technique are transmitted to the **DAQ** subsystem in a file.

## Conclusion

A multi-user complex of tools for building distributed SAE with service-oriented architecture was developed.

The proposed mechanism of interaction of system components according to protocols implemented in **DiCME** and **SLP** allows different users in the same local network to use unified programs, provides freedom to expand the functionality and configuration of a distributed software control system. Using dual task-specific service identity (**GUID** and **Owner** codes) eliminates conflicts when using services with the same name and code in different applications on the same LAN.

The proposed structure of the service simplifies their development, ensures the continuity of these components of the system and gives a significant saving of SAE modification time when changing the experimental technique. In addition, this approach encourages the standardization of a number of sample environment devices.

Using a unified experiment management program and services in executable format (.exe), the ability to use ready-made services in different systems, dynamic integration of components into the software system of the experiment provide a significant reduction in the time of development or modification of software systems for specific experiments. The same way of saving data makes it possible to use ready-made statistical control utilities, visualization, data processing in different experiments.

The proposed technology for developing software systems is more effective in large neutron centers, where dozens of neutron guides are used, the equipment used (devices for changing collimators, filters, targets, **DAQ** systems, etc.) is standardized and often there is a need to change the experimental technique.

## References

1. [https://elibrary.com.ua/m/articles/view/PULSING\\_NUCLEAR\\_REACTOR\\_IBR-2M](https://elibrary.com.ua/m/articles/view/PULSING_NUCLEAR_REACTOR_IBR-2M).
2. *Salamatin K.M.* DiCME - distributed environment for interaction of components of the experimental automation system for low-energy physics // Software engineering, 2014. No. 3, p.p. 3–11.
3. Service Location Protocol RFC 2608.
4. *Shvetsov V.N.; Alpatov S.V.; Astakhova N.V.* et al. An eight-channel system for neutron-nuclear investigations by the time-of-flight method // Instruments and Experimental Techniques, Vol. 55, No. 5, pp. 561–568, 2012.

# **Nuclear Analytical Methods in the Life Sciences**

## USING XRF ANALYSIS TO DETERMINE THE ELEMENTAL COMPOSITION OF PIGMENTS IN THE PAINTING OF MEDIEVAL ORIENTAL FAIENCES

V.Yu. Koval<sup>1</sup>, A.Yu. Dmitriev<sup>\*2</sup>, V.S. Smirnova<sup>2</sup>, V.V. Lobachev<sup>2</sup>

<sup>1</sup>*Institute of Archaeology of the Russian Academy of Sciences, Moscow, Russian Federation*

<sup>2</sup>*Frank Laboratory of Neutron Physics, Joint Institute for Nuclear Research, Dubna, Moscow Region, Russian Federation*

\*e-mail: [andmitriev@jinr.ru](mailto:andmitriev@jinr.ru)

An X-ray fluorescence analysis (XRF) of the glaze of a glazed medieval Oriental ceramics batch was carried out in the NAA group of the IREN research facility of the Frank Laboratory of Neutron Physics, JINR, to determine the marker elements characteristic of various types of raw glaze materials used to manufacture of pigments. As a result, it was found that the blue color in the studied samples is due to the addition of cobalt, green one is due to copper or chromium, brown – manganese or iron, and turquoise – copper.

### Sampling

13 samples of glazed medieval eastern ceramics were obtained from the Institute of Archeology, RAS to the NAA group of the IREN research facility of the Frank Laboratory of Neutron Physics, JINR. Each sample was examined from the glazed sides. This type of artifact is not only very numerous but also the most informative object. Studies of the composition of glazes of oriental faience have already been carried out in the past [1, 2], but the number of analyzed samples remains insufficient. This article presents the results of a study of 13 glaze samples obtained from fragments of imported ceramics discovered during excavations of the city of Bulgar (X–XV centuries, in the territory of Tatarstan, Russian Federation). Of these, 6 samples belonged to the products of the urban centers of the Golden Horde in the Lower Volga region (No. 1, 3, 4, 6, 7, 13), Persia (No. 2, 5, 9–12) and the not yet established center in Persia or Syria (No. 8). All of them came from layers and buildings dated by the middle – the second half of the 14<sup>th</sup> century.

The remarkable thing is that this study of archaeological ceramics in the NAA group is not carried out for the first time [3].

### Equipment

A portable Bruker Tracer 5<sup>i</sup> device (Fig. 1) was used for carrying out the X-ray fluorescence analysis [4]. The device is equipped with a 40 mm<sup>2</sup> SDD detector with resolution <140 eV on the Mn-K<sub>a</sub> line (250,000 pulses/s). The features of the device are the ability to install interchangeable collimators and the availability of a built-in video camera (Fig.2, Fig.3Fig.). The collimator with a diameter of 3 mm was used for the study. The built-in video camera made it possible to position the sample under investigation relative to the place of the X-ray beam penetration. These features of the device allowed to study the elemental composition of not only the glaze itself, but also to carry out a non-destructive research of various decorative elements with dimensions of more than three millimeters.

## Experiment

Spectra of glazes, glaze decoration elements with different colors and sizes greater than 3 mm, and background ceramics spectra were collected for each sample.

For the analysis of the spectrogram, only those peaks were selected that were present in one color and were absent in the others ones. If such peaks were found, it was concluded that the corresponding chemical element was the main component of the coloring pigment to obtain this color. To exclude the possibility of influence the spectrum of the ceramic substrate on the glaze spectrum, the spectrum of ceramic substrate was also added to the final spectrogram. For example, in Fig. 7, we see that the peaks of copper (Cu) is present only in the glaze spectra and is completely absent in ceramic substrate.



Fig. 1. Bruker Tracer 5<sup>1</sup> XRF device.

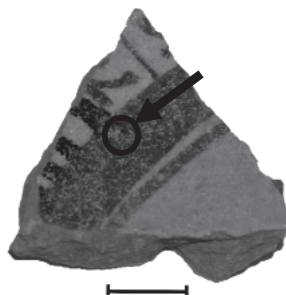


Fig. 2. Sample with marked test point.

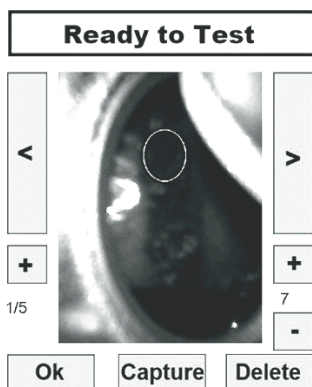


Fig. 3. Test point on built-in video camera.

Investigated samples were grouped as follows:

- turquoise transparent glazes without additional decor,
- white and greenish covered with tin glazes, including luster painting,
- transparent colored glazes with over-glaze colorful and luster decor, and
- colorless glazes of vessels decorated with polychrome underglaze painting.

Each of groups is considered in detail below.

a) Figs. 4 and 5 illustrate the turquoise transparent glazes without additional decor.



Fig. 4. Sample C-3.

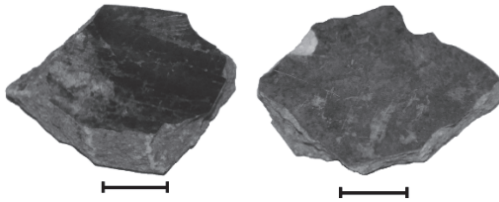


Fig. 5. Sample C-7.

The turquoise color in the group of turquoise transparent glazes without additional decor is caused by a high content of copper oxide in the mixture (Figs. 6 and 7). An opalescent view was obtained by iridescence.

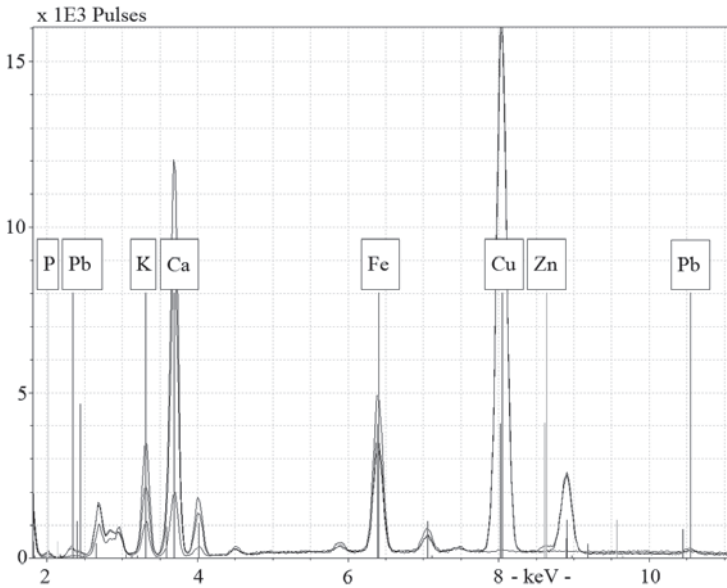


Fig.6. Full spectra of glaze and ceramic base of C-7 sample.

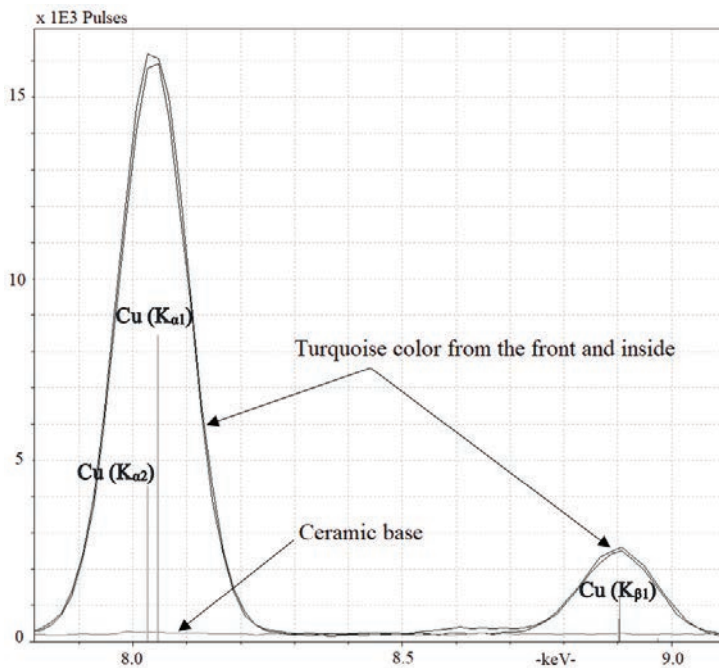


Fig.7. Peaks of Cu in spectrum of C-7 sample.

b) White and greenish samples covered with tin glazes, including luster painting, are shown in Figs. 8, 9 and 10.



Fig. 8. Sample C-5.

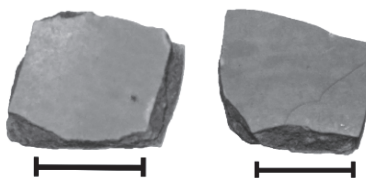


Fig. 9. Sample C-13.

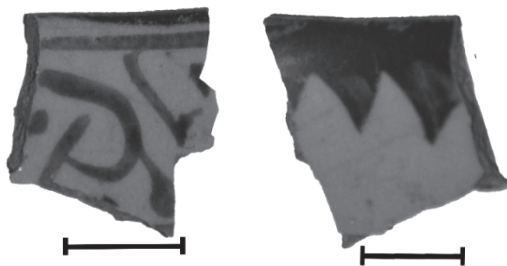
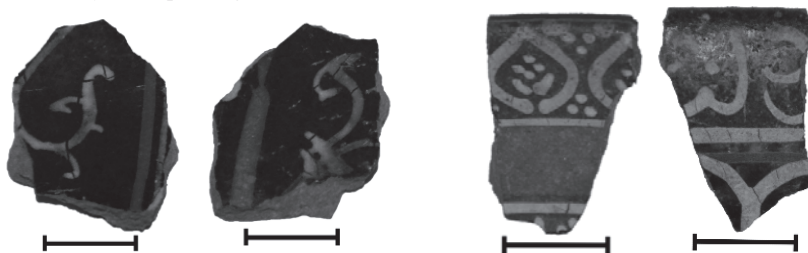


Fig. 10. Sample C-9.

Tin is present in large quantities in white glazes muffled by tin, as well as lead – an impurity to tin. A small amount of arsenic is possible. There is an interesting sample in this group (Fig. 8). A gold pigments (luster) is applied on this sample. This color is based on the addition of silver to the mixture.

c) Transparent colored glazes with over-glaze colorful and luster are shown in Figs. 11–13. Two samples belong to vessels of the "lajvardina" type – with transparent deep-blue (C-2) and turquoise (C-10) glazes, last one (C-8) were parts of bowl covered by deep-blue glaze, decorated by lustre painting.



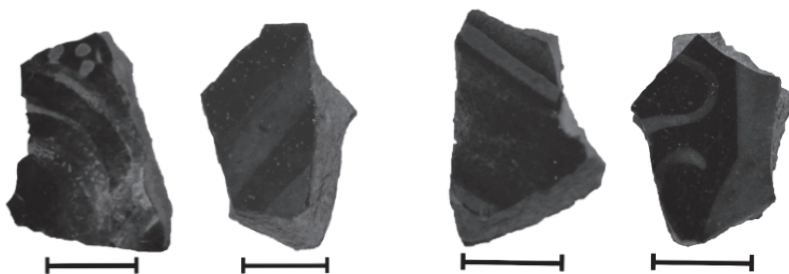
I. The first fragment.

II. The second fragment.



III. The third fragment.

Fig. 11. Sample C-2 (three fragments).



I. The first fragment.

II. The second fragment.

Fig. 12. Sample C-8 (two fragments).

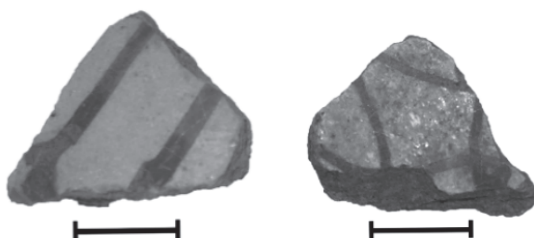


Fig. 13. Sample C-10.

The group of transparent glazes colorful cobalt-blue (Fig. 11 (I) and (III), 12) and copper-blue or turquoise (Fig. 11 (II), 13) is represented by samples with multi-colored (white, brown-red) overglazed patterns (Fig. 11, 13) and luster decor (Fig. 12). The blue color everywhere in the group is due to the presence of cobalt in the pigment, which has a strong coloring effect. Turquoise color, as in group 1, was obtained by adding copper to the pigment. Green one in luster (Fig.12) is also due to the presence of copper. Brown one is formed by iron. Tin, lead and arsenic are noted in some samples.

d) Colorless glazes of vessels decorated with polychrome underglaze painting are shown in Figs. 14–18.

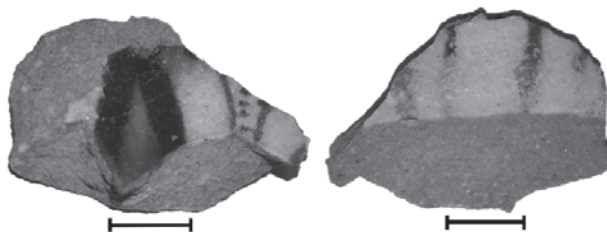


Fig. 14. Sample C-1.

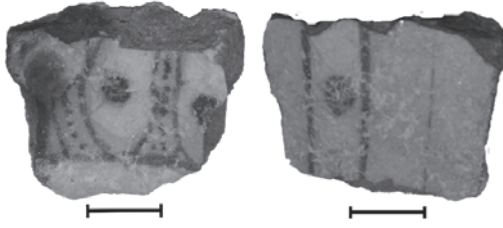


Fig. 15. Sample C-4.

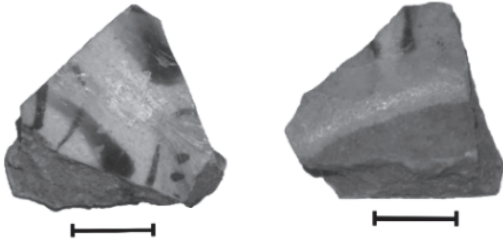


Fig. 16. Sample C-6.

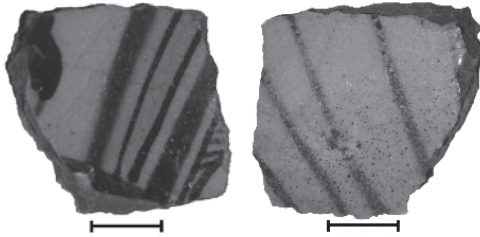


Fig. 17. Sample C-11.

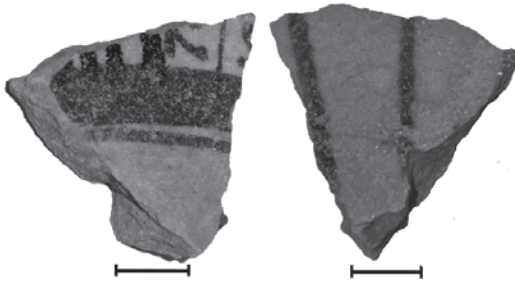


Fig. 18. Sample C-12.

The study of colorless glazes with underglaze painting was complicated by the fact that X-ray fluorescence analysis is a surface method. This fact limited the ability to fix the elements under the glaze. However, some elements of the pigments were found: manganese, causing brown color, cobalt – blue one, chromium (Fig. 14) and copper (Figs. 15–18) – green, copper – turquoise colors.

### Conclusions

Portable XRF device Bruker Tracer 5<sup>i</sup> was used for research of glazed medieval eastern ceramics. The elemental composition of not only the glaze was studied, but non-destructive studies of various decor elements with dimensions of more than three millimeters were also carried out. It was found that the blue color in the test samples was due to the addition of cobalt, the green due to copper or chromium, the brown due to manganese or iron, and the turquoise to copper.

### References

---

1. V.Yu. Koval. *Oriental Ceramics in Rus' 9<sup>th</sup> –17<sup>th</sup> centuries*. Moscow: Nauka, 2010. P. 30.
2. E.V. Sayko. *Glazed ceramics of Central Asia 12<sup>th</sup> –15<sup>th</sup> centuries*. Dushanbe: Donish, 1969. P. 106–123.
3. V.Yu. Koval, A.Yu. Dmitriev, S.B. Borzakov, O.E. Chepurchenko, Yu.G. Filina, V.S. Smirnova, V.V. Lobachev, N.N. Chepurchenko, M.V. Bulavin. *Ceramics of Bolgar: the first results of usage of neutron activation analysis*. *Physics of Particles and Nuclei Letters*, 2019, Vol. **16**, №6, pp. 1004–1020.
4. <https://www.bruker.com/products/x-ray-diffraction-and-elemental-analysis/handheld-xrf/tracer-5-series/overview.html>

# **Investigation of the Element Composition of Barmas Medallion (the 12th – First Half of the 13th Centuries) by Method of Neutron Resonance Capture Analysis**

N.V. Simbirtseva<sup>1,2</sup>, P.V. Sedyshev<sup>1</sup>, S.T. Mazhen<sup>1,2</sup>, Yu.D. Mareev<sup>1</sup>, V.N. Shvetsov<sup>1</sup>,  
A.M. Yergashov<sup>1,2</sup>, A.Yu. Dmitriev<sup>1</sup>, I.A. Saprykina<sup>3</sup>, A.N. Khokhlov<sup>3</sup>,  
O. Kozlova<sup>4</sup>, T. Artemicheva<sup>4</sup>

<sup>1</sup>*Frank Laboratory of Neutron Physics, Joint Institute for Nuclear Research, Dubna, Russia*

<sup>2</sup>*Institute of Nuclear Physics, Almaty, 050032, the Republic of Kazakhstan*

<sup>3</sup>*Institute of Archaeology of the Russian Academy of Sciences, Moscow, Russia*

<sup>4</sup>*Tver Scientific and Restoration Center, Tver, Russia*

## **Abstract**

The analysis of element composition of the medallion was carried at IREN Facility in Frank Laboratory of Neutron Physics by Neutron resonance capture analysis (NRCA). The method is based on the registration of neutron resonances and the measurement of the yield of reaction products in the resonances. The resonance energies are known practically for all stable nuclei and the set of energies does not coincide completely for any pair of isotopes. It allows determining the isotope-element composition.

The Barmas medallion dates back to the 12th – first half of the 13th centuries (the ancient Russian time). It was found in historical part of Tver city near the Tver Kremlin. Analogues of this medallion are in the expositions of the Moscow Kremlin which consist mostly of silver or gold; but until today nobody studied the elemental composition of the metal of such objects. The result of investigation of element composition of medallion will be presented in report.

## **1. INTRODUCTION**

In this paper the application of Neutron Resonance Capture Analysis (NRCA) will be discussed. It is a relatively new method for investigation elemental composition of objects. NRCA is based on the detection of the prompt  $\gamma$ -radiation following neutron capture as a function of neutron energy, the latter being determined with the time-of-flight technique [1]. This method is currently being developed in the Frank Laboratory of Neutron Physics [2].

The analysis was applied to a medallion (Fig.1). The medallion is historical artifact, which was discovered during the archeological excavations of Tver scientific and restoration center. The medallion dates back to the 12th – first half of the 13th centuries. It was found in historical part of Tver city near the Tver Kremlin. This is a unique artifact that characterizes the daily life of the ancient Russian city. On the face of medallion on niello layer was engraved a traditional image of six-pointed prosperous cross on triangular base. Most of such medallions were found in the cultural layer dated from the second half of XII c. till 1240, but some medallions were from the cultural layer dated by later period – XIII–XIV c. in the territory of Tver.



Fig. 1. The real view of medallion.

Analogues of such medallion are in the expositions of the Moscow Kremlin Museum which consist mostly of silver or gold. One of the aims of this research is a determination of the main type of metal (silver or copper) on the surface and into the bulk of medallion, and reconstruction the possibility type of manufacturing procedure (silvering etc.).

## 2. EXPERIMENT

The sample was irradiated with neutrons by pulsed neutron source (IREN) and the time-of-flight spectrum of reactions  $(n,\gamma)$  was registered [3]. The main part of the IREN facility is a linear electron accelerator. The facility parameters: the average energy of electrons was  $\sim 40$  MeV, the peak current was  $\sim 1.5$  A, the width of electron pulse was  $\sim 100$  ns, and the repetition rate was 25 Hz. The total neutron yield was about  $3 \cdot 10^{11} \text{ s}^{-1}$ . The measurements were carried out at the 58.6 meters flight path of the 3rd channel of the IREN. The big liquid scintillator detector was used for the registration of  $\gamma$ -quanta [4]. The sample was placed inside the detector. The neutron flux was permanently monitored by the SNM-17 neutron counter. The signals from the detector and the monitor counter were simultaneously fed to the two independent inputs of time-to-digital converter.

The measurements with the sample lasted about 41 hours. The resonance energies were determined according to the formula:

$$E = \frac{5227L^2}{t^2}, \quad (1)$$

where  $t$  – time of flight in microseconds,  $L$  – flight path in meters,  $E$  – kinetic energy of a particle in eV.

The resonances of silver, gold and copper were identified on the time-of-flight spectrum (Fig. 2) [5, 6]. The measurements with standard samples of silver, gold and copper were made in addition to the measurement with the investigated sample.

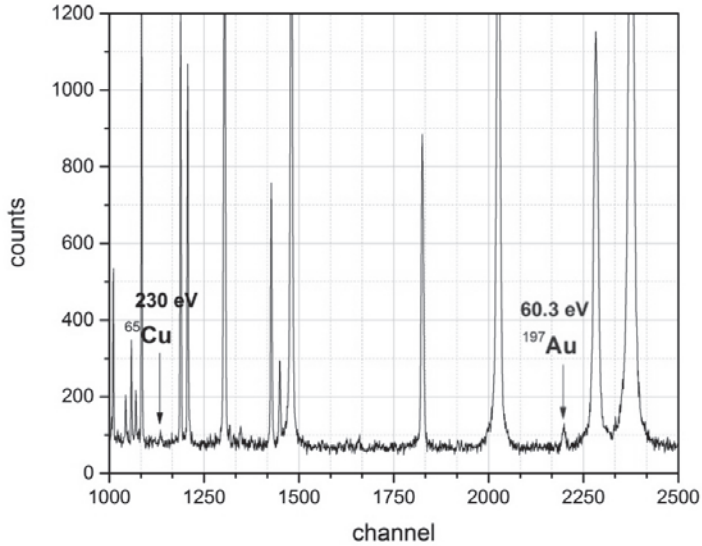


Fig. 2. The time-of-flight spectrum of reactions  $(n,\gamma)$  on the medallion material. The unmarked resonances are resonances of silver. The width of the time channel is  $0.25 \mu\text{s}$ .

### 3. DATA ANALYSIS AND RESULTS

Five resonances of silver, one resonance of copper and one resonance of gold were selected during the analysis of the experimental data. The sum of the detector counts in resonance is expressed by the formula:

$$\sum N = f(E_0) \cdot S \cdot t \cdot \varepsilon_\gamma \cdot \frac{\Gamma_\gamma}{\Gamma} A. \quad (2)$$

Here  $f(E_0)$  is the neutron flux density at the resonance energy  $E_0$ ,  $S$  – the sample area,  $t$  – measuring time,  $\varepsilon_\gamma$  – the detection efficiency of the detector radiative capture,  $\Gamma_\gamma$ ,  $\Gamma$  – the radiative and total resonance widths.

$$A = \int_{-\infty}^{+\infty} [1 - T(E)] dE \quad (3)$$

is resonance area on the transmission curve, where

$$T(E) = e^{-n\sigma(E)} \quad (4)$$

is the energy dependence of the neutron transmission by the sample;  $\sigma(E)$  – the total cross section at the energy  $E$  with Doppler broadening,  $n$  – the number of isotope nuclei per unit area. The value  $A$  was determined from experimental data for investigated sample by the formula:

$$A_x = \frac{\sum N_x \cdot M_s \cdot S_s}{\sum N_s \cdot M_x \cdot S_x} \cdot A_s. \quad (5)$$

Here  $\sum N_x$ ,  $\sum N_s$  are counts under the resonance peak of the investigated and standard samples,  $S_x$ ,  $S_s$  – the areas of the investigated and standard samples,  $M_x$ ,  $M_s$  – the numbers of monitor counts during the measurement of the investigated and standard samples.

The value  $A_s$  was calculated by means of well-known parameters of resonances for the standard sample, the value  $n_x$  was determined from the value of  $A_x$  for the investigated sample. The  $\sigma(E)$  and  $A$  values were numerically determined by using the algorithm which was described in [7]. The analysis results are presented in the Table 1.

Table 1. The results of measurements with the medallion by NRCA (the bulk)

№	Element	Mass, g	Weight, %
1	Ag	23.32±0.36	75.5±1.2
2	Cu	1.78±0.83	5.8±2.7
3	Au	0.12±0.02	0.390±0.065

Additional measurements were carried out by X-ray fluorescence (XRF) by Neutron-activation-analysis group in FLNP (Table 2).

Table 2. The results of measurements with the medallion by XRF (the surface)

№	Element	Weight, %
1	Ag	89.78±0.65
2	Cu	1.872±0.077
3	Au	0.653±0.039
4	Pb	2.30±0.14
5	Sn	1.36±0.41

#### 4. CONCLUSION

Analogues of the medallion are in the expositions of the Moscow Kremlin which consist mostly of silver or gold. But knowledge of archaeologists about chemical composition of these metals, especially of their microimpurities, is very scanty. Our study of the elemental composition could clarify this issue.

The application of the XRF analysis allowed us to determining the elemental composition on the medallion surface. To determine the real component of impurities in the metal of archaeological object, an investigation of elemental composition is needed to be carried out in the “bulk-form” without destruction. Thanks to analytical tool of NRCA there was found out that the medallion mostly consists of silver and we know that content of silver in the bulk is less than on the surface. This data is very important fact to further understanding the process of “aging” of silver that we can remark for the archaeological metal. In fact, using this analytical tool of NRCA we can certify the process of silver transition to the surface of objects (segregation).

**Acknowledgements.** The authors express their gratitude to the staff of the IREN facility and to A.P. Sumbaev, the head of the development of the facility, to V.V. Kobets, the head of sector No.5 of the Scientific and Experimental Injection and Ring Division of the Nuclotron (Veksler and Baldin Laboratory of high energy physics), for the supporting with uninterrupted operation of the facility in the process of measurements.

## REFERENCES

1. H. Postma, M. Blaauw, P. Schillebeeckx, G. Lobo, R.B. Halbertsma, and A.J. Nijboer, *Non-destructive elemental analysis of copper-alloy artefacts with epithermal neutron-resonance capture*, Czech Republic: N. p., 2003. Web.doi:10.1007/s10582-003-0030-y.
2. N.V. Bazhazhina, Yu.D. Mareev, L.B. Pikelner, P.V. Sedyshev, V.N. Shvetsov, *Analysis of element and isotope composition of samples by neutron spectroscopy at the IREN facility*, Physics of Particles and Nuclei Letters, **12** (2015) 578–583.
3. O.V. Belikov, A.V. Belozerov, Yu. Becher, Yu. Bulycheva, A.A. Fateev, A.A. Galt, A.S. Kayukov, A.R. Krylov, V.V. Kobetz, P.V. Logachev, A.S. Medvedko, I.N. Meshkov, V.F. Minashkin, V.M. Pavlov, V.A. Petrov, V.G. Pyataev, A.D. Rogov, P.V. Sedyshev, V.G. Shabratov, V.A. Shvec, V.N. Shvetsov, A.V. Skrypnik, A.P. Sumbaev, A.V. Ufimtsev, V.N. Zamrij, *Physical start-up of the first stage of IREN facility*, Journal of Physics: Conf. Ser. 205 (2010) 012053.
4. H. Maletsky, L.B. Pikelner, K.G. Rodionov, I.M. Salamatin, E.I. Sharapov, *Detector of neutrons and gamma rays for work in the field of neutron spectroscopy*, Communication of JINR 13-6609, Dubna, JINR, (1972) 1–15 (in Russian).
5. S.F. Mughabghab. *Neutron Gross Sections, Neutron Resonance Parameters and Thermal Gross Sections*. Academic Press, New York, 1984.
6. S.I. Sukhoruchkin, Z.N. Soroko, V.V. Deriglazov, *Low Energy Neutron Physics*. Landolt-Bornstein V. I., 16 B, Berlin: Springer Verlag, 1998.
7. V.N. Efimov, I.I. Shelontsev, *Calculation for graphs of determining the parameters of neutron resonances by the transmission method*. Communications of the JINR P-641, Dubna, (1961) 1–19 (in Russian).

# TRACE ELEMENT CONCENTRATIONS IN THE PROSTATIC SECRETION OF PATIENTS WITH CHRONIC PROSTATITIS AND BENIGN PROSTATIC HYPERPLASIA INVESTIGATED BY X-RAY FLUORESCENCE

V. Zaichick<sup>1</sup>, S. Zaichick<sup>1,2</sup>

<sup>1</sup> *Medical Radiological Research Centre, Korolyev St., 4, Obninsk, 249036, Russia, e-mail: [vzaichick@gmail.com](mailto:vzaichick@gmail.com)*

<sup>2</sup> *Feinberg School of Medicine, Northwestern University, Chicago, IL 60611-4296, USA*

## Introduction

Prostatitis is the most common urologic disease in adult males younger than 50 years and the third most common urologic diagnosis in males older than 50 years.<sup>[1]</sup> Chronic prostatitis (CP) is functional, somatoform disorder with a high worldwide prevalence estimated in systematic reviews or population studies at 10-32%.<sup>[2,3]</sup> However, CP is a more common condition, with 35–50% of men reported to be affected by symptoms suggesting prostatitis during their lifetime.<sup>[4]</sup>

Benign prostatic hyperplasia (BPH) is an internationally important health problem of the man, particularly in developed countries, and represents the most common urologic disease among of men after the age of fifty.<sup>[5-8]</sup> Incidence of histological BPH could be over 70% at 60 years old and over 90% at 70 years old.<sup>[5,6]</sup> To date, we still have no precise knowledge of the biochemical, cellular and molecular processes underlying the pathogenesis of BPH. Although the influence of androgens and estrogens has been demonstrated, hormonal factors alone may not fully explain BPH development.<sup>[7,8]</sup>

Thus, the both BPH and CP is the very common urologic disease in adult males. Moreover, use systematic review methods provide the statistical evidence that the association between BPH and CP is significant. Prostatitis, as well as BPH, can be a cause of an elevated prostate specific antigen (PSA) level in blood. This warrants the need of reliable diagnostic tool which has ability not only to diagnose CP reliably but also to differentiate it from the BPH.

It was reported that the risk of having BPH and CP depends on lifestyle and diet, including the intake of Zn and some other trace elements (TE). TE have essential physiological functions such as maintenance and regulation of cell function, gene regulation, activation or inhibition of enzymatic reactions, and regulation of membrane function. They can play the significant role in the oxidative stress. Essential or toxic (mutagenic, carcinogenic) properties of TE depend on tissue-specific need or tolerance, respectively.<sup>[9]</sup> Excessive accumulation or an imbalance of the TE may disturb the cell functions and may result in cellular degeneration or death.<sup>[9]</sup>

In our previous studies a significant involvement of Zn and some TE in the function of prostate was observed.<sup>[10-24]</sup> Moreover, it was found that intracellular Zn and Ca excess is one of the main factors in the etiology of BPH. One of the main functions of prostate gland is a production of prostatic fluid<sup>[25]</sup> with extremely high concentration of Zn and some other

chemical elements. The first finding of remarkable high level of Zn concentration in human expressed prostatic fluid (EPF) was reported in the beginning of 1960s.<sup>[26]</sup> Analyzing EPF expressed from prostate of 8 apparently healthy men aged 25-55 years it was found that Zn concentration varied in range from 300 to 730 mg/L. After this finding several investigators have suggested that the measurement of Zn level in EPF may be useful as a marker of prostate secretory function.<sup>[27,28]</sup> It promoted a more detailed study of Zn concentration in EPF of healthy subjects and in those with different prostate diseases, including BPH and CP.<sup>[28,29]</sup> A detailed review of these studies, reflecting the contradictions within accumulated data, was given in our earlier publication.<sup>[29]</sup>

In present study it was supposed by us that apart from Zn the levels of some other TE in EPF have to reflect a difference between functional changes of chronic inflamed prostate and hyperplastic prostate. Thus, this work had four aims. The first one was to present the design of the method and apparatus for micro analysis of Br, Fe, Rb, Sr, and Zn in the EPF samples using energy dispersive X-ray fluorescence (EDXRF) with radionuclide source <sup>109</sup>Cd. The second aim was to assess the Br, Fe, Rb, Sr, and Zn concentration in the EPF samples received from patients with CP and BPH. The third aim was to evaluate the quality of obtained results and to compare obtained results with published data. The last aim was to compare the concentration of Br, Fe, Rb, Sr, and Zn in EPF samples of chronic inflamed and hyperplastic prostate.

All studies were approved by the Ethical Committee of the Medical Radiological Research Center, Obninsk.

## Experimental

Specimens of EPF were obtained from 33 patients with CP (mean age 50±9 years, range 37-65 years) and from 52 patients with BPH (mean age 63±6 years, range 52-75 years) by qualified urologists in the Urological Department of the Medical Radiological Research Centre using standard rectal massage procedure. In all cases the diagnosis has been confirmed by clinical examination and in cases of PCa additionally by morphological results obtained during studies of biopsy and resected materials. Subjects were asked to abstain from sexual intercourse for 3 days preceding the procedure. Specimens of EPF were obtained in sterile containers which were appropriately labeled. Twice twenty µL (microliters) of fluid were taken by micropipette from every specimen for trace element analysis, while the rest of the fluid was used for cytological and bacteriological investigations. The chosen 20 µL of the EPF was dropped on 11.3 mm diameter disk made of thin, ash-free filter papers fixed on the Scotch tape pieces and dried in an exsiccator at room temperature. Then the dried sample was covered with 4 µm Dacron film and centrally pulled onto a Plexiglas cylindrical frame.

To determine concentration of the elements by comparison with a known standard, aliquots of solutions of commercial, chemically pure compounds were used for a device calibration.<sup>[30]</sup> The standard samples for calibration were prepared in the same way as the samples of prostate fluid. Because there were no available liquid Certified Reference Material (CRM) ten sub-samples of the powdery CRM IAEA H-4 (animal muscle) were analyzed to estimate the precision and accuracy of results. Every CRM sub-sample weighing about 3 mg was applied to the piece of Scotch tape serving as an adhesive fixing backing. An acrylic stencil made in the form of a thin-walled cylinder with 11.3 mm inner diameter was used to apply the sub-sample to the Scotch tape. The polished-end acrylic pestle which is a constituent of the stencil set was used for uniform distribution of the sub-sample within the

Scorch surface restricted by stencil inner diameter. When the sub-sample was slightly pressed to the Scotch adhesive sample, the stencil was removed. Then the sub-sample was covered with 4  $\mu\text{m}$  Dacron film. Before the sample was applied, pieces of Scotch tape and Dacron film were weighed using analytical balance. Those were again weighed together with the sample inside to determine the sub-sample mass precisely.

The facility for radionuclide-induced energy dispersive X-ray fluorescence included an annular  $^{109}\text{Cd}$  source with an activity of 2.56 GBq, Si(Li) detector with electric cooler and portable multi-channel analyzer combined with a PC. Its resolution was 270 eV at the 6.4 keV line. The facility functioned as follows. Photons with the 22.1 keV energy from  $^{109}\text{Cd}$  source are sent to the surface of a specimen analyzed, where they excite the characteristic fluorescence radiation, inducing the  $K_{\alpha}$  X-rays of trace elements. The fluorescence radiation got to the detector through a 10 mm diameter collimator to be recorded.

The duration of the Zn concentration measurement was 10 min. The duration of the Zn concentration measurement together with Br, Fe, Rb, and Sr was 60 min. The intensity of  $K_{\alpha}$ -line of Br, Fe, Rb, Sr, and Zn for EPF samples and standards was estimated on calculation basis of the total area of the corresponding photopeak in the spectra.

All EPF samples for EDXRF were prepared in duplicate and mean values of TE contents were used in final calculation. Using the Microsoft Office Excel programs, the summary of statistics, arithmetic mean, standard deviation, standard error of mean, minimum and maximum values, median, percentiles with 0.025 and 0.975 levels was calculated for TE concentrations in EPF of chronic inflamed and hyperplastic prostate. The difference in the results between two groups of samples (CP and BPH) was evaluated by the parametric Student's *t*-test and non-parametric Wilcoxon-Mann-Whitney *U*-test

## Results and discussion

Table 1 depicts our data for Br, Fe, Rb, Sr, and Zn mass fractions in ten sub-samples of CRM IAEA H-4 (animal muscle) and the certified values of this reference material. Of 4 (Br, Fe, Rb, and Zn) TE with certified values for the CRM IAEA H-4 (animal muscle) we determined contents of all certified elements (Table 1). Mean values ( $M \pm SD$ ) for Br, Fe, Rb, and Zn were in the range of 95% confidence interval. Good agreement of the TE contents analyzed by  $^{109}\text{Cd}$  radionuclide-induced EDXRF with the certified data of CRM IAEA H-4 (Table 1) indicate an acceptable accuracy of the results obtained in the study of the prostatic fluid presented in Tables 2-4.

**Table 1.** EDXRF data of Br, Fe, Rb, Sr, and Zn contents in the IAEA H-4 (animal muscle) reference material compared to certified values (mg/kg, dry mass basis)

Element	Certified values			This work results
	Mean	95% confidence interval	Type	Mean $\pm$ SD
Fe	49	47 - 51	C	48 $\pm$ 9
Zn	86	83 - 90	C	90 $\pm$ 5
Br	4.1	3.5 - 4.7	C	5.0 $\pm$ 1.2
Rb	18	17 - 20	C	22 $\pm$ 4
Sr	0.1	-	N	<1

Mean – arithmetical mean, SD – standard deviation, C- certified values, N – non-certified values

Table 2 presents certain statistical parameters (arithmetic mean, standard deviation, standard error of mean, minimal and maximal values, median, percentiles with 0.025 and 0.975 levels) of the Br, Fe, Rb, Sr, and Zn concentrations in EPF of patients with CP and BPH. The mean values and all selected statistical parameters were calculated for 5 (Br, Fe, Rb, Sr, and Zn) TE concentrations (Table 2). The concentrations of Br, Fe, Rb, and Zn were measured in all, or a major portion of EPF samples of inflamed and hyperplastic prostate. The Sr concentration was measured in major portion of EPF samples of hyperplastic prostate and in a few samples of prostate with CP.

**Table 2.** Some basic statistical parameters of Br, Fe, Rb, Sr, and Zn concentration (mg/L) in prostate fluid of patients with prostatitis and BPH

Condition	Element	M	SD	SEM	Min	Max	Med	Per. 0.025	Per. 0.975
Prostatitis 37-65 years n=33	Br	3.35	2.64	0.69	0.120	9.85	2.98	0.201	8.73
	Fe	10.9	9.6	2.3	3.85	41.9	6.97	4.06	35.6
	Rb	2.32	1.13	0.30	0.730	4.54	1.75	0.935	4.34
	Sr	≤1.57	-	-	0.210	2.93	-	-	-
	Zn	382	275	48	62.0	1051	295	75.0	950
BPH 52-75 years n=52	Br	2.32	1.84	0.30	0.230	8.70	1.62	0.268	5.84
	Fe	11.5	10.8	1.8	1.06	54.1	9.31	1.09	38.9
	Rb	1.70	1.41	0.23	0.210	5.04	1.46	0.254	5.04
	Sr	1.41	1.09	0.26	0.230	4.79	1.12	0.300	4.02
	Zn	488	302	42	45.0	977	427	81.4	962

M - arithmetic mean, SD - standard deviation, SEM - standard error of mean, Min - inimum value, Max - maximum value, Med - Median, Per. 0.025 - percentile with 0.025 level, Per. 0.975 - percentile with 0.975 level, DL - detection limit.

The comparison of our results with published data for Br, Fe, Rb, Sr, and Zn concentrations in EPF of inflamed and hyperplastic prostate <sup>[31-34]</sup> is shown in Table 3. A number of values for Zn concentrations in EPF were not expressed on a wet mass basis in the cited literature. Therefore, we calculated these values using the published data for water - 93.2%. <sup>[35]</sup>

The mean of Zn concentration obtained for CP group of prostate fluid, as shown in Table 3, agrees well with median of means cited by other researches. The mean of Rb concentration obtained for EPF samples of CP group agrees well with our data reported 38 years ago. <sup>[31]</sup> No published data referring to Br, Fe, Rb, and Sr concentrations in EPF samples of patients with CP were found.

In the EPF samples of hyperplastic prostate our results were comparable with published data for Zn concentrations (Table 3). The mean of Rb concentration obtained for EPF samples of BPH group was some lower than our data reported 38 years ago. <sup>[31]</sup> No published data referring to Br, Fe, and Sr concentrations in EPF samples obtained from patients with PCA were found.

From Table 4, it is observed that there are no any differences between the Br, Fe, Rb, Sr, and Zn concentrations in EPF samples of BPH and CP group.

**Table 3.** Median, minimum and maximum value of means of Br, Fe, Rb, Sr, and Zn concentration (mg/L) in prostate fluid of patients with prostatitis and BPH according to data from the literature

Condition	El	Published data [Reference]			This work results M±SD
		Median of means (n)*	Minimum of means M or M±SD, (n)**	Maximum of means M±SD, (n)**	
Prostatitis	Br	-	-	-	3.35±2.64
	Fe	-	-	-	10.9±9.6
	Rb	2.26 (1)	2.26±1.28 (18) [31]	2.26±1.28 (18) [31]	2.32±1.13
	Sr	-	-	-	≤1.57
	Zn	222 (7)	88.9 (29) [32]	564±239 (10) [33]	382±275
BPH	Br	-	-	-	2.32±1.84
	Fe	-	-	-	11.5±10.8
	Rb	2.35 (1)	2.35±1.85 (11) [31]	2.35±1.85 (11) [31]	1.70±1.41
	Sr	-	-	-	1.41±1.09
	Zn	459 (7)	268 (7) [34]	9870±10130 (11) [33]	488±302

El – element, M – arithmetic mean, SD – standard deviation, (n)\* – number of all references, (n)\*\* – number of samples.

**Table 4.** Comparison of mean values (M±SEM) of Br, Fe, Rb, Sr, and Zn concentration (mg/L) in prostate fluid of patients with prostatitis and BPH

Element	Age groups				Ratios BPH to Prostatitis
	Prostatitis	BPH	Student's t-test <i>p</i> ≤	<i>U</i> -test* <i>p</i>	
Br	3.35±0.69	2.32±0.30	0.183	>0.05	0.69
Fe	10.9±2.3	11.5±1.8	0.836	>0.05	1.06
Rb	2.32±0.30	1.70±0.23	0.113	>0.05	0.73
Sr	≤1.57	1.41±0.26	0.856	>0.05	-
Zn	382±48	488±42	0.103	>0.05	1.28

M – arithmetic mean, SEM – standard error of mean, \*Wilcoxon-Mann-Whitney *U*-test

### Conclusions

In this work, TE measurements were carried out in the EPF samples of inflamed and hyperplastic prostate using non-destructive instrumental EDXRF micro method developed by us. It was shown that this method is an adequate analytical tool for the non-destructive determination of Br, Fe, Rb, Sr, and Zn concentration in the EPF samples of human prostate. No differences between TE concentrations in EPF samples of BPH and CP group were found.

### Acknowledgements

The authors are extremely grateful to Dr Tatyana Sviridova, Medical Radiological Research Center, Obninsk for supplying EPF samples.

## References

1. Paulis G. "Inflammatory mechanisms and oxidative stress in prostatitis: the possible role of antioxidant therapy". *Research and Reports in Urology* **10** (2018): 75–87.
2. ProPERT KJ., *et al.* "Chronic prostatitis collaborative research network (CPCRN). Responsiveness of the National Institutes of Health Chronic Prostatitis Symptom Index (NIH-CPSI)". *Quality of Life Research* **15** (2006): 299–305.
3. Ihsan AU., *et al.* "Role of oxidative stress in pathology of chronic prostatitis/chronic pelvic pain syndrome and male infertility and antioxidants function in ameliorating oxidative stress". *Biomedicine and Pharmacotherapy* **106** (2018): 714–723.
4. Krieger JN., *et al.* "Epidemiology of prostatitis". *International Journal of Antimicrobial Agents* **31**(Suppl. 1) (2008): S85–S90.
5. Burnett A and Wein AJ. "Benign prostatic hyperplasia in primary care: what you need to know". *Journal of Urology* **175** (2006): S19–S24.
6. Gong EM and Gerber GS. "Saw palmetto and benign prostatic hyperplasia". *American Journal of Chinese Medicine* **32** (2004): 331–338.
7. Lee K and Peehl DM. "Molecular and cellular pathogenesis of benign prostatic hyperplasia". *Journal of Urology* **172** (2004): 1784–1791.
8. Li W., *et al.* "Stromally expressed c-jun regulates proliferation of prostate epithelial cells". *American Journal of Pathology* **171** (2007): 1189–1198.
9. Zaichick V. "Medical elementology as a new scientific discipline". *Journal of Radioanalytical and Nuclear Chemistry* **269** (2006): 303–309.
10. Zaichick V. "INAA and EDXRF applications in the age dynamics assessment of Zn content and distribution in the normal human prostate". *Journal of Radioanalytical and Nuclear Chemistry* **262** (2004): 229–234.
11. Zaichick S and Zaichick V. "INAA application in the age dynamics assessment of Br, Ca, Cl, K, Mg, Mn, and Na content in the normal human prostate". *Journal of Radioanalytical and Nuclear Chemistry* **288.1** (2011): 197–202.
12. Zaichick V., *et al.* "The effect of age on 12 chemical element contents in intact prostate of adult men investigated by inductively coupled plasma atomic emission spectrometry". *Biological Trace Element Research* **147.1-3** (2012): 49–58.
13. Zaichick V and Zaichick S. "Age-related histological and zinc content changes in adult nonhyperplastic prostate glands". *Age* **36.1** (2014): 167–181.
14. Zaichick S and Zaichick V. "The effect of age on Ag, Co, Cr, Fe, Hg, Sb, Sc, Se, and Zn contents in intact human prostate investigated by neutron activation analysis". *Applied Radiation and Isotopes* **69.6** (2011): 827–833.
15. Zaichick V and Zaichick S. "The effect of age on Br, Ca, Cl, K, Mg, Mn, and Na mass fraction in pediatric and young adult prostate glands investigated by neutron activation analysis". *Applied Radiation and Isotopes* **82** (2013): 145–151.
16. Zaichick V and Zaichick S. "INAA application in the assessment of Ag, Co, Cr, Fe, Hg, Rb, Sb, Sc, Se, and Zn mass fraction in pediatric and young adult prostate glands". *Journal of Radioanalytical and Nuclear Chemistry* **298.3** (2013): 1559–1566.
17. Zaichick V and Zaichick S. "NAA-SLR and ICP-AES Application in the assessment of mass fraction of 19 chemical elements in pediatric and young adult prostate glands". *Biological Trace Element Research* **156.1** (2013): 357–366.

18. Zaichick V and Zaichick S. "Use of neutron activation analysis and inductively coupled plasma mass spectrometry for the determination of trace elements in pediatric and young adult prostate". *American Journal of Analytical Chemistry* **4** (2013): 696–706.
19. Zaichick V and Zaichick S. "INAA application in the assessment of chemical element mass fractions in adult and geriatric prostate glands". *Applied Radiation and Isotopes* **90** (2014): 62–73.
20. Zaichick V and Zaichick S. "Determination of trace elements in adults and geriatric prostate combining neutron activation with inductively coupled plasma atomic emission spectrometry". *Open Journal of Biochemistry* **1.2** (2014): 16–33.
21. Zaichick V and Zaichick S. "Use of INAA and ICP-MS for the assessment of trace element mass fractions in adult and geriatric prostate". *Journal of Radioanalytical and Nuclear Chemistry* **301.2** (2014): 383–397.
22. Zaichick V. "The variation with age of 67 macro- and microelement contents in nonhyperplastic prostate glands of adult and elderly males investigated by nuclear analytical and related methods". *Biological Trace Element Research* **168.1** (2015): 44–60.
23. Zaichick V and Zaichick S. "Androgen-dependent chemical elements of prostate gland". *Andrology and Gynecology: Current Research* **2** (2014): 2.
24. Zaichick V and Zaichick S. "Differences and relationships between morphometric parameters and zinc content in nonhyperplastic and hyperplastic prostate glands". *British Journal of Medicine and Medical Research* **8.8** (2015): 692–706.
25. Zaichick V. "The prostatic urethra as a Venturi effect urine-jet pump to drain prostatic fluid". *Medical Hypotheses* **83** (2014): 65–68.
26. Mackenzie AR., *et al.* "Zinc content of expressed human prostate fluid". *Nature (London)* **193.4810** (1962): 72–73.
27. Marmar JL., *et al.* "Values for zinc in whole semen, fraction of split ejaculate and expressed prostatic fluid". *Urology* **16.5** (1980): 478–480.
28. Zaichick V., *et al.* "Method for diagnostics of prostate diseases". Certificate of invention No 997281 (30.03.1981), Russia.
29. Zaichick V., *et al.* "Zinc concentration in human prostatic fluid: normal, chronic prostatitis, adenoma, and cancer". *International Urology and Nephrology* **28.5** (1996): 687–694.
30. Zaichick V. "Applications of synthetic reference materials in the medical Radiological Research Centre". *Fresenius' Journal of Analytical Chemistry* **352** (1995): 219–223.
31. Zaichick V., *et al.* "Method for diagnostics of prostate diseases". Certificate of invention No 997281 (30.03.1981), Russia.
32. Kavanagh JP and Darby C. "The interrelationships between acid phosphatase, aminopeptidase, diamine oxidase, citric acid,  $\beta$ -glucuronidase, pH and zinc in human prostate fluid". *International Journal of Andrology* **5.5** (1982): 503–512.
33. Gómez Y., *et al.* "Zinc levels in prostatic fluid of patients with prostate pathologies". *Investigacion Clinica* **48.3** (2007): 287–294.
34. Romics I and Bach D. "Zn, Ca and Na levels in the prostatic secretion of patients with prostatic adenoma". *International Urology and Nephrology* **23.1** (1991): 45–49.
35. Huggins C., *et al.* "Chemical composition of human semen and of the secretion of the prostate and seminal vesicles". *American Journal of Physiology* **136.3** (1942): 467–473.

# NEUTRON ACTIVATION ANALYSIS OF Br, Ca, Cl, K, Mg, Mn, Na, AND Sr CONCENTRATIONS IN HUMAN SALIVA IN HEALTH AND PARODONTOPATHY

V. Zaichick<sup>1</sup>, S. Zaichick<sup>1,2</sup>

<sup>1</sup> *Medical Radiological Research Centre, Korolyev St., 4, Obninsk, 249036, Russia,  
e-mail: [vzaichick@gmail.com](mailto:vzaichick@gmail.com)*

<sup>2</sup> *Feinberg School of Medicine, Northwestern University, Chicago, IL 60611-4296, USA*

## Introduction

Periodontal diseases and dental caries are the most common diseases in the oral cavity.<sup>[1,2]</sup> Periodontal diseases are chronic inflammatory disorders encompassing destructive and nondestructive diseases of the periodontal supporting tissues of teeth. Gingivitis is a nondestructive disease ubiquitous in populations of children and adults globally. Aggressive periodontitis is characterized by severe and rapid loss of periodontal attachment often commencing at or after puberty and common among Caucasians. Chronic periodontitis is a common disease and may occur in most age groups, but is most prevalent among adults and seniors world-wide. Approximately 48% of United States adults have chronic periodontitis, and similar or higher rates have been reported in other populations. Moderate and advanced periodontitis is more prevalent among the older age groups, and rates of 70% or more have been reported in certain populations.

However, case definitions and criteria that are used to diagnose periodontal diseases are not yet consistent worldwide. Thus, there are needs to find additional parameters to characterize the periodontal diseases. Salivary main electrolytes and trace element can be involved in the etiology and pathogenesis of periodontal diseases.<sup>[3-10]</sup>

## Aim of the study

The aim of this work was to assess the Br, Ca, Cl, K, Mg, Mn, Na and Sr contents in the samples of mixed saliva using non-destructive instrumental neutron activation analysis with high resolution spectrometry of short-lived radionuclides (INAA-SLR) and to estimate the possibilities of using the data about concentration of some main electrolytes and trace elements in mixed non-stimulated saliva as biomarkers in the diagnosis of periodontal disease.

All studies were approved by the Ethical Committees of the Medical Radiological Research Centre, Obninsk. All procedures performed in studies involving human participants were in accordance with the ethical standards of the institutional and/or national research committee and with the 1964 Helsinki declaration and its later amendments or comparable ethical standards.

## Materials and Methods

Samples of the mixed non-stimulated saliva of 52 apparently healthy subjects and 60 patients with parodontopathy (gingivitis and periodontitis) were collected in the dental clinics

of Moscow and Obninsk. The samples of mixed saliva were obtained in period between 10 a.m. and 12 a.m., then cooled and lyophilized. The age of the persons examined (80 females and 32 males) was in the range from 17 to 49 years. There were no any metallic oral inclusions or prosthesis in all persons involved in the study. Dental diseases were diagnosed according to the complex data of special clinical examinations (disease anamnesis, inspection assessment of pathological dental and gingival pouch state, panoramic X-radiography).

For INAA-SLR dry saliva samples each about 50 mg were separately sealed in polyethylene ampules washed beforehand with pure alcohol. The content of Br, Ca, Cl, K, Mg, Mn, Na and Sr were determined by INAA-SLR using a horizontal channel equipped with the pneumatic rabbit system of the WWR-c research nuclear reactor (Branch of Karpov Institute, Obninsk). The neutron flux in the channel was  $1.7 \times 10^{13} \text{ n cm}^{-2} \text{ s}^{-1}$ . Ampoules with dry saliva samples, SSB, intralaboratory-made standards, and certified reference material were put into polyethylene rabbits and then irradiated separately for 30 s. Copper foils were used to assess neutron flux.

### Measurement and Statistic

The measurement of each sample was made twice, 1 and 180 min after irradiation. The duration of the first and second measurements was 10 and 20 min, respectively. A coaxial 98-cm<sup>3</sup> Ge (Li) detector and a spectrometric unit (NUC 8100), including a PC-coupled multichannel analyzer, were used for measurements. The spectrometric unit provided 2.9-keV resolution at the <sup>60</sup>Co 1,332-keV line. Details of used nuclear reactions, radionuclides, and gamma-energies were presented in our earlier publications concerning the INAA-SLR chemical element contents in human bone, thyroid, scalp hair, and prostate.

A dedicated computer program for INAA mode optimization was used. All saliva samples were prepared in duplicate, and mean values of chemical element contents were used in final calculation. Using Microsoft Office Excel, a summary of the statistics, including, arithmetic mean, standard deviation, standard error of mean, minimum and maximum values, median, percentiles with 0.025 and 0.975 levels was calculated for chemical element contents. The difference in the results between two sample groups (Normal and Parodontopathy) was evaluated by the parametric Student's *t*-test and non-parametric Wilcoxon-Mann-Whitney *U*-test.

### Results and Discussion

The concentration of almost all elements studied in mixed saliva of patients with parodontopathy is higher than the normal level in 1.9-6.3 times (Table 1). The exception is only for Sr which mean concentrations in the Normal and Parodontopathy groups are similar. The level of changes correlates with the severeness of parodontopathy. The data about changes of main electrolytes and trace element contents in saliva can be useful for more detail understanding of parodontopathy etiology and pathogenesis, for more accurate diagnostics and individual prognosis of these diseases, as well as for developing on new methods for their treatment.

### Conclusions

In this work, the Br, Ca, Cl, K, Mg, Mn, Na and Sr measurements were carried out in the mixed non-stimulated saliva of 52 apparently healthy subjects and 60 patients with

parodontopathy (gingivitis and periodontitis) using non-destructive instrumental INAA-SLR method developed by us. It was shown that this method is an adequate analytical tool for the non-destructive determination of Br, Ca, Cl, K, Mg, Mn, Na and Sr concentration in the samples of human non-stimulated saliva. The great differences between chemical element concentrations in non-stimulated saliva of Normal and Parodontopathy groups were found.

Table 1. Concentrations of main electrolytes and some trace elements ( $M \pm SEM$ , mg/L) in mixed non-stimulated saliva of health persons and patients with parodontopathy

Element	Norm	Parodontopathy	Student's <i>t</i> -test <i>p</i> <	U-test <i>p</i>	$M_2 / M_1$
	$M_1$ (n=52)	$M_2$ (n=60)			
Br	1.50±0.09	2.87±0.24	0.001	≤0.01	1.91
Ca	37±7	109±9	0.001	≤0.01	2.95
Cl	288±18	684±31	0.001	≤0.01	2.38
K	416±30	817±41	0.001	≤0.01	1.96
Mg	7.9±1.1	30.2±3.7	0.001	≤0.01	3.81
Mn	0.0095±0.0010	0.0593±0.0068	0.001	≤0.01	6.27
Na	51±4	176±14	0.001	≤0.01	3.42
Sr	0.180±0.035	0.172±0.018	>0.05	>0.05	0.96

### Acknowledgements

The authors are extremely grateful to Dr Shamil Bagirov for his help in supplying saliva samples.

### References

1. Costa F.O., Susin C., Cortelli J.R., Pordeus I.A., Epidemiology of Periodontal Disease. Int. J. Dent. 2012; 2012: 848641.
2. Natto Z.S., Abu Ahmad R.H., Alsharif L.T., Alrowithi H.F., Alsini D.A., Salih H.A., Bissada N.F., Chronic Periodontitis Case Definitions and Confounders in Periodontal Research: A Systematic Assessment. Biomed. Res. Int. 2018 Nov. 28; 2018: 4578782. doi: 10.1155/2018/4578782. eCollection 2018.
3. Bagirov Sh.T., Zaichick V.Ye., Kalashnikov V.M., Physiological changeability of the element concentrations in mixed non-stimulated human saliva. I. Na, Cl, Ca. Azerbaijan Med. Zhurnal 1985; 8: 29–35.
4. Bagirov Sh.T., Zaichick V.Ye., Trace elements of mixed human saliva for parodontosis pathology in accordance with the data of X-ray fluorescent analysis. In: Application of Mathematical and Engineering Methods for Radiological Study, Obninsk, 1985, pp.75–78.
5. Bagirov Sh.T., Zaichick V.Ye., Kalashnikov V.M., Physiological changeability of the element concentrations in mixed non-stimulated human saliva. II. K, Mg, Mn, W. Azerbaijan Med. Zhurnal 1986; 2: 14–20.

6. Bagirov Sh.T., Zaichick V.Ye., Physiological changeability of the element concentrations in mixed non-stimulated saliva. III. Fe, Cu, Zn, Br, Rb, Sr, I, Ba. Azerbaijan Med. Zhurnal 1987; **10**: 29–35.
7. Zaichick V.Ye., Bagirov Sh.T., The chemical composition of human saliva as an indicator of environmental quality. In: Nuclear Analytical Methods for Environmental Monitoring. Gidrometeoisdat, Leningrad, 1987, pp.61–67.
8. Zaichik V.E., Bagirov Sh.T., The chemical element content of mixed unstimulated saliva from a healthy subject. Stomatologiya (Moscow). 1991; **70**(1): 14–17.
9. Zaichik V.E., Bagirov Sh.T., The chemical element content of mixed unstimulated saliva in periodontal diseases. Stomatologiya (Moscow). 1994; **73**(1): 8–11.
10. Zaichick V., Tsyb A., Bagirov Sh., Neutron activation analysis of saliva: Application in clinical chemistry, environmental and occupational toxicology. J. Radioanal. Nucl. Chem. 1995; **195**(1): 123–132.

# RELATIONSHIP BETWEEN Ca, Cl, K, Mg, Mn, Na, P, AND Sr CONTENTS IN THE INTACT CROWNS OF FEMALE TEETH INVESTIGATED BY NEUTRON ACTIVATION ANALYSIS

V. Zaichick<sup>1</sup>, S. Zaichick<sup>1,2</sup>

<sup>1</sup> *Medical Radiological Research Centre, Korolyev St., 4, Obninsk, 249036, Russia, e-mail: [vzaidchick@gmail.com](mailto:vzaidchick@gmail.com)*

<sup>2</sup> *Feinberg School of Medicine, Northwestern University, Chicago, IL 60611-4296, USA*

## Introduction

To use chemical element composition as estimation of bone and teeth health in stomatological, geographical, environmental and occupational medicine, paleoanthropology, and other directions, it is necessary to know normal levels and age- and gender-related changes of chemical element contents and their ratios.<sup>[1-22]</sup>

In our previous studies it was shown that samples are contaminated by trace elements from stainless steel tools during the sample preparation.<sup>[23]</sup> There is evidence that some chemical elements are lost if tooth samples are treated with solvents in order to remove the organic matrix, and are then ashed and acid digested.<sup>[24, 25]</sup>

This work had three aims. The first was to determine the Ca, Cl, K, Mg, Mn, Na, P, and Sr mass fractions in the intact crowns of female teeth by instrumental neutron activation analysis with high resolution spectrometry of short-lived radionuclides (INAA-SLR) and to calculate some statistical parameters of Cl/Ca, K/Ca, Mg/Ca, Mn/Ca, Na/Ca, P/Ca, Sr/Ca, Ca/P, Cl/P, K/P, Mg/P, Mn/P, Na/P, Sr/P, Ca/Mg, Cl/Mg, Mn/Mg, Na/Mg, P/Mg, Sr/Mg, Ca/Cl, K/Cl, Mg/Cl, Mn/Cl, Na/Cl, P/Cl, Sr/Cl, Ca/K, Cl/K, Mg/K, Mn/K, Na/K, P/K, Sr/K, Ca/Na, Cl/Na, K/Na, Mg/Na, Mn/Na, P/Na, and Sr/Na mass fraction ratios. The second aim was to evaluate the effect of age on mean values of ratios of chemical element mass fractions. The third aim was to estimate the inter-correlations between Ca, Cl, K, Mg, Mn, Na, P, and Sr mass fractions in the intact crowns of female teeth.

All studies were approved by the Ethical Committee of the Medical Radiological Research Center, Obninsk.

## Experimental

Tooth root samples were obtained at postmortems from intact cadavers (38 female, 16–55 years old) within 24 h of death. Samples were freeze dried until constant mass was obtained. All subjects died mainly due to trauma. A titanium tool was used to cut and to scrub samples as well as to cut teeth crowns. The samples weighing about 100 mg for INAA-SLR were sealed separately in thin polyethylene film washed beforehand with acetone and rectified alcohol. The sealed samples were placed in labeled polyethylene ampoules.

To determine contents of the elements by comparison with a known standard, biological synthetic standards (BSS) prepared from phenol–formaldehyde resins and chemically pure compounds were used.<sup>[26]</sup> Ten certified reference materials (CRM) IAEA H-5 (Animal Bone) and standard reference materials (SRM) NIST 1486 (Bone Meal) sub-samples weighing about

50–100 mg were analyzed in the same conditions as teeth samples to estimate the precision and accuracy of results.

The mass fractions of Ca, Cl, K, Mg, Mn, Na, P, and Sr were determined by INAA-SLR using a horizontal channel equipped with the pneumatic rabbit system of the WWR-c research nuclear reactor. The information of used nuclear reactions, radionuclides, gamma-energies, neutron flux, spectrometer and other details of the analysis including the quality control of results were reported by us before.<sup>[6, 26]</sup>

A dedicated computer program of NAA mode optimization was used.<sup>[27]</sup> Using the Microsoft Office Excel software, the summary of statistics were calculated for different ratios of chemical element mass fractions. The reliability of difference in the results between two age groups of females was evaluated by Student's *t*-test. The Pearson's correlation analysis was used to identify relationships between elements.

## Results and discussion

Table 1 represents certain statistical parameters (arithmetic mean, standard deviation, standard error of mean, minimal and maximal values, median, percentiles with 0.025 and 0.975 levels) of 42 different ratios of Ca, Cl, K, Mg, Mn, Na, P, and Sr mass fractions in the intact crowns of female teeth.

The obtained values for Ca/P ratio, as shown in Table 1, agree well with median of means cited by other researchers for the teeth enamel.<sup>[28,29]</sup> No published data referring to ratios of Ca/P or other chemical element mass fractions in the intact crowns of female teeth was found.

To estimate the effect of age on the chemical element ratios in the intact crowns of female teeth we examined two age groups: one comprised a younger group with ages from 15 to 35 years and the other comprised older people with ages ranging from 36 to 55 years (Table 2). In the intact crowns of female teeth it was found a statistically significant age-related decrease of the Sr/Ca, Sr/P, Sr/Mg, Sr/Na, and Cl/Na ratios accompanied an increase of the K/Cl, Na/Cl, and P/Cl ratios.

No published data referring to age-related differences of ratios of chemical element mass fractions in the intact crowns of female teeth were found.

Table 3 depicts the inter-correlation calculations including all chemical elements identified by us. For example, the positive inter-correlations of P mass fractions with Ca ( $p < 0.001$ ) and Cl ( $p < 0.01$ ), as well as Mn mass fractions with K ( $p < 0.05$ ) and Sr ( $p < 0.01$ ) mass fractions were found in female teeth crowns. If some correlations between the elements were predictable (e.g., Ca–P), the interpretation of other observed relationships requires further study for a more complete understanding.

## Conclusions

INAA-SLR is a satisfactory analytical tool for the non-destructive precise determination of mass fraction of 8 chemical elements (Ca, Cl, K, Mg, Mn, Na, P, and Sr) in the crown samples of permanent teeth. It was found the statistically significant changes of some chemical element mass fraction ratios in the intact crowns of female teeth with age. All the deceased were citizens of Obninsk, a small city of non-industrial region near Moscow. None of those who died a sudden death had suffered from any systematic or chronic disorders before. Thus, our data for element mass fraction ratios in the intact crowns of female teeth may serve as indicative normal values for residents of the Central European region of Russia.

**Table 1.** Some statistical parameters of 42 different ratios of Ca, Cl, K, Mg, Mn, Na, P, and Sr mass fractions in the intact crowns of female (16-55 years)

Ratio	M	SD	SEM	Min	Max	Med	P0.025	P0.975
(Cl/Ca)×10 <sup>3</sup>	8.41	4.05	0.72	2.37	17.3	8.03	2.71	17.0
(K/Ca)×10 <sup>3</sup>	2.84	2.67	0.47	0.351	15.2	2.27	0.788	10.0
(Mg/Ca)×10 <sup>2</sup>	1.28	0.65	0.11	0.127	2.80	1.16	0.510	2.77
(Mn/Ca)×10 <sup>6</sup>	7.68	5.98	1.07	0.273	30.4	7.96	1.04	19.8
(Na/Ca)×10 <sup>2</sup>	1.84	0.35	0.06	1.08	2.68	1.75	1.32	2.55
P/Ca	0.527	0.075	0.013	0.377	0.714	0.522	0.402	0.764
(Sr/Ca)×10 <sup>3</sup>	0.974	0.589	0.103	0.342	3.11	0.819	0.356	2.17
Ca/P	1.93	0.28	0.05	1.40	2.65	1.91	1.42	2.49
(Cl/P)×10 <sup>2</sup>	1.57	0.72	0.13	0.581	3.11	1.44	0.599	3.09
(K/P)×10 <sup>2</sup>	0.502	0.387	0.069	0.0719	2.13	0.432	0.0996	1.73
(Mg/P)×10 <sup>2</sup>	2.48	1.32	0.23	0.239	6.17	2.23	0.947	5.43
(Mn/P)×10 <sup>6</sup>	14.2	10.9	1.93	0.615	56.1	15.5	1.28	35.4
(Na/P)×10 <sup>2</sup>	3.48	0.85	0.15	1.43	5.55	3.34	2.40	5.46
(Sr/P)×10 <sup>3</sup>	1.88	1.14	0.20	0.650	5.73	1.53	0.709	4.69
Ca/Mg	111	127	22	35.7	790	86.3	36.1	290
Cl/Mg	0.942	1.04	0.18	0.121	5.95	0.717	0.154	3.27
K/Mg	0.316	0.427	0.074	0.0348	1.87	0.182	0.0455	1.71
(Mn/Mg)×10 <sup>4</sup>	8.5	12.5	2.3	0.183	70.8	5.88	0.687	32.7
Na/Mg	1.89	1.72	0.30	0.656	10.9	1.51	0.749	4.37
P/Mg	59.0	66.6	11.4	16.2	416	45.0	18.5	149
Sr/Mg	0.098	0.076	0.013	0.0137	0.383	0.080	0.0234	0.253
Ca/Cl	156	93	17	58.0	421	135	58.9	370
K/Cl	0.378	0.312	0.055	0.0829	1.48	0.287	0.104	1.14
Mg/Cl	2.14	1.00	0.35	0.168	8.26	1.30	0.341	6.62
(Mn/Cl)×10 <sup>4</sup>	10.4	8.46	1.52	0.100	34.3	10.4	0.905	31.0
Na/Cl	2.86	1.83	0.32	0.952	7.43	2.14	0.996	6.87
P/Cl	79.1	30.5	6.9	32.1	172	60.4	32.4	167
Sr/Cl	0.149	0.120	0.021	0.0374	0.510	0.126	0.0408	0.505
Ca/K	561	484	86	65.7	2847	441	106	1487
Cl/K	4.29	2.83	0.50	0.675	12.1	3.49	0.893	9.72
Mg/K	7.34	6.14	1.07	0.535	28.7	5.50	0.586	20.8
(Mn/K)×10 <sup>4</sup>	34.5	19.8	3.5	9.79	87.1	33.9	9.95	78.4
Na/K	10.3	9.2	1.6	1.30	56.1	7.78	2.23	26.3
P/K	305	255	44	46.9	1391	231	58.4	1029
Sr/K	0.558	0.542	0.094	0.0438	2.76	0.376	0.0566	2.05
Ca/Na	56.2	11.2	1.9	37.3	92.9	57.3	39.3	76.4
Cl/Na	0.498	0.276	0.048	0.134	1.05	0.468	0.146	1.00
K/Na	0.150	0.131	0.023	0.0178	0.767	0.129	0.046	0.479
Mg/Na	0.709	0.317	0.054	0.0916	1.52	0.664	0.293	1.34
(Mn/Na)×10 <sup>4</sup>	4.20	3.41	0.60	0.165	17.4	3.89	0.548	12.1
P/Na	30.6	9.0	1.5	18.0	69.9	30.0	18.3	43.8
Sr/Na×10	0.566	0.359	0.062	0.181	1.78	0.437	0.204	1.46

*M* arithmetic mean, *SD* standard deviation, *SEM* standard error of mean, *Min* minimum value, *Max* maximum value, *Med* median, *P0.025* percentile with 0.025 level, *P0.975* percentile with 0.975 level

**Table 2.** Effect of age on mean values ( $M \pm SEM$ ) of ratios of chemical element in the intact crowns of female teeth (Student's *t*-test)

Ratio	Age			Ratio $M_2/M_1$
	15-35 year ( $M_1$ )	36-55 year ( $M_2$ )	$p \leq$	
(Cl/Ca) $\times 10^3$	9.79 $\pm$ 1.06	7.33 $\pm$ 0.92	0.09	0.75
(K/Ca) $\times 10^3$	2.29 $\pm$ 0.22	3.27 $\pm$ 0.82	0.26	1.43
(Mg/Ca) $\times 10^2$	1.22 $\pm$ 0.11	1.35 $\pm$ 0.18	0.54	1.11
(Mn/Ca) $\times 10^6$	9.13 $\pm$ 1.98	6.48 $\pm$ 1.06	0.25	0.71
(Na/Ca) $\times 10^2$	1.74 $\pm$ 0.07	1.92 $\pm$ 0.09	0.12	1.10
P/Ca	0.519 $\pm$ 0.013	0.534 $\pm$ 0.021	0.56	1.03
(Sr/Ca) $\times 10^3$	1.28 $\pm$ 0.20	0.750 $\pm$ 0.075	<b>0.022</b>	0.59
Ca/P	1.95 $\pm$ 0.06	1.92 $\pm$ 0.07	0.83	0.99
(Cl/P) $\times 10^2$	1.82 $\pm$ 0.17	1.37 $\pm$ 0.17	0.07	0.75
(K/P) $\times 10^2$	0.415 $\pm$ 0.041	0.575 $\pm$ 0.121	0.22	1.39
(Mg/P) $\times 10^2$	2.31 $\pm$ 0.21	2.61 $\pm$ 0.37	0.49	1.13
(Mn/P) $\times 10^6$	16.3 $\pm$ 3.6	12.4 $\pm$ 1.8	0.33	0.76
(Na/P) $\times 10^2$	3.28 $\pm$ 0.24	3.65 $\pm$ 0.17	0.23	1.11
(Sr/P) $\times 10^3$	2.43 $\pm$ 0.35	1.44 $\pm$ 0.16	<b>0.018</b>	0.59
Ca/Mg	90.3 $\pm$ 7.7	127 $\pm$ 38	0.36	1.40
Cl/Mg	0.889 $\pm$ 0.106	0.986 $\pm$ 0.323	0.78	1.11
K/Mg	0.201 $\pm$ 0.031	0.412 $\pm$ 0.131	0.13	2.05
(Mn/Mg) $\times 10^4$	7.47 $\pm$ 1.56	9.40 $\pm$ 3.97	0.66	1.26
Na/Mg	1.51 $\pm$ 0.13	2.19 $\pm$ 0.51	0.22	1.45
P/Mg	48.3 $\pm$ 4.4	67.5 $\pm$ 20.2	0.36	1.40
Sr/Mg	0.115 $\pm$ 0.017	0.084 $\pm$ 0.019	<b>0.23</b>	0.73
Ca/Cl	123 $\pm$ 17	182 $\pm$ 25	0.06	1.48
K/Cl	0.260 $\pm$ 0.043	0.484 $\pm$ 0.091	<b>0.036</b>	1.86
Mg/Cl	1.58 $\pm$ 0.36	2.60 $\pm$ 0.55	0.13	1.65
(Mn/Cl) $\times 10^4$	9.79 $\pm$ 2.16	11.0 $\pm$ 2.2	0.70	1.12
Na/Cl	2.16 $\pm$ 0.35	3.45 $\pm$ 0.47	<b>0.036</b>	1.60
P/Cl	63.2 $\pm$ 7.0	92.4 $\pm$ 10.3	<b>0.026</b>	1.46
Sr/Cl	0.160 $\pm$ 0.033	0.139 $\pm$ 0.028	0.63	0.86
Ca/K	507 $\pm$ 59	603 $\pm$ 146	0.55	1.19
Cl/K	5.23 $\pm$ 0.75	3.46 $\pm$ 0.62	0.08	0.66
Mg/K	6.69 $\pm$ 0.95	7.89 $\pm$ 1.81	0.57	1.18
(Mn/K) $\times 10^4$	37.3 $\pm$ 5.9	31.9 $\pm$ 4.1	0.46	0.86
Na/K	9.16 $\pm$ 1.08	11.2 $\pm$ 2.8	0.50	1.22
P/K	304 $\pm$ 53	306 $\pm$ 70	0.98	1.01
Sr/K	0.661 $\pm$ 0.112	0.472 $\pm$ 0.146	0.31	0.71
Ca/Na	58.6 $\pm$ 2.2	54.4 $\pm$ 3.0	0.26	0.93
Cl/Na	0.610 $\pm$ 0.070	0.404 $\pm$ 0.059	<b>0.032</b>	0.66
K/Na	0.130 $\pm$ 0.013	0.166 $\pm$ 0.040	0.41	1.28
Mg/Na	0.726 $\pm$ 0.058	0.696 $\pm$ 0.088	0.78	0.96
(Mn/Na) $\times 10^4$	5.05 $\pm$ 1.13	3.45 $\pm$ 0.51	0.21	0.68
P/Na	33.2 $\pm$ 3.0	28.5 $\pm$ 1.3	0.16	0.86
Sr/Na	0.785 $\pm$ 0.110	0.393 $\pm$ 0.035	<b>0.004</b>	0.50

*M* arithmetic mean, *SEM* standard error of mean, *bold* statistically significant

**Table 3.** Intercorrelations of the chemical element mass fractions in the intact crowns of female teeth ( $r$  – coefficient of correlation)

Element	Ca	Cl	K	Mg	Mn	Na	P	Sr
Ca	<b>1.00</b>	0.34	-0.04	-0.13	0.03	0.24	0.68 <sup>c</sup>	-0.10
Cl	0.34	<b>1.00</b>	0.15	-0.29	0.19	-0.20	0.46 <sup>b</sup>	0.04
K	-0.04	0.15	<b>1.00</b>	-0.22	0.39 <sup>a</sup>	0.21	0.26	-0.09
Mg	-0.13	-0.29	-0.22	<b>1.00</b>	-0.16	0.27	-0.17	0.02
Mn	0.03	0.19	0.39 <sup>a</sup>	-0.16	<b>1.00</b>	0.19	0.21	0.50 <sup>b</sup>
Na	0.24	-0.20	0.21	0.27	0.19	<b>1.00</b>	0.18	-0.18
P	0.68 <sup>c</sup>	0.46 <sup>b</sup>	0.26	-0.17	0.21	0.18	<b>1.00</b>	0.01
Sr	-0.10	0.04	-0.09	0.02	0.50 <sup>b</sup>	-0.18	0.01	<b>1.00</b>

Statistically significant values: <sup>a</sup>  $p \leq 0.05$ , <sup>b</sup>  $p \leq 0.01$ , <sup>c</sup>  $p \leq 0.001$ .

### References

1. Zaichick V., J. Radioanal. Nucl. Chem., Articles, 1993, **169**, 307–316.
2. Zaichick V., J. Radioanal. Nucl. Chem., Articles, 1994, **179**, 295–303.
3. Zaichick V., Ovchjarenko N.N., J. Trace and Microprobe Techniques, 1996, **14**, 143–152.
4. Zaichick V., Morukov B., Appl. Radiat. Isot., 1998, **49**, 691–694.
5. Zaichick V., Ovchjarenko N., Zaichick S., Appl. Rad. Isot., 1999, **50**, 283–293.
6. Zaichick V., Dyatlov A., Zaichick S.J., Radioanal. Nucl. Chem., 2000, **244**, 189–193.
7. Zaichick V., Tzaphlidou M., Appl. Rad. Isot., 2002, **56**, 781–786.
8. Tzaphlidou M., Zaichick V., Appl. Rad. Isot., 2002, **57**, 779–783.
9. Tzaphlidou M., Zaichick V., Biol. Trace Elem. Res., 2003, **93**, 63–74.
10. Zaichick V., Tzaphlidou M., Appl. Rad. Isot., 2003, **58**, 623–627.
11. Zaichick V.J., Radioanal. Nucl. Chem., 2004, **259**, 351–354.
12. Tzaphlidou M., Zaichick V.J., Radioanal. Nucl. Chem., 2004, **259**(2), 347–349.
13. Zaichick V.J., Radioanal. Nucl. Chem., 2006, **269**(3), 653–659.
14. Zaichick V.J., Radioanal. Nucl. Chem., 2007, **271**(3), 573–576.
15. Zaichick V., Zaichick S., J. Radioanal. Nucl. Chem., 2009, **281**, 47–52.
16. Zaichick V., J. Radioanal. Nucl. Chem., 2009, **281**, 41–45.
17. Zaichick S., Zaichick V., Journal of Trace Element in Medicine and Biology, 2010, **24**, 1–6.
18. Zaichick S., Zaichick V., Biol. Trace Elem. Res., 2010, **137**, 1–12.
19. Zaichick S., Zaichick V. J., Radioanal. Nucl. Chem., 2012, **293**, 241–246.
20. Zaichick V., Biol. Trace Elem. Res., 2013, **153**, 84–99.
21. Zaichick V., Radiat. Environ. Biophys., 2013, **52**, 65–85.
22. Zaichick V., Zaichick S., Biol. Trace Elem. Res., 2014, **159**, 32–38.
23. Zaichick V., Zaichick S., J. Anal. Chem., 1996, **51**(12), 1200–1205.
24. Zaichick V., In: Harmonization of Health-Related Environmental Measurements Using Nuclear and Isotopic Techniques. Vienna: IAEA, 1997, pp. 123–133.
25. Zaichick V., Trace Elements in Medicine, 2004, **5**(3), 17–22.
26. Zaichick V., Fresenius J. Anal. Chem., 1995, **352**, 219–223.
27. Korelo A., Zaichick V., In: Activation analysis in environment protection. Dubna: JINR, 1993, pp. 326–332.
28. Antunes A. et al., Laser Phys. Lett., 2005, **2**, 318–323.
29. Liu H. et al., Advances in Anthropology, **2013**, 3, 71–77.

# **Fission**

N. Carjan<sup>1,2</sup>, M. Rizea<sup>2</sup>

<sup>1</sup>Joint Institute for Nuclear Research, FLNR, 141980 Dubna, Moscow Region, Russia

<sup>2</sup>“Horia Hulubei” National Institute for Physics and Nuclear Engineering, Str.

Reactorului no.30, P.O.BOX MG-6, Bucharest - Magurele, Romania

## Abstract

The effect of the acceleration of a nucleus on the neutron states is studied in the frame of the independent-particle nuclear shell model. For this we solve numerically the time-dependent Schrödinger equation, with a moving mean-field of Woods-Saxon type. The time evolution of a neutron states at the Fermi level is calculated for  $^{236}\text{U}$  and acceleration parameter  $A=0.5$  (in  $10^{44}$  [fm/sec<sup>2</sup>]). It is roughly the acceleration during the Coulomb repulsion of two  $^{236}\text{U}$  nuclei when they are 20 fm apart. We keep this acceleration constant for  $10^{-21}$  sec before we switch it off ( $A=0$ ) and follow the wave packet for another  $10^{-21}$  sec. During the acceleration, the wave function oscillates with increasing amplitude until it escapes, mainly in the direction opposite to the motion of the nucleus. The mean value of its energy (in the nuclear system) increases from -4.80 MeV to -3.15 MeV and 12% of the wave packet leave the nucleus. During the uniform motion, the wave packet continues to oscillate and to escape at a lower rate: an extra 2%. We repeated the calculations for two neighbouring states and found the emission rate to depend strongly on the position of the neutron state with respect to the Fermi energy. Finally, the effect of the nuclear deformation on the acceleration induced neutron emission is studied. In this case the period of oscillation is larger and the amplitude smaller. The angular distribution with respect to the direction of motion is also different: it has, in the nuclear system, an intense component almost perpendicular to the deformation axis.

## 1. Introduction

What if, like a fully-filled water tank, a nucleus will spill its less bound nucleons when accelerated? Most probable this could happen to neutrons since, contrary to protons, they are not protected by a Coulomb barrier. In case the answer is “yes”, we are dealing with a new nuclear process. To give a first answer to this captivating question we choose a simple framework: the independent particle shell model [1]. We therefore solve the time-dependent Schrödinger equation with a moving mean-field of Woods-Saxon type and study the change in the neutron eigenstates during  $10^{-21}$  sec of constant acceleration followed by  $10^{-21}$  sec of constant velocity. This scenario is borrowed from the design of a linear accelerator [2].

The motion of a quantum particle in a moving one-dimensional potential well has been already studied in the field of control systems. Controlability is a mathematical concept that, in very general terms, means the ability to do whatever we want with a given dynamical system; in particular, to transfer a quantum system from any initial state to any final state [3, 4] or to manipulate the position of a nano-particle using dynamical potential traps [5].

## 2. Formalism

In our case, we consider a neutron in a moving nuclear potential that has axial symmetry. It is represented by a wave function solution of the Schrödinger equation

$$i\hbar \frac{\partial \Theta(\rho, z, t)}{\partial t} = \mathcal{H}(\rho, z, t)\Theta(\rho, z, t), \quad (1)$$

where  $\mathcal{H}$  is the single-particle Hamiltonian.

$$\mathcal{H} = -\frac{\hbar^2}{2m} \left[ \frac{1}{\rho} \frac{\partial}{\partial \rho} + \frac{\partial^2}{\partial \rho^2} + \frac{\partial^2}{\partial z^2} - \frac{\Lambda^2}{\rho^2} \right] + V(\rho, z - \alpha(t)).$$

$\alpha(t)$  describes the displacement of the potential in time along the  $z$  axis.  $\Lambda$  is the projection of the orbital angular momentum on the symmetry axis. For simplicity the spin-orbit term is neglected.

By the Liouville transformation  $\Phi = \rho^{1/2}\Theta$ , the first derivative with respect to  $\rho$  from  $\mathcal{H}$  is removed, resulting a simplified Hamiltonian  $H$  of the form:

$$H = -\frac{\hbar^2}{2m} \left[ \frac{\partial^2}{\partial \rho^2} + \frac{\partial^2}{\partial z^2} - \frac{\Lambda^2 - 1/4}{\rho^2} \right] + V(\rho, z - \alpha(t)).$$

One arrives to the equation

$$i\hbar \frac{\partial \Phi(\rho, z, t)}{\partial t} = H(\rho, z, t)\Phi(\rho, z, t). \quad (2)$$

To solve this equation, a transformation of both the variable and the function from the non-inertial (laboratory) to the inertial (nuclear) system is convenient. It avoids an interpolation of the potential between the grid points at each time step.

We will explain this transformation on the 1-D TDSE:

$$i\hbar \frac{\partial \Phi(t, z)}{\partial t} = -\frac{\hbar^2}{2m} \frac{\partial^2 \Phi(t, z)}{\partial z^2} + V(z - \alpha(t))\Phi(t, z) \quad (3)$$

We go in the nuclear frame by the following changes of the variable  $z \rightarrow q$  and of the function  $\Phi \rightarrow \Psi$  [6]:

$$q = z - \alpha(t), \quad \Phi(t, z) = \exp(u)\Psi(t, q) \quad (4)$$

where

$$u = ib \left( z\dot{\alpha} - \alpha\dot{\alpha} + \frac{1}{2} \int_0^t \dot{\alpha}^2(t') dt' \right).$$

By taking  $b = \frac{m}{\hbar}$ , it can be shown that Eq.(3) will be transformed in

$$i\hbar \frac{\partial \Psi(t, q)}{\partial t} = -\frac{\hbar^2}{2m} \frac{\partial^2 \Psi(t, q)}{\partial q^2} + V(q)\Psi(t, q) + mq\ddot{\alpha}(t)\Psi(t, q). \quad (5)$$

To eliminate the linear term in  $q$  (which tends to  $\infty$  as  $q \rightarrow \infty$ ), a further function transformation is performed [7]

$$\Psi(t, q) = \exp\left(-i\frac{\lambda}{\hbar}\right) \chi(t, q) \quad (6)$$

with

$$\lambda(t, q) = qm \int_0^t \ddot{\alpha}(t') dt' = q\beta(t).$$

In our particular case  $\alpha(t) = \frac{1}{2}At^2$ .

$$\dot{\alpha} = At, \ddot{\alpha} = A, \lambda = Bqt, B = mA$$

$$u = ib \left( zAt - \frac{1}{3}A^2t^3 \right)$$

and the equation for  $\chi$  is:

$$i\hbar \frac{\partial \chi(t, q)}{\partial t} = -\frac{\hbar^2}{2m} \left( \frac{\partial^2 \chi(t, q)}{\partial q^2} + \frac{2}{\hbar i} Bt \frac{\partial \chi(t, q)}{\partial q} - \frac{1}{\hbar^2} B^2 t^2 \chi(t, q) \right) + V(q)\chi(t, q). \quad (7)$$

The advantage of these transformations is that they lead to equations in which the potential depends on a time-independent variable, the dependence on  $\alpha(t)$  being transferred in the coefficients of Eqs.(5),(7).

### 3. Computational aspects

We work with the variables  $\rho$  and  $q$  on a finite numerical grid:  $[0,160] \times [-256,256]$ ,  $\Delta\rho = \Delta q = 1/8$  fm,  $\Delta t = 1/128 \times 10^{-22}$  sec. The equations (5) and (7) are solved numerically by the Crank-Nicolson method. One obtains a linear system which is solved by a routine based on the Strong Implicit Procedure [8]. As initial solutions (at  $t = 0$ ) we consider eigenfunctions of the original Hamiltonian.

The propagation in time is done in two steps. We consider a quadratic  $\alpha(t)$  and use Eq.(7) for  $10^{-21}$  sec. Then we consider a linear  $\alpha(t)$  and use Eq.(5) without the  $\ddot{\alpha}$  term for another  $10^{-21}$  sec. At any time, by performing the inverse transformations, we can retrieve the solution  $\Phi(\rho, z, t)$  of the original equation. For the 1st step we choose the constant acceleration  $A=0.5[10^{44} \text{ fm/sec}^2]$  resulting a constant velocity  $v=5[10^{22} \text{ fm/sec}]$  for the 2nd step.

### 4. Results

As an example we take spherical  $^{236}\text{U}$  and study 3 neutron states with  $\Lambda=0$  around the Fermi level. The parameters of the Woods-Saxon potential are fitted to single-particle and single-hole states in the  $^{208}\text{Pb}$  region [9].

Fig.1 shows the result for the 14th eigenstate laying at -4.8 MeV. For  $T > 0$ , the wave packet exhibits a changing asymmetry with respect to the  $\rho$  axis indicative of an oscillation. In fact, we are dealing with an oscillation over the usual vibration of a quasi-stationary state. A similar vibration causes the barrier assaults in the Gamow picture of  $\alpha$  decay [10]. The presence of the neutron inside the nucleus, measured by  $N_{in}$ , decreases from 1.00 (at  $T=0$ ) to 0.88 (at  $T=10$ ). A neutron, initially occupying this state, has therefore 12% chance to be emitted during the acceleration phase. For  $T > 10$  the oscillatory motion continues. At  $T=20$   $N_{in}$  reaches an even lower value (0.86) because at  $T=10$  the wave packet has short unbound tails which inevitably leave the nucleus.

The most probable direction of emission is  $180^\circ$  with respect to the displacement of the nucleus as in classical mechanics. There is however a weaker branch at  $\approx 150^\circ$  which

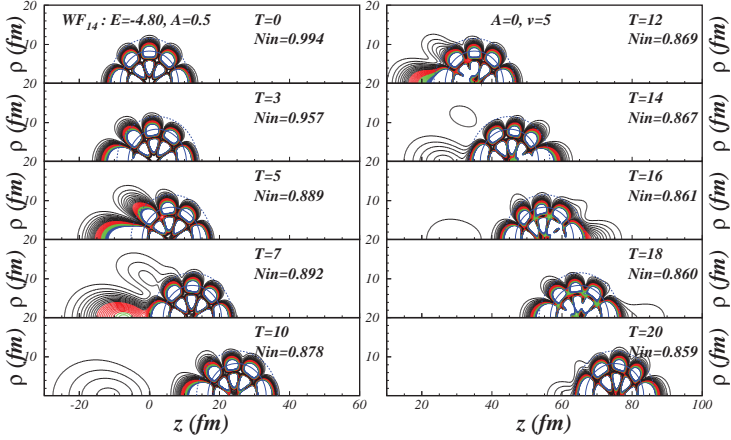


Figure 1: Time evolution of  $|\Phi_{14}^0|^2$  during (left) and after (right) acceleration for spherical  $^{236}\text{U}$ .  $N_{in}$  is the norm inside the dotted circle defined by  $V_0/100$ . T is the time in  $10^{-22}$  sec.

has a quantum origin. It is known that the tunneling path of a metastable state is mainly dictated by its quantum numbers [14, 15]. In other words the emission preserves the spatial distribution of the respective state. Hence we expect a 2nd peak at  $125^\circ$  in the nuclear system which translates into an emission at  $150^\circ$  in the laboratory system.

Figs. 2 and 3 show the time dependence of two other neutron states with energies below (-8.3 MeV) and above (-3.4 MeV) the Fermi level respectively. The wave function with lower energy oscillates during both regimes: quadratic and linear  $\alpha(t)$ . It doesn't however succeed to escape: its presence inside the nucleus is practically unchanged. On the contrary, 49% of the wave function with higher energy is emitted, in the same interval of time, through strong oscillations. Predictably, the emission starts earlier and is more intense. As for  $\Phi_{14}^0$ , there are also two directions of emission: one intense at  $180^\circ$  and one weak at an angle between  $180^\circ$  and  $90^\circ$ .

For a better understanding of the physics involved, we divide the total energy in the laboratory system in significant terms:

$$\begin{aligned}
 \langle \Phi | H | \Phi \rangle &= -\frac{\hbar^2}{2m} \iint \left( \Psi^* \frac{\partial^2 \Psi}{\partial \rho^2} + \Psi^* \frac{\partial^2 \Psi}{\partial q^2} \right) d\rho dq + \frac{\hbar^2}{2m} b^2 \dot{\alpha}^2 \iint |\Psi|^2 d\rho dq \\
 &- \frac{\hbar^2}{2m} 2ib\dot{\alpha} \iint \Psi^* \frac{\partial \Psi}{\partial q} d\rho dq + \frac{\hbar^2}{2m} (\Lambda^2 - 1/4) \iint \frac{1}{\rho^2} |\Psi|^2 d\rho dq + \iint V(\rho, q) |\Psi|^2 d\rho dq.
 \end{aligned} \tag{8}$$

The 1st term is the average kinetic energy in the nuclear frame. The 2nd term reduces to  $m\dot{\alpha}^2/2$ ; it is the extra kinetic energy due to the velocity of the potential. The 3rd

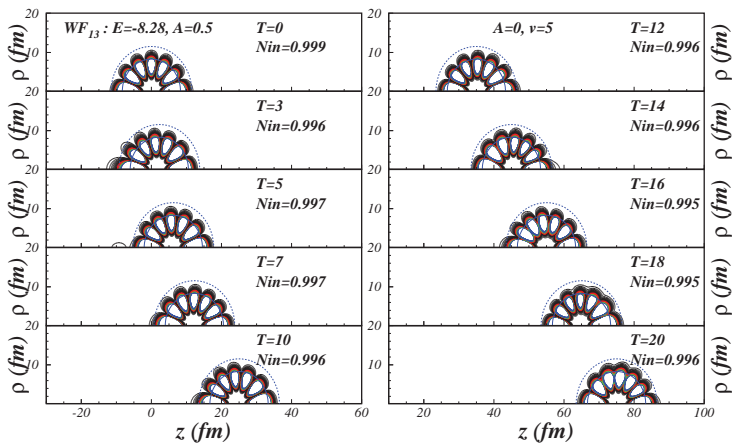


Figure 2: The same as in Fig. 1 but for  $\Phi_{13}^0$ .

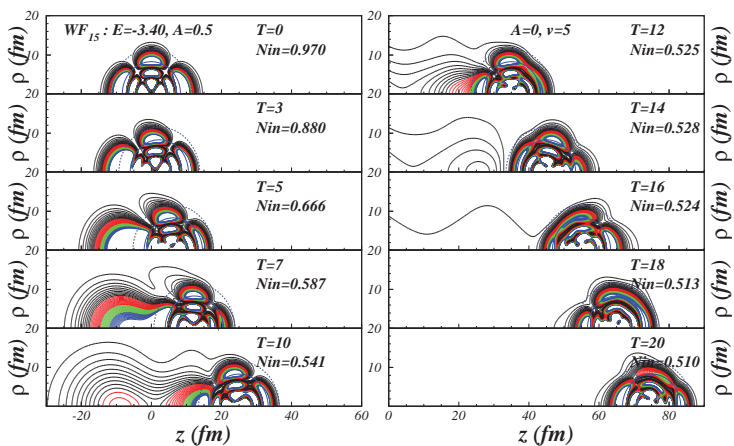


Figure 3: The same as in Fig. 1 but for  $\Phi_{15}^0$ .

term reduces to  $\dot{\alpha} \langle p \rangle$  where  $\langle p \rangle$  is the average momentum in the nuclear frame.

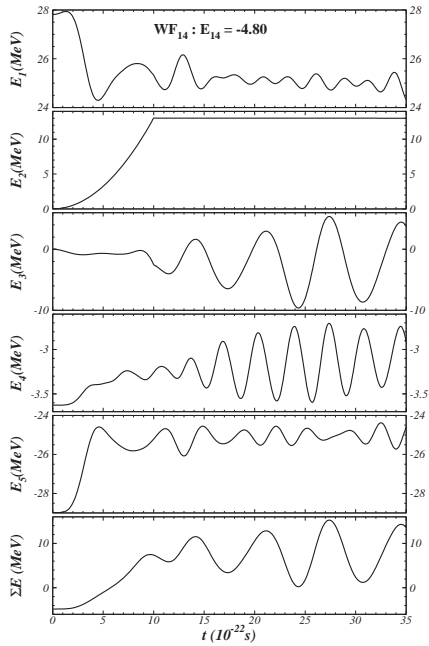


Figure 4: The five terms which form the neutron energy in the laboratory system.

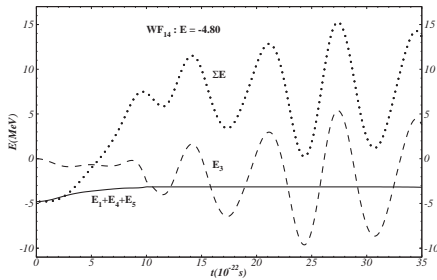


Figure 5: The neutron energy in the laboratory system (dotted line), in the nuclear system (solid) and the energy due to the interaction with the moving potential (dashed).

It represents the variation of the neutron energy due to the interaction with the moving wall of the potential; equivalent to the "one-body" dissipation [11]. The last two terms are the average centrifugal and nuclear potentials respectively.

These 5 terms as well as their sum are plotted in Fig.4 as a function of time for the neutron state close to the Fermi energy. Their variation during acceleration is explained by two facts: a) the emitted fraction of the wave packet is more and more present in the nuclear surface or even outside the nucleus. This e.g., diminishes E1 and boosts E4 and E5. b) the emission is accompanied by an oscillatory motion. From the variation of E2, one observes that our neutron reaches 13 MeV in  $10^{-21}$  sec. In a linear accelerator a  $^{236}\text{U}$  ion can easily attain the same velocity but in a much longer time.

After  $T=10$  there is only this oscillatory motion left. The sum  $E1+E4+E5$  i.e., the neutron energy in the nuclear frame, is constant and the oscillations of E are due only to E3 as clearly seen in Fig.5.

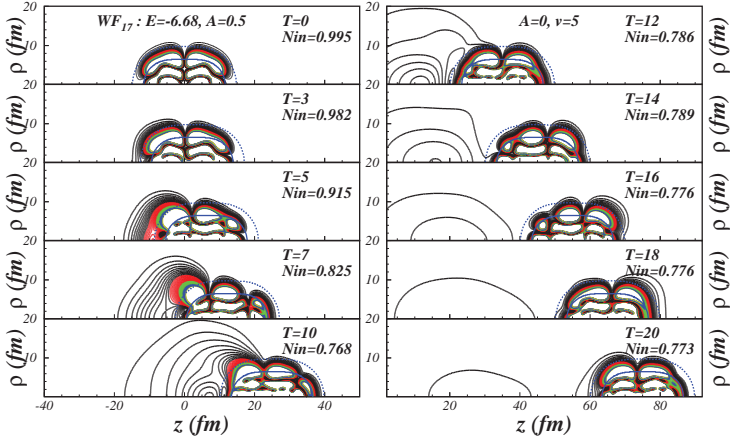


Figure 6: Time evolution of  $|\Phi_{17}^0|^2$  during (left) and after (right) acceleration for the shape isomer (deformation parameter  $\epsilon=0.52$ ) of  $^{236}\text{U}$ .  $N_{in}$  is the norm inside the dotted ellipse defined by  $V_0/100$ . T is the time in  $10^{-22}$  sec.

Finally we study the effect of nuclear deformation on the neutron emission due to acceleration of the nucleus along the deformation axis. For this we describe the nuclear shape by a pure Cassini oval with deformation parameter  $\epsilon=0.52$ . It is the shape isomer of  $^{236}\text{U}$  [16]. The results for two neutron states, one below and one above the Fermi level, are presented in Figs. 6 and 7 respectively. The emission probability is again larger in the latter case:  $N_{in} = 0.39$  vs 0.77. One can also notice that the emission at angles smaller than  $180^\circ$  to the z-axis is much intenser than in the previous cases. It is because a quasi-stationary state in a deformed nucleus tunnels most probably perpendicularly to

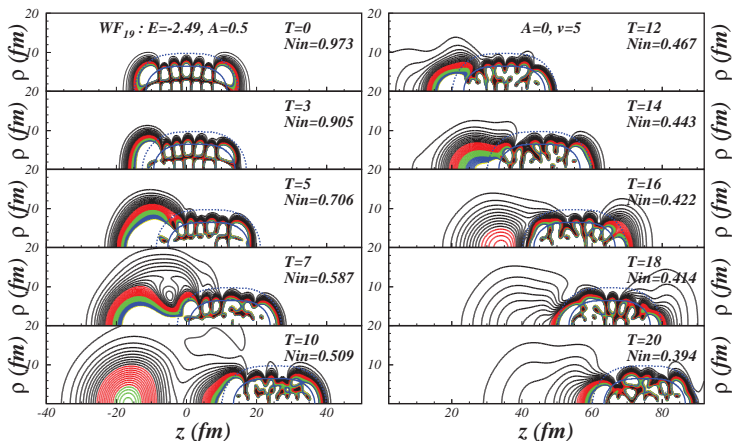


Figure 7: The same as in Fig.6 but for  $|\Phi_{17}^0|^2$ .

the deformation axis [17], irrespective if the barrier is lower or higher along this direction. It is what happens here: the emission occurs at  $90^\circ$  in the nuclear system. Due to the displacement of the nucleus however, in the laboratory system, the emission occurs at slightly larger angles ( $\approx 110^\circ$ ). Hence there is qualitative difference between spherical and strongly deformed nuclei: in the latter case, the direction imposed by quantum mechanics competes in intensity with the classically expected direction of emission.

## 5. Concluding remarks

A similar emission takes place during the slowing down ( $A < 0$ ) of a projectile when it approaches a target. Among possible effects, an increase of the neutron-transfer cross section is expected. The value chosen ( $A = 0.5$ ) is larger than the acceleration during the Coulomb repulsion of two equal fission fragments from  $^{236}\text{U}$  separated by  $D_{cm} = 20$  fm ( $A = 0.13$ ) but comparable with that attained during the collision of two  $^{236}\text{U}$  nuclei at the same distance of approach ( $A = 0.52$ ). In conclusion, there is probably no acceleration induced excitation of the fission fragments during their separation. On the other hand, a heavy projectile is expected to become excited (even to emit neutrons) when it approaches a heavy target or moves away from it. However, the acceleration produced in Coulomb interactions is not constant (it depends on  $D_{cm}$ ) and a high level cannot be maintained for  $10^{-21}$  sec, a long time at the scale of the above mentioned processes. For a quantitative answer a dedicated study is necessary.

The process of acceleration induced neutron emission has similarities with the release of neutrons at scission i.e., during the last stage of nuclear fission. They are both due to a fast change of the potential in which they move that transforms each neutron state into a

wave packet with components in the continuum [12, 13]. In the case of scission neutrons however, it is the shape of the potential and not its position that changes.

## Acknowledgements

We are grateful to Gurgen Ter-Akopian and Jorgen Randrup for their interest in this work and illuminating discussions. This work was done in the frame of the projects PN-III-P4-ID-PCE-2016-0649 (contract nr. 194/2017) and PCE-2016-0014 (contract nr.7/2017).

## References

- [1] M. Goeppert-Mayer, J.H.D. Jensen, *Nuclear Shell Structure* (John Wiley and Sons, New York, 1955).
- [2] H. Wiedemann, *Particle Accelerator Physics* (Springer, Berlin, 1999).
- [3] P. Rouchon, *Control of a quantum particle in a moving potential well in: Proceedings of the 2nd IFAC Workshop on Lagrangian and Hamilton Methods for Nonlinear Control, Seville, 2003* p.317.
- [4] K. Beauchard, J.-M. Coron, *Controllability of a quantum particle in a moving potential well*, J. Functional Analysis **232**, 328 (2006).
- [5] S. Miyashita, *Conveyance of a quantum particle by a moving potential well*, J. Phys. Soc. Japan **76**, 104003 (2007).
- [6] A.G. Butkovsky, Y.I. Samoilenko, *Control of Quantum- Mechanical Processes and Systems*, Vol.56 of *Mathematics and its Applications (Soviet Series)*, (Kluwer Academic Publishers Dordrecht/Boston/London. English edition, 1990).
- [7] C-C Chou, R.E. Wyatt, *Time-dependent Schrodinger equation with Markovian outgoing wave boundary conditions: Applications to quantum tunneling dynamics and photoionization*, Int. J. Quantum Chem. **113**, 39 (2013).
- [8] C. R. Jesshope, *SIPSOL - suite of subprograms for the solution of the linear equations arising from elliptic partial differential equations*, Comp. Phys. Commun. **17**, 383 (1979).
- [9] E. Rost, *Proton shell-model potential for lead and the stability of superheavy nuclei*, Phys. Lett. B **26**, 184 (1968).
- [10] S. A. Gurwitz, G. Kalberman, *Decay width and shift of a quasistationary state*, Phys. Rev. Lett. **59**, 262 (1987).
- [11] J. Blocki, Y. Boneh, J. R. Nix, M. Robel, A.J. Sierk, W. J. Swiatecki, *One-Body Dissipation and the Super-Viscosity of Nuclei*, Ann. of Phys. **113**, 330 (1978).
- [12] M. Rizea, N. Carjan, *Dynamical Scission Model*, Nuc. Phys. A **909**, 50 (2013).

- [13] N. Carjan, M. Rizea, *Similarities between calculated scission-neutron properties and experimental data on prompt fission neutrons*, Phys. Lett. B **747**, 178 (2015).
- [14] P. Talou, N. Carjan, D. Strottman, *Time-dependent approach to bidimensional quantum tunneling: application to the proton emission from deformed nuclei*, Nuc. Phys. A **647**, 21 (1999).
- [15] N. Carjan, P. Talou, D. Strottman, *Angular distribution of protons emitted from oriented nuclei: toward imaging single-particle wave functions*, *The Nucleus: New Physics for the New Millenium*, Eds. Smit et al., (Kluver Academic/Plenum Publishers, New York, 2000) p 115.
- [16] V. Pashkevich, *On the asymmetric deformation of fissioning nuclei*, Nucl. Phys. A **169**, 275 (1971).
- [17] D. Strottman, N. Carjan, P. Talou, *New Aspects in the Decay of Quasi-Stationary States by Multidimensional Tunneling*, Physica Scripta **T88**, 148 (2000).

# Measuring Method of the Delayed Neutron Time Parameters for U-236 Fission by Neutrons with Energies from 14 to 18 MeV

D.E. Gremyachkin, V.M. Piksaikin, A.S. Egorov, V.F. Mitrofanov, K.V. Mitrofanov

*Joint Stock Company "State Scientific Center of the Russian Federation – Institute for Physics and Power Engineering" named after A. I. Leypunsky, Obninsk, Russia*

## Abstract

Analysis of existing database on the relative abundances of delayed neutrons and half-lives of their precursors measured for neutron induced fission of heavy nuclei in the energy range above 14 MeV shows that such data are not available for many nuclides which are important for nuclear fuel cycle. In the present work for the first time the time dependence of delayed neutron activity for the neutron-induced fission of  $^{236}\text{U}$  in the energy range from 14.2 to 18 MeV.

## Introduction

In the last decades the efforts on improvement of the database on delayed neutron characteristics have been dedicated to analysis of delayed neutron characteristics for the fission of  $^{235}\text{U}$ ,  $^{238}\text{U}$ ,  $^{239}\text{Pu}$  by neutrons from thermal to several MeV [1]. Energy range and choice of nuclei under investigation have been determined by the needs of nuclear energy. At the same time in the range from 5 to 20 MeV these characteristics are studied much worse. Firstly, it related to the range from 14 MeV or more.

The delayed neutron data at present could be used not only in calculation and control of reactor kinetics but in broad range of applications. Due to development of compact neutron generators based on D(d,n) and T(d,n) reactions delayed neutrons can be used in geology (well logging industry), investigations of nuclear physical characteristics, security applications, control of non-proliferation of the nuclear materials, medicine, educational purposes [2].

## The origin of $^{236}\text{U}$

$^{236}\text{U}$  could be produced in three ways. The first one is radioactive capture of thermal neutrons by  $^{235}\text{U}$ , and consequent gamma emission it consist for 15% of all reactions in the core of nuclear reactors. The second source of  $^{236}\text{U}$  production is alpha decay of  $^{240}\text{Pu}$  ( $T_{1/2}=6561$  y.) formed in the result of radioactive capture of thermal neutron by  $^{239}\text{Pu}$ , the second of the most used isotopes in nuclear energy [3, 4]. The third way of  $^{236}\text{U}$  production is the  $^{238}\text{U}(n, 3n)$  reaction which goes by fast neutrons, this reaction is the main contributor of the  $^{236}\text{U}$  abundance in the atmosphere due to the restrictions on the spreading of the  $^{236}\text{U}$  formed in nuclear reactors.

## Experimental method and preliminary analysis of the obtained data

The experimental method used in present experiments is based on cyclic irradiation of the fissile sample in a well-known neutron flux and consequent measurement of the time dependence of delayed neutron activity. For that, the guide tube of pneumatic transport system with the sample under investigation have been placed between two ionization fission chambers near the target of the electrostatic generator CG-2.5.

Experimental set-up used in the present work has been placed on the beam of electrostatic accelerator CG-2.5 of SSC RF – IPPE. The basic components of the set-up are shown on the Fig. 1.

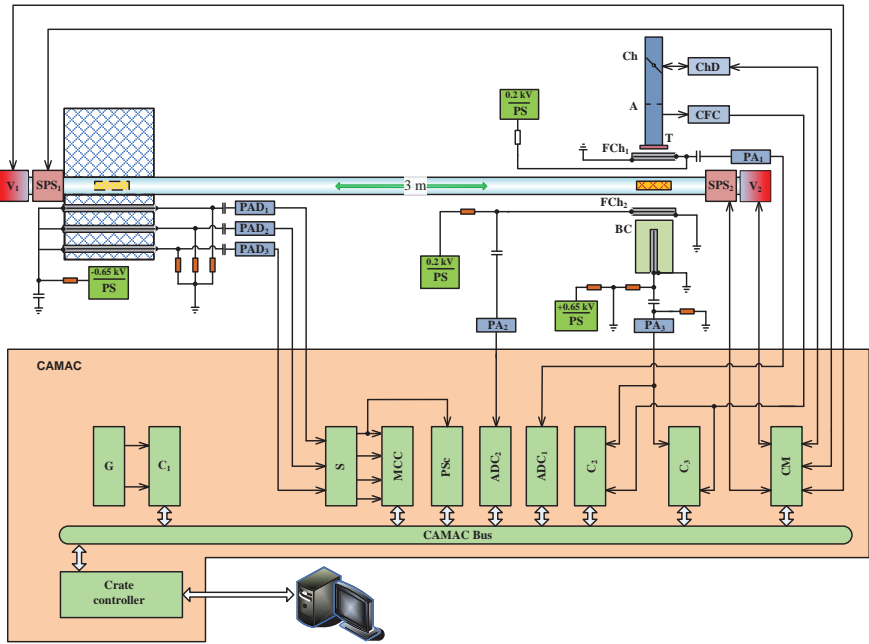


Fig. 1. Block diagram of the experimental setup: (PAD) preamplifier, amplifier, and discriminator; (A) adder; (PA) preamplifier and amplifier; (V) electromagnetic valve; (SPS) sample position sensor; (CM) controlled unit; (CFC) current-to-frequency converter; (ADC) analog-to-digital converter; (PSc) preset-scaler; (MCC) multichannel counter; (G) quartz generator of pulses; (PS) power source; (Ch) chopper; (ChD) magnetic chopper drive; (A) ion guide aperture; (T) accelerator target; (FCh) fission chamber; (BC) boron counter of neutrons; (C1) counter with a preset exposure time; (C2) counter of total counts from the CFC and BC; and (C3) counter of the CFC and BC counts within preset time intervals.

Boron counters SNM-11 have been chosen as the main element of the registration of detector, because of their low sensitivity to  $\gamma$ -rays. Detector presents the assay of 30 counters, distributed in polyethylene moderator. It consists of three concentric circles, which have radiuses 53, 80 and 110 mm. Inner ring consists of 6 boron counters, medium and outer rings consist of 12 counters each. Outer diameter of moderator was equal to 400 mm, length – 300 mm. The counters were operating in proportional mode at bias voltage 650 V [5]. There was an opening  $\varnothing 36$  mm in the center of detector provided for installation of the fissile sample under investigation. The detector was shielded with boron carbide, cadmium and borated polyethylene. Detector has been installed 3 meters away from accelerator target.

Experimental technique used in the present work is based on the periodical irradiation of the fissile samples in the well-known neutron flux and the consequent measuring of the time dependence of the delayed neutron intensity. It has been possible to irradiate the samples under investigation for different time intervals to increase the abundance of the concerned delayed neutrons' group in the integral delayed neutron curve.

### Experimental conditions and additional experiments

It should be noted that specific features of the  $T(d,n)^4\text{He}$  reaction, concerned with high intensity and high energy of generated neutrons beams essentially increase the complexity of the processing procedure of measured data, which is usually used for the work with neutron sources based on  $T(p,n)^3\text{He}$  and  $D(d,n)^3\text{He}$  reactions. Analysis of the existing data on the time parameters of delayed neutrons have shown that the data obtained by different authors for the energy above the 14 MeV are significantly differs from each other. One of the possible reasons of such significant difference could be related to the effect of additional source –  $D(d,n)^3\text{He}$  reaction, which is inevitably arising in the investigations using the  $T(d,n)^4\text{He}$  reaction on the solid targets. Another possible reason should be the blocking effect of the detector in the intensive neutron flux generated in the  $T(d,n)^4\text{He}$  reaction. To estimate the magnitude of the effect, concerned with blocking of the neutron detector being in the intensive neutron flux and the effect of the additional source additional experiments have been made.

### Processing of the experimental data

The number of counts of delayed neutron detector  $N(t_k)$ , registered in the  $k$ -channel of time analyzer  $t_k$  with duration  $\Delta t_k$  after the sample irradiation using the neutrons from  $T(d,n)^4\text{He}$  and  $D(d,n)^3\text{He}$  reactions can be represented as follows

$$N_l(t_k) = A_l \cdot \sum_{i=1}^n F_{ii} \cdot \frac{a_{ii}}{\lambda_{ii}} \cdot \exp(-\lambda_{ii} \cdot t_k) \cdot (1 - \exp(-\lambda_{ii} \cdot \Delta t_k)) + B_l(t_k) \cdot \Delta t_k, l = (T, D), k = (1, \dots, m) \quad (1)$$

where T and D related to the measurements using  $T(d,n)^4\text{He}$  and  $D(d,n)^3\text{He}$  reactions correspondingly,  $a_{ii}$  and  $\lambda_{ii}$  – relative abundance and decay constant of  $i$ -th delayed neutron group,  $B_l(t_k)$  – intensity of neutrons background,  $A_l$  – saturation activity,

$$F_{ii} = (1 - \exp(-\lambda_{ii} \cdot t_{ir})) \cdot \left( \frac{N}{1 - \exp(-\lambda_{ii} \cdot T)} - \exp(-\lambda_{ii} \cdot T) \cdot \left( \frac{1 - \exp(-n \cdot \lambda_{ii} \cdot T)}{(1 - \exp(-\lambda_{ii} \cdot T))^2} \right) \right) \quad (2)$$

presents the expression considering the irradiation history of the sample and registration of accumulated activity, which includes the following experimental parameters:  $N$  – the number of irradiation cycles,  $T$  – duration of the one measurement cycle, which consisted of irradiation time in one cycle  $t_{ir}$ , transportation time of the sample to the neutron detector and the count time of delayed neutron intensity [6].

### Results

Time dependence of neutron intensity after neutron induced fission of  $^{236}\text{U}$  in the energy range from 14.2 to 18 MeV obtained in the present work considering the blocking effect and effect of additional source (circles) are shown on figure 2. Data obtained as result of estimation of delayed neutrons parameters represented by continuous curves. Estimation of

the parameters  $A$ ,  $B$ ,  $a_i$ ,  $\lambda_i$  ( $i = 1, \dots, n$ ) on the observed values of time dependence  $N(t_k)$  ( $k=1, \dots, m$ ) (eq. 1, 2) was made within the 6-group representation using the iteration least squares method.

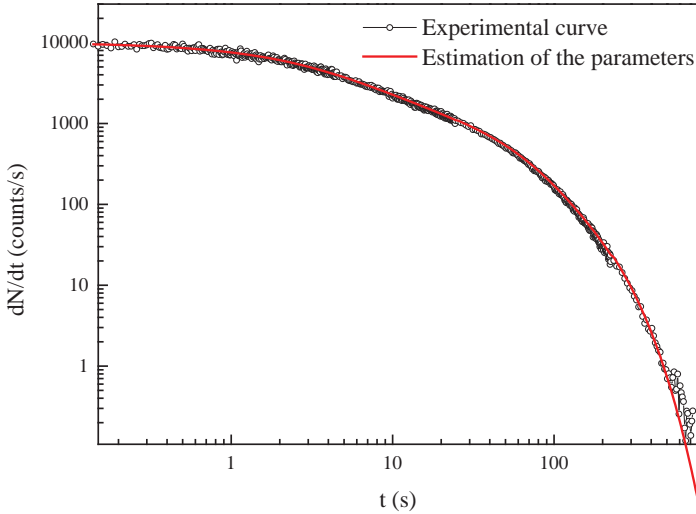


Fig. 2 – Time dependence of  $^{236}\text{U}$  sample intensity after irradiation by 15.83 MeV neutrons. Irradiation time 180 s. Rings – experimental data including the corrections on the blocking effect and effect of additional source; red curve – data obtained as result of estimation of delayed neutrons parameters.

The obtained results on energy dependence of relative abundances of the separate delayed neutron group  $a_i$  and half-lives of their precursors  $T_i$  for the fission of  $^{236}\text{U}$  by neutrons in the energy range from 14.2 to 18 MeV are presented in the Table 1. Values of group parameters ( $a_i, T_i$ ) shown in the Table 1 in a six-group representation was obtained by averaging of these parameters of several series of the measurements, corresponding to the similar energy of the primary neutrons. The average half-life was calculated for each energy using the following formula

$$\langle T \rangle = \frac{\sum_i a_i T_i}{\sum_i a_i}$$

where  $a_i$  – the relative abundance of the  $i$ -th delayed neutron group;  $T_i$  – the half-life of the  $i$ -th delayed neutron group.

The obtained values of relative abundances and half-lives of the DN precursors for the fission of the  $^{236}\text{U}$  by neutrons in the range from 14.23 to 17.98 MeV shown in the Table 1.

Table 1 – Relative abundances and half-lives for the fission of  $^{236}\text{U}$  by neutrons in the energy range from 14.23 to 17.98 MeV.

$E_n$ , MeV	$i$	Group number						Average half-life, s
		1	2	3	4	5	6	
14,23±0,23	$a_i$	0,0389 ±0,0006	0,165 ±0,003	0,321 ±0,005	0,431 ±0,007	0,025 ±0,001	0,0190 ±0,0004	7,48 ± 0,07
	$T_i$	55,01 ±0,32	20,46 ±0,17	4,09 ±0,04	1,49 ±0,02	0,47 ±0,01	0,214 ±0,005	
15,83±0,20	$a_i$	0,040 ±0,001	0,172 ±0,003	0,318 ±0,007	0,423 ±0,008	0,026 ±0,001	0,020 ±0,001	7,79 ± 0,22
	$T_i$	54,78 ±0,31	20,58 ±0,19	4,32 ±0,05	1,57 ±0,03	0,48 ±0,01	0,214 ±0,006	
17,98±0,25	$a_i$	0,0393 ±0,0006	0,199 ±0,003	0,324 ±0,005	0,391 ±0,007	0,026 ±0,001	0,0194 ±0,0004	8,20 ± 0,09
	$T_i$	52,95 ±0,32	20,62 ±0,16	4,31 ±0,05	1,51 ±0,03	0,47 ±0,01	0,214 ±0,005	

Energy dependence of the average half-life of DN precursors from the fission of  $^{236}\text{U}$  by neutrons in the energy range from 14.23 to 17.98 MeV is shown on fig. 3. There are values obtained in the separate measurements and the data points obtained in the result of averaging on the values obtained in the separate measurements.

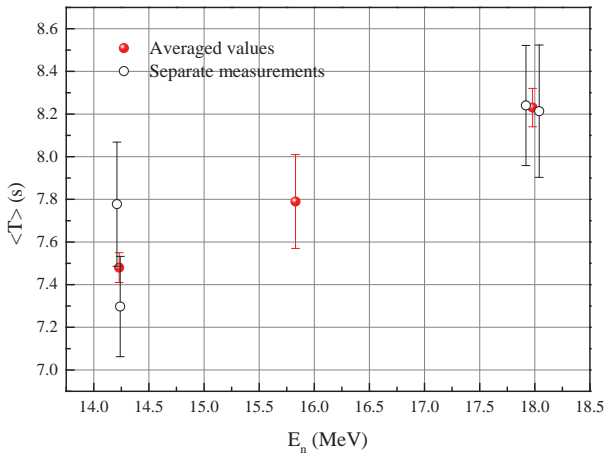


Fig. 3. Energy dependence of the average half-life of delayed neutron precursors for neutron induced fission of the  $^{236}\text{U}$  in the energy range from 14,2 to 18 MeV. Black rings – values obtained in the separate measurements, red points – data obtained in the result of averaging of the separate measurements.

For each neutron energy the correlation matrix has been obtained. Correlation matrix of the DN group parameters for the fission of  $^{236}\text{U}$  by 15.83 MeV neutrons is presented in the Table 2.

Table 2 – Correlation matrix of DN group parameters obtained for the fission of  $^{236}\text{U}$  by 15.83 MeV neutrons.

	a1	T1	a2	T2	a3	T3	a4	T4	a5	T5	a6	T6
a1	1	0	0	0	0	0	0	0	0	0	0	0
T1	0	1	0.79	0.43	0.46	0.15	0.55	0.12	0.02	0.01	0.01	0.01
a2	0	0.79	1	0.18	0.43	-0.19	0.42	0.15	0.01	0.01	0.01	0.01
T2	0	0.43	0.18	1	0.42	0.59	0.56	0.06	0.01	0.01	0	0.01
a3	0	0.46	0.43	0.42	1	-0.27	-0.1	-0.45	0	0	0	0
T3	0	0.15	-0.19	0.59	-0.27	1	0.63	0.14	0.01	0.01	0	0
a4	0	0.55	0.42	0.56	-0.1	0.63	1	0.18	-0.02	-0.02	-0.01	-0.01
T4	0	0.12	0.15	0.06	-0.45	0.14	0.18	1	0.03	0.01	0.01	0.02
a5	0	0.02	0.01	0.01	0	0.01	-0.02	0.03	1	0	0	0
T5	0	0.01	0.01	0.01	0	0.01	-0.02	0.01	0	1	0	0
a6	0	0.01	0.01	0	0	0	-0.01	0.01	0	0	1	0
T6	0	0.01	0.01	0.01	0	0	-0.01	0.02	0	0	0	1

## Conclusion

Measurements of the time dependence of delayed neutron intensity after the fission of  $^{236}\text{U}$  by neutrons with energies from 14.23 to 17.98 MeV have been done for the first time. Obtained decay curves have been corrected for the effects that affect to its shape inevitably when reaction  $\text{T}(d,n)^4\text{He}$  is using as a neutron source. Using the least square technique on the basis of result dependences the time parameters of delayed neutrons have been obtained for any energy of primary neutrons. Energy dependence of the average half-life is calculated on the basis of the obtained time parameters.

## References

1. A. D'Angelo, An international cooperation to improve delayed neutron data, Progress in Nuclear Energy, Vol. **41**, No. 1–4, pp. 1–3, 2002.
2. V. Valkovic, 14 MeV Neutrons, Physics and application, CRC Press, 2014.
3. V.E. Murshalkin, V.M. Povyshv, Natural transmutation of the actinides by the fission reaction in the closed thorium-uranium-plutonium fuel cycle, VANT: Nuclear reactor physics series, V. **4**, 2016.
4. K.B. Denisevich, U.A. Landau, V.A. Neiman, V.N. Suleymanov, B.A. Shilyaev, The development of atomic energy and integrated power systems, Kiev: [w.o. p.], 2005.
5. <http://www.ortec-online.com/download/428.pdf> (application data 04.06.19).
6. V.M. Pikaikin, L.E. Kazakov, S.G. Isaev, M.Z. Tarasko, V.A. Roshchenko, R.G. Tertychnyi, G.D. Springs, J.M. Campbell, Energy dependence of relative abundances and periods of delayed neutrons from neutron-induced fission of  $^{235}\text{U}$ ,  $^{238}\text{U}$ ,  $^{239}\text{Pu}$  in 6- and 8-group model representation, Prog. Nucl. Energy, **41** (1–4), 203–222, 2002a.

# Dependence of the ROT Effect on the Energy of Light Charged Particles and on the Incident Neutron Energy

Irina Guseva<sup>1</sup>, Alexei Gagarski<sup>1</sup>, Friedrich Gönnerwein<sup>2</sup>, Yuri Gusev<sup>1</sup>

<sup>1</sup>*Petersburg Nuclear Physics Institute of National Research Centre “Kurchatov Institute”, 188300 Gatchina, Russia*

<sup>2</sup>*Physikalisches Institut, Universität Tübingen, D-72076 Tübingen, Germany*

**Abstract.** The shift of the angular distribution of different light charged particles in ternary fission of  $^{235}\text{U}$  induced by cold polarized neutrons was estimated by modified trajectory calculations, which take into account the rotation of the compound nucleus. In previous publications only  $\alpha$ -particles were considered. It was shown here that the inclusion of tritons significantly improves the agreement of the energy dependence of the ROT effect with experiment while the involvement of  $^3\text{He}$  particles practically did not influence this dependence. The change in the magnitude of the ROT effect depending on the energy of the incident neutrons is predicted. The ROT effect for gamma quanta and neutrons in binary fission is discussed along the same lines, because all mentioned effects are proportional to the effective angular velocity of the compound nucleus at the moment of scission.

## 1 Introduction

The ROT effect was discovered in 2005. It corresponds to a shift of the angular distribution of light charged particles (LCPs), mainly alphas, which was observed in ternary fission of  $^{235}\text{U}$  induced by cold polarized neutrons [1, 2]. It was assumed that this experimentally detected shift of the angular distribution is associated with the presence of rotational states in the level structure of the deformed compound nucleus. The validity of such hypothesis was confirmed by Monte Carlo calculations [3, 4]. The rotational structure was known for a long time [5] but usually the rotations of different compound nuclei are randomly oriented in space and cannot influence on the angular distribution of ternary particles, namely on their shift. Without a general orientation of rotation in space the mentioned shift cannot be seen in ternary fission experiments. The required result can arise only due to the spin polarization of the compound nucleus. Using spin-flip of a polarized neutron beam it is possible to observe the shift of the LCPs angular distribution doubled. This is the ROT effect phenomenon which is evaluated and reported.

## 2 Experimental technique and data analysis

In Figure 1 is shown the scheme of the experimental setup for the measurements being discussed. The longitudinally polarized neutron beam was hitting the fissile target  $^{235}\text{U}$  mounted at the center of a reaction chamber. Detectors for fission fragments (FFs) and LCPs were installed in a plane perpendicular to the neutron beam.

We presume that the ROT effect mostly develops after the rupture of the nucleus when nuclear forces have ceased to be of importance and cannot significantly affect trajectories of FFs and LCPs flying apart. The ROT phenomenon then emerges due to the motion of charged objects in the rotating field of Coulomb forces between fission fragments and LCPs.

The time dependence of the motion for two fission fragments and a ternary particle due to their mutual Coulomb interaction can be reproduced using Monte Carlo simulations [3, 4]. To start, it is necessary to perform calculations without any rotation of the fissile system [6].

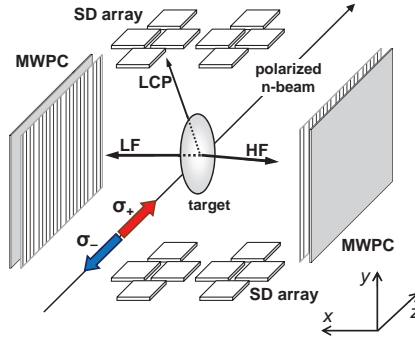


**Fig.1:** Scheme of experimental setup: two multiwire proportional counters (MWPC) facing each other to the left and right of the target intercept fission fragments. Light charged particles are measured by two arrays of up to twelve Si detectors on the top and bottom of the target.

Since the particle trajectories cannot be calculated in closed analytical form, it is necessary to replace the differential equations of motion

$$\frac{dX_{ij}}{dt} = V_{ij}, \quad m_i \frac{dV_{ij}}{dt} = F_{ij} \quad (1)$$

by a set of difference equations

$$X_{ij}^{n+1} = X_{ij}^n + \tilde{V}_{ij}^n \Delta t, \quad V_{ij}^{n+1} = \tilde{V}_{ij}^n + \frac{1}{2m_i} F_{ij}^n \Delta t, \quad (2)$$

where

$$\tilde{V}_{ij}^n = V_{ij}^n + \frac{1}{2m_i} F_{ij}^n \Delta t. \quad (3)$$

Here  $n$  is the number of iterative step, the subscript  $i$  denotes the particle with masse  $m_i$ , while  $j$  corresponds to the component index for the coordinates  $X_{ij}$ , velocity  $V_{ij}$  and force  $F_{ij}$  acting on this particle.

By iterations, the time dependence of coordinates for fission fragments and LCP are found step by step.

Such standard trajectory calculations are commonly applied to describe spontaneous ternary fission or ternary fission induced by unpolarized neutrons [7, 8]. Our goal at this first stage of calculations is to find parameters of the nuclear system at a moment close to its rupture. It is necessary to determine mass distributions of FFs, positions of all partners with respect to the center of mass and initial velocity distributions of FFs and LCP. In the case of correctly fitted initial parameters of the considered system, the calculated final distributions for fission fragments and light charge particles should coincide with those that were experimentally recorded for a non-rotating fission system, in our case for ternary fission induced by unpolarized neutrons.

Determining the initial configuration of a nuclear system allows us to evaluate its moment of inertia right at the time of the nucleus scission.

Then the initial angular velocity is calculated as the ratio of the mean value of the compound nucleus spin projection onto the axis of neutron beam polarization to the moment of inertia  $\mathfrak{I}$ :

$$\omega(J, K) = \langle J_z(K) \rangle / \mathfrak{I}. \quad (4)$$

In the process of nuclear fission induced by slow polarized neutrons two spins of the compound nucleus may appear. They are equal to  $J_+=I+1/2$  and  $J_-=I-1/2$ , where  $I$  is the spin of the target nucleus.

The partial angular velocities, in addition to the moment of inertia, depend on these spins, their projection  $K_{+/-}$  onto the fission axis, and on neutron beam polarization  $p_n$  [9]:

$$\omega_{+/-}(J, K) = \begin{cases} + \frac{J_+(J_+ + 1) - K_+^2}{J_+} \cdot \frac{\hbar}{2\mathfrak{I}} \cdot p_n \\ - \frac{J_-(J_- + 1) - K_-^2}{(J_- + 1)} \cdot \frac{\hbar}{2\mathfrak{I}} \cdot p_n \end{cases} \quad (5)$$

The different signs of the angular velocities for  $J_+$  and  $J_-$  indicate opposite directions of rotation of the fissile system.

The ROT effect, observed as the double shift  $2\Delta$  in the angular distribution of ternary particles, is proportional to the initial effective angular velocity. This velocity is the sum of the two partial angular velocities with coefficients depending on the partial fission cross sections associated with two possible spins of the compound nucleus.

$$\omega_{eff} = \omega_+(J_+, K_+) \frac{\sigma_f(J_+)}{\sigma_f(J_+) + \sigma_f(J_-)} + \omega_-(J_-, K_-) \frac{\sigma_f(J_-)}{\sigma_f(J_+) + \sigma_f(J_-)} \quad (6)$$

Based on this effective angular velocity, one can proceed to the second stage of trajectory calculations. In the case of a rotating nuclear system it is only necessary to modify the initial velocities of the described objects, namely, to take into account their additional components due to the rotation of the fissioning system around the z-axis in Figure 1. With spin-flip of the polarized neutron beam, these calculations must be performed twice. The following iterative steps of the calculations are no different from the standard method. Finally, one has to recalculate all distributions depending on  $(J, K)$  on the basis of these modified trajectory calculations.

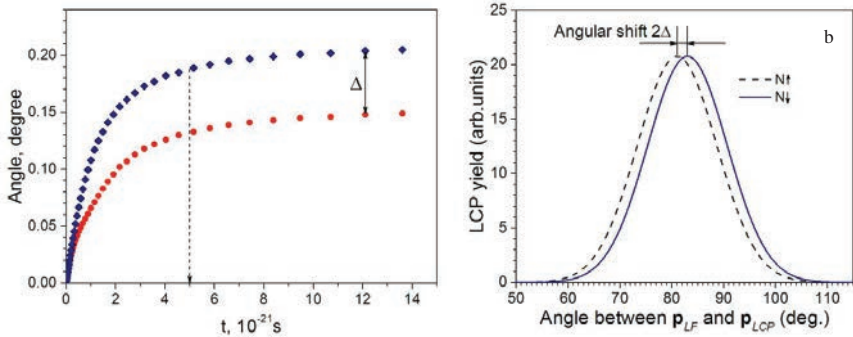


**Fig.2.** a) Time dependencies of deflection angles  $\theta_\alpha$  for  $\alpha$ -particle (full dots) and  $\theta_{LF}$  for LF (rhombs).  $\Delta = \theta_{LF} - \theta_\alpha$ . Calculations were performed with  $\langle J_z \rangle = 1\hbar$ ,

b) Double shift  $2\Delta$  of the angular distribution of ternary particles in  $(n,f)$  reactions depending on the orientation of neutron spin inducing fission.  $N_\uparrow$  and  $N_\downarrow$  are emission rates for neutron spin parallel and antiparallel to  $(\mathbf{p}_{LF} \times \mathbf{p}_{LCP})$ , respectively.

As follows from the calculations (see Fig.2a), the rotational speed of the nuclear system after scission is variable. It depends on the moment of inertia of the fissile system at any given time. This rotation starts with a huge angular velocity. It reaches about  $10^{18}$  turns per second immediately after scission and tends to zero after about 5 zs.

As a result of the rapid decrease in the angular velocity, the fission fragments and the ternary particle can change their directions of motion only during a very short time. Then they move along straight lines. Already after a short time the angle of rotation of each object gets its final value. In other words, each object gets its final direction of motion leading to a detector for registration.

In experiment the angle of the  $\alpha$ -particle is measured relative to the final direction of motion of the light fragment. With the trajectory calculations it is shown that the  $\alpha$ -particle rotates somewhat slower than the fission fragments. This lag leads to the observed shift  $\Delta$  in the angular distribution of  $\alpha$ -particles. On account of the spin-flip technique, it is necessary to repeat the trajectory calculations where the sign of rotation of the fissile system is inverted.

The difference in the angular distributions of ternary particles corresponding to different signs of the neutron beam polarization gives the sought-for double shift  $2\Delta$  of the angular distributions, called the ROT effect (see Fig.2b).

To get the best fit for the experimental shift one can in the trajectory calculations only play with the spin projections  $K$  of the compound nucleus on the fission axis. These variations can be implemented in the small range from  $K = 0$  to  $K = J$ .

### 3 Results of calculations

For the reaction  $^{235}\text{U}(n,f)$  induced by cold neutrons it was concluded that combinations  $(J, K)$  of the nucleus spin and its projection  $(J_+, K_+) = (4, 0)$  and  $(J_-, K_-) = (3, 2)$  dominate. Originally these calculations were performed only with alphas as the third particle since they dominate in ternary fission. The evaluated angular shift averaged over the energy of  $\alpha$ -particles was in good agreement with experiment, but the detailed distribution of the calculated ROT-effect values depending on the energy of ternary particles deviated from the experimental data. The experimental angular shift was larger than the calculated result in the low energy range from 8 to 13 MeV of the  $\alpha$ -particle (see Fig.15 in [2]).

Experiments were performed without precise identification of the ternary particle type. The above deviations can be explained by the presence of other ternary particles besides alphas. The second most important LCP yield is for tritons contributing about 7% to the total LCP yield. Including tritons in the calculations gave a much better approach to experiment. Results were presented in [10].

However, at closer inspection  $\alpha$ -particles observed have two different sources. There are first "true"  $\alpha$ 's ejected right at scission and second there are  $\alpha$ 's from the decay of  $^5\text{He}$  providing a sizable contribution to ternary fission. Therefore, it was decided to start a new version of trajectory calculations taking into account also the  $^5\text{He}$  isotope. We relied on reference [11]. The authors of this paper studied the LCP yields in the spontaneous fission of  $^{252}\text{Cf}$ . They found that in addition to "true" ternary  $\alpha$ -particles about 20% of  $\alpha$ 's in the spectrum are due to disintegrations of  $^5\text{He}$  into an  $\alpha$ -particle and a neutron. The contribution of  $\alpha$ 's from  $^5\text{He}$  decay should also be present in neutron induced fission. Due to the lack of experimental data it was assumed that the fraction of emitted  $^5\text{He}$  particles and their energy distribution in ternary fission of  $^{235}\text{U}(n,f)$  are close to the corresponding data for  $^{252}\text{Cf}(sf)$  in Table 1.

Evidently it was necessary to take into account that the lifetime of  $^5\text{He}$  is very short. It equals approximately  $1 \times 10^{-21}$  s. This isotope rapidly decays into  $^4\text{He}$  and a neutron. In addition, the smaller energies of residual  $^4\text{He}$  from  $^5\text{He}$  decay could affect the energy

dependence of the ROT effect. The energy dependent ROT effect was studied separately for the 3 isotopes at issue.

**Table 1.** Experimentally obtained energy distributions of LCP for spontaneous fission of  $^{252}\text{Cf}(\text{sf})$  [11].

LCP	$\langle E \rangle$	FWHM
$^4\text{He}$	15.7(2)	10.9(2)
true $^4\text{He}$	16.4(3)	10.3(3)
residues from $^5\text{He}$	12.4(3)	8.9(5)

Figure 3 shows the energy distributions for tritons, true  $\alpha$ -particles and  $^5\text{He}$ , which were obtained using standard trajectory calculations reproducing the known average energies. The initial parameters of the system undergoing fission were chosen suitable to reproduce the energy distributions of ternary particles in the spontaneous fission of  $^{252}\text{Cf}$ . The yields of emitted particles were taken from experimental data for neutron induced fission of  $^{235}\text{U}$  and evaluations in the paper [11].

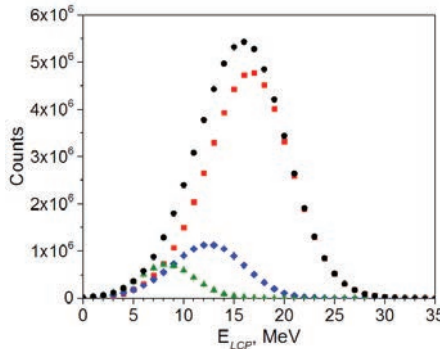


**Fig.3.** The calculated LCPs energy distributions: for  $^3\text{H}$  (triangles), for true  $\alpha$ -particles (squares), for  $^5\text{He}$ , which turns into  $\alpha$ -particle plus a neutron (rhombs), and for the sum of true and residual  $\alpha$ -particles (full dots).

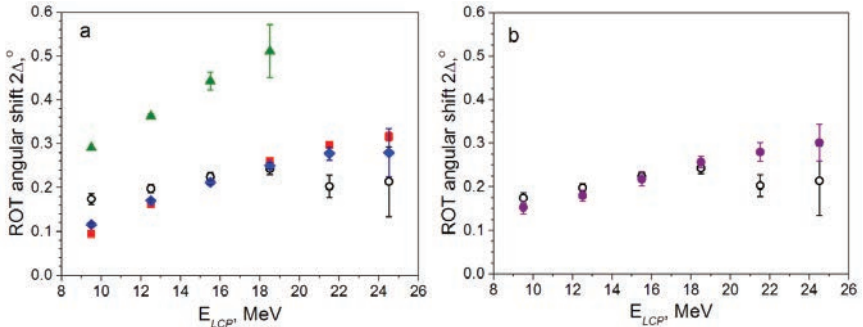


**Fig.4.** a) The calculated ROT effect for  $^3\text{H}$  (triangles), true  $^4\text{He}$  (squares),  $^5\text{He}$ , which decays into an  $\alpha$ -particle and a neutron (rhombs) and experimental data (open dots); b) the calculated ROT effect for the sum of all LCP components added with their corresponding weights (full dots) in comparison with experimental data (open dots).

Based on the starting parameters the effective angular velocities were calculated independently for the 3 isotopes. From trajectory calculations the angular shifts for tritons, true alpha particles, and the  $^5\text{He}$  isotope were evaluated as a function of LCP energy.

It should be stressed that, in particular at small LCP energies, the inclusion of tritons as LCP's gives a significant contribution to the energy dependence of the ROT effect and improves agreement with experiment. In contrast, the inclusion of  $^5\text{He}$  has virtually no influence on the model prediction of the energy-dependent ROT effect. But it should be pointed out that, in the high energy tail of the LCP distribution, the present model of the ROT effect does not perfectly match the experimental findings, though experimental errors in this energy region are large. Averaged over LCP energies the ROT effect amounts to  $2\Delta = 0.215^\circ$  for neutron induced fission of  $^{235}\text{U}$ . It is a tiny effect which is safely assessed by the spin flip technique.

#### 4 Dependence of the ROT effect on the incident neutron energy

As discussed in connection with eq. (5), the rotational speeds for the two possible spins of the  $^{236}\text{U}^*$  compound nucleus,  $J_+=4$  and  $J_- = 3$  have different signs. Both contribute to the effective angular velocity  $\omega_{eff}$  in eq. (6) as the start velocity for trajectory calculations and ensuing ROT effects. But the sign and size of the effective angular velocity and, therefore, the sign and magnitude of the ROT effect also depend on the partial fission cross-sections, more precisely, on their ratio. This ratio varies with the energy of the incident neutron.

The energy dependence of the spin-separated fission cross sections for neutron induced fission of  $^{235}\text{U}$  were calculated by the computer code SAMMY. The figure 5 shows two curves for the partial fission cross sections and their sum for the target of  $^{235}\text{U}$  as a function of incoming neutron energy. In these calculations the data of resonance parameters were taken from ENDF/B-VIII.0 (USA, 2018) [12].

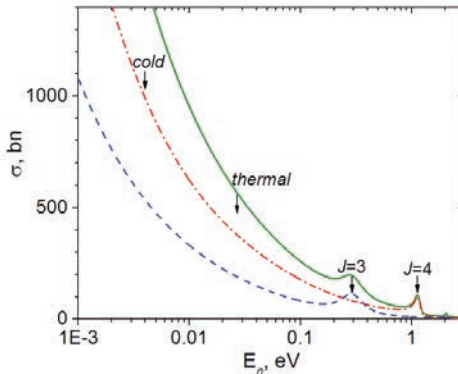


**Fig.5.** Spin-separated fission cross sections for the target of  $^{235}\text{U}$  depending on the energy of the incident neutron: dashed line for  $J=3$ , dash-dotted line for  $J=4$ , solid line corresponds to the sum of both.

Experiments in ternary fission were performed in the energy region of cold neutrons. Here, the partial fission cross section for  $J=4$  is approximately 2 times larger than the corresponding value for  $J=3$ . Furthermore, as follows from eq.(5), the positive partial angular velocity  $\omega_+$  of the state  $(J_+, K_+) = (4, 0)$  exceeds in absolute value the negative rotational speed  $\omega_-$  of the compound state  $(J_-, K_-) = (3, 2)$ . As a result, we get in this region a positive and sizable value of the ROT effect.

Practically the same results should be expected for thermal neutrons. Closer to the resonance at  $E_n=0.3$  eV the situation is different. The spin of this resonance is defined as  $J=3$ . Although at its top the partial fission cross section is slightly larger than the value corresponding to spin  $J=4$ , the rotation in the positive direction continues to dominate due to the significant larger absolute value of the positive partial angular velocity  $\omega_+$  compared to the negative velocity  $\omega_-$ . As a result, the sign of the ROT effect remains also here positive, but its size becomes two times less than for thermal or cold neutrons. For the resonance region near 1 eV, on the contrary, we can expect an increase in the ROT effect compared to the cold or thermal region by a factor 2.3.

Experiments for ROT effect in ternary fission beyond thermal neutron energies have not yet been staged. It should be interesting to see whether the above predictions are confirmed.

## 5 Summary and Outlook

In the present semi-classical interpretation of the ROT effect, the main cause of the shift in the angular distribution of light charged particles observed in the ternary fission induced by polarized neutrons is the interaction of charged objects when they move in a rotating Coulomb field. It is especially important to take into account the development of this phenomenon in time, namely, that the angular velocity very quickly tends to zero. If case the angular velocity would remain constant for a long period of time, no experiments of this type could have predictable results, since this would lead to a dependence of the magnitude of the effect on the distance between the detectors and the target.

The evolution in time of the motion of three charged objects in a Coulomb field can well be described classically. The quantum-mechanical aspect of the ROT effect phenomenon is represented by the initial angular velocity  $\omega_{eff}$ . Moreover, using the values of partial fission cross sections calculated by the computer code SAMMY based on the most recent Nuclear Data Files, the interference of  $s$ -resonances with the same spins is duly described.

The need to take into account the interference of  $s$ -resonances with different spins, on which the authors [13, 14] insist to describe the ROT effect, cannot be considered proven. Justifying the correctness of their approach, they do not perform real calculations in accordance with their formulas, but simply fitted the corresponding coefficients to the experimental ones. In these calculations, the resonance parameters are not used at all, not to mention the interference between them.

In contrast to the authors of [13, 14], we obtained real parameters of  $s$ -resonances from the Evaluated Nuclear Data File in a fairly wide energy range and used them to correctly calculate spin-separated fission cross sections. We need them in order to determine the ratio of rotations of compound-nuclei in two opposite directions. In addition, we can quite adequately estimate the moment of inertia of the fissile system from the point of its rupture to the end of rotation, which the authors [13, 14] do not have. They do not at all follow the change in time of the size of the rotating system, which is characterized by the distances between interacting charged objects and determines the moment of inertia of interest to us, as well as the change in their kinematic parameters.

Our evaluation of the magnitude of the ROT effect occurs independently of the experimental results and only after performance of calculations are these values compared.

As was shown, the result of our calculations for the magnitude and sign of the ROT effect are in good agreement with experimental data, both averaged over the energy of LCPs as well as their detailed LCP energy dependence.

At present, all measurements of the ROT effect in ternary fission are carried out only at incident neutrons from the cold energy region. To test our predictions about the dependence of the ROT effect on the neutron energy, it should be of great interest to measure this effect at neighboring  $s$ -resonances.

Finally, it should be noted that this predicted energy dependence is also valid for the ROT effect for neutrons and gammas in binary fission, because these effects are likewise proportional to the effective angular velocity of the compound nucleus at the moment of scission. These conclusions can be tested by comparing the ROT effect values obtained experimentally in the resonance region [15] with corresponding results for nuclear fission induced by thermal neutrons [16, 17]. Although the accuracy of determining the magnitude of the ROT effect for  $\gamma$ -rays  $(6.5 \pm 3.9) \cdot 10^{-5}$  in the resonance region with neutron energy about  $E_n=0.3$  eV is not very high, nevertheless, it can be argued that this value of the angular asymmetry in comparison with the corresponding result  $(16.6 \pm 1.6) \cdot 10^{-5}$ , which was obtained in the thermal region, is approximately 2.5 times less, i.e. consistent with the energy dependence of the ROT effect predicted here.

We did not use the ROT asymmetry data for neutrons from [15] because the angular dependence used in this paper to fit the corresponding experimental results was incorrect. The correct form of the angular behavior of ROT asymmetry for neutrons is presented in [18].

## References

- [1] F. Gönnerwein, M. Mutterer, A. Gagarski, I. Guseva, G. Petrov, V. Sokolov, T. Zavarukhina, Yu. Gusev, J. von Kalben, V. Nesvizhevski, and T. Soldner, *Phys. Lett. B* **652**, 13 (2007).
- [2] A. Gagarski, F. Gönnerwein, I. Guseva, et al., *Phys. Rev. C* **93**, 054619 (2016).
- [3] I. S. Guseva and Yu. I. Gusev, *Bull. Russ. Acad. Sci., Phys. Ser.* **71**, 367 (2007).
- [4] I. Guseva and Yu. Gusev, *AIP Conf. Proc.* **1175**, 355 (2009).
- [5] A. Bohr and B. R. Mottelson, *Nuclear Structure, vol. 2: Nuclear Deformations* (W.A. Benjamin, New York, Amsterdam, 1974; Mir, Moscow, 1977).
- [6] Y. Bohne, Z. Fraenkel and I. Nebenzahl, *Phys. Rev.* **156**, 1305 (1967).
- [7] M. Borkovski, Yu. Gusev, Yu. Zalite, D. Seliverstov, *Proceedings of the 18th International Symp. on Nucl. Physics, Physics and Chemistry of Fission, Gaussig, 1988*, pp. 181.
- [8] W. Baum, PhD Thesis, Institute für Kernphysik, TH Darmstadt, 1992.
- [9] V. E. Bunakov and S. G. Kadmsky, *Phys. At. Nucl.* **71**, 1200 (2008).
- [10] I. Guseva, A. Gagarski, F. Gönnerwein, Yu. Gusev, *Proceedings of the XXV International Seminar on Interaction of Neutrons with Nuclei, Dubna, May 22-26, 2017, JINR, E3-2018-12 (Dubna, Russia, 2018)*, p. 355.
- [11] Yu. N. Kopatch, M. Mutterer, D. Schwalm, P. Thirolf, and F. Gönnerwein, *Phys. Rev. C* **65**, 044614, (2002).
- [12] D.A. Brown, M.B. Chadwick, R. Capote, A.C. Kahler, A. Trkov, M.W. Herman, A.A. Sonzogni, Y. Danon, A.D. Carlson, M. Dunn et al., *Nucl. Data Sheets*, **148**, (2018).
- [13] S.G. Kadmsky, V.E. Bunakov, and D.E. Lyubashevsky, *Bull. Russ. Acad. Sci. Phys.* **83**, 1128 (2019).
- [14] S.G. Kadmsky, D.E. Lyubashevsky, and P.V. Kostryukov, *Phys. At. Nucl.* **82**, 267 (2019).
- [15] Yu. Kopatch, V. Novitsky, G. Ahmadov, A. Gagarsky, D. Berikov, G. Danilyan, V. Hutannu, J. Klenke, and S. Masalovich, *EPJ Web of Conferences* 169, 00010 (2018), Theory-4.
- [16] G. Danilyan, V. Krakhotin, et al., *Phys. At. Nucl.*, **72**, 1812 (2009).
- [17] G.V. Valsky, A.M. Gagarski, I.S. Guseva, et al., *Bull. Russ. Acad. Sci. Phys.* **74**, 767 (2010).
- [18] I.S. Guseva, *Proceedings of the XVIII International Seminar on Interaction of Neutrons with Nuclei, Dubna, May 26-29, 2010, JINR, E3-2011-26 (Dubna, Russia, 2011)*, p.84.

# MEASUREMENT OF GAMMA AND NEUTRON ROT-EFFECTS IN 0.3 eV RESONANCE OF $^{235}\text{U}$ AT A HOT SOURCE OF POLARIZED NEUTRONS

Yu.N. Kopatch<sup>1</sup>, V.V. Novitsky<sup>1,2</sup>, G.S. Ahmadov<sup>1,6</sup>, A.M. Gagarsky<sup>3</sup>, D.B. Berikov<sup>1,7</sup>,  
K.Sh. Zhumadilov<sup>7</sup>, G.V. Danilyan<sup>1,2</sup>, V. Hutanu<sup>4</sup>, J. Klenke<sup>5</sup>, S. Masalovich<sup>5</sup>

<sup>1</sup>Joint Institute for Nuclear Research, 141980 Dubna, Russia

<sup>2</sup>Institute for Theoretical and Experimental Physics of National Research Centre "Kurchatov Institute",  
117218 Moscow, Russia

<sup>3</sup>Petersburg Nuclear Physics Institute of National Research Centre "Kurchatov Institute", 188300  
Gatchina, Russia

<sup>4</sup>Institut für Kristallographie, RWTH Aachen and Jülich Centre for Neutron Science at Heinz Maier-  
Leibnitz Zentrum (MLZ), Lichtenbergstr. 1, 85748 Garching, Germany

<sup>5</sup>Forschungs-Neutronenquelle Heinz Maier-Leibnitz, D-85747 Garching, Germany

<sup>6</sup>National Nuclear Research Centre, Baku, Azerbaijan

<sup>7</sup>L.N. Gumilyov Eurasian National University, 010000 Nur-Sultan, Kazakhstan

**Abstract.** The present paper describes the first attempt to get "clean" data by performing the measurement of gamma and neutron ROT-asymmetries in an isolated resonance of  $^{235}\text{U}$  at the POLI instrument of the FRM2 reactor in Garching. The measurement was performed in 0.3 eV resonance of  $^{235}\text{U}$  at a hot source of polarized neutrons. Thin low-pressure multiwire proportional counters (LPMWPC) were used as fission fragment detectors, being placed on two sides of  $^{235}\text{U}$  target at a distance of  $\sim 3$  cm (start detector) and  $\sim 11$  cm (stop detector). In order to register gamma rays and neutron, the fission chamber was surrounded by 8 plastic (for both gamma rays and neutron) and 4 NaI scintillation detectors (for gamma rays) placed at different angles with respect to the fission detector. The statistic was accumulated during 30 days. The analysis of collected events showed that gamma and neutron asymmetries in 0.3 eV resonance energy of  $^{235}\text{U}$  were definitely smaller than that in the cold neutron induced fission.

## 1. Introduction

The search for the T-odd asymmetries in the angular distributions of the products in ternary fission of heavy nuclei induced by cold polarized neutrons began in the last years of the 20th century. The aim was that to discover the effects of T-invariance violation in nuclear fission processes (following the idea, proposed in [1]), by analyzing 3-fold angular correlation between fission fragments, neutron spin (polarization) and ternary particle in ternary fission. Although the effect was discovered, the observed asymmetry could not be an indisputable evidence of time-invariance violation. The reason is related to the significant influence of the interaction between fission products in final states and the interference of reaction amplitudes related to neighboring compound states. The result of these investigations by now has been the discovery of T-odd asymmetries of the TRI and ROT types in the ternary fission of a number of actinide nuclei with the emission as a third particles of both charged particles,  $\alpha$  particles and tritons, and neutral particles, neutrons and  $\gamma$ -quanta. Both, TRI and ROT effects are formally T-odd, but have no direct connection with the violation of the time reversal invariance.

At present, there are several theoretical models, which can describe both effects [2–7]. According to the model, proposed in [7], both effects depend on the quantum numbers J and

K (the total angular momentum and its projection on the deformation axis), which characterize the fission channel. For the thermal (or cold) neutron induced fission (where all previous data are obtained), there is a mixture of several spin states, and the weights of these states are not known. The only way to get "clean" data is to perform measurements in isolated resonances. Such an experiment was performed at the POLI instrument of the FRM2 reactor in Garching, which provides the necessary polarized neutron beam with the energy of 0.27 eV, corresponding to the lowest resonance of  $^{235}\text{U}$ . Preliminary results of this experiment are presented in this paper.

## 2. Experiment

We used the polarized hot neutron beam provided by the POLI instrument [8] at the FRM-II reactor in Garching. In the POLI instruments, a monochromator made of a mosaic of Cu crystals was used to select a narrow neutron beam with the mean energy of 270 meV ( $\lambda=0.55 \text{ \AA}$ ). This energy exactly coincides with the position of the lowest resonance of  $^{235}\text{U}$  [9]. The monochromator also allows simultaneous focusing of the neutron beam on the target position providing the maximum intensity of unpolarized neutrons of about  $4 \cdot 10^6 \text{ n/cm}^2/\text{sec}$ . Detailed description of the POLI instruments was given [10].

The neutrons were polarized using specially designed  $^3\text{He}$  gas cells [11]. The same type of cell was also used as analyzer for measuring beam polarization. Since polarized nuclei of  $^3\text{He}$  possess very high spin-dependent neutron absorption efficiency over a wide range of energies, the  $^3\text{He}$  cell can be used as a broadband neutron polariser or analyser, with the possibility to optimise its efficiency for nearly all neutron wavelengths. In our experiment, the size of the cells was  $\text{\O}60 \times 130 \text{ mm}$  and the gas pressure 2.5 bar (0.25 MPa), which provided the maximal neutron polarization of about 70% (fig. 1). The polarizer and analyzer cells were polarized in an external lab and placed into a special magnetic housing with highly homogeneous constant magnetic field. The polarization of  $^3\text{He}$  in the cell exponentially decreased with the time constant of about 40 hours, therefore both cells were replaced every 24 hours.

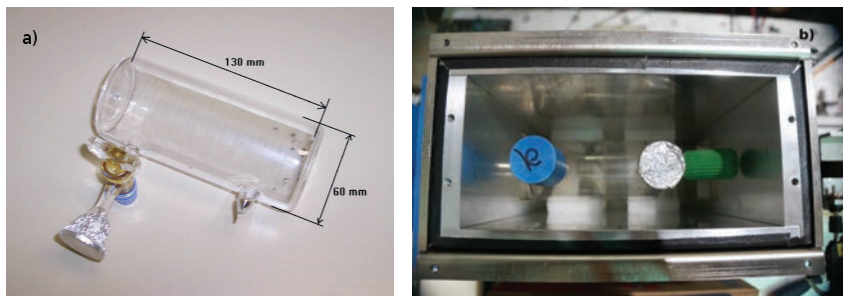


Fig. 1. Spin filter cell, made of fused silica. a) General view of the cell; b) inside of magnetic housing.

The polarization of the incoming beam is determined by the transmission measurement of the  $^3\text{He}$  cells using two beam monitors. The general formulas that describe the transmittance  $T$  of a spin-filter for an incident unpolarized monochromatic neutron beam and neutron polarization  $P$  after passing through the cell with a polarized  $^3\text{He}$  gas can be written as:

$$T = T_0 \cdot e^{-\eta} \cdot \cosh(\eta P_{\text{He}}), \quad (1)$$

$$P = \tanh(\eta P_{\text{He}}). \quad (2)$$

Here  $T_0$  is a neutron beam transmission measured for an evacuated  $^3\text{He}$  cell and  $P_{\text{He}}$  the polarization of the  $^3\text{He}$  gas used. The parameter  $\eta$  defines a filter opacity related directly to the  $\sigma_0$ ,  $\sigma_p$ ,  $N$  and  $d$ , where  $N$  is the number of atoms per unit volume,  $d$  is the filter thickness,  $\sigma_0$  is the spin-independent part of the total cross-section and  $\sigma_p$  is the so-called polarization cross-section. For practical purposes the value of the opacity of the  $^3\text{He}$  gas at room temperature can be estimated using the relation

$$\eta = 7.32 \cdot 10^{-2} \cdot p(\text{bar}) \cdot d(\text{cm}) \cdot \lambda(\text{\AA}), \quad (3)$$

where  $p$  is the gas pressure,  $d$  is the neutron path length in the gas and  $\lambda$  is the neutron wavelength. For clarity, the dependence of the transmission and the degree of polarization of neutrons on the degree of polarization of the  $^3\text{He}$  from equations (1–2) are plotted in fig. 2.

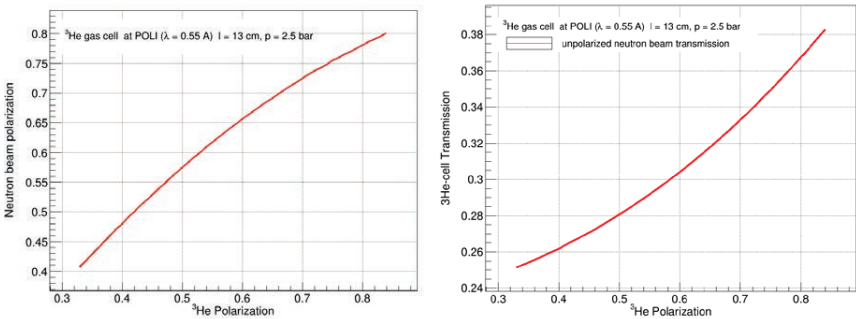


Fig. 2. Dependence of the transmission and the degree of polarization of neutrons on the degree of polarization of the  $^3\text{He}$ .

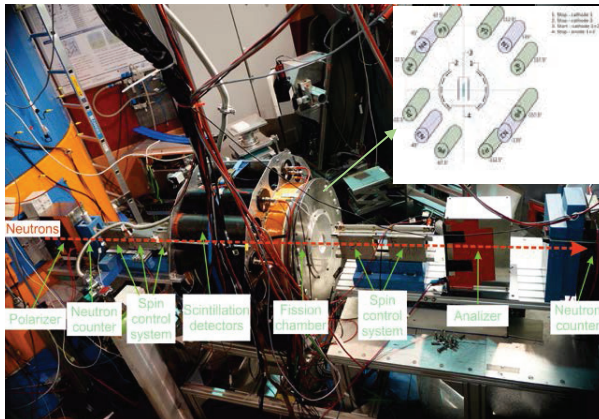


Fig. 3. The photograph of the experimental setup and the schematic drawing of fission chamber (upper right and view from the beam direction).

Both, polarizer and analyzer provided vertical polarization of the neutron beam while the searched effect requires horizontal (longitudinal) polarization. For changing the polarization direction from vertical to horizontal, a specially designed spin control system was used, consisting of several  $\mu$ -metal shielded magnetic coils, which allowed also flipping the spin at the target position by 180 degrees every 1.3 seconds.

The photograph of the experimental setup is shown in fig. 3. The schematic view (upper right) of the fission chamber surrounded by a set of gamma-ray detectors is illustrated in fig. 3 (upper right) too.

The chamber was filled with the  $\text{CF}_4$  gas at a pressure of about 10 mbar. A uranium target containing about 82 mg of  $^{235}\text{U}$  (99.99%) oxide-protioxide deposited on the two sides of a thick  $40 \times 100 \text{ mm}^2$  aluminium backing was arranged along the chamber axis. Thin low-pressure multiwire proportional counters (LPMWPC) were used as fission fragment detectors, being placed on two sides of the target at a distance of  $\sim 3$  cm (start detector) and  $\sim 11$  cm (stop detector) (fig. 4).

The chamber was filled with the  $\text{CF}_4$  gas at a pressure of about 10 mbar. A uranium target containing about 82 mg of  $^{235}\text{U}$  (99.99%) oxide-protioxide deposited on the two sides of a thick  $40 \times 100 \text{ mm}^2$  aluminium backing was arranged along the chamber axis. Thin low-pressure multiwire proportional counters (LPMWPC) were used as fission fragment detectors, being placed on two sides of the target at a distance of  $\sim 3$  cm (start detector) and  $\sim 11$  cm (stop detector) (fig. 4).

Basic advantages of LPMWPCs which make them very suitable for registration of heavy ions such as fission fragments (FFs) are the following: excellent timing characteristics, high efficiency, high transparency and low energy losses inside the detector, large surface area, high counting rate capability, good position resolution with proper signal readout, long term stability. The table below contains typical parameters of LPMWPCs:

Table 1: Typical parameters of LPMWPC

Working pressure	$\sim 0.1\text{--}10$ mbar
Counting gases	isobutane, heptane, ethylene
Anode–cathode gap	$\sim 1.6\text{--}3.2$ mm
Anode wire spacing	$\sim 1$ mm
Anode wire diameter	$\sim 10\text{--}25$ $\mu\text{m}$
Reduced electric field in the constant field region	$\sim 10^2\text{--}10^3$ V/(cm· mb)
Reduced electric field on the wire surface	$\sim 10^4\text{--}10^5$ V/(cm· mb)
Total gas amplification	$\sim 10^4\text{--}10^6$
Amplification on the wires	$\sim 10^1\text{--}10^3$
Signal current pulses rise time	$\sim 2\text{--}5$ ns
Timing resolution	$\sim 0.1\text{--}1$ ns

The fission fragment detector consisted of two start detectors placed on both sides of the target and 10 stop detectors, 5 on each side of the target. They were used for measuring the fragment velocities (momenta). The start detectors were also used for measuring the time-of-flight of the gamma-rays and neutrons, which were detected by eight cylindrical plastic scintillators and four NaI(Tl) scintillators. They were inserted in a rotatable holder at a distance of about 30 cm from the target center that ensures subsequent measurements of coincidences of prompt fission gamma rays and neutrons with fission fragments at angles of

$\pm 22.5$ ,  $\pm 67.5$ ,  $\pm 112.5$  and  $\pm 157.5$  degrees with respect to the mean axis of the detection of fragments. The detectors of gamma rays and fission fragments were arranged in the plane orthogonal to the neutron beam direction, which also coincides with the axis of the polarization of  $^{236}\text{U}$  nuclei.

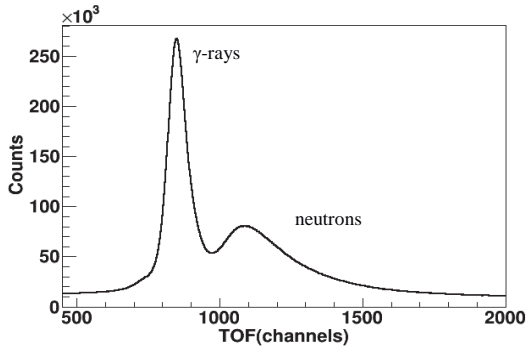


Fig. 5. Time-of-flight spectrum from one of the plastic detectors.

Prompt neutrons could be rather well separated from the prompt gamma-rays using the time-of-flight method (see fig. 5). Every event matching coincidence of the signals from the gamma/neutron and fragment detectors is digitized by a multichannel TDC CAEN V775N and stored together with the information about the direction of polarization of the neutron beam. A reversal of the polarization occurs at a frequency of 1.3 Hz, the input of the TDC being inhibited by the time of the neutron spin flip. At the same time, for the on-line control of the installation, the coincidence count rates of neutrons/ $\gamma$ -rays and the fission fragments were recorded by counters, which were read out every 5 min for each detector. The values of the asymmetries calculated by the formula:

$$R = (N^+ - N^-) / (N^+ + N^-) \quad (4)$$

were constantly monitored. Here  $N^+$  and  $N^-$  are the coincidence count rates for opposite directions of the neutron polarization. Simultaneously, the asymmetry of the fragment count rates was measured and controlled.

### 3. Results and discussion

Fig. 6 shows the anisotropy ratio  $R$  determined from the experimental data according to formula (4), for prompt gamma-rays (top) and neutrons (below), detected in coincidence with one of the fission fragments. The 16 points in the figure are 16 possible combinations of angles between the scintillators and the fragment detectors. At each point, events from different scintillators and fragment detectors, but having the same angles, are summed up. The angular dependence at first approximation can be fitted by the function  $F = A \cdot \sin(2\theta)$ , which is shown on the plots. The anisotropy parameter  $A$  could be determined from the fit and equals to  $A_\gamma = (-3.8 \pm 2.8) \cdot 10^{-5}$  for the  $\gamma$ -rays and  $A_n = (2.6 \pm 3.1) \cdot 10^{-5}$  for the neutrons,  $\chi^2/N$  being 0.87 and 0.96, respectively. These results can be compared to the corresponding values for  $^{235}\text{U}$

obtained with cold neutrons:  $A_\gamma = (-16.6 \pm 1.6) \cdot 10^{-5}$  (at 45 degrees) and  $A_n = (-21.2 \pm 2.5) \cdot 10^{-5}$  (at 22.5 degrees). It follows that the effect is definitely smaller than that in the induced fission.

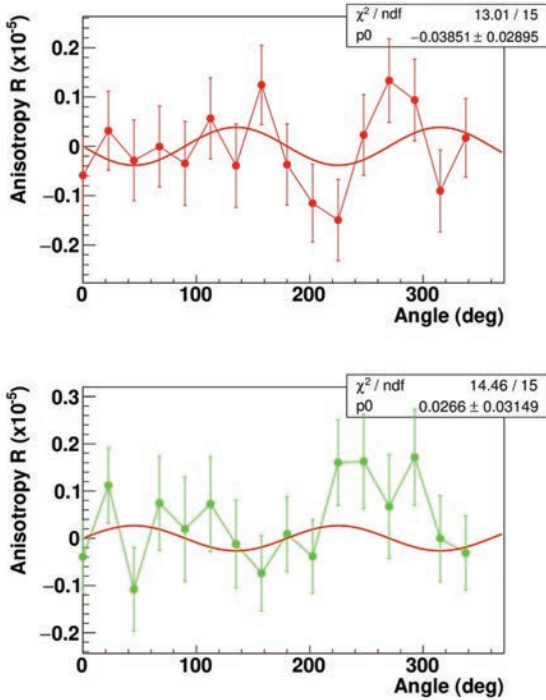


Fig. 6. Anisotropy ratio  $R$  as a function of angle for the gamma-rays (top) and neutrons (below).

It should be mentioned that the authors of [12], who developed one of the most comprehensive models of the TRI- and ROT-effects, predicted such a decrease of the anisotropy coefficient for the 0.27 eV resonance of  $^{235}\text{U}$ , based on the known contributions of the  $J=3$  and  $J=4$  partial cross sections for this nucleus and on the value of the most probable K-channel for these spins, derived from their work. Thus, the results of our experiment are in agreement with the most modern theoretical model prediction.

We believe that it is important to continue this type of experiments and extend the measurements to higher energies, e.g. to the 1.14 eV resonance where the effect should be larger than for cold neutrons and where practically only the  $J=4$  spin state is present.

### Acknowledgments

This work has been supported by the Russian Ministry for Science and Education, German Ministry for Education and Research BMBF through the project 05K13PA3. The instrument POLI is operated by RWTH Aachen in cooperation with JCMS FZ Jülich (Jülich

Aachen Research Alliance JARA). We're grateful to A. Sazonov, W. Luberstetter, and P. Stein for their help in setting up and conducting the experiment.

## References

1. K. Schreckenbach, J. van Klinken, and J. Last, Proceedings of the 2nd International Workshop on Time Reversal Invariance and Parity Violation in Neutron Reactions, Dubna, Russia, May 4–7, 1993, (World Scientific Publishing Company, Singapore, 1994), p. 187.
2. V.E. Bunakov and S.G. Kadmsky, Phys. At. Nucl. **66**, 1846 (2003).
3. V.E. Bunakov, S.G. Kadmsky, and S. S. Kadmsky, Phys. At. Nucl. **71**, 1887 (2008).
4. V.E. Bunakov and S.G. Kadmsky, Phys. At. Nucl. **74**, 1655 (2011).
5. A.L. Barabanov, in Proceedings of the IX International Seminar on Interaction of Neutrons with Nuclei, Dubna, May 23–26, 2001 (Dubna, Russia, 2001), p. 93.
6. A.L. Barabanov, Phys. Part. Nucl. Lett. **10**, 336 (2013).
7. A. Gagarski F. Goennenwein, I.Guseva et al., Phys. Rev. C **93**, 054619 (2016).
8. V. Hutanu, J. Large-Scale Res. Facil. 1, **A16** (2015).
9. L.C. Leal, G. de Saussure & R. B. Perez, Nuclear Science and Engineering Vol. **109**, Iss. 1, 1991.
10. <https://www.mlz-garching.de/poli>
11. V. Hutanu, M. Meven, S. Masalovich, G. Heger, and G. Roth, J. Phys.: Conf. Ser. 294, 012012 (2011).

# THE ROT-EFFECT IN THE ANGULAR DISTRIBUTION OF PROMPT $\gamma$ -RAYS IN BINARY FISSION INDUCED BY POLARIZED NEUTRONS WITH THE ENERGY OF 60 meV

Yu.N. Kopatch<sup>1,2</sup>, D.B. Berikov<sup>1,3</sup>, G.S. Ahmadov<sup>1,4,5</sup>, A.M. Gagarsky<sup>6</sup>,  
V.V. Novitsky<sup>1,2</sup>, G.V. Danilyan<sup>1,2</sup>, V. Hutanu<sup>7</sup>, S. Masalovich<sup>8</sup>, J. Klenke<sup>8</sup>,  
and H. Deng<sup>7</sup>

<sup>1</sup>Joint Institute for Nuclear Research, 141980 Dubna, Russia

<sup>2</sup>Institute for Theoretical and Experimental Physics of National Research Centre “Kurchatov Institute”, 117218 Moscow, Russia

<sup>3</sup>L.N.Gumilyov Eurasian National University, 010000 Nur-Sultan, Kazakhstan

<sup>4</sup>Azerbaijan National Academy of Sciences- CSSR and IRP, AZ1143 Baku, Azerbaijan

<sup>5</sup>National Nuclear Research Centre, Baku, Azerbaijan

<sup>6</sup>Petersburg Nuclear Physics Institute of National Research Centre “Kurchatov Institute”, 188300 Gatchina, Russia

<sup>7</sup>Institute of Crystallography, RWTH Aachen University and Julich Centre for Neutron Science at Heinz Maier-Leibnitz Zentrum (MLZ), 85748 Garching, Germany

<sup>8</sup>Heinz Maier-Leibnitz Zentrum (MLZ), Technical University of Munich, 85748 Garching, Germany

**Abstract.** The investigation of the ROT effect for the fissioning nuclei in the process has been continued at the FRM-II Munich reactor (Germany). The experiment with <sup>235</sup>U target was performed at a polarized monochromatic neutron beam with an energy of 60 meV provided by the POLI instrument, in order to figure out the dependence of the effect on the incident neutron energy. Up to now all measurements of the ROT effect were performed for the cold neutron induced fission, where several fission channels are mixed with unknown weights. The correlation coefficient for 60 meV neutrons was found to be  $A_\gamma = (1.25 \pm 0.31) \cdot 10^{-4}$ , which is compared with the corresponding values for <sup>235</sup>U, obtained with the cold neutrons:  $A_\gamma = (1.66 \pm 0.16) \cdot 10^{-4}$  (by the ITEP group).

## I. INTRODUCTION

The ROT-effect in the angular distributions of prompt  $\gamma$ -rays emitted from neutron induced fission was measured, which is expressed as the angular correlations between the spin of the incident neutron  $\sigma$ , momentum direction of the light (heavy) fission fragment (FF)  $p_f$  and the direction of the prompt fission  $\gamma$ -ray emission of the type:

$$W(\Omega) \sim 1 + R_\gamma \cdot \sigma \cdot [p_f \times p_\gamma].$$

The ROT-effect, which is formally T-odd effect, was measured for the first time in the emission of alpha particles in ternary fission of <sup>235</sup>U induced by cold polarized neutrons [1]. It was observed as a small rotation of the angular distribution of  $\alpha$ -particles from ternary fission relative to a plane formed by FF momentum and the neutron spin direction. This effect was explained in a semi-classical model as a result of the collective rotation of the fissile nucleus at the moment of its rupture and named as ROT-effect (from the rotation). Due to rotation of the fissioning system, fission fragments receive the orbital momentum, and the axis of fragment emission slightly rotates relative to the deformation axis of the nucleus at the moment of scission.

In ternary fission, the description of the ROT-effect of a fissile nucleus is complicated by the fact that the  $\alpha$ -particle emitted by the fissile nucleus at the moment of its rupture can also receive the orbital momentum. In addition, its motion is significantly affected by the electric field of the emitted fragments. All this leads to the fact that the ROT-effect in ternary fission is difficult to describe in the classical approximation, without involving model parameters and trajectory calculations. Existing quantum models [3-5] explain the presence of the ROT-effect, but not its magnitude.

Nevertheless, after the discovery of the ROT effect for  $\alpha$ -particles in ternary fission, it was clear that it can also manifest itself in the angular distribution of prompt  $\gamma$ -rays and neutrons accompanying the binary fission, where its theoretical description can be simpler. The ROT-effect for gamma-rays and neutrons is possible, because the angular distribution is anisotropic with respect to the deformation axis of the fissioning nucleus at the moment of scission, and the asymmetry with respect to the initial direction of the deformation axis is fully or partly conserved after the escape of the fragments to infinity. Indeed, a similar effect has been observed in the emission of prompt  $\gamma$ -rays and neutrons in fission of  $^{235}\text{U}$  and  $^{233}\text{U}$ , although its value was an order of magnitude smaller than in the  $\alpha$ -particle emission from ternary fission [6-8]. As for the ROT-effect in the angular distribution of  $\alpha$ -particles of ternary fission of  $^{235}\text{U}$  and  $^{233}\text{U}$  nuclei [2], the ROT-effect in the angular distribution of prompt  $\gamma$ -rays and neutrons for these two uranium isotopes was very different.

At present, there are several theoretical models which can describe the ROT-effect. These models use two fundamentally different approaches to the description, "classical" and "quantum". In the classical model, due to the impossibility of dividing the process of ternary fission into two consecutive stages, trajectory calculations are used. And quantum models at the moment suffer from a lack of predictive power.

Further study of the ROT-asymmetry in the angular distribution of prompt  $\gamma$ -rays and neutrons from fission may shed light on the question of the applicability of various models describing the ROT-asymmetry in the angular distribution of  $\alpha$ -particles from the ternary fission. At present, one of the main problems is to understand why two very similar uranium isotopes  $^{235}\text{U}$  and  $^{233}\text{U}$  exhibit a quite different behavior with respect to the effects of T-odd asymmetry in ternary fission. According to the authors of [4], the reason for this difference lies in the different phase factors of the interfering neighboring neutron resonances. In any case, it seems important to clarify this issue. Obviously, the most direct way to answer this question is to provide the measurement of Todd effects for isolated resonances with well-known spins.

The next problem is the dependence of the magnitude of the ROT-effect on the energy of neutrons causing the fission. The study of this dependence can help understanding such details of the fission mechanism as the transition of the nuclear polarization at the angular momentum of fission fragments. According to the model proposed in [10], the ROT-effect depends on the quantum numbers J and K (angular momentum and its projection on the deformation axis, respectively), which characterize the fission channels introduced by A. Bohr [9]. Up to now, all measurements of the T-odd effects were performed for the cold neutron induced fission, where several fission channels are mixed with unknown weights [10]. In order to disentangle different spin states and get "clean" data on the J and K channel-weights one can perform measurements with different incident neutron energies. The FRM-II reactor at MLZ in Garching with its unique hot neutron source provides an almost perfect instrumentation for such measurements.

## II. DESCRIPTION OF THE EXPERIMENT

The experiments on binary fission were carried out for (n, f) reactions with  $^{235}\text{U}$  as a target and a neutron beam from the POLI diffractometer at the FRM-II reactor at the Maier-Leibnitz Zentrum in Garching (Germany). The experimental setup shown below (Fig. 1) was similar to the previous experiment discussed in [11]. The main difference was the neutron polarizer. In the current experiment, the neutrons were polarized using in-situ SEOP (Spin Exchange Optical Pumping) polarizer [12]. The polarizer employs a high opacity  $^3\text{He}$  neutron spin filter with continuous  $^3\text{He}$  polarization provided by two laser array bars frequency narrowed by an ultra-compact volume Bragg grating. The degree of neutron beam polarization was close to 100 % and kept constant during the experiment.

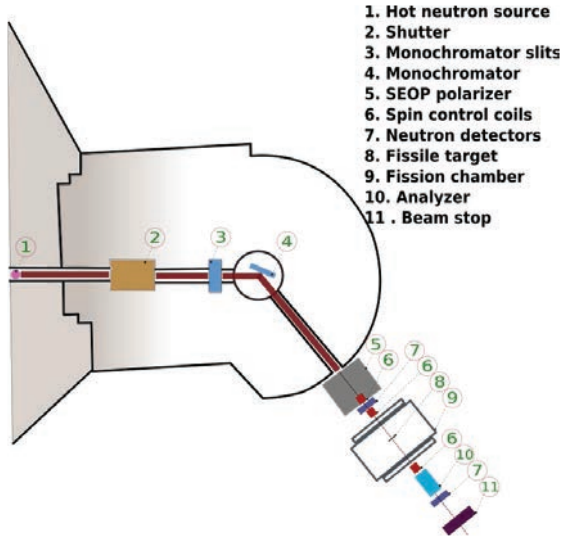


FIG. 1. Schematic view of the experimental setup with POLI instrument at MLZ.

The monochromatic polarized neutron beam passes through a thin Al window into the cylindrical fission chamber filled with tetrafluoromethane gas ( $\text{CF}_4$ ) at a pressure of about 10 mbar. Si(311) non-polarizing variable double-focusing monochromator was used to produce an intense monochromatic narrow neutron beam with the wavelength of  $1.15 \text{ \AA}$  (62 meV). The value for the maximal non-polarized neutron flux was estimated as  $1.8 \cdot 10^7 \text{ n/sm}^2/\text{sec}$ .

The two-sided fissile target, containing about 82 mg of  $^{235}\text{U}$  oxide-protioxide deposited on the thick  $40 \times 100 \text{ mm}^2$  aluminum backing is mounted on the axis of the chamber along the longitudinally polarized neutron beam direction. Two low-pressure angular sensitive multiwire proportional counters (LPMWPC) facing each other to the left and right of the target at a distance 3 cm (start detector) and 11 cm (stop detector) were recorded fission fragments. Each stop counter consists of five independent segments at the angles of  $0, \pm 22.5, \pm 45$  degrees on the left and  $\pm 135, \pm 157.5, 180$  degrees on the right side of the target to increase the angular sensitivity of the detector. Prompt fission  $\gamma$ -ray and neutron detectors are

located outside the fission chamber. Each of these detectors is a scintillation counter. As a scintillator, plastic and NaI(Tl) crystals were used, which made it possible to effectively register not only  $\gamma$ -quanta, but also neutrons, separating them by the time-of-flight. Eight cylindrical plastic scintillators with a diameter of 70 mm and a length of 120 mm and four NaI scintillators optically connected to a photomultiplier tube, wrapped with an antimagnetic screen and placed in a sealed aluminum case were inserted in a rotatable holder at a distance of about 30 cm from the target center. The schematic view of the used detector array inside/outside the fission chamber is shown in Fig. 2.

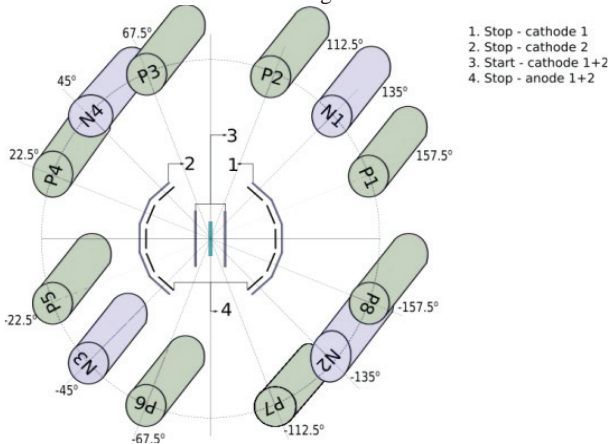


FIG. 2. The layout of the detector positioning around the target inside/outside the fission chamber. view from the beam direction. 1, 2 – stop MWPC, 3 – start MWPC, 4 – target. P1-P8 – plastic scintillators, N1-N4 – NaI scintillators.

Plastic detectors, located at the angles of  $\pm 22.5^\circ$ ,  $\pm 67.5^\circ$ ,  $\pm 112.5^\circ$  and  $\pm 157.5^\circ$  degrees ensures subsequent measurements of coincidences of prompt fission gamma rays and fission fragments with respect to the mean axis of the detection of fragments. The centers of gamma/neutron and fragment detectors are located in the plane orthogonal to the longitudinally polarized neutron beam direction. Prompt neutrons and prompt  $\gamma$ -rays from fission were separated in plastic scintillators using the time-of-flight technique. The start signal was the signal from the fission fragment detectors, which also served as a trigger indicating the fission event. The incoming polarization is periodically flipped between parallel and antiparallel to the beam propagation. The spin was flipped by  $180^\circ$  every 1.3 seconds, the flipping frequency was controlled by the quartz clock.

The data acquisition system (DAQ) includes preamplifiers (PAM), timing filter amplifiers (TFA), constant fraction discriminators (CFD) for time pick-up, Time-to-Digital Converters (TDCs), logical modules AND, OR, Logic fan-in/fan-out (FIFO), Analog-to-Digital Converters (ADCs), delays, scaler, and the VME-PC interface running on the Linux operating system [13]. The DAQ consisted of three signal lines of pulse processing: recording event times in TDC boards, recording pulse heights via ADC and counting events in scaler. Every event matching coincidence of the signals from the  $\gamma$ /neutron and fragment detectors is digitized by TDC and stored together with the information about the direction of polarization of the neutron beam. The input of the TDC was inhibited by the transition time of the neutron

spin flip. The coincidence count rates of  $\gamma$ -rays and fission fragments were recorded by the counters for two opposite directions of the neutron-beam polarization. These count rates were used to monitor the status of the setup and instrumental asymmetry. The frequent spin flip of the incident neutron beam served as one of the main mechanisms for suppressing instrumental asymmetry. Therefore, special attention was paid to the stability of the measurement time for opposite values of the neutron spin. The scaler controlled the data acquisition time with an accuracy of  $10^{-6}$  sec. For each triggered event (coincidence between one of the FF detectors and one of the  $\gamma$ -ray/neutron detectors) the data from the TDC and ADC were stored as list-mode-data together with the information about the spin sign. During one day of measurements, about 5 GB of compressed data were collected, divided into 5-minute expositions, which were then analyzed off-line.

### III. EXPERIMENTAL RESULTS

The main goal of the data processing was to determine the T-odd asymmetry coefficients of the number of coincidences of prompt fission  $\gamma$ -rays and fission fragments with respect to the direction of neutron beam polarization for each angle, calculated by the formula:

$$R(\theta) = [N^+(\theta) - N^-(\theta)]/[N^+(\theta) + N^-(\theta)], \quad (1)$$

where  $N^+(\theta)$  and  $N^-(\theta)$  are the  $\gamma$ -ray count rates for a selected angle between the detectors at two opposite directions of neutron polarization. In the Table I presented the asymmetry coefficient  $R_\gamma$  determined from the experimental data according to Eq. 1, measured for coincidences of the pulses from eight independent plastic detectors with each pulse from ten stop counters. Thus data were accumulated for 16 different angles between the axes of the fission fragment and  $\gamma$ -ray detectors in the experiment.

TABLE I. Angular dependence of the ROT asymmetry

Angle	$R_\gamma, 10^{-4}$	Angle	$R_\gamma, 10^{-4}$
0	$-0.6 \pm 0.9$	180	$-0.2 \pm 0.9$
22.5	$-0.4 \pm 0.8$	202.5	$-0.8 \pm 0.9$
45	$-2.0 \pm 0.9$	225	$-0.1 \pm 0.9$
67.5	$-0.3 \pm 0.9$	247.5	$-0.8 \pm 0.9$
90	$1.8 \pm 0.9$	270	$-0.5 \pm 0.9$
112.5	$1.5 \pm 0.9$	292.5	$0.3 \pm 0.9$
135	$2.2 \pm 0.9$	315	$1.4 \pm 0.9$
157.5	$0.7 \pm 0.9$	337.5	$1.3 \pm 0.8$

The coefficient of  $\gamma$ -ray emission anisotropy  $A$  with respect to the fission axis for the fragments of binary fission of a polarized  $^{236}\text{U}^*$  compound nucleus was measured in the same experiment (Fig. 3).

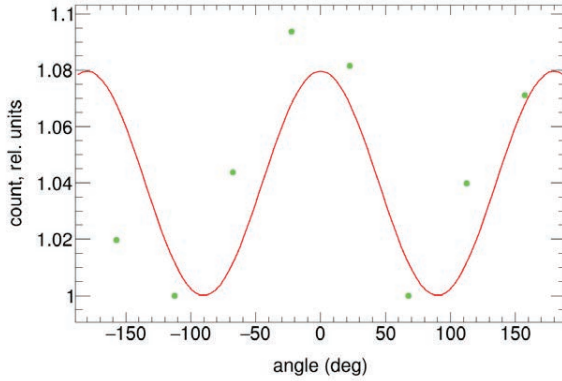


FIG. 3. Prompt  $\gamma$ -ray angular distribution. The curve is the result of approximation by Eq. (2).

The number of  $\gamma$ -quanta and their energy distribution in the process of  $^{235}\text{U}$  nuclei fission by thermal neutrons was studied in more detail in [14]. According to this work, on average,  $6.51 \pm 0.3$   $\gamma$ -quanta, the average energy of which is  $0.99 \pm 0.07$  MeV, fall on the act of fission. The angular distribution of the prompt  $\gamma$ -rays relative to the fission axis is anisotropic. The simplest integral parameter characterizing this anisotropy is the anisotropy coefficient  $A$ , defined as  $A = 1 - W(0^\circ)/W(90^\circ)$ . The value of the anisotropy coefficient for the angular distribution of prompt fission  $\gamma$ -rays of  $^{235}\text{U}$  is  $A \approx 0.13$  [15]. Although this value is significantly lower than in the angular distribution of  $\alpha$ -particles of ternary fission, such a noticeable anisotropy nevertheless makes it possible to search and study the ROT-effect of the fissile nucleus in the angular distribution of prompt fission  $\gamma$ -rays. For gamma radiation of an unpolarized fissioning system, the angular distribution can be expressed by [16]:

$$N(\theta) = N(90^\circ) \cdot (1 + A \cdot \cos^2\theta), \quad (2)$$

where  $A$  is the angular anisotropy coefficient. The obtained experimental value of the anisotropy coefficient in this work was  $A = 0.08(2)$ . It has to be noted that this value is not corrected for the angular spread of the fission fragments and  $\gamma$ -rays in the detectors. For the analysis of the ROT effect this uncorrected value has to be used, as all possible effects, connected with the geometry of the experimental setup are the same in both cases.

When a polarized fissioning system rotates around its polarization direction the axis before the moment of emission and detection of the  $\gamma$ -rays rotates by a small angle  $\pm\delta$  [17]. The sign of  $\delta$  depends on the captured neutron polarization direction. Taking into consideration a smallness of the angle  $\delta$  for fission axis rotation, the angular dependence of the T-odd asymmetry coefficient of prompt fission  $\gamma$ -rays can be written by this equation:

$$R(\theta) = -A \cdot \delta \cdot \sin(2\theta) / [1 + A \cdot \cos^2(\theta)]. \quad (3)$$

The results listed in the table 1 are shown in Fig. 4. These experimental data were approximated by Eq. (3). The given expression makes it possible to obtain the angle of rotation  $\delta$  of the polarized fissioning system. The angle of rotation of the  $^{236}\text{U}^*$  nucleus was found to be  $\delta = 0.09(2)^\circ$ . The result is still preliminary, as not all systematic errors are taken into account.

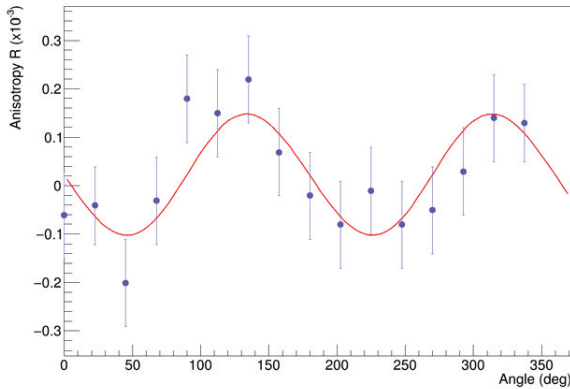


FIG. 4. Experimental angular dependence of the T-odd asymmetry coefficient  $R$  of  $\gamma$ -ray emission in  $^{236}\text{U}^*$  fission.

### Acknowledgments

This work has been supported by the Russian Ministry for Science and Education, German Ministry for Education and Research BMBF through the project 05K13PA3. The instrument POLI is operated by RWTH Aachen in cooperation with JCNS FZ Jülich (Jülich Aachen Research Alliance JARA). We are grateful to K. Lehmann, P. Stein, H. Saul and W. Luberstetter for their help in setting up and conducting the experiment.

### REFERENCES

1. F. Goennenwein, M. Mutterer, A. Gagarski, et al., Phys. Lett. B **652**, 13 (2007).
2. G.A. Petrov, A.M. Gagarski, I.S. Guseva, et al., *Proceedings of the XVI International Seminar on Interaction of Neutrons with Nuclei*, Dubna, 2009, p. 362.
3. V.E. Bunakov and S.G. Kadmsky, Phys. At. Nucl. **66**, 1846 (2003).
4. V. Bunakov, S.G. Kadmsky, and S.S. Kadmsky, Phys. At. Nucl. **71**, 1887 (2008).
5. V.E. Bunakov and S.G. Kadmsky, Phys. At. Nucl. **74**, 1655 (2011).
6. G.V. Danilyan, J. Klenke, V.A. Krakhotin, et al., Phys. At. Nucl. **72**, 1812 (2009).
7. G. Danilyan, J. Klenke, V. Krakhotin, Y. Kopach, et al., Phys. At. Nucl. **74**, 671 (2011).
8. G.V. Danilyan, J. Klenke, Yu.N. Kopach, et al., Phys. At. Nucl. **77**, 677 (2014).
9. A. Bohr, in *Proceedings of the International Conference on the Peaceful Uses of Atomic Energy*, Geneva, August, 1955, Vol. 2 (UN, New York, 1956), p. 151.
10. A. Gagarski, F. Goennenwein, I. Guseva, et al., Phys. Rev. C **93**, 054619 (2016).
11. Yu. Kopach, V. Novitsky, G. Ahmadov, et al., EPJ Web of Conf. **169**, 00010 (2018).
12. Z. Salhi, E. Babcock, et al., J. Phys. Conf. Ser. **1316**, 012009 (2019).
13. D. Berikov, V. Hutanu, Yu. Kopach, et al., JINST **15**, P01014 (2020).
14. F. Pleasonton, R.L. Ferguson, H.W. Schmitt, Phys. Rev. C **6**, 1023 (1972).
15. S.S. Kapoor, R. Ramanna, Phys. Rev. **133**, B598 (1964).
16. V. Strutinskii, Zh. Eksp. Teor. Fiz. **37**, 861 (1959).
17. G.V. Valsky, A.M. Gagarski, I.S. Guseva, et al., Bull. Russ. Acad. Sci. Phys. **74**, 767 (2010).

## NEW SIDE OF THE COLLINEAR CLUSTER TRI-PARTITION SCENARIO

Yu.V. Pyatkov<sup>1,2</sup>, D.V. Kamanin<sup>2</sup>, A.A. Alexandrov<sup>2</sup>, I.A. Alexandrova<sup>2</sup>,  
Z.I. Goryainova<sup>2</sup>, V. Malaza<sup>3</sup>, G.V. Mishinsky<sup>2</sup>, E.A. Kuznetsova<sup>2</sup>, A.N. Solodov<sup>2</sup>,  
A.O. Strekalovsky<sup>2</sup>, O.V. Strekalovsky<sup>4,2</sup>, V.E. Zhuchko<sup>2</sup>

<sup>1</sup>National Nuclear Research University MEPhI (Moscow Engineering Physics Institute), Moscow, Russia

<sup>2</sup>Joint Institute for Nuclear Research, Dubna, Russia

<sup>3</sup>University of Stellenbosch, Faculty of Military Science, Military Academy, Saldanha 7395, South Africa

<sup>4</sup>Dubna State University, 141980 Dubna, Russia

### INTRODUCTION

In our previous publications we discussed different manifestations of a new decay channel of the low excited heavy nuclei called collinear cluster tri-partition (CCT) [1–4]. The most populated CCT mode was revealed in the mass correlation distribution of fission fragments (FFs) as a local region (“bump”) of increased yields below the loci linked to the conventional binary fission. The bump was dubbed the “Ni-bump” because it is centered at the masses associated with the magic isotopes of Ni. The bulk of the results has been obtained by using the “missing mass” approach. It means that two decay products (fragments) are detected in coincidence using a double armed time-of-flight spectrometer, while the significant difference between their total mass  $M_s = M_1 + M_2$  and the mass of a mother system serves as a sign of at least ternary decay. Mainly a scattering of fragments at the entrance of an  $E$ -detector gives background events simulating ternary decay. Observation of the specific linear structures in the  $M_1$ – $M_2$  distributions (mass correlation plots) served as a criterion for a sufficient suppression of the background. Analysis of the fission events from the “Ni-bump” allowed us to draw a conclusion that the ternary fission observed should be treated as “almost sequential”, but it is very close to the sequential one [4]. Here we present our new experimental result that decisively confirms this conclusion.

### EXPERIMENT

The experiment was performed at the beam of the MT-25 microtron, FLNR, JINR, using VEGA (V-E Guide based Array) setup. The scheme of the spectrometer is shown in Figure 1.

Fission fragments (FFs) from the  $^{235}\text{U}(\gamma, f)$  reaction in the target (1) is captured by the electrostatic guide system (EGS) consisted of the tube (2) and the central wire (3). The FF energy  $E$  and velocity  $V$  required for calculation of the FF mass are measured in the time-of-flight spectrometer consisted of the microchannel-plates based timing detector (4) and the mosaic of four PIN diodes (5).

Presence of the EGS is a principal difference between VEGA setup and other time-of-flight spectrometers used in our experiments earlier. The EGS constitutes a cylindrical capacitor with a thin wire as a central electrode. Some part of the ions emitted from the target at one end of the guide can be involved in the spiral-like movement along the guide axis thanks to the radial electric field, which dims the radial component of the ion velocity. According to [5], where the EGS was proposed for the first time, the collection efficiency  $F_c$

of the guide for an extended uniform target of radius  $b$ , equal to the tube (outer cylinder) radius  $R$ , is estimated to be:

$$Fc = 0.153qV_0 / \{E_{ff} \ln(R/s)\}, \quad (1)$$

where  $V_0$  – is the potential difference between the two conductors,  
 $E_{ff}$  – is the kinetic energy of the fission fragment,  
 $s$  – is the radius of the central wire of the guide,  
 $q$  – is the ionic charge of the fragment.

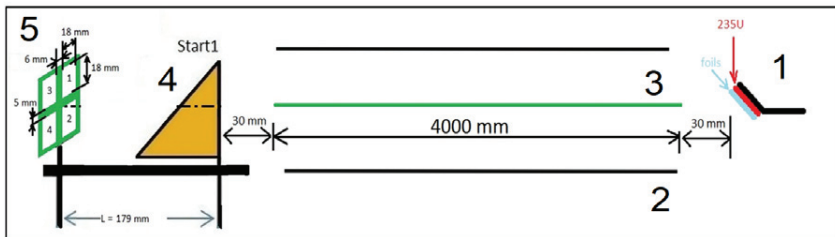


**FIGURE 1.** The scheme of the VEGA setup. Target (1) of  $^{235}\text{U}$  isotope is irradiated by brake gamma quanta of the electron beam of the MT-25 microtron. Some fraction of the fission fragments is captured by the electrostatic guide system (EGS) consisted of the tube (2) at zero potential and the central wire (3) at a potential  $-6$  kV. At the exit of the EGS, the FF energy  $E$  and velocity  $V$  for calculation of the FF mass are measured in the time-of-flight spectrometer consisted of the timing detector (4) and mosaic of PIN diodes (5). The main dimensions are marked in the figure.

For instance, for the ion of  $^{52}\text{Ca}$  with  $E_{ff} = 57$  MeV and ionic charge  $q = 4$  the maximum angle of capture  $\beta_{\max}$  is about  $1^\circ$  in the EGS, with the following parameters:  $V_0 = 10$  kV,  $R = 56$  mm,  $s = 0.1$  mm, target diameter  $d = 5$  mm.

According to Eq. (1), only minor part of the ions already caught in the guide will be lost along the flight-pass even if it is very long. Thus, the EGS allows to increase a counting rate at the detector placed few meters away from the target. A spectrometer with extremely long flight-pass is also useful for estimating of the shape isomers' lifetime lying even in the microsecond range [6].

We planned to use the EGS for transporting the FFs from the target in the vicinity of the IBR-2 reactor (FLNP, JINR) active zone to the detectors placed several meters from the target [7]. Similar guide system has been already used at the vertical reactor channel [8]. Due to the technical problems finally the project VEGA was realized at the beam of the microtron MT-25.

## RESULTS

The mass correlation distribution for the FFs detected in coincidence in two different PIN diodes of the mosaic (Figure 1) is presented in Figure 2.

Some structures inside the box w1 (Figure 2a) attract attention. This region is shown on a larger scale in Figure 2b. Solid lines (1–4) match the expression  $M_1 + M_2 = \text{const}$ . Likely there are two lines (5, 6) approximately perpendicular to them, and some points are grouping around the line (7)  $M_2 = \text{const} = 12$  u. Earlier, similar linear structures were observed for the FFs from  $^{252}\text{Cf}(sf)$  [2]. Concentration of points (8) is seen around  $M_1 \approx 130$  u. The origin of the lines (1, 2) is discussed below while treating of other mentioned peculiarities are beyond the scope of the present paper.

The fission events constituting the lines (1, 2) are characterized by the following mean values of energies and velocities:  $\langle E_1 \rangle \approx 64$  MeV,  $\langle E_2 \rangle \approx 3$  MeV,  $\langle V_1 \rangle = 0.96$  cm/ns;  $\langle V_2 \rangle = 0.43$  cm/ns.

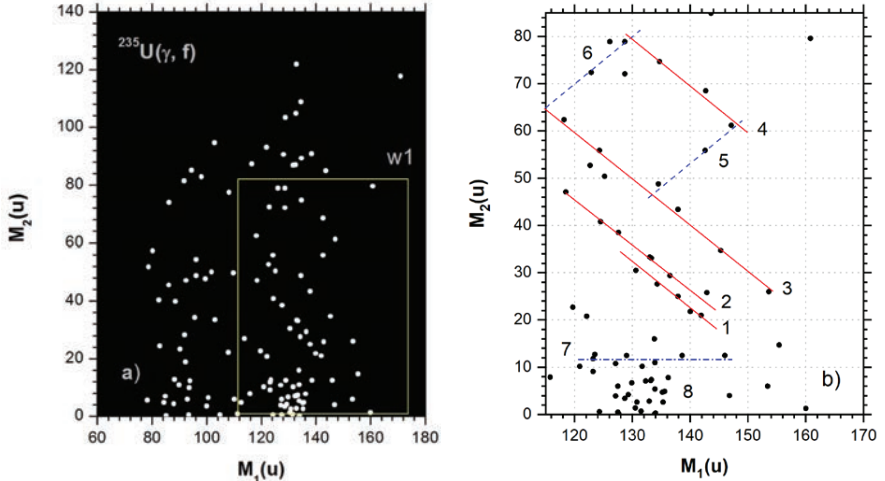


**FIGURE 2.** Mass correlation distribution for the FFs detected in coincidence in two different PIN diodes (a) and its part from box  $w1$  (b).

## DISCUSSION

The lines (1, 2) in Figure 2b correspond to the missing masses 72 u and 68 u respectively. These masses are associated with magic isotopes of  $^{72}\text{Ni}$  and  $^{68}\text{Ni}$ . In our previous experiments at the double-armed time-of-flight spectrometers FOBOS and COMETA just these fragments manifested themselves as “Ni-bump” [1, 2]. The region of the Ni-bump in the FFs mass correlation distribution is presented in Figure 3.

Kinematical analysis of the events from the Ni-bump [4] allowed us to suppose that the pre-scission configuration leading to the ternary decay looks like the one shown in Figure 4. The events forming peaks in Figure 3b are predominantly due to the nucleus shape shown in Figure 4b and the first rupture is supposed to occur in the vicinity of the surface of Sn cluster. Deformation energy of the light nascent fragment of Cd is enough for its fission with formation of Ni nucleus as one of the decay products. Thus, the ternary sequential decay (CCT) takes place. Ni-bump is observed also in the FFs mass correlation distribution from the reaction  $^{235}\text{U}(\text{n}_{\text{th}}, f)$  [1] and the pre-scission configurations similar to those shown in Figure 4 could be decisive for its appearance.

Keeping in mind all said above, the following scenario for the events constituting the lines (1, 2) in Figure 2b could be proposed. Binary fission of the excited  $^{235}\text{U}$  nucleus in the pre-scission configuration similar to that shown in Figure 4a occurs, with formation of Ni nucleus as the light fragment. The fragment stops in the target backing, while the heavy fragment which is flying in the opposite direction is caught into EGS (Figure 1). After approximately 400 ns ( $\langle V_1 \rangle \approx 1$  cm/ns and the EGS length is about 400 cm) the heavy fragment reaches the start detector where its brake-up in very thin foil ( $50 \mu\text{g}/\text{cm}^2$  of  $\text{Al}_2\text{O}_3$ )

occurs. The main conclusion which can be drawn from the result under discussion is that *the heavy fragment of photo-fission of  $^{235}\text{U}$  nucleus is born in the shape isomer state and the life time of this state exceeds 400 ns.* The result was obtained for the first time.

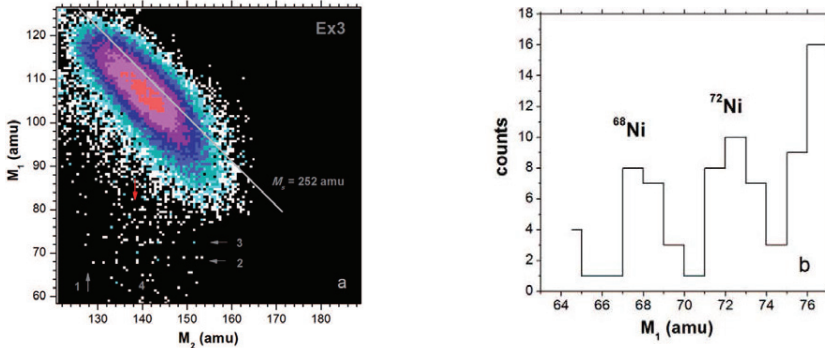


**FIGURE 3.** The region of the “Ni-bump” in the mass correlation distribution of the FFs from  $^{252}\text{Cf}(\text{sf})$  measured using COMETA setup (a). Projection of the bump onto the  $M_1$  axis (b). It should be noted that this figure was published in Ref. [2].

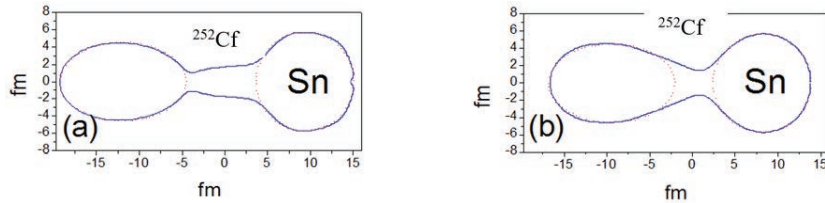


**FIGURE 4.** Shapes of the fissioning  $^{252}\text{Cf}$  nucleus for large system elongations in two different fission valleys [4, 9].

## REFERENCES

1. Yu.V. Pyatkov et al., Eur. Phys. J. A **45**, 29 (2010).
2. Yu.V. Pyatkov et al., Eur. Phys. J. A **48**, 94 (2012).
3. D.V. Kamanin and Yu.V. Pyatkov, in *Clusters in Nuclei*, Lecture Notes in Physics No. 875, edited by C. Beck (Springer, Berlin, 2013), Vol. **3**, p. 183.
4. Yu.V. Pyatkov et al., Phys. Rev. C **96**, №6, 064606 (2017)
5. N.C. Oakey, P.D. McFarlane, NIM. 1967. V. **49**. P. 220–228.
6. D.V. Kamanin et al., Proceedings of the 22<sup>th</sup> International Seminar on Interaction of Neutrons with Nuclei, Dubna, Russia, 27–30 May 2014. E3-2015-13, Dubna 2015, p. 70–76.
7. D.V. Kamanin et al., Proceedings of the 20<sup>th</sup> International Seminar on Interaction of Neutrons with Nuclei, Alushta, Ukraine, 21–26 May 2012. E3-2013-22, Dubna 2013, p. 111–116.
8. A.A. Alexandrov et al., NIM A. 1991. V. **303**. P. 323–331.
9. Yu.V. Pyatkov et al., Nucl. Phys. A **624**, 140 (1997).

# FISSION FRAGMENTS BINARY BRAKE-UP AT CROSSING OF THE SOLID-STATE FOILS

A.O. Strekalovsky<sup>1</sup>, D.V. Kamanin<sup>1</sup>, Yu.V. Pyatkov<sup>1,2</sup>, Z.I. Goryainova<sup>1</sup>,  
V.E. Zhuchko<sup>1</sup>, A.A. Alexandrov<sup>1</sup>, I.A. Alexandrova<sup>1</sup>, R. Korsten<sup>3</sup>, V. Malaza<sup>3</sup>,  
E.A. Kuznetsova<sup>1</sup>, O.V. Strekalovsky<sup>1,4</sup>

<sup>1</sup>*Joint Institute for Nuclear Research, Dubna, Russia*

<sup>2</sup>*National Nuclear Research University MEPhI (Moscow Engineering Physics Institute), Moscow, Russia*

<sup>3</sup>*University of Stellenbosch, Faculty of Military Science, Military Academy, Saldanha 7395, South Africa*

<sup>4</sup>*Dubna State University, 141980 Dubna, Russia*

## INTRODUCTION

Earlier we discussed [1–3] the manifestations of a new original effect appeared at the crossing of metal foils by fission fragments (FF). A significant mass deficit in the total mass  $M_{sum}$  of the fission fragments detected in coincidence with ions knocked out from the foil was observed. It has been shown that at large angles of scattering of the knocked-out ions, predominantly conventional elastic Rutherford scattering occurs at energies below the Coulomb barrier. As the result,  $M_{sum}$  corresponds to the mean mass of the mother system after emission of fission neutrons (no missing mass). In contrast, in near frontal impacts, the fission fragment misses essential part of its mass; and the bulk of the brake-up residuals show the magic nucleon compositions. Here we present one of the new results, obtained using thick carbon foil as a degrader.

## EXPERIMENT

The experiment was performed at the LIS (Light Ions Spectrometer) spectrometer in FLNR (JINR). The layout of the setup is shown in figure 1. LIS setup in the current modification is a double-armed time-of-flight spectrometer, which includes five micro-channels plates based time detectors (1–5), and two PIN diodes (6, 7). Compared to the previous version of the spectrometer [1–3], all time-of-flights were measured using only micro-channel plates based time detectors, in order to exclude an influence of the plasma delay effect in the PIN diode. Each PIN diode provides information for estimation of both FF energy and time-of-flight. Solid foils (degraders) of different thicknesses can be placed in the detector (2). The aperture for fission fragments, detected in coincidence in the opposite PIN diodes, does not exceed 3°.

The data acquisition system consists of the fast digitizer CAEN DT5742 and a personal computer. The digital images of all the signals were obtained for further off-line processing. Mass reconstruction procedure used is presented in Ref. [4]. The construction of the spectrometer allows measuring of the FF mass  $M_{it}$  using two velocities calculated via time-of-flights at the bases ( $a$  and  $c$ ). Thus, the fragment's mass  $M_{1it}$  before the fragment passes the degrader (9) in the arm-1 of the spectrometer was reconstructed. The mass  $M_{1te}$  of the same fragment after passing the degrader was calculated using "velocity-energy" method, which involves measuring the FF time-of-flight at the base ( $b$ ) and the FF energy using PIN diode (6). Thus, we know the mass of each FF before and after it crosses the degrader-foil for their

comparison event-by-event. The reference arm-2 is free from the degrader and serves to demonstrate a conventional FF mass spectrum obtained in the same experiment.

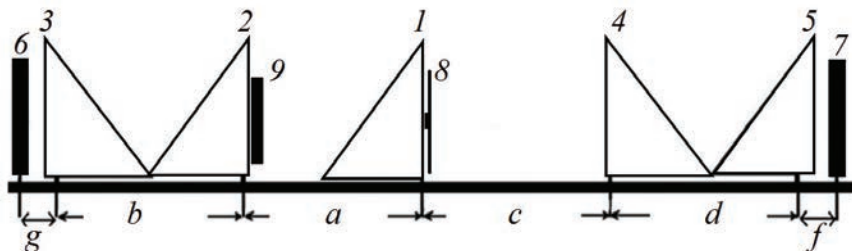


**FIGURE 1.** Layout of the two-armed time-of-flight LIS spectrometer. In the actual modification it includes five timing detectors, from 1 to 5, two PIN diodes (6, 7) and  $^{252}\text{Cf}(\text{sf})$  source (8). Additional metal foil (degrader) (9) could be placed in the detector (2). The flight-passes ( $a \div d$ ) do not exceed 140 mm each. The distances ( $g$ ) and ( $d$ ) between the PIN diodes and the nearest timing detectors are near 15 mm. The spectrometer arm to the left from the start detector (1) will be called below as “arm-1” while the opposite one as “arm-2”.

## RESULTS

The carbon degrader, 9.6  $\mu\text{m}$  thick, facing the arm-1, was used in the experiment under discussion. As can be inferred from figure 2, the degrader is thick enough to cut off the low energy part of the FF heavy mass peak. The energy  $E_{1lin}$  without correction for the pulse-height defect is shown.

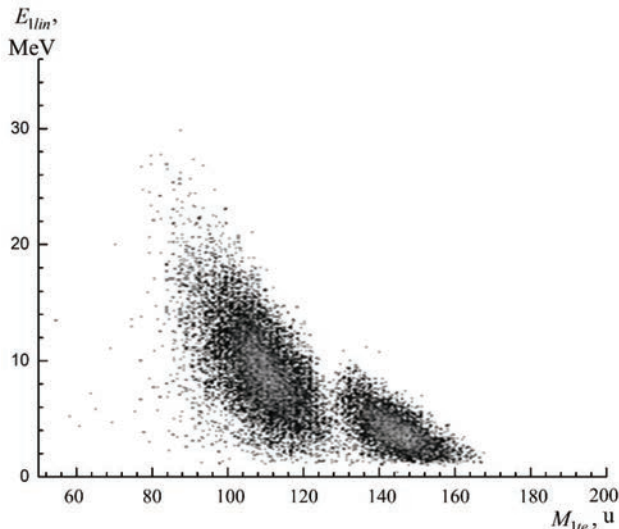


**FIGURE 2.** Mass-energy distribution of the fragments after passing of the carbon degrader. A low energy part of the heavy mass peak is cut off.

The FF masses before and after passing of the degrader are compared event-by-event in figure 3.

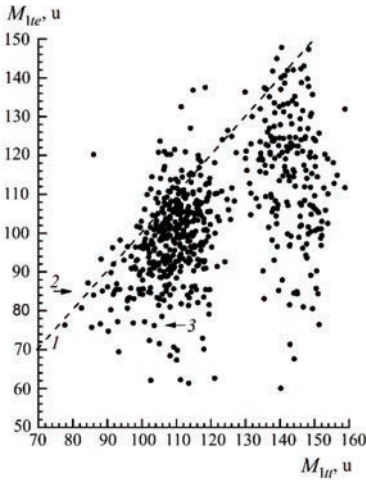


**FIGURE 3.** Distribution of the masses of the FF before ( $M_{1tr}$ ) and after ( $M_{1te}$ ) it passes the degrader. The dashed line (1) marks the points with equal masses  $M_{1tr} = M_{1te}$ . Specific linear structure marked by the arrows is seen in the light mass peak. The line (2) corresponds presumably to the magic isotope of  $^{85}\text{As}$ , while line (3) to also magic isotope of  $^{77}\text{Zn}$ . See text for details.

The linear structure, at least in the light FF mass peak, is clearly seen. More structure that is complicated is observed as well in the heavy peak with slightly large statistics (figure 4).

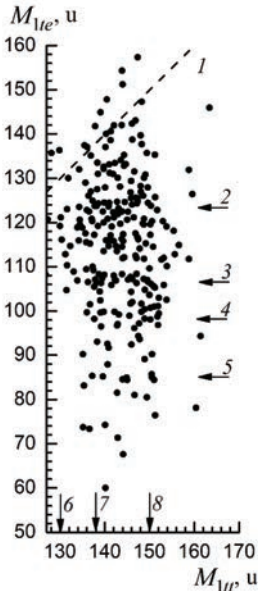


**FIGURE 4.** Distribution of the fragments from the heavy FF mass peak before ( $M_{1tr}$ ) and after ( $M_{1te}$ ) the fragment passes the degrader. The dashed line (1) marks the points with equal masses  $M_{1tr} = M_{1te}$ . The structure consisting of some rectangles bounded by magic isotopes is observed. The sides of the rectangles are marked by the numbered arrows and correspond presumably to the following magic isotopes:  $^{121}\text{Ag}$ ,  $^{123}\text{Cd}$  (2),  $^{108}\text{Mo}$  (3),  $^{98}\text{Sr}$  (4),  $^{82}\text{Ge}$ ,  $^{84}\text{Se}$  (5),  $^{130}\text{Sn}$  (6),  $^{138}\text{I}$  (7),  $^{150}\text{Ce}$  (8). See text for details

Figure 5 shows the projection of the mass-mass distribution from figure 4 onto  $M_{1te}$  axis in order to demonstrate statistical significance of the most pronounced peaks.

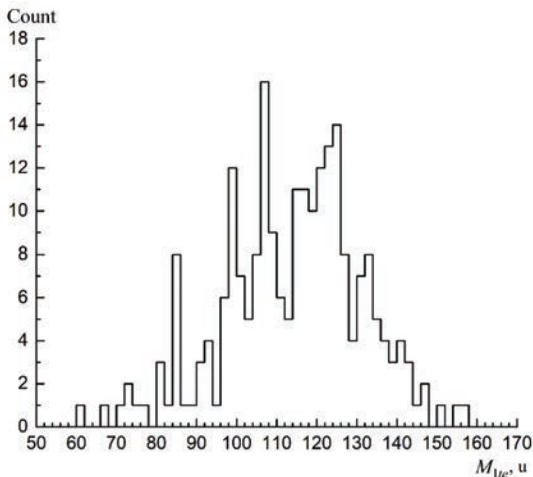


**FIGURE 5.** Projection of the mass-mass distribution shown in figure 4 onto  $M_{1te}$  axis. The most pronounced peaks, centered at the mass numbers  $A \sim 100$  and  $A \sim 108$ , correspond to the lines (3, 4) in figure 4.

## DISCUSSION

For the first time we have observed fragmentation of the FF from the light mass peak with the passage of the foil (figure 3). The line (2)  $M_{1te} = 85$  u starts from the point  $M_{1tr} = 85$  u, where  $M_{1te} = M_{1tr}$ , i.e. missing mass is absent in this point. The line continues up to the  $M_{1tr}$  mass partition 120/132. The sum of the facts can be treated as follows. There is the fission mode of  $^{252}\text{Cf}$  nucleus with the pre-scission configuration of the fissioning system consisting of the light ( $^{85}\text{As}$ ) and heavy ( $^{132}\text{Sn}$ ) magic clusters connected by the neck, including the rest of the nucleons. The magic of  $^{85}\text{As}$  is conditioned by the strongly deformed neutron shell  $N \sim 85$  [4] and the heavy cluster is the double magic spherical  $^{132}\text{Sn}$  nucleus [5]. In conventional binary fission, the ruptures occur along all the length of the neck that leads to the formation of the light FF in the mass range 85–120 u. With the passage of the foil, the light FF loses the nucleons beyond the magic core ( $^{85}\text{As}$ ). The key point in the scenario is that the magic core is supposed to be already preformed in the light fragment after its forming, and the “memory” about this circumstance is conserved at least for fourteen nanoseconds (mean flight time between the Cf source and the degrader) till the FF interaction with the degrader. In other words, the light FF under discussion is likely borne in the shape isomer state with the life time at least in the nanoseconds range.

Similar scenario stands behind the line (3) in figure 3. Presumably it is a manifestation of the fission mode built on the magic  $^{77}\text{Zn}$  and  $^{148}\text{Ce}$  [6] as the side clusters connected by the neck. In conventional binary fission, the ruptures can occur along all of the neck. Passing the degrader, the light FF undergoes binary brake-up which results in the release of its magic core.

More complicated rectangular structures are observed in the heavy mass peak (figure 4). Let us discuss the most pronounced structure namely the rectangle bounded by the lines marked by the numbered arrows (3, 4, 7, 8). The mass correlations observed could be explained in the frame of the following scenario. At some stage of the descent from the fission barrier in the valley of the symmetric nuclear shapes [7] the chain of clusters shown in Fig. 6 is preformed with the side constituents (1, 2) to be the deformed magic nuclei of  $^{98}\text{Sr}$  and  $^{138}\text{I}$

[5, 6]. The ruptures along the neck result in forming of the heavy FF with the  $M_{1tr} = (154 \div 138)$  u. All these fragments undergo the bake-up in the degrader showing the  $^{98}\text{Sr}$  as the detected product. For explanation of this fact, it is reasonable to suppose that the Sr cluster is preformed in the body of the  $^{138}\text{I}$  nucleus (figure 6). Likely, the  $^{40}\text{S}$  and  $^{98}\text{Sr}$  are the most preferable components for clusterization of the  $^{138}\text{I}$  nucleus while it deforms in the process of elongation of the  $^{252}\text{Cf}$  nucleus just before scission. The vertical line  $M_{1tr} = 138$  u which bounds the rectangle under discussion from the left side is due to the nucleon transfer from the cluster (4) to the cluster (5) after they become free due to the brake-up of the  $^{138}\text{I}$  nucleus in the degrader. In other words, we observe how the magic  $^{98}\text{Sr}$  nucleus “completes” up to the next magic shell in heavier magic nuclei of  $^{106}\text{Nb}$  and  $^{108}\text{Mo}$  [6] (line 3 in figure 4).

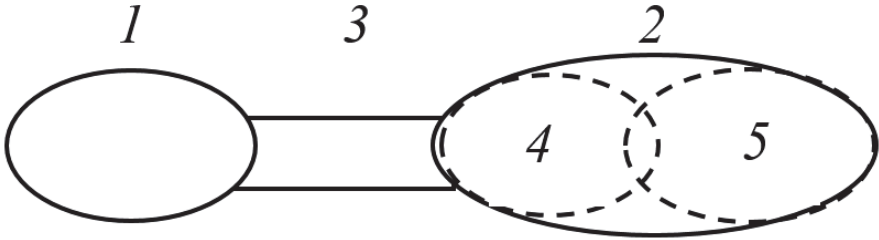


**FIGURE 5.** Presumable precission configuration giving rise to the line (4) in figure 5. The constituents involved are numbered as follows: 1 –  $^{98}\text{Sr}$ , 2 –  $^{138}\text{I}$ , 3 – the neck corresponding to  $^{16}\text{C}$  nucleus by the nucleon composition, 4 –  $^{40}\text{S}$ , 5 –  $^{98}\text{Sr}$ .

Similar process is decisive for the forming of the vertical lines  $M_{1tr} = (146 \div 154)$  u. These masses correspond to nuclei from  $^{146}\text{Ce}$  to  $^{154}\text{Nd}$  with the number of protons  $Z = 58\text{--}60$  from the region on the map of shell corrections with a noticeable negative shell correction for the quadrupole strain parameter  $\beta_2 \approx 0.4$  [6]. Isotope masses were estimated in the framework of the hypothesis of constant charge density.

Again, the  $^{98}\text{Sr}$  cluster plays a role of the acceptor for the nucleons from the lighter clusters analogous to the  $^{40}\text{S}$  (figure 6). The question arises why we do not observe similar vertical lines starting from all the  $M_{1tr} = (138 \div 154)$  u? Likely, it is important that the masses at the ends of this mass interval correspond to the magic nuclei as it was mentioned above. Immediately after its formation, the deformed heavy fragment with magic nucleon composition is already clusterized into  $^{98}\text{Sr}$  and additional light cluster. Due to such composition, the fragment undergoes the binary brake-up in the degrader. In contrast, in the non-magical heavy fragment three clusters are preformed (figure 6), namely some part of the neck (3), cluster (4) and cluster (5). Then the ternary brake-up can occur in the degrader with the kinematics preventing further nucleon transfer between the decay partners.

Similar scenario could explain the less pronounced rectangles above and below the analyzed one. They differ by the magic clusters involved (the clusters are listed in the caption to figure 4).

## CONCLUSION

The results discussed here give evidence that the FFs from conventional binary fission are born in the shape isomer states both in the fission valley of the mass-symmetric and mass-asymmetric shapes. This obstacle reflects the basic feature of the multimode nuclear fission: preformation of two magic cores in the body of the fissioning nucleus that defines its further

evolution till fission. These mode-forming cores are revealed due to the FF brake-up in the degrader. The effect has been observed for the first time.

### ACKNOWLEDGMENTS

This work was supported by the research project № 18-32-00538 of the Russian Foundation for Basic Research (RFBR) and partially by the MEPhI Academic Excellence Project (Contract No. 02.a03.21.0005, 27.08.2013) of the Russian Science Foundation, as well as by the Department of Science and Technology of the Republic of South Africa (RSA).

### REFERENCES

1. Yu.V. Pyatkov et al., Proceedings of the 22<sup>th</sup> International Seminar on Interaction of Neutrons with Nuclei, 2014, p. 83.
2. Yu.V. Pyatkov et al., International Symposium on Exotic Nuclei “EXON-2014”, Conference proceedings, World Scientific Publishing Co. Pte. Ltd, 2015, p. 383.
3. Yu.V. Pyatkov et al., International Symposium on Exotic Nuclei “EXON-2016”, Conference proceedings, World Scientific Publishing Co. Pte. Ltd, 2017, p. 284.
4. S.I. Mulgin et al., Nucl. Phys. A **640**, 375 (1998).
5. B.D. Wilkins et al., Phys. Rev. C **14**, 1832 (1976).
6. H. Märton, Proceedings of the “Seminar on Fission Pont D’Oye II. 1991, p. 15.
7. Yu.V. Pyatkov et al., Nucl. Phys. A**624**, 140 (1997).

# Measurements and Analysis of Angular Distributions and Anisotropy of Fission Fragments from Neutron-Induced Fission of $^{232}\text{Th}$ , $^{233}\text{U}$ , $^{235}\text{U}$ , $^{238}\text{U}$ , $^{239}\text{Pu}$ , $^{237}\text{Np}$ , $^{\text{nat}}\text{Pb}$ , and $^{209}\text{Bi}$ in Intermediate Energy Range 1–200 MeV

A.S. Vorobyev<sup>1</sup>, A.M. Gagarski<sup>1</sup>, O.A. Shcherbakov<sup>1</sup>, L.A. Vaishnene<sup>1</sup>, A.L. Barabanov<sup>2,3</sup>

<sup>1</sup>*NRC “Kurchatov Institute”, B.P. Konstantinov Petersburg Nuclear Physics Institute, 188300, Gatchina, Leningrad district, Russia*

<sup>2</sup>*NRC “Kurchatov Institute”, 123182, Moscow, Russia*

<sup>3</sup>*Moscow Institute of Physics and Technology, 141700, Dolgoprudny, Moscow Region, Russia*

## Abstract

Angular distributions of fission fragments from the neutron-induced fission of  $^{232}\text{Th}$ ,  $^{233}\text{U}$ ,  $^{235}\text{U}$ ,  $^{238}\text{U}$ ,  $^{239}\text{Pu}$ ,  $^{237}\text{Np}$ ,  $^{\text{nat}}\text{Pb}$  and  $^{209}\text{Bi}$  have been measured in the energy range 1–200 MeV at the neutron TOF spectrometer GNEIS based on the spallation neutron source at 1 GeV proton synchrocyclotron SC-1000 of the NRC KI - PNPI (Gatchina, Russia). The data in the neutron energy range above 20 MeV for  $^{233}\text{U}$ ,  $^{239}\text{Pu}$ ,  $^{237}\text{Np}$ ,  $^{\text{nat}}\text{Pb}$  and  $^{209}\text{Bi}$  have been obtained for the first time. Recently, the list of nuclei to be studied within the framework of present investigation was filled with isotope  $^{237}\text{Np}$ . Neptunium is a major component of spent nuclear fuel, therefore an accurate knowledge of the fission cross-section and fragment properties is needed for waste transmutation and advanced nuclear facilities (reactors, ADS, etc.) studies. A description of the experimental equipment and measurement procedure is given. The underlying ideas of the theoretical approach developed for analysis of the obtained experimental data are discussed.

## 1. Introduction

The experimental study of angular distributions of fission fragments near the threshold and low chance fission is a way to determine the properties of transition states of fissioning nucleus at the saddle point. The information about angular distribution of fission fragment is also very important to verify parameters of theoretical models used for adequate fission process description in neutron energy range above 20 MeV. The data on nuclear fission in intermediate energy range 1–200 MeV are of prime importance for the advanced nuclear technologies such as Accelerator-Driven Systems (for nuclear power generation and nuclear transmutation). The systematic study of angular distributions of fission fragments is limited to that these experimental data are very scarce in neutron energy range above 20 MeV and are practically absent for neutron energy range above 100 MeV.

In this report, we summarize the results of the measurements carried out at the neutron time-of-flight (TOF) spectrometer GNEIS of the NRC KI - PNPI during the last few years. The main features of the experimental set-up are also described. To demonstrate the quality of obtained data, the comparison with the results obtained by other experimental groups is performed. The data obtained in recent measurement for the reaction  $^{237}\text{Np}(n,f)$  are also shown. Besides, we present a method for calculation of fission fragment angular distribution and compare the results of calculations with the experimental data for  $^{237}\text{Np}$  nucleus.

## 2. General description of the experiment

The measurements were carried out at the 36 m flight path of the neutron TOF-spectrometer GNEIS based on the spallation neutron source at 1 GeV proton synchrocyclotron SC-1000 of the NRC KI - PNPI (Gatchina, Russia) [1, 2]. The short pulse width 10 ns of the neutron source enables to carry out TOF-measurements with the energy resolution from 0.8% (at 1 MeV) to 13% (at 200 MeV). A schematic view of the experimental set-up is shown in Fig. 1. The main features of the measurements are described below. A detailed description of the set-up can be found in our previous publications [3–10].

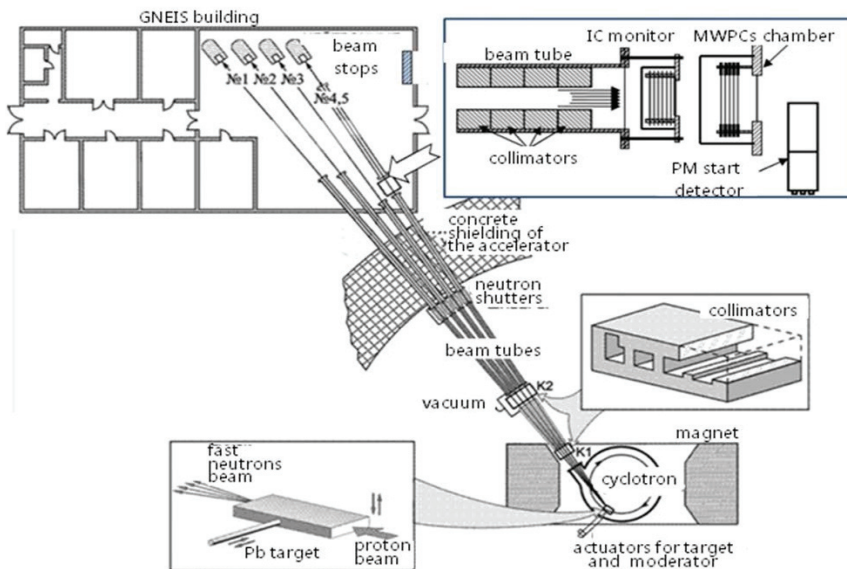


Fig. 1. Schematic view of the experimental set-up.

The measurements of angular distributions of fission fragments (FF) were carried out using the FF detector which consists of two low pressure gaseous coordinate-sensitive multiwire proportional counters D1 and D2 (MWPC, see in upper right corner of Fig. 1). The counters D1 and D2 were placed close to the target in the beam, one after the other. The neutron beam axis came through the geometrical centers of the target and the MWPC's electrodes being perpendicular to them. Data acquisition system was based on two waveform digitizers Acqiris DC-270 with sampling rate of 500 MSamples/s. This system as well as the methods of digital processing of signals from FF detector used enabled to perform measurements in a wide interval of neutron energy with a zero dead time. Herewith, almost perfect separation between fission events and products of other reactions was achieved at a practically zero FF registration threshold. To demonstrate the quality of this separation, for  $^{237}\text{Np}$  measurements the two-dimensional plots of the amplitudes of correlated cathode signals from two MWPCs are shown in Fig. 2 for all events and for “useful” fission events (left part and right part, respectively) selected by means of the procedure described in [4].

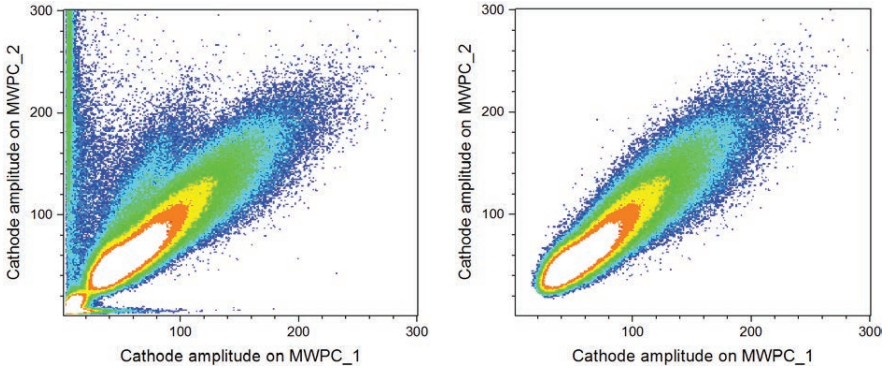


Fig. 2. A two-dimensional plot of the amplitudes of the cathode signals from two MWPCs in  $^{237}\text{Np}$  experiment. Right part of this figure shows only “useful” fission events.

The measured angular distributions for selected fission fragment events were corrected for the efficiency of fission fragment registration. This efficiency was calculated by means of the Monte-Carlo method taking into account the real geometry, design and features of the fission fragment detector.

Note that the effect of momentum transfer from the incident neutron to the fissioning system on the angular distributions in the laboratory system should be taken into account. To determine this effect, angular distributions of fission fragments in the laboratory system were measured for two set-up orientations relative to the beam direction (downstream and upstream). In the first, downstream, position, the beam direction coincides with the longitudinal momentum component of the detected fission fragment. In the second, upstream, position, the beam direction is opposite to the longitudinal momentum component of the detected fission fragment.

The angular distributions of fission fragments in the center-of-mass system were deduced from the corrected  $\cos(\theta)$  angular distributions in the laboratory system for two set-up orientations relative to the neutron beam direction ( $\cos(\theta)$  bins were equal to 0.01). Then, these distributions were fitted in the range  $0.24 < \cos(\theta) < 1.0$  by the sum of even Legendre polynomials up to the 4-th order and their anisotropy  $W(0^\circ)/W(90^\circ)$  was calculated using the coefficients  $A_2$  and  $A_4$  ( $A_0=1$ ) for the corresponding Legendre polynomials:

$$\frac{W(0^\circ)}{W(90^\circ)} = \frac{1 + A_2 + A_4}{1 - A_2/2 + 3A_4/8}. \quad (1)$$

### 3. Results and discussion

The experimental data on angular distributions of fission fragments in the neutron-induced fission have been accumulated over decades, mostly for neutron energy less than 20 MeV. A new age in experimental investigations of the fission fragment angular distributions started when new experiments dedicated to this problem have been initiated nearly simultaneously by the GNEIS team at NRC KI - PNPI [3–11], the n\_TOF Collaboration at CERN [12–16], and the NIFFTE Collaboration in Los Alamos [17, 18]. The

pulsed high-intensity “spallation” neutron sources of these facilities enable to carry out TOF-measurements of the neutron-induced fission cross sections and fission fragment angular distributions in intermediate neutron energy range 1–300 MeV. The other two principally important features of the experimental techniques employed by these research groups are usage of the multichannel position-sensitive detectors of fission fragments of different degree of complexity (MWPCs, PPACs, TPC), and application of the waveform digitizers for detector pulse processing. The results of these investigations are presented in Table 1.

Table 1. Status of experiments on angular distributions of fission fragment study.

Nucleus	GNEIS, KI-PNPI	n-TOF, CERN	LANSCE, LANL	TSL, Uppsala University
	Reference, EXFOR [19]		Accession #	
<sup>232</sup> Th	[3, 6, 10]- #41608	[12, 13], [14]- #23209		[20]- #22898
<sup>233</sup> U	[4, 8, 10]- #41616			
<sup>235</sup> U	[3, 6, 10]- #41608	[15, 16]	[17, 18]	
<sup>238</sup> U	[3, 6, 10]- #41608	[15]		[20]- #22898
<sup>237</sup> Np	[11]			
<sup>239</sup> Pu	[5, 9]- #41658			
<sup>nat</sup> Pb	[5, 9]- #41658			
<sup>209</sup> Bi	[4, 8, 10]- #41616			

It is seen that a large amount of new data has been obtained recently at the TOF spectrometer GNEIS. Comparison of angular distributions of fission fragments obtained in this work and literature data in neutron energy range less 20 MeV demonstrates that there is a good agreement between all experimental data. For example, Fig. 3 shows the angular distributions of fission fragments in the center-of-mass system for <sup>233</sup>U and <sup>239</sup>Pu for two neutron energy intervals,  $1.49 \pm 0.16$  MeV (left part of Fig. 3) and  $15.7 \pm 1.4$  MeV (right part of Fig. 3) in comparison with experimental data of other authors [21–25]. The results of the data fitting by the sum of even Legendre polynomials up to the 4th order are also shown in Fig. 3. It should be noted that experimental techniques used by referred authors differ both in fragment detectors and in neutron sources. It may be interpreted as a convincing proof of accuracy and reliability of our measurement technique and data handling procedure, at least in the neutron energy range below 20 MeV.

The reliability of the experimental set-up and data processing applied in this work is confirmed by the fact that the obtained energy dependence of anisotropy is the same as in the other works (see [3–11]). It can be stated that the results obtained at the GNEIS below ~ 20 MeV adequately represent the structures in energy behavior of the anisotropy observed in early measurements. A comparison of our results obtained in the neutron energy range 20–200 MeV with the latest data measured by NEFFTE and n\_TOF collaborations demonstrates a good agreement between these data within experimental uncertainties.

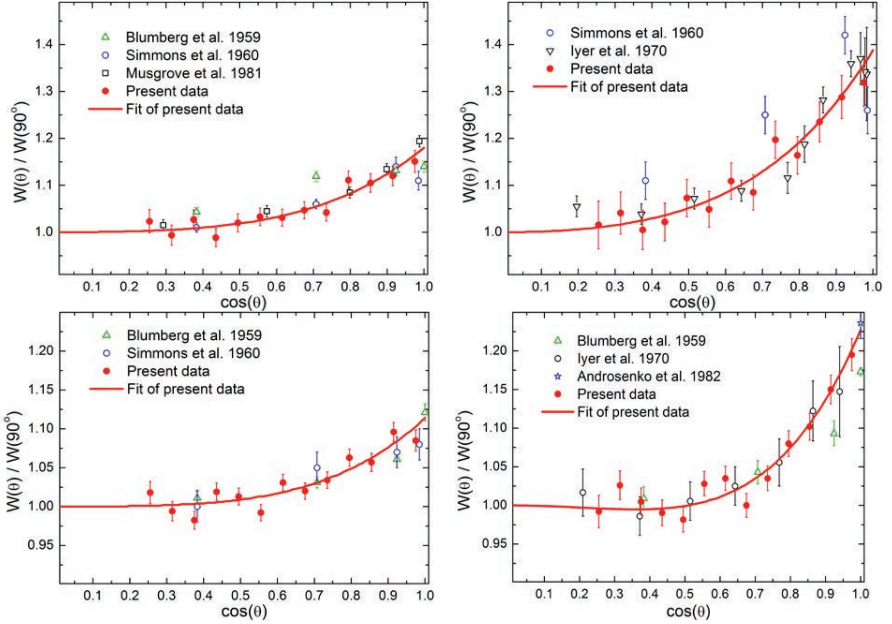


Fig. 3. Example of angular distributions for  $^{233}\text{U}(n,f)$  – upper part and  $^{239}\text{Pu}(n,f)$  – lower part. The error bars represent statistical uncertainties. Solid line is a result of the fitting by the sum of even Legendre polynomials up to the 4th order.

The anisotropy of the angular distribution of fragments is a consequence of the spin orientation of the fissioning nucleus, which arises due to the orbital momentum of incident neutrons is perpendicular to the direction of their motion ( $z$  axis). The angular distribution of fragments from fission of the nucleus with spin  $J$  and parity  $\pi$  is described by the formulas

$$\frac{dw^{J\pi}(\theta)}{d\Omega} = \sum_M \eta^{J\pi}(M) \sum_K \rho^{J\pi}(K) \frac{dw_{MK}^J(\theta)}{d\Omega}, \quad dw_{MK}^J(\theta) = \frac{2J+1}{4\pi} |d_{MK}^J(\theta)|^2 d\Omega. \quad (1)$$

The diagonal elements of spin density matrix  $\eta^{J\pi}(M)$  and the quantities  $\rho^{J\pi}(K)$  determine the probability distributions over projections  $M$  and  $K$  of spin  $J$  on the axis  $z$  and the nuclear deformation axis, respectively. The distribution over  $K$  is defined by the fission mechanism as well as by the shape of the nucleus at the saddle point; here  $\rho^{J\pi}(K) = \rho^{J\pi}(-K)$ , if we neglect the very small effects of parity violation. The spin orientation can also be given by irreducible components of the density matrix or, in other words, by the orientation spin-tensors

$$\tau_{Q0}(J\pi) = \sum_M C_{JM0}^{JM} \eta^{J\pi}(M), \quad (2)$$

where  $C_{BbDd}^{Aa}$  are Clebsch-Gordan coefficients.

Expressions (2) can be conveniently converted to the following form

$$\frac{dw^{J\pi}(\theta)}{d\Omega} = \frac{1}{4\pi} \sum_Q (2Q+1) \tau_{Q0}(J\pi) \beta_Q(J\pi) P_Q(\cos\theta), \quad (3)$$

where the anisotropy parameters are defined by the formula

$$\beta_Q(J\pi) = \sum_K C_{JKQ0}^{JK} \rho^{J\pi}(K), \quad (4)$$

and  $P_Q(\cos\theta)$  are the Legendre polynomials. Summation is carried out only over even values of  $Q$  due to  $\rho^{J\pi}(K) = \rho^{J\pi}(-K)$ . If the distribution  $\rho^{J\pi}(K)$  ( $\eta^{J\pi}(M)$ ) is smooth, then the parameters  $\beta_Q(J\pi)$  (the spin-tensors  $\tau_{Q0}(J\pi)$ ) decrease rapidly with an increase of  $Q$ .

In neutron-induced reaction, an arising compound nucleus decays either into a particle and residual nucleus (generally, excited) or into two fragments. Another possibility is that after the collision, some particle and some residual nucleus are formed as a result of a direct or pre-equilibrium process (we neglect the output channels with three or more particles). We assume for simplicity that all excited residual nuclei are in equilibrium compound states and, consequently, their further decay (into a particle and a new residual nucleus or into two fragments) is described by the statistical model (as the decay of the primary compound nucleus). Let the index  $i$  numerates the levels of a nucleus (with  $Z$  protons and  $N$  neutrons) with the same spin  $J$  and parity  $\pi$ ,  $\sigma_{ZN}(J\pi i)$  is the population cross section of the corresponding level, and  $P_f^{ZN}(J\pi i)$  is the fission probability for the nucleus on this level. Thus, the observed fission cross section is determined by

$$\sigma_f = \sum_{ZNI\pi} \sigma_{ZN}(J\pi i) P_f^{ZN}(J\pi i), \quad (5)$$

where summation over  $i$  is an integration if the levels lie in the continuum. Clearly, each cross section  $\sigma_{ZN}(J\pi i)$  is a sum of population cross sections  $\sigma_{ZN}(J\pi i M)$  of states  $(J, \pi, i)$  with definite spin projection  $M$  on the axis  $z$  (then  $\eta_{ZN}^{J\pi i}(M) = \sigma_{ZN}(J\pi i M) / \sigma_{ZN}(J\pi i)$ ), while the probability  $P_f^{ZN}(J\pi i)$  is a sum of probabilities of fission  $P_f^{ZN}(J\pi i K)$  via transition states with projection  $K$  of spin on the deformation axis (then  $\rho_{ZN}^{J\pi}(K) = P_f^{ZN}(J\pi i K) / P_f^{ZN}(J\pi i)$ ). Therefore, the observed differential fission cross section takes the form

$$\frac{d\sigma_f(\theta)}{d\Omega} = \sum_{ZNI\pi} \sigma_{ZN}(J\pi i) P_f^{ZN}(J\pi i) \frac{dw_{ZN}^{J\pi i}(\theta)}{d\Omega} = \frac{1}{4\pi} \sum_{Q=0,2,4,\dots} \sigma_{fQ} P_Q(\cos\theta), \quad (6)$$

where

$$\sigma_{fQ} = (2Q+1) \sum_{ZNI\pi} \sigma_{ZN}(J\pi i) P_f^{ZN}(J\pi i) \tau_{Q0}^{ZN}(J\pi i) \beta_Q^{ZN}(J\pi i), \quad (7)$$

and  $\sigma_{f0} = \sigma_f$ .

Thus, the observed fission fragment angular distribution

$$W(\theta) \equiv \frac{1}{\sigma_f} \frac{d\sigma_f(\theta)}{d\Omega} = \frac{1}{4\pi} \left( 1 + \sum_{Q=2,4,\dots} A_Q P_Q(\cos\theta) \right) \quad (8)$$

is a series over Legendre polynomials. Since, in practice, at least one of the distributions over  $M$  or over  $K$  is smooth, the coefficients  $A_Q$  rapidly decrease with increasing of  $Q$ , so that with rare exceptions, the shape of the angular distribution is determined by a single parameter  $A_2$ . This parameter can be derived from angular anisotropy  $W(0^\circ)/W(90^\circ)$ . But even if  $A_4$  is significantly different from zero (but always significantly less than  $A_2$ ), the results of measurements of angular distributions of fragments are usually recalculated into anisotropy by the formula (1).

Earlier, only in the work [20] an appropriate attempt was made to describe the angular distribution of fragments in nuclear fission by neutrons in a wide range of energies, up to 100 MeV. The results of the calculations were compared with the experimental data on  $^{232}\text{Th}$  and  $^{238}\text{U}$  target nuclei presented in the same work. However, there were no further publications by these authors, which would have provided the necessary details about the method used or performed calculations for other target nuclei.

We made simplifications in the calculation scheme using the following qualitative considerations. The spin  $\vec{J} = \vec{s} + \vec{I} + \vec{l}$  of the compound nucleus consists of the spins of the incident particle  $s$ , the target nucleus  $I$ , and the relative orbital momentum  $l$ . If  $s$  and  $I$  are not oriented, then the spin  $J$  is directed primarily across the axis  $z$ . At high energies  $l$  (and  $J$ ) is large, so that the spin orientation of the compound core is very noticeable. At the same time, the particles emitted during the statistical decay of the compound nucleus have relatively low energies, of the order of nuclear temperature, and, consequently, carry away small angular momenta. Therefore, the orientation of the residual core remains noticeable. If there is a direct or pre-equilibrium process, the particles are usually emitted with high energies and, consequently, with large angular momenta. Therefore, there is no reason to expect that the residual nuclei will have a noticeable spin orientation. Therefore, we have identified two components in the total fission cross section,  $\sigma_f^{DPE}$  and  $\sigma_f^C$ . The first one is due to the fission of residual nuclei, the formation of which was preceded by a direct (D) or preequilibrium (PE) process, while the second contribution (C) is due to the fission of the compound nucleus and the residual nuclei formed at some stage of statistical decay of the primary compound nucleus. Assuming the DPE component of the differential fission cross section is completely isotropic, instead of (7), (8) we get

$$\frac{d\sigma_f(\theta)}{d\Omega} = \frac{\sigma_f}{4\pi} + \frac{1}{4\pi} \sum_{Q=2,4,\dots} \sigma_{fQ}^C P_Q(\cos\theta), \quad (9)$$

where the quantities

$$\sigma_{fQ}^C = (2Q+1) \sum_{ZNI\pi} \sigma_{ZN}^C(J\pi i) P_f^{ZN}(J\pi i) \tau_{Q0}^{CZN}(J\pi i) \beta_Q^{ZN}(J\pi i) \quad (10)$$

are determined by the population cross sections  $\sigma_{ZN}^C(J\pi i)$  and the orientation spin-tensors  $\tau_{Q0}^{CZN}(J\pi i)$  of the levels, which belong either to the primary compound nucleus or to the residual nuclei formed in the statistical decay of this compound nucleus.

The details of the calculation of the anisotropy parameters (5) are given in the article [11]. Here we only point out that above the barrier we use a statistical distribution,  $\rho_{ZN}^{J\pi i}(K) \sim e^{-K^2/2K_0^2}$ , where the parameter  $K_0^2 = J_{\text{eff}}T / \hbar^2$  is determined by the nuclear temperature  $T$  on the barrier and the effective moment of inertia  $J_{\text{eff}}$ , while below the barrier we take  $\rho_{ZN}^{J\pi i}(K) \sim e^{-\alpha(|K|-K_1)^2}$ , where  $\alpha$  is a fixed parameter, and  $K_1$  is the spin projection for the dominant transition state. In the region of intermediate collision energies, fissioning nuclei tend to have sufficiently high excitation energies, so that the shape of distribution over  $K$  for energies below the barrier is insignificant for most isotopes. Only in the region of very low collision energies, when the fission of the compound nucleus  $^{238}\text{Np}$  is sub-barrier, the value of  $K_1$  for the isotope  $^{238}\text{Np}$  determines the type of angular distribution of the fragments; the choice of  $K_1$  for the isotope  $^{237}\text{Np}$  in the region of the threshold energy for the reaction  $(n,n'f)$  is also significant. We have considered the parameter  $K_1$  as adjustable only for  $^{238}\text{Np}$ , but  $K_1$  was assumed to be 0.5 for  $^{237}\text{Np}$  and 1.5 for all other isotopes.

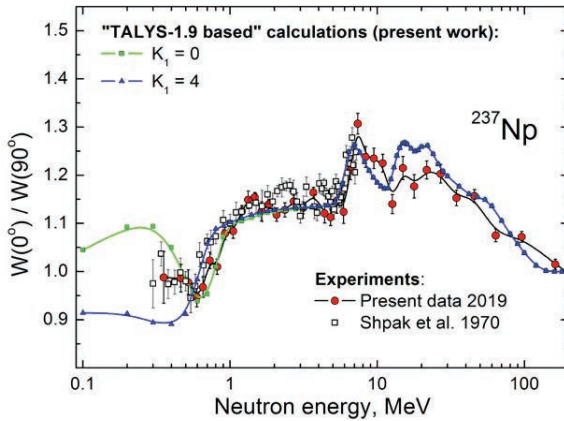


Fig. 4. Anisotropy of fission fragments of  $^{237}\text{Np}$ . Points with error bars – experimental data. Lines with symbols – calculation performed using the proposed method with  $K_1$  equals to 0 and 4 for  $^{238}\text{Np}$ .

There are a lot of computer codes that simulate collisions of particles with nuclei at energies from low to intermediate; the multi-purpose complex TALYS [26] is one of them. However, the angular distributions of fission fragments cannot be calculated either in TALYS or in other similar programs, even at low energies, as well as at the entire intermediate region up to 200 MeV. We made the additions to the TALYS program to calculate the orientation spin-tensors of nuclear states and the anisotropy parameters. Thus, we obtained a tool for calculating the angular distributions of fragments. The results obtained for the reaction  $^{237}\text{Np}(n,f)$  are shown in Fig. 4 together with our experimental data and values of the anisotropy from Ref. [27]. There is a good agreement between the experiment and model calculation.

## 4. Conclusion

The purpose of our research is to obtain new experimental data on the angular distributions of fission fragments for different target nuclei in the neutron energy range from 1 to 200 MeV, as well as to develop theoretical models and computer codes describing experimental distributions. In this paper we presented the results of recent measurements for the reaction  $^{237}\text{Np}(n,f)$  as well of the calculations for the same reaction. For the entire specified energy range, such results are obtained and demonstrated for the first time. We used a modified software package TALYS. At this initial stage of the work with this code, simplifications were introduced to the model to minimize the number of additional parameters, in addition to those used in TALYS. So, for example, for all fissioning nuclei at all excitation energies, one value of the effective moment of inertia was used, obviously, this is some average value. With a reasonable value of this parameter, the calculated curve describes the gross structure of the energy dependence of the angular anisotropy of the fragments in the whole energy range of 0.5–200 MeV. An agreement of the calculated values of the angular anisotropy of fission fragments with the measured ones is also due to taking into account the connection between the formation of angular anisotropy and compound nuclei decays. This allowed us to relate the decrease in the angular anisotropy in the region of neutron energies above 20–30 MeV with increase of the contributions of pre-equilibrium reactions. These results indicate both the appropriateness of our approach and the prospects for its further improvement in order to obtain new, more detailed information about characteristics of nuclei on barriers, as well as the role of preequilibrium processes in the interaction of nuclei with neutrons. Our next goal is the measurement and analysis of the fission fragment angular distributions for  $^{240}\text{Pu}$ . The only two data sets for this nucleus were obtained earlier [28, 29]. An upper neutron energy range of these data does not exceed 10 MeV.

## Acknowledgments

The authors would like to thank the staff of the Accelerator Department of the NRC KI - PNPI for their permanent friendly assistance and smooth operation of the synchrocyclotron during the experiment, and T.E. Kuz'mina (Khlopin Radium Institute, St. Petersburg, Russia) for cooperation in the preparation of high-quality actinide targets. This work was supported in part by the Russian Foundation for Basic Research (Project no. 18-02-00571).

## References

1. N.K. Abrosimov, G.Z. Borukhovich, A.B. Laptev, V.V. Marchenkov, G.A. Petrov, O.A. Shcherbakov, Yu.V. Tuboltsev, V.I. Yurchenko. Nucl. Instrum. Methods Phys. Res. A **242**, 121 (1985).
2. O.A. Shcherbakov, A.S. Vorobyev, E.M. Ivanov. Phys. Part. Nucl. **49**, 81 (2018).
3. A.S. Vorobyev, A.M. Gagarski, O.A. Shcherbakov, L.A. Vaishnene, A.L. Barabanov. JETP Letters **102**(4), 203 (2015).
4. A.S. Vorobyev, A.M. Gagarski, O.A. Shcherbakov, L.A. Vaishnene, A.L. Barabanov. JETP Letters **104**(6), 365 (2016).
5. A.S. Vorobyev, A.M. Gagarski, O.A. Shcherbakov, L.A. Vaishnene, A.L. Barabanov. JETP Letters **107**(9), 521 (2018).
6. A.M. Gagarski, A.S. Vorobyev, O.A. Shcherbakov, L.A. Vaishnene. In: "XXIII International Seminar on Interaction of Neutrons with Nuclei", Dubna, May 25–29, 2015. JINR, E3-2016-12, 2016, p.73.

7. A.M. GagarSKI, A.S. Vorobyev, O.A. Shcherbakov, L.A. Vaishnene. In: "XXIV International Seminar on Interaction of Neutrons with Nuclei", Dubna, May 24–27, 2016. JINR, E3-2017-8, 2017, p.343.
8. A.S. Vorobyev, A.M. GagarSKI, O.A. Shcherbakov, L.A. Vaishnene, A.L. Barabanov. In: "XXIV International Seminar on Interaction of Neutrons with Nuclei", Dubna, May 24–27, 2016. JINR, E3-2017-8, 2017, p.413.
9. A.M. GagarSKI, A.S. Vorobyev, O.A. Shcherbakov, L.A. Vaishnene, A.L. Barabanov. In: "XXV International Seminar on Interaction of Neutrons with Nuclei", Dubna, May 22–26, 2017. JINR, E3-2018-12, 2018, p.342.
10. A.S. Vorobyev, A.M. GagarSKI, O.A. Shcherbakov, L.A. Vaishnene, A.L. Barabanov. Proc. of the Int. Conf. "Nuclear data for Science and Technology ND-2016", September 11–16, 2016, Bruges, Belgium. EPJ Web of Conferences **146**, 04011 (2017).
11. A.S. Vorobyev, A.M. GagarSKI, O.A. Shcherbakov, L.A. Vaishnene, A.L. Barabanov. JETP Letters **110**(4), 242 (2019).
12. L.S. Leong. PhD Thesis, Universite Paris Sud, CERN-Thesis-2013-254.
13. L.S. Leong, L. Tassan-Got, D. Tarrío, et al. Proc. of the Int. Conf. "Nuclear data for Science and Technology ND-2013", March 4–8, 2013, New York, USA. EPJ Web of Conferences **62**, 08003 (2013).
14. D. Tarrío, L.S. Leong, L. Audouin et al. Nuclear Data Sheets, **119**, 35 (2014).
15. E. Leal-Cidoncha, I. Duran, C. Paradela, et al. Proc. of "4<sup>th</sup> International Workshop on Nuclear Data Evaluation for Reactor applications WONDER-2015", October 5–8, 2015, Aix-en-Provence, France. EPJ Web of Conferences **111**, 10002 (2016).
16. E. Leal-Cidoncha, et al. FIESTA 2017, LANL FIESTA Fission School & Workshop, Santa Fe, 17–22 September 2017. <https://t2.lanl.gov/fiesta2017/Talks/Leal-Cidoncha.pdf>
17. V. Kleinrath. PhD Thesis, Technischen Universität Wien, 2015.
18. V. Geppert-Kleinrath, F. Tovesson, J.S. Barrett et al. (NIFTE Collaboration), Phys. Rev. C **99**, 064619 (2019).
19. V.V. Zerkín, B. Pritychenko. Nuclear Instruments and Methods. 2018. V. **888**. P. 31. <http://www.nndc.bnl.gov/exfor>
20. I.V. Ryzhov, M.S. Onegin, G.A. Tutin, J. Blomgren, N. Olsson, A.V. Prokofiev, P.-U. Renberg. Nucl. Phys. A **760**, 19 (2005).
21. J.E. Simmons, R.L. Henkel. Phys. Rev. **120**, 198 (1960).
22. R.H. Iyer, M.L. Sagú. Proc. of the Nuclear Physics and Solid State Physics Symposium, Dec. 27–30, 1970; Madurai, India: Nuclear Physics, Vol. **2**, p.57 (1970).
23. A.R. Musgrove, J.W. Boldeman, J.L. Cook, D.W. Lang, E.K. Rose, R.L. Walsh, J. Caruana, J.N. Mathur. J. Phys. G: Nucl. Phys. **7**, 549 (1981).
24. L. Blumberg, R.B. Leachman. Phys. Rev. **116**, 102 (1959).
25. Kh.D. Androsenko, G.G. Korolev, D.L. Shpak. VANT, Ser. Yadernye Konstanty **46**(2), 9 (1982).
26. A.J. Koning, S. Hilaire, M.C. Duijvestijn. "TALYS-1.0", Proc. Int. Conf. on Nuclear Data for Science and Technology (Nice, France, 2007), ed. by O. Bersillon, F. Gunsing, E. Bauge, R. Jacqmin, and S. Leray, EDP Sciences (2008), p.211.
27. D.L. Shpak, B.I. Fursov, G.N. Smirenkin. Sov. J. of Nucl. Physics **12**, 19 (1971).
28. Kh.D. Androsenko, G.N. Smirenkin. Sov. J. of Nucl. Physics **12**, 142 (1971).
29. J.E. Simmons, R.B. Perkins, R.L. Henkel. Phys. Rev. **137**, B809 (1965).

Научное издание

**FUNDAMENTAL INTERACTIONS & NEUTRONS, NUCLEAR STRUCTURE,  
ULTRACOLD NEUTRONS, RELATED TOPICS**  
**XXVII International Seminar on Interaction of Neutrons with Nuclei**

*Proceedings of the Seminar*

**ФУНДАМЕНТАЛЬНЫЕ ВЗАИМОДЕЙСТВИЯ И НЕЙТРОНЫ,  
СТРУКТУРА ЯДРА, УЛЬТРАХОЛОДНЫЕ НЕЙТРОНЫ,  
СВЯЗАННЫЕ ТЕМЫ**

**XXVII Международный семинар по взаимодействию нейтронов с ядрами**

*Труды семинара*

Ответственная за подготовку сборника к печати *Л. В. Мицына*.

Сборник отпечатан методом прямого репродуцирования с оригиналов,  
предоставленных оргкомитетом.

E3-2020-10

Подписано в печать 20.04.2020

Формат 60×90/16. Бумага офсетная. Печать офсетная  
Усл. печ. л. 16,88. Уч.-изд. л. 29,29. Тираж 85 экз. Заказ № 59909

Издательский отдел Объединенного института ядерных исследований  
141980, г. Дубна, Московская обл., ул. Жолио-Кюри, 6.

E-mail: [publish@jinr.ru](mailto:publish@jinr.ru)

[www.jinr.ru/publish/](http://www.jinr.ru/publish/)